UNIVERSITY OF CALIFORNIA,
IRVINE

Searches for Supersymmetry in Multilepton Final States with the ATLAS Detector

DISSERTATION

submitted in partial satisfaction of the requirements
for the degree of

DOCTOR OF PHILOSOPHY

in Physics

by

Steve Farrell

Dissertation Committee:
Associate Professor Anyes Taffard, Chair
Associate Professor Daniel Whiteson
Professor Timothy Tait

2014

DEDICATION

For my mother, who brought me into this world,
and for my father, who inspired me to master it

TABLE OF CONTENTS

LIST OF FIGURES

LIST OF TABLES

ACKNOWLEDGMENTS

Physics graduate school has been a very rich and rewarding experience. My time spent studying coursework, researching at CERN, and socializing with the many great people met along the way has had a considerable impact on my intellectual and personal development. This thesis represents the culmination of the past five years of hard work. Many late nights making plots and checking numbers went into this, as well as more meetings than any human should ever withstand. I am proud of this achievement, of making a contribution to science at the front lines of our understanding of nature, but I owe a great deal of credit to the brilliant colleagues and fantastic friends that have helped me to learn and grow as a scientist and a person.

First and foremost, my wife, whom I met and married during my graduate studies, deserves considerable acknowledgment for her support and patience throughout the ordeal. Not only did she put up with my odd working hours and long distance correspondence, she was a great source of comfort during my times of stress and a good friend with whom to share ideas and laughter.

Special thanks are given to the UCI faculty who have guided me. I would like to thank my research advisor Anyes Taffard for her leadership, wisdom, and her encouragement to always keep pushing forward. Next, I thank Daniel Whiteson for his intellect, valued advice, and inspiring communication skills. Also, Timothy Tait deserves my gratitude for being on my thesis and advancement committees.

The students and post-docs of the UCI ATLAS group have all been great people to know and work alongside. Thanks to Brokk, Kanishka, Matt, Mike, Andy, Serhan, and Ning for keeping things interesting in the office and for great beer-breaks and general banter.

The electroweak SUSY multilepton group is my analysis family. Big thanks go to analysis contacts Tina Potter and Zoltan Gecse who lead the efforts and were very pleasant to work with. Thanks are also due for my fellow plot-making students for being dependable hard workers. The late night unblinding sessions were intense but also pretty fun.

To the rest of the SUSY group, the conveners, sub-conveners, and other analyzers: thank you for your analysis expertise and general brilliance. Special thanks to Anadi Canepa for her advice and encouragement.

Thank you to my colleagues of the Data Quality group, Tobias Golling, Peter Onyisi, and Peter Waller for their expertise and assistance in my service work.

I would like to thank all my additional friends at UCI and at CERN, who have made graduate school a truly unforgetable experience. Pub nights, PGC parties, snowboarding trips, and jam sessions were instrumental in countering the stresses of analysis reviews and deadlines. I won't list you all by name, but you know who you are.

To my father and step-mother: thank you for all the emotional support, for always keeping

a place for me to stay (in the same mess I left it), and for generally being awesome people. You have all my gratitude and love.

To my French family: thank you for being so welcoming and generous with your hospitality during my visits to France.

Finally, I'd like to spend a moment to acknowledge that even with all of this human support, one cannot make it this far without some assistance from a higher, spiritual power. So, I must give the biggest thanks of all to... the flying spaghetti monster. Ramen.

Steven A Farrell
Curriculum Vitae

University of California, Irvine
Physics and Astronomy
2107 Frederick Reines Hall
Irvine, CA 92697-4575
☎ *+1 218-348-4855*
✉ *steven.farrell@cern.ch*

Education

2014 **Ph.D. in Physics**, *University of California, Irvine*,
Searches for Supersymmetry in Multilepton Final States with the ATLAS Detector.
Advisor: Prof. Anyes Taffard

2011 **M.S. in Physics**, *University of California, Irvine*.

2007 **B.S. in Physics and Mathematics**, *University of Minnesota, Duluth*.

Research Experience

2009–present **Research Assistant**, *University of California, Irvine*, ATLAS Experiment, CERN.
Advisor: Prof. Anyes Taffard
Performance of missing transverse energy
Searches for supersymmetry in events with three or more leptons using simplified models
Data acquisition monitoring
Development and improvement of data quality monitoring infrastructure

2008 **Research Assistant**, *Duke University*.
Advisor: Prof. Kate Scholberg
The Supernova Early Warning System
Simulation studies of the CLEAR detector

2006-2008 **Research Assistant**, *University of Minnesota, Duluth*, MINOS Experiment.
Advisor: Prof. Alec Habig
Cosmic ray studies with the MINOS Far Detector

Teaching Experience

2008-2009 **Teaching Assistant**, *University of California, Irvine*.
Taught general physics laboratory and discussion sessions for engineering and biology students

2006-2007 **Teaching Assistant**, *University of Minnesota, Duluth*.
Taught laboratory courses for general physics

2005-2007 **Grader**, *University of Minnesota, Duluth*.
Graded homework and quizzes for general physics courses

Awards

2008 Regent's Fellowship, *University of California, Irvine*

2007 Sigma Pi Sigma

2006 The Peterson Memorial Scholarship *University of Minnesota, Duluth*

2006 The Hanson Scholarship *University of Minnesota, Duluth*

Technical Skills

Operating systems	UNIX, Linux, Windows, and Mac OSX
Programming languages	C++, Python, Perl, Fortran
Software tools	ROOT, Geant4, Matlab, Mathematica, Labview

Presentations

Sep 2013	"Searches for Supersymmetry with the ATLAS Detector in Multilepton Final States", invited talk, University of California, Santa Barbara.
August 2013	"Search for direct production of charginos and neutralinos in events with three leptons and missing transverse momentum with the ATLAS detector", contributed talk at the APS DPF Meeting, University of California, Santa Cruz.
July 2013	"Search for direct production of charginos and neutralinos in events with three leptons and missing transverse momentum", contributed talk at the US ATLAS Physics Workshop, Argonne National Laboratory.
May 2013	"SUSY Searches for EWK Production of Gauginos and Sleptons at the LHC", invited talk at the 25th Rencontre de Blois - Particle Physics and Cosmology.
May 2012	"ATLAS offline data quality upgrade", poster presented at CHEP 2012.
April 2011	"Search for new physics in the trilepton channel with the ATLAS detector", contributed talk at the APS April Meeting.

Publications

This is a partial list, including only papers with significant contributions.

Journal Articles

[1] G. Aad *et al.* [ATLAS Collaboration], "Search for R-parity-violating supersymmetry in events with four or more leptons in $\sqrt{s} = 7$ TeV pp collisions with the ATLAS detector," JHEP **1212**, 124 (2012) [arXiv:1210.4457 [hep-ex]].

[2] G. Aad *et al.* [ATLAS Collaboration], "Search for direct production of charginos and neutralinos in events with three leptons and missing transverse momentum in $\sqrt{s} = 7$ TeV pp collisions with the ATLAS detector," Phys. Lett. B **718**, 841 (2013) [arXiv:1208.3144 [hep-ex]].

[3] G. Aad *et al.* [ATLAS Collaboration], "Search for supersymmetry in events with three leptons and missing transverse momentum in $\sqrt{s} = 7$ TeV pp collisions with the ATLAS detector," Phys. Rev. Lett. **108**, 261804 (2012) [arXiv:1204.5638 [hep-ex]].

Conference Papers

[4] G. Aad *et al.* [ATLAS Collaboration], "Search for direct production of charginos and neutralinos in events with three leptons and missing transverse momentum in 21 fb^{-1} of pp collisions at $\sqrt{s} = 8$ TeV with the ATLAS detector," ATLAS-CONF-2013-035, CERN, Geneva, Mar 2013.

[5] G. Aad *et al.* [ATLAS Collaboration], "Search for supersymmetry in events with four or more leptons in 21 fb^{-1} pp collisions at $\sqrt{s} = 8$ TeV with the ATLAS detector," ATLAS-CONF-2013-036, CERN, Geneva, Mar 2013.

[6] G. Aad *et al.* [ATLAS Collaboration], "Search for direct production of charginos and neutralinos in events with three leptons and missing transverse momentum in 13.0 fb^{-1} of pp collisions at $\sqrt{s} = 8$ TeV with the ATLAS detector," ATLAS-CONF-2012-154, CERN, Geneva, Nov 2012.

[7] G. Aad *et al.* [ATLAS Collaboration], "Search for supersymmetry in events with four or more leptons in 13 fb^{-1} pp collisions at $\sqrt{s} = 8$ TeV with the ATLAS detector," ATLAS-CONF-2012-153, CERN, Geneva, Nov 2012.

[8] G. Aad *et al.* [ATLAS Collaboration], "Search for supersymmetry in events with four or more leptons and missing transverse momentum in pp collisions at $\sqrt{s} = 7$ TeV with the ATLAS detector," ATLAS-CONF-2012-001, CERN, Geneva, Jan 2012.

Conference Proceedings

[9] "ATLAS offline data quality system upgrade," S. Farrell, on behalf of the ATLAS Collaboration, CHEP Conference Proceedings, 2012, in print.

ABSTRACT OF THE DISSERTATION

Searches for Supersymmetry in Multilepton Final States with the ATLAS Detector

By

Steve Farrell

Doctor of Philosophy in Physics

University of California, Irvine, 2014

Associate Professor Anyes Taffard, Chair

Two searches for supersymmetry in multilepton final states are presented using pp collisions at $\sqrt{s} = 8$ TeV in the ATLAS detector. First, a search for electroweak production of charginos and neutralinos in the three-lepton plus missing transverse momentum channel is detailed with an emphasis on the fake-lepton background estimation technique. No significant excess above the Standard Model prediction is observed in the signal regions. Exclusion limits are thus placed on simplified models of $\tilde{\chi}_1^{\pm} \tilde{\chi}_2^0$ production and decays via intermediate sleptons, SM gauge bosons, and Higgs bosons. The results are also interpreted in terms of the phenomenological MSSM. Next, a search for R-parity violating and R-parity conserving supersymmetric scenarios in the four-lepton channel is presented. No significant excess is observed, so exclusion limits are placed on R-parity violating simplified models in which the lightest supersymmetric particle is the lightest neutralino, which promptly decays to leptons. Exclusion limits are also placed on R-parity conserving simplified models of $\tilde{\chi}_2^0 \tilde{\chi}_3^0$ production.

Chapter 1

Introduction

In the heart of mankind lies an interminable curiosity and desire to understand nature. This thirst for knowledge has propelled mankind into the modern age and is probably our greatest strength as a species. The study of physics embodies this spirit and has profound impacts on our society. Advancements in this field not only lead to a greater understanding of our universe, they also pave the way for achievements in technology and intellectual culture.

The study of physics teaches us to always keep asking questions: What is the nature of matter and energy? What is the nature of space and time? How did the universe begin, and how does it evolve? These questions not only make us think about our surroundings, they also relate to fundamental questions about our own existence and our future.

To answer these questions, particle physicists study the smallest constituents of matter and the interactions between them. Over the last century, many experiments have been carried out to measure particle phenomena and many models have been developed to explain the results. The volume of work has culminated in the formation of a Standard Model of particle physics which explains three of the four known fundamental interactions in nature: the electromagnetic, the strong, and the weak interactions. The gravitational interaction

is not handled in the Standard Model due to difficulties in maintaining consistency in the theory. Luckily this is sufficient for predictive power in the theory because the strength of the gravitational interaction is very small compared to the other three. However, because of this, the Standard Model is understood to be an effective model which describes nature well at low energies, while gravitational effects should only become important at very high energies which are currently inaccessible in laboratories.

Since the Standard Model is known to be incomplete, the field of particle physics is naturally imbued with a sense of humility and open mindedness. It is not a field weighed down by dogma, but one that is constantly striving to reinvent itself. Experiments are often designed with the goal of disproving current theories by looking for deviations from predictions. When evidence for beyond-Standard-model (BSM) physics is uncovered, excitement ripples throughout the field as experimentalists work to confirm the evidence with independent measurements and theorists try to develop new models which can describe the findings.

So far, experimental evidence for BSM physics has presented itself in a few different ways. Observations in neutrino experiments have shown that neutrinos have mass and can oscillate between the three known types. The Standard Model, however, assumes neutrinos to be massless and doesn't give an explanation for their observed nature. The next two pieces of evidence come from the cosmic frontier. Astronomical observations of galaxy rotation and gravitational lensing suggest that there is a significant amount of matter in space which does not interact via the electromagnetic interaction. This new type of matter is deemed dark matter and seems to make up 23% of the total energy content in the universe[1]. Again, the Standard Model has no explanation for this result and gives no further hint of the nature of this new type of matter. Finally, by studying the red-shift of supernovae at varying distances, astronomers are able to deduce that the universe is undergoing rapid expansion via an unknown mechanism. The mysterious phenomena is dubbed dark energy, and little

---

[1]The total mass-energy in the Universe is about 4% ordinary matter, ∼23% dark matter, and ∼73% dark energy [2]

is known about the source of the effect.

Several models for new physics have been proposed which can describe the BSM evidence observed in experiments and/or provide a more elegant theory which explains SM features in a new light. One of the most popular extensions to the SM is supersymmetry (SUSY), an idea which introduces a new symmetry of nature and doubles the number of particles in the SM. This extension can provide a Dark Matter candidate as well as explain several interesting features of the SM.

Experimental particle physics is collaborative in nature. Colliders such as the Large Hadron Collider (LHC) in Switzerland are home to experiments that seek to unravel the above mentioned mysteries as well as perform Standard Model measurements. The LHC is currently the highest energy collider in the world. It started taking data in 2010 and reached a center of mass energy of 8 TeV in 2012. In 2015 it is scheduled to restart at the design energy of 14 TeV. Two of the primary experiments on the LHC are ATLAS and CMS, multi-purpose experiments with large collaborations that can accomplish multiple physics goals: discover the Higgs boson and measure its properties (or disprove its existence), measure the parameters of the Standard Model in a new energy regime with great precision, and look for evidence of BSM physics. One important milestone already achieved at the LHC was the discovery in 2012 of a new particle consistent with the Higgs boson, the last remaining unconfirmed piece of the Standard Model.

The following thesis represents my contributions to this ever expanding field in the energy frontier as part of the ATLAS experiment. The first chapter details the Standard Model, its features, and its problems. The second chapter discusses supersymmetry as a way to address some of the SM problems. The third chapter will discuss the experimental apparatus: the Large Hadron Collider and the ATLAS detector. The fourth chapter will talk about data quality in ATLAS in terms of my contributions. The fifth chapter covers a search for electroweak SUSY in the three-lepton channel.

Chapter 2

The Standard Model

2.1   Overview

The Standard Model (SM) of particle physics is the most complete and experimentally verified model of nature at the fundamental level. It is a renormalizable quantum field theory (QFT) consistent with special relativity that describes the smallest indivisible constituents of matter and the interactions between them. The elementary particle content includes fermions (particles with half-integer spin) and bosons (particles with integer spin). The fermions, consisting of leptons and quarks, make up the ordinary matter observed in the universe. The vector bosons (with spin $= 1$) are the force carriers for the electromagnetic, weak, and strong interactions. These interactions are explained in the SM as emergent features of gauge symmetries imposed on the fermionic fields. Finally, a single scalar boson, the Higgs, plays an important role in the breaking of the electroweak symmetry and in the generation of masses for the fermions and vector bosons [3].

The fermionic fields in the Standard Model, the quarks and leptons, are organized as shown in Table 2.1. There are three generations of leptons and three generations of quarks. In each

generation is a charged lepton (e, μ, τ) paired with a neutral neutrino (ν_e, ν_μ, ν_τ), as well as an up-type quark (u, c, t) and a down-type quark (d, s, b). The masses of the charged leptons and quarks increase with each generation.

Table 2.1: The fermion content of the Standard Model [1].

Generation	Leptons			Quarks		
	Particle	Charge	Mass [MeV]	Particle	Charge	Mass [MeV]
1	e	± 1	0.511	u	+2/3	2.3
	ν_e	0	$< 2 \times 10^{-6}$	d	-1/3	4.8
2	μ	± 1	105.7	c	+2/3	1.3×10^3
	ν_μ	0	$< 2 \times 10^{-6}$	s	-1/3	95
3	τ	± 1	1.777×10^3	t	+2/3	173×10^3
	ν_τ	0	$< 2 \times 10^{-6}$	b	-1/3	4.2×10^3

The vector bosons in the Standard Model shown in Table 2.2 arise out of interactions from gauge symmetries. The SM is the most general renormalizable QFT locally invariant under transformations of the gauge symmetry $SU(3)_C \times SU(2)_L \times U(1)_Y$. In this expression, $SU(3)_C$ is the symmetry of the strong interaction. The generators of this symmetry provide 8 gluons to mediate the interaction. Gluons and particles which couple to gluons carry the color charge (hence the subscript "C"). $SU(2)_L \times U(1)_Y$ is the symmetry of the unified electroweak interaction. The generators of the $SU(2)_L$ piece give the three spin-one bosons W_μ^a, and the generator of the $U(1)_Y$ gives the spin-one B_μ. In the SM, the electroweak symmetry is spontaneously broken to the electromagnetic and weak symmetries and the W_μ^a and B_μ are replaced with the physical bosons mediating those interactions, the $W^\pm$ and the Z bosons for the weak interaction and the photon for the electromagnetic interaction. The mechanism for this symmetry breaking is explained in Section 2.2.

The gauge group representations for the fermions are shown in Table 2.3. Colored particles are in the triplet representation of $SU(3)_C$, which means there are three "colors": red, blue, and green. The left handed fermions within each generation form doublets under $SU(2)_L$ while the right handed fermions are in the singlet representation. Equivalently, the weak

Table 2.2: The vector boson content of the Standard Model [1].

Particle	Interaction	Charge	Mass [GeV]
γ	electromagnetic	0	0
g	strong	0	0
$W^{\pm}$	weak	± 1	80.385 ± 0.015
Z	weak	0	91.188 ± 0.002

interaction only couples to left handed fermions.

Table 2.3: The SM fermion gauge symmetry group representations for $SU(3)_C$ and $SU(2)_L$, as well as the quantum number for weak hypercharge, $U(1)_Y$ [3].

1st gen	2nd gen	3rd gen	$SU(3)_C$	$SU(2)_L$	$U(1)_Y$
$\begin{pmatrix} u_L \\ d_L \end{pmatrix}$	$\begin{pmatrix} c_L \\ s_L \end{pmatrix}$	$\begin{pmatrix} t_L \\ b_L \end{pmatrix}$	**3**	**2**	$\frac{1}{6}$
u_R	c_R	t_R	**3**	**1**	$\frac{2}{3}$
d_R	s_R	b_R	**3**	**1**	$-\frac{1}{3}$
$\begin{pmatrix} e_L \\ \nu_{eL} \end{pmatrix}$	$\begin{pmatrix} \mu_L \\ \nu_{\mu L} \end{pmatrix}$	$\begin{pmatrix} \tau_L \\ \nu_{\tau L} \end{pmatrix}$	**1**	**2**	$-\frac{1}{2}$
e_R	μ_R	τ_R	**1**	**1**	-1

2.2 Electroweak Symmetry Breaking: The Higgs Mechanism

The gauge symmetries of the previous section forbid the existence of mass terms for the charged fermions and vector bosons in the SM lagrangian. However, the masses of all of these particles (except the photon) have been measured to be nonzero. In fact, the formation of atomic matter depends on these particles having nonzero mass! The only way to allow for masses while preserving the predictive power and elegance of the gauge symmetry approach is to introduce a mechanism that *spontaneously* breaks the symmetry. This means that although the symmetry is respected in the model, it is not respected in the ground state of the vacuum.

The solution which has been adopted to spontaneously break the SM gauge symmetry is known as the *Higgs mechanism.* The idea was proposed by three different groups independently in 1964: Robert Brout and Francois Englert [4]; Peter Higgs [5]; and Gerald Guralnik, Carl R. Hagen, and Tom Kibble [6]. In the Higgs mechanism, a complex $SU(2)_L$ doublet scalar field is added to the SM with the following self-interaction potential:

$$V(\phi, \phi^\dagger) = \lambda(\phi^\dagger\phi)^2 - \mu^2\phi^\dagger\phi \qquad (2.1)$$

In this expression, λ must be positive to ensure stability and λ and μ^2 must be real to maintain unitarity in the SM. Furthermore, if μ^2 is positive then the potential takes the shape shown in Figure 2.1. The minimum of the potential resides not at zero but rather along a ring of constant $|\phi|$. Hence, the scalar field (known as the Higgs field) acquires a nonzero vacuum expectation value (VEV) which breaks the electroweak symmetry. The value of the VEV is given by $v = \sqrt{\mu^2/\lambda}$. By expanding the Higgs field about the true minimum, three of the four degrees of freedom of the complex doublet Higgs field become longitudinal components of the weak bosons and one real scalar field remains: the *Higgs boson, h.* The rotational symmetry in Figure 2.1 implies the existence of a surviving gauge symmetry. In fact, what happens in electroweak symmetry breaking is $SU(2)_L \times U(1)_Y \xrightarrow{breaks} U(1)_{\text{EM}}$, where $U(1)_{\text{EM}}$ corresponds to the unbroken electromagnetic symmetry with a massless photon.

After electroweak symmetry breaking, the SM fields acquire masses via their interaction terms with the Higgs field. The strength of the couplings with the Higgs field then determine the mass hierarchy of the SM. The fermion masses come from the Yukawa couplings with the Higgs field. The electroweak bosons W_μ^a and B_μ mix to form the new mass eigenstates
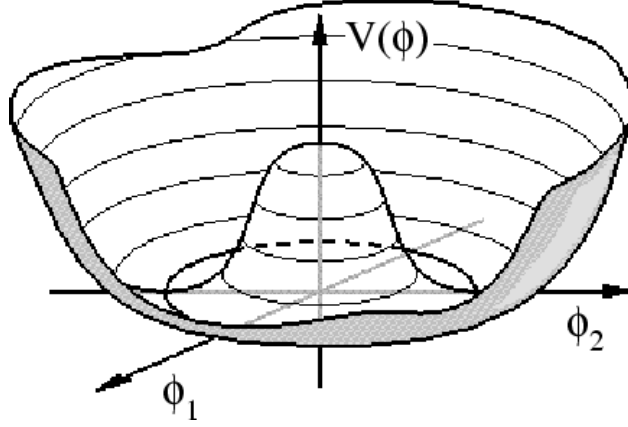
Figure 2.1: The SM Higgs potential. The two components ϕ_1 and ϕ_2 represent the real and imaginary components of the complex ϕ.

of the weak and electromagnetic interactions:

$$W_\mu^\pm = \frac{1}{\sqrt{2}}(W_\mu^1 \mp iW_\mu^2)$$

$$Z_\mu = W_\mu^3 \cos\theta_W - B_\mu \sin\theta_W$$

$$A_\mu = W_\mu^3 \sin\theta_W + B_\mu \cos\theta_W$$

In the above equations, θ_W is the weak-mixing angle defined in terms of the coupling strengths of the B_μ (g_1) and the W_μ^a (g_2) to the fermions:

$$\cos\theta_W = \frac{g_2}{\sqrt{g_1^2 + g_2^2}}$$

$$\sin\theta_W = \frac{g_1}{\sqrt{g_1^2 + g_2^2}}$$

The masses of the W and Z bosons are given in terms of the coupling strengths and the

Higgs VEV:

$$M_W = \frac{g_2 v}{2}$$
$$M_Z = \frac{1}{4}(g_1^2 + g_2^2)v^2$$
$$\frac{M_W}{M_Z} = \cos\theta_W$$

Finally, the mass of the Higgs boson is given by $m_h^2 = 2\lambda v^2 = 2\mu^2$ [3].

2.3 Limitations of the Standard Model

The Standard Model has been very successful at standing up to experimental tests over the past several decades, but it does suffer from some problems. The first problem is that the model is known to be incomplete; it has no description of gravity. Next, a few problems are related to experimental measurements which the SM cannot account for. These include the phenomena of neutrino masses, dark matter, and dark energy. These are the most glaring of issues, and require some as-yet unknown amendments to the model. Finally, the remaining issues are aesthetic and come from a desire to explain SM features in a more elegant and less empirical way. Some of these issues are described more fully below, though this is not an exhaustive list.

Despite considerable efforts by physicists to develop a quantum description of gravity, a successful theory has not yet been discovered. Most models typically suffer from non-renormalizable divergences. The Standard Model thus completely neglects the gravitational interaction, which means it is only an effective model relevant at low energies where the strength of the interaction is very small compared to the other three. One potential solution for this dilemma is superstring theory, which attempts to form a fully unified theory of everything. Unfortunately, superstring theory currently does not make any experimentally

9

testable predictions, so its real validity as a possible solution is unknown.

The most well understood example of the SM's incompatibility with experimental results is the case of neutrino masses. The Higgs mechanism described in the previous section does not, as is, generate masses for the (left handed) neutrinos. However, measurements of the neutrino flux from solar and atmospheric sources support the notion that neutrinos can oscillate between types, a feature that explicitly requires neutrinos to have mass [7]. Neutrino mass can be added to the SM in various ways. The simplest approaches involve adding Majorana mass terms for the neutrinos and/or adding additional right-handed neutrinos with a very heavy mass. The addition of right-handed neutrinos and other more exotic solutions involve new physics scales and could reveal physics beyond the SM.

The other experimental incompatibilities, Dark Matter and Dark Energy, are less well understood and could have dramatic implications for BSM physics. Dark Matter does not emit or absorb light at any significant level, but is observed in astrophysical measurements via its gravitational effects. For example, the rotation curves of galaxies suggest that there is considerably more mass in galaxies than accounted for in ordinary observable matter [8, 9]. Also, the effect of Dark Matter can be seen in the gravitational lensing of light passing through galaxy clusters [10]. The nature of the Dark Matter particle(s) is unknown, though a popular idea is that it consists of weakly-interacting massive particles (WIMPs) which could be detected in experiments [11]. Supersymmetry is one idea that can provide a WIMP candidate which will be explained in Chapter 3. Even less is known about Dark Energy. This feature comes from observations of the red-shift of supernovae in the universe as a function of distance [12]. Further galaxies are undergoing more rapid expansion than what can be explained already by particle physics and cosmology. Dark energy can be accounted for with a cosmological constant, but the true nature of the phenomena is unknown.

The remaining issues with the Standard Model are aesthetic in nature. The SM is a complex theory with many particles and 19 free parameters. There is no theoretical explanation

for *why* there are exactly three generations of fermions, or why the gauge symmetry is $SU(3)_C \times SU(2)_L \times U(1)_Y$. There is also no known fundamental reason why the electroweak scale is so small compared to the Planck scale. This issue is known as the hierarchy problem and has implications for the quantum corrections to the Higgs mass which will be explained in Section 3.1.

Chapter 3

Supersymmetry

3.1 Stabilizing the Higgs Mass

When calculating the quantum corrections to the Higgs mass via its SM interactions, one-loop diagrams like the one shown in Figure 3.1(a) give a contribution proportional to the cutoff scale squared, $\Delta m_h^2 \sim \Lambda^2$ [13]. In renormalization, these divergences require extreme fine tuning to maintain a low, stable Higgs mass. However, it is possible to remove the divergences in an elegant way by introducing additional particles with appropriate couplings and spin to cancel the contributions from each SM particle. This can be seen in the lower diagram of Figure 3.1.
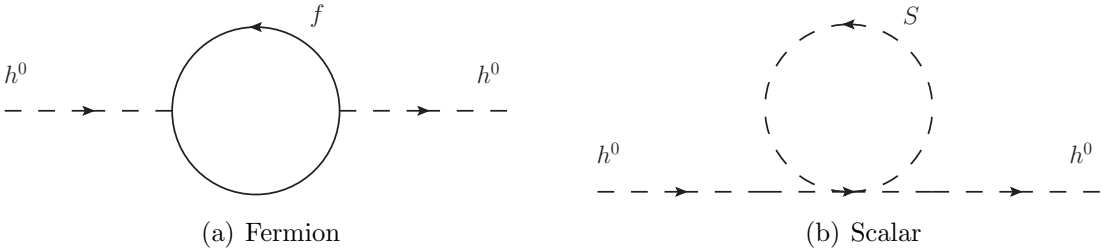
(a) Fermion   (b) Scalar

Figure 3.1: Loop level corrections to the Higgs mass from a fermion and a scalar.

By introducing partner particles for each SM particle which contributes to the Higgs mass in this way, the quantum divergences can be completely removed, resulting in a stable mass. This cancellation works at higher loop order as well. In each instance, the partner particle introduced must have the same mass and spin difference of one half relative to the SM counterpart, resulting in a pairing of degenerate fermions and bosons. This feature is strongly suggestive of a new theory of nature: supersymmetry.

3.2 General Features

Supersymmetry [13] is a symmetry that relates fermions to bosons. The symmetry algebra is generated with an operator Q that can transform fermions into bosons, and vice versa:

$$Q|\text{Boson}\rangle = |\text{Fermion}\rangle$$
$$Q|\text{Fermion}\rangle = |\text{Boson}\rangle$$

This transformation is unique compared to usual SM symmetries because Q is a *spinor*. Thus, it is fermionic and its symmetry algebra is defined in terms of anti-commutators:

$$\{Q_a, Q_b^\dagger\} = -2\sigma_{ab}^\mu P_\mu,$$
$$\{Q_a, Q_b\} = 0, \qquad \{Q_a^\dagger, Q_b^\dagger\} = 0,$$
$$[Q_a, P_\mu] = 0, \qquad [Q_a^\dagger, P_\mu] = 0.$$

The first anti-commutator relation gives back the generator of spacetime translations, P_μ, which suggests that supersymmetry is actually a *spacetime* symmetry. The Coleman-Mandula theorem states that no new spacetime symmetries can exist with non-trivial Lorentz trans-

formation properties [2]. However, this theorem did not consider conserved quantities that transform as *spinors*. Thus, it is often said that supersymmetry is the only possible extension of the known spacetime symmetries of particle physics [14].

In supersymmetric theories, the field content is grouped into *supermultiplets* that contain equal numbers of fermionic and bosonic degrees of freedom. In group theory terminology, each supermultiplet is an irreducible representation of the supersymmetry algebra. The fermion and boson states are called *superpartners* of each other. Superpartners must have the same mass and be in the same representation of the gauge group; i.e., they must have the same electric charges, weak isospin, and color.

The first type of supermultiplet contains a spin-1/2 Weyl fermion and two scalars ($n_B = n_F = 2$). It is convenient to group the two scalars into one complex scalar field. This type of supermultiplet is called a *chiral supermultiplet*. For the Standard Model fermions, whose chirality states transform under different representations of the gauge group, the left handed components and right handed components would each have to be in their own chiral supermultiplet with a corresponding complex scalar.

The second type of supermultiplet contains a spin-1 vector boson and a single spin-1/2 Weyl fermion. The boson must be massless for the theory to be renormalizable, so that again $n_B = n_F = 2$. Such a supermultiplet is called a *vector supermultiplet*.

There is still one more case we need to consider for a complete theory of nature. If we consider gravity in the SM, then there is a spin-2 graviton field which must also sit in a multiplet. The graviton is massless so there are two helicity states. It is then partnered with a spin-3/2 fermion. This describes a *gravity multiplet*, though it will not be described in depth in this thesis.

---

[2]According to Coleman and Mandula, only translations (with generator P_μ), rotations and boosts (with generator $M_{\mu\nu}$), and Lorentz scalars (like electric charge) are allowed. Scalars have trivial Lorentz transformation properties.

The spacetime aspect of supersymmetry can be made more explicit by introducing the concepts of *superspace* and *superfields*. Superspace is an extension of spacetime coordinates with two additional fermionic dimensions θ and $\theta^\dagger$. The SUSY operators Q then generate translations in superspace. In fact, the operators can be defined as:

$$Q = i\frac{\partial}{\partial\theta}$$
$$Q^\dagger = i\frac{\partial}{\partial\theta^\dagger}.$$

A superfield then combines the fields of a supermultiplet into a single entity which is a function of the superspace coordinates: $S = S(x^\mu, \theta, \theta^\dagger)$. The most general form for a chiral superfield Φ is given by

$$\Phi(x,\theta) = \phi(x) + \sqrt{2}\theta\chi(x) + \theta\theta F(x),$$

where ϕ is a complex scalar, χ is a Weyl fermion, and F is an auxiliary scalar field which is introduced to balance out the additional fermionic degrees of freedom when the Weyl fermion is off-shell. The auxiliary field is not given a kinetic term so it does not propagate, but it is necessary for consistency. Similarly, the general form for a vector superfield V is given by

$$V(x,\theta,\theta^\dagger) = \theta^\dagger\bar{\sigma}^\mu\theta A_\mu + \theta^\dagger\theta^\dagger\theta\lambda^\dagger + \frac{1}{2}\theta\theta\theta^\dagger\theta^\dagger D$$

where A_μ is the vector field, λ is a Weyl fermion, and D is another auxiliary field added to preserve supersymmetry off-shell. Finally, using superfields it is straightforward to write down interaction terms via the *superpotential*. The general form for a system of chiral superfields Φ_i is

$$W = L_i\Phi_i + \frac{1}{2}M_{ij}\Phi_i\Phi_j + \frac{1}{6}y_{ijk}\Phi_i\Phi_j\Phi_k.$$

The type of supersymmetry described in this thesis is $N = 1$ *global supersymmetry*. N in this case refers to the number of supersymmetry generators Q. Theories with $N > 1$ suffer from phenomenological problems. In the standard four dimensions, they are unable to account for the SM phenomenology. However, in some theories with extra dimensions, these models may be viable. Theories that consider *local supersymmetry* and include gravitational effects are also studied. More information on these ideas can be found in the literature [15, 16, 17, 18].

3.3   The Minimal Supersymmetric Standard Model

In the general formulation, supersymmetry allows for an arbitrary number of supermultiplets. It is natural to first consider the simplest case, however, in which only the minimal particle content is introduced to solve the hierarchy problem, and no additional supermultiplets are added. This is referred to as the Minimal Supersymmetric Standard Model (MSSM) and is (for now) the primary focus of most SUSY experimental and phenomenological studies.

It is natural to wonder if any of the existing SM particles can be superpartners of each other. The requirement of consistent gauge group representations within a supermultiplet rules out all of these possibilities except one. The Higgs boson is a scalar that must reside in a chiral supermultiplet with a neutral fermion that is a color singlet and part of an $SU(2)_L$ doublet. The neutrino is indeed such a particle, and there has been some theoretical interest in the idea that the neutrino is the superpartner of the Higgs [19, 20]. However, it turns out that this idea suffers from several challenging problems, including anomalies, lepton-number violation, and a neutrino mass inconsistent with experimental bounds. Thus, it is generally assumed that the partners of the SM particles are all new, undiscovered particles.

The particle content of the MSSM can be seen in Tables 3.1 and 3.2. The SUSY partners of the quarks, leptons, and neutrinos are scalar particles called squarks, sleptons, and

sneutrinos, respectively. The partners of the gauge bosons and Higgs bosons are fermions called gauginos and higgsinos, respectively. It is important to note that SUSY requires the existence of two SM Higgs doublets. In supersymmetry, two Higgs doublets are required to generate mass terms for the up and down type quarks via the Yukawa interactions. The result is that after electroweak symmetry breaking there are five Higgs particles: two CP-even neutral bosons h^0 and H^0, a CP-odd neutral boson A^0, and two charged bosons $H^\pm$. The lightest of these, h^0, is associated with the usual SM Higgs boson which has most likely been discovered at the LHC [21, 22].

Table 3.1: The chiral supermultiplet particle content of the MSSM. The quarks and squarks ($\times 3$ generations), the leptons and sleptons ($\times 3$ generations), and the Higgs and higgsinos each form chiral multiplets. The second column gives the superfield nomenclature. The last column specifies the gauge group representations and electric charge.

Names		Spin-0	Spin-1/2	$SU(3)_C, SU(2)_L, U(1)_Y$
squarks, quarks	Q	$(\tilde{u}_L, \tilde{d}_L)$	(u_L, d_L)	$(\mathbf{3}, \mathbf{2}, \frac{1}{6})$
	$\bar{u}$	$\tilde{u}_R^*$	$u_R^\dagger$	$(\bar{\mathbf{3}}, \mathbf{1}, -\frac{2}{3})$
	$\bar{d}$	$\tilde{d}_R^*$	$d_R^\dagger$	$(\bar{\mathbf{3}}, \mathbf{1}, \frac{1}{3})$
sleptons, leptons	L	$(\tilde{\nu}_L, \tilde{e}_L)$	(ν_L, e_L)	$(\mathbf{1}, \mathbf{2}, -\frac{1}{2})$
	$\bar{e}$	$\tilde{e}_R^*$	$e_R^\dagger$	$(\bar{\mathbf{1}}, \mathbf{1}, 1$
Higgs, higgsinos	H_u	(H_u^+, H_u^0)	$(\widetilde{H}_u^+, \widetilde{H}_u^0)$	$(\mathbf{1}, \mathbf{2}, \frac{1}{2})$
	H_d	(H_d^0, H_d^-)	$(\widetilde{H}_d^0, \widetilde{H}_d^-)$	$(\mathbf{1}, \mathbf{2}, -\frac{1}{2})$

Table 3.2: The vector supermultiplet particle content of the MSSM. The gluons and gluinos, the winos and W bosons, and the bino and B boson each form vector multiplets. The last column specifies the gauge group representations and electric charge.

Names	Spin-1/2	Spin-1	$SU(3)_C, SU(2)_L, U(1)_Y$
gluinos, gluons	$\tilde{g}$	g	$(\mathbf{8}, \mathbf{1}, 0)$
winos, W bosons	$\widetilde{W}^\pm, \widetilde{W}^0$	$W^\pm, W^0$	$(\mathbf{1}, \mathbf{3}, 0)$
bino, B boson	$\widetilde{B}$	B	$(\mathbf{1}, \mathbf{1}, 0)$

After electroweak symmetry breaking, the flavor eigenstates of the gauginos and higgsinos can mix to form the mass eigenstates. The neutral particles ($\widetilde{B}$, $\widetilde{W}^0$, $\widetilde{H}_u^0$, $\widetilde{H}_d^0$) mix to form four *neutralinos*: $\tilde{\chi}_1^0$, $\tilde{\chi}_2^0$, $\tilde{\chi}_3^0$, and $\tilde{\chi}_4^0$. The charged particles ($\widetilde{W}^\pm$, $\widetilde{H}_u^+$, $\widetilde{H}_d^-$) mix to form four *charginos*: $\tilde{\chi}_1^\pm$ and $\tilde{\chi}_2^\pm$. The decay characteristics of these particles depend on the mixing

parameters.

The superpotential of the MSSM is given by

$$W_{\text{MSSM}} = \bar{u}\boldsymbol{y}_u Q H_u - \bar{d}\boldsymbol{y}_d Q H_d - \bar{e}\boldsymbol{y}_e L H_d + \mu H_u H_d, \tag{3.1}$$

where the parameters $\boldsymbol{y}_u$, $\boldsymbol{y}_d$, and $\boldsymbol{y}_e$ are the SM Yukawa couplings as 3×3 matrices in family space.

3.4 Breaking the Symmetry

As mentioned in Section 3.1, the addition of the SUSY sparticles in the MSSM can completely cancel the divergent contributions to the Higgs mass when the partner pairs are mass degenerate. However, the existence of sparticles at SM masses is inconsistent with current experimental constraints. Luckily, it is possible to preserve supersymmetry as a viable extension to the SM and generate new mass terms via spontaneous symmetry breaking. The situation is then analogous to electroweak symmetry breaking which generates the fermion and gauge boson masses in the SM. Under this idea, supersymmetry is unbroken at some high energy scale at which all particle-sparticle pairs are degenerate. In the low energy theory, additional mass terms are generated for the sparticles which push their total masses beyond current experimental limits. The actual mechanism for SUSY breaking is unknown, but several possible ideas have been studied extensively. The general approach is to assume there is a "hidden sector" of fields where SUSY is spontaneously broken by some field acquiring a VEV (like the Higgs described in Section 2.2). The hidden sector then communicates the SUSY breaking to the MSSM sector via loop effects, such that *soft SUSY-breaking* terms are generated[3]. Three SUSY-breaking mediation schemes are studied extensively [13, 23]:

---

[3]Soft terms refers to mass terms like $M^2\phi^2$, $M\psi^2$, etc., with *positive* mass dimension. These terms are *super-renormalizable* and pose no risk to introduce quadratic radiative corrections which can re-introduce

Gravity mediated The soft terms are generated via gravitational sized interactions between the hidden sector and the MSSM. These interactions can be gravitational loop effects or higher dimension operators suppressed by the Planck scale. The most well studied and predictive of this type of scenario is minimal supergravity (mSUGRA), a locally-supersymmetric theory that only introduces four new parameters: grand unification mass parameters for the scalars (m_0) and gauginos/higgsinos ($m_{1/2}$), A_0, $\tan\beta$, and the sign of μ.

Gauge mediated The soft terms are generated via electroweak and strong interaction loop diagrams with new messenger particles. The messengers are new chiral supermultiplets that are charged under $SU(3)_C \times SU(2)_L \times U(1)_Y$. In this scenario, the scale for SUSY-breaking is below the Planck scale, even as low as 10^4 GeV.

Anomaly mediated This scenario is popular for theories with extra dimensions. One possibility is that in a 5-dimensional universe the MSSM supermultiplets are confined to a 4-dimensional brane and the hidden sector is confined on a separate, parallel brane. The soft terms are generated via anomalous violation of a local superconformal invariance.

If a specific SUSY breaking mechanism is assumed, then the resulting SUSY models can be very predictive and complete, with only a handful of free parameters (like the example of mSUGRA with four parameters). If no SUSY breaking scheme is assumed, then general parametrization of the soft SUSY breaking terms in the MSSM lagrangian yields 105 free parameters in the theory. This can be reduced, however, by imposing experimental and phenomenological constraints [13].

---

the hierarchy problem described in Section 3.1

3.5   R-Parity

In the general formulation described in the preceding sections, the following terms are allowed in the MSSM superpotential [13]:

$$W_{\not{R}_p} = \mu_i H_u L_i + \frac{1}{2}\lambda_{ijk} L_i L_j E_k^c + \lambda'_{ijk} L_i Q_j D_k^c + \frac{1}{2}\lambda''_{ijk} U_i^c D_j^c D_k^c. \tag{3.2}$$

These terms violate lepton and baryon number. An important consequence of this is that the proton is allowed to decay at a very high rate ($< 1s$), a feature which strongly disagrees with experimental constraints on the proton lifetime ($> 10^{32}s$). A common way to solve this problem is to introduce a discrete symmetry which forbids these terms called R-parity:

$$R\text{-parity} = (-1)^{2S+3B+L} = \begin{cases} +1 & \text{for ordinary particles} \\[2mm] -1 & \text{for super-partners} \end{cases} \tag{3.3}$$

If R-parity is conserved in the theory, then the proton is guaranteed to be stable.

An interesting consequence of R-parity conservation is that the lightest superpartner (LSP) cannot decay to Standard Model particles and is thus stable. A neutralino LSP is then an ideal candidate for WIMP dark matter. Many areas of SUSY parameter space are capable of producing a dark matter relic density which agrees with astronomical observations [24].

Models with R-parity violating terms are also interesting for experimental searches. Since proton decay requires the existence of both lepton and baryon number violation, a model which allows one or the other, but not both, will survive these constraints. These models do not provide a nice dark matter candidate but still preserve most of the other attractive features of supersymmetry.

3.6　Natural SUSY

As explained in Section 3.4, unbroken supersymmetry results in perfect cancellation of the Higgs mass divergences. However, a broken symmetry can partially destroy this nice feature and result in a theory that still depends on some amount of fine tuning. Natural SUSY models are those models which maintain relatively low fine tuning. In order to determine which models are natural and which are not requires this to be quantified. One possible choice is the stability of the electroweak scale identified by the Z boson mass, m_Z, with respect to SUSY model parameters [25]:

$$m_Z^2 = -2\mu^2 + 2\frac{m_{H_d}^2 - \tan^2\beta\, m_{H_u}^2}{\tan^2\beta - 1}$$
$$\Delta = \max_{a_i}\left(\left|\frac{a_i}{m_Z^2}\frac{\partial m_Z^2(a_i)}{\partial a_i}\right|\right)$$

The second expression quantifies the fine tuning, Δ. The important a_i parameters are:

- μ, the Higgs mass parameter, which enters at tree-level

- Third generation quark mass parameters

Once a criteria for ranking models by naturalness is defined, one can look at the features of natural models and draw conclusions about the sparticle mass spectra. Assuming that the new Higgs-like boson discovered recently at the LHC is the lightest Higgs boson of the MSSM, and taking into account current experimental constraints, some features of mass spectra in surviving natural SUSY models are common [26]:

- The stop quark masses should be below 500–700 GeV.

- The higgsinos (rather, one chargino and two neutralinos) should be below 200–350 GeV.

- The gluino should be below 900 GeV–1.5 TeV.

One can intuitively understand why these particles are important for naturalness because of the contributions of the associated SM particles to the Higgs quantum corrections. For example, the top quark is very heavy for a SM particle and thus its contribution is large and is the most important one in the cancellation of the divergences. Figure 3.2 shows an example mass hierarchy for natural models that are not yet fully excluded by experimental results.
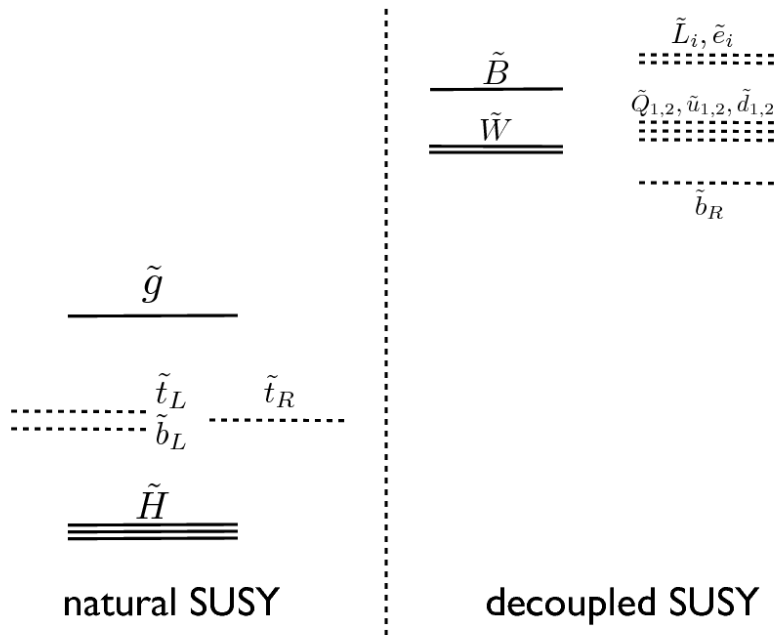
Figure 3.2: An example natural SUSY mass hierarchy. Stops, higgsinos, and gluinos should be not too high above the electroweak scale (174 GeV). Remaining particles can be higher without introducing much fine-tuning [26].

The discovery of the Higgs boson at a mass of 125 GeV has strong implications for viable natural SUSY models. In the limit of decoupling one Higgs doublet, the lightest Higgs mass is given by

$$m_h^2 = M_Z^2 \cos^2 2\beta + \delta_t^2,$$

where δ_t^2 is a loop contribution from top quarks and stop squarks. Bringing the Higgs to 125 GeV requires large stop masses, which then contributes to fine tuning. With maximal mixing in the stop squark masses, usually a minimum of 1% fine tuning is expected. Non-minimal supersymmetric models, such as the NMSSM which will be explained in Section 3.8, can accommodate a 125 GeV Higgs with significantly improved fine-tuning [27].

3.7   Experimental Signatures

Supersymmetry is a large, complex framework for building models with many different possible experimental signatures which can depend strongly on the parameters of the theory. The bottom line is that under the assumption that sparticles couple to the SM, they can be produced in particle colliders so long as the collision energy is high enough to produce them at rest. Beyond that, the nature of the production and decay modes depends on whether or not we assume conservation of R-parity.

3.7.1   R-parity Conserving Signatures

When R-parity is conserved, there are limitations on the types of couplings allowed in the theory and thus on the production modes allowed. In particle colliders, sparticles can only be produced in even numbers (usually two at a time), and each sparticle must decay to a final state of SM particles and an odd number of LSPs (possibly via additional intermediate sparticles). As mentioned in Section 3.5, the LSP is stable; it cannot decay to SM particles. Thus, the LSP will escape detection and result in a missing momentum signature in a particle detector.

At the LHC, sparticles can be produced via the strong or electroweak interactions. Some examples of strong pair production modes of gluinos and squarks can be seen in Figure 3.3.

Some examples of electroweak production modes can be seen in Figure 3.4. Electroweak production modes include pair production of charginos, neutralinos, and sleptons.
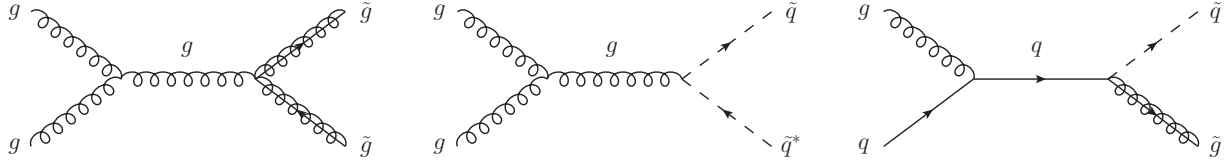
Figure 3.3: Tree level s-channel diagrams for strong production of gluinos and squarks. Additional t-channel and u-channel diagrams exist for each of these.
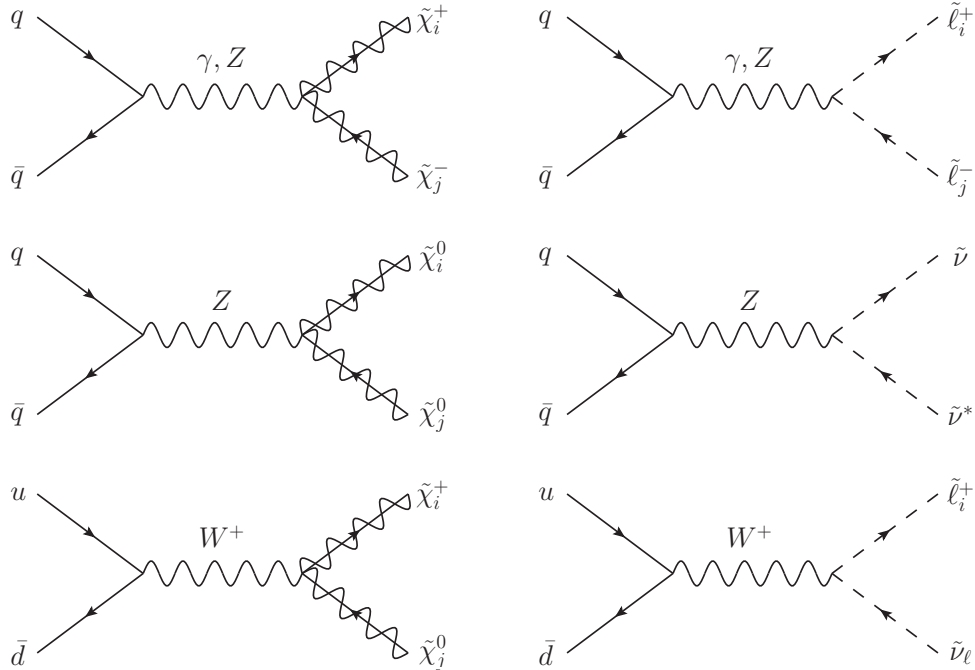
Figure 3.4: Tree level s-channel diagrams for electroweak production of charginos, neutralinos, and sleptons. Additional t-channel and u-channel diagrams exist for the diagrams on the left.

Decay modes and branching fractions of sparticles depend on model parameters such as sparticle masses and the mixing parameters. For example, the $\tilde{\chi}_1^\pm$ might decay to a slepton and a lepton if the slepton mass is less than the $\tilde{\chi}_1^\pm$ mass ($\tilde{\chi}_1^\pm \to \ell^\pm \tilde{\ell}$). If the slepton mass is instead much heavier than the $\tilde{\chi}_1^\pm$ mass then the $\tilde{\chi}_1^\pm$ will more likely decay to a $W^\pm$ and a $\tilde{\chi}_1^0$ ($\tilde{\chi}_1^\pm \to W^\pm \tilde{\chi}_1^0$).

Since the number of production and decay modes is very high, experimental signatures

are very diverse. A common feature is that the decay chains are long and the final states are complex, often resulting in leptons, neutrinos, quarks and gluons, and LSPs. Strong production modes will usually have at least two quarks or gluons which hadronize into jets, whereas electroweak modes and decays can occur without any hadronic activity. It is thus important to search for SUSY in as many final states as possible to ensure coverage of many different scenarios.

3.7.2   R-parity Violating Signatures

In RPV scenarios it is usually assumed that the R-parity conserving (RPC) couplings dominate the sparticle production modes, whereas the RPV couplings participate in the prompt decay of the LSP to SM particles. So, production modes of RPV models tend to be the same as the ones described in the previous section. The primary difference is then in the final state, which no longer has a stable LSP and thus no missing momentum signature. The decay modes of the LSP will depend on which RPV couplings are allowed in the model. If the lepton number violating terms of Equation 3.2 are assumed to be present, then the LSP can decay to leptons giving final states with high lepton multiplicity, as seen in the top two diagrams of Figure 3.5 [13].
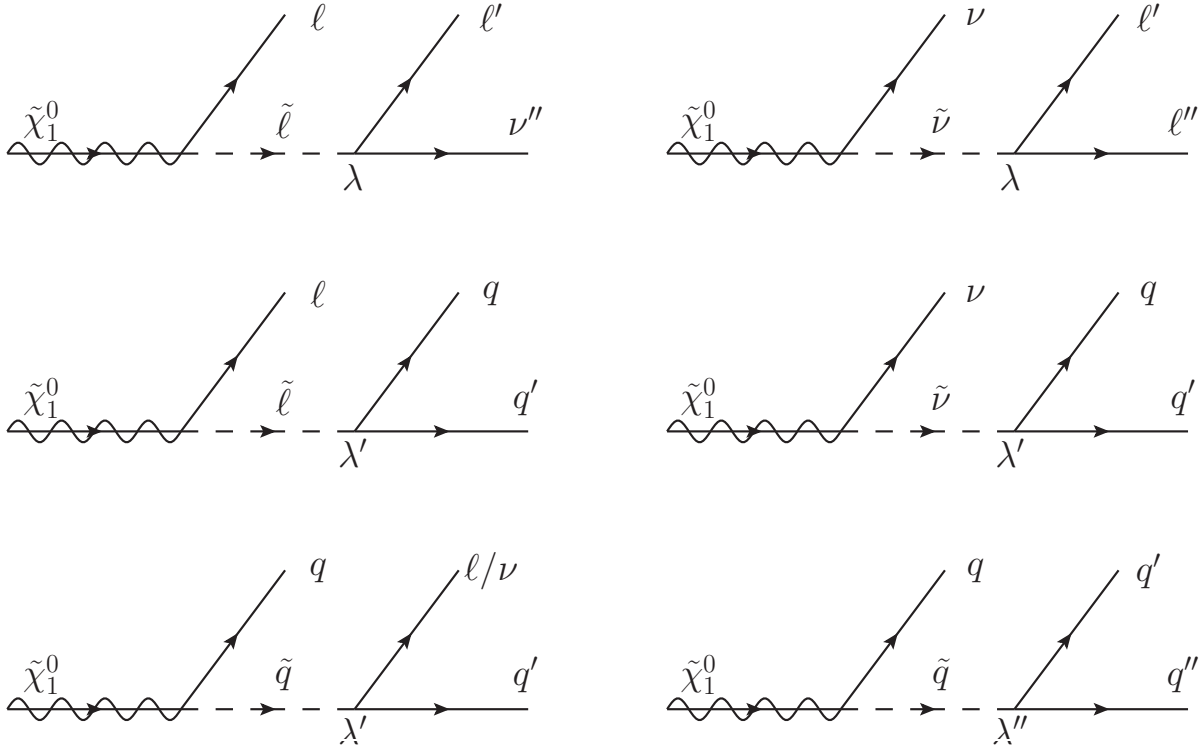
Figure 3.5: Decays of the $\tilde{\chi}_1^0$ LSP in models with R-parity violation. The top two diagrams give high lepton multiplicity final states. Decays via the λ and λ' couplings violate lepton number, while decays via the λ'' coupling violate baryon number.

3.8   Beyond the MSSM

One can extend the MSSM by including additional supersymmetry multiplets beyond the minimal set described in the preceding sections. The logical next step in complexity occurs when one additional gauge singlet chiral supermultiplet S is added to the MSSM. This case is known as the Next to Minimal Supersymmetric Standard Model (NMSSM). The most general renormalizable superpotential is

$$W_{\text{NMSSM}} = W_{\text{MSSM}} + \lambda S H_u H_d + \frac{1}{3}\kappa S^3 + \frac{1}{2}\mu_S S^2.$$

In the NMSSM, the scalar part of S gets a VEV and dynamically generates the Higgs mass parameter μ via the $\lambda S H_u H_d$ term above. This is an attractive feature of the model because

in the MSSM there is no explanation for why the μ parameter is at the electroweak scale (known as "the μ problem"). In the NMSSM, this parameter is generated dynamically. The NMSSM provides additional particles that mix with MSSM fields: a real scalar which mixes with the h^0 and H^0 to produce an additional CP-even Higgs, a pseudo scalar which mixes with A^0 to produce an additional CP-odd Higgs, and a Weyl fermion dubbed the "singlino" which mixes with the four existing neutralinos to produce a fifth neutralino [28].

Chapter 4

ATLAS

This chapter discusses the experimental apparatus used in the research of this thesis. The first section discusses the Large Hadron Collider, which provides the proton beam and particle collisions for the experiment. The second section describes the detector used to measure the outgoing particles of the collisions and all of its subsystems. Both of these machines are marvels of modern engineering and represents the culmination of decades of work in design, testing, and installation.

4.1   The Large Hadron Collider

The Large Hadron Collider (LHC) [29] is a large scale particle accelerator and collider residing in the former LEP tunnel at CERN on the Franco-Swiss border. It is currently the highest energy particle collider in the world and is used to study the energy frontier of particle physics by smashing together protons or lead ions to study the interaction products.

In the LHC, protons are collided via two opposing proton beams traveling around the 27 km tunnel. At design specifications, each beam will be composed of 25ns-spaced bunches of up
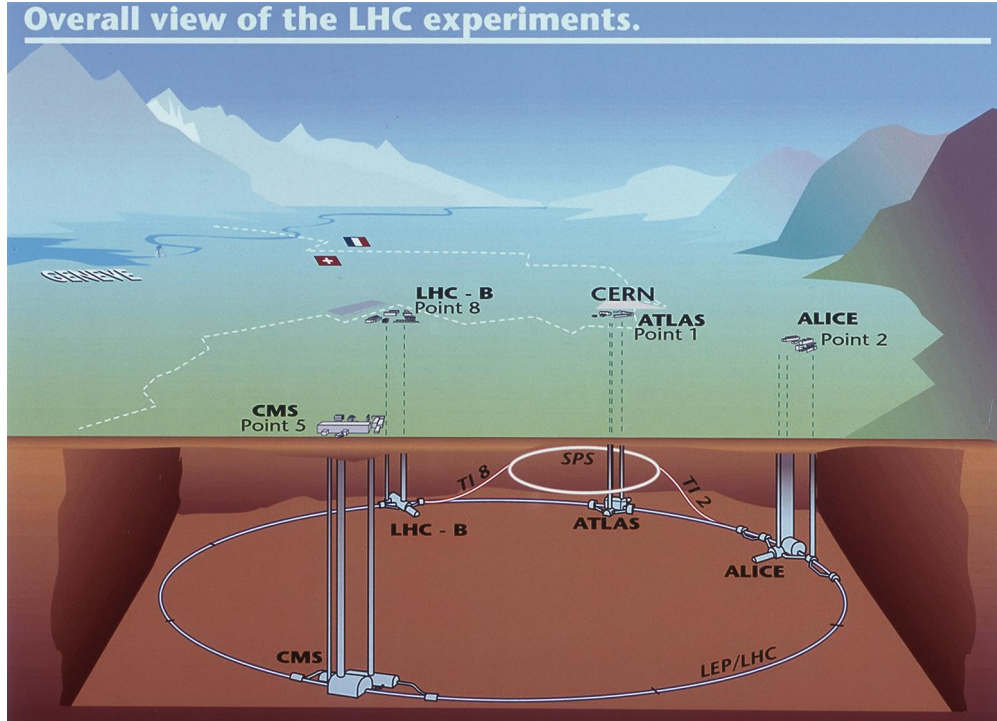
Figure 4.1: Layout of the LHC and location of four of the main experiments: ATLAS, CMS, ALICE, and LHCb. The LHC resides 50m-150m underneath the French-Swiss border. The SPS, which is part of the proton acceleration chain, and its connection tunnels to the LHC are shown.

to 10^{11} protons with an energy of up to 14 TeV per nucleon. Superconducting magnets are used to maintain the curved trajectory of the protons. Near the interaction points, additional magnets are used to focus the beams to an instantaneous luminosity of up to $10^{34} \text{cm}^{-2}\text{s}^{-1}$.

Proton collisions in the LHC begin with the extraction of protons from hydrogen gas, followed by acceleration and injection into successively larger storage rings. The Linear Accelerator 2 (LINAC 2) provides the first stage of acceleration, bringing the protons up to 50 MeV before they are injected into the Proton Synchroton Booster (PSB or Booster). The PSB is composed of four parallel accelerator rings that accelerate the protons to 1.4 GeV before they are injected into the Proton Synchrotron (PS). Next, the PS accelerates the protons further, bringing them up to 25 GeV before they are injected into the Super Proton Synchrotron (SPS). The SPS then accelerates the protons even further, up to 450 GeV, which is the LHC

injection energy. Finally in the LHC, the protons are accelerated up to design energy [31].

The LHC is also designed to accelerate and collide lead ions (Pb^{82+}). The collisions used for physics are Pb-Pb and Pb-p. The acceleration of these ions uses much of the same machinery as proton acceleration. In this case, the Linear Accelerator 3 (LINAC 3) provides the first stage of acceleration, bringing the ions up to 3.2 MeV per nucleon. Next, the Low Energy Ion Ring (LEIR) accelerates them to 72.2 MeV per nucleon before they are injected in the PS and from then on follow the same path as the protons described above. After acceleration by the PS, SPS, and the LHC, the ions reach a final energy of up to 2.76 TeV per nucleon, or 575 TeV per ion.

The LHC ring is home to seven detector experiments. ATLAS and CMS are the largest detectors and are general-purpose. ALICE is a heavy ion experiment. LHCb is b-physics experiment. The remaining experiments, TOTEM, MoEdal, and LHCf, are smaller and used for more specialized research.
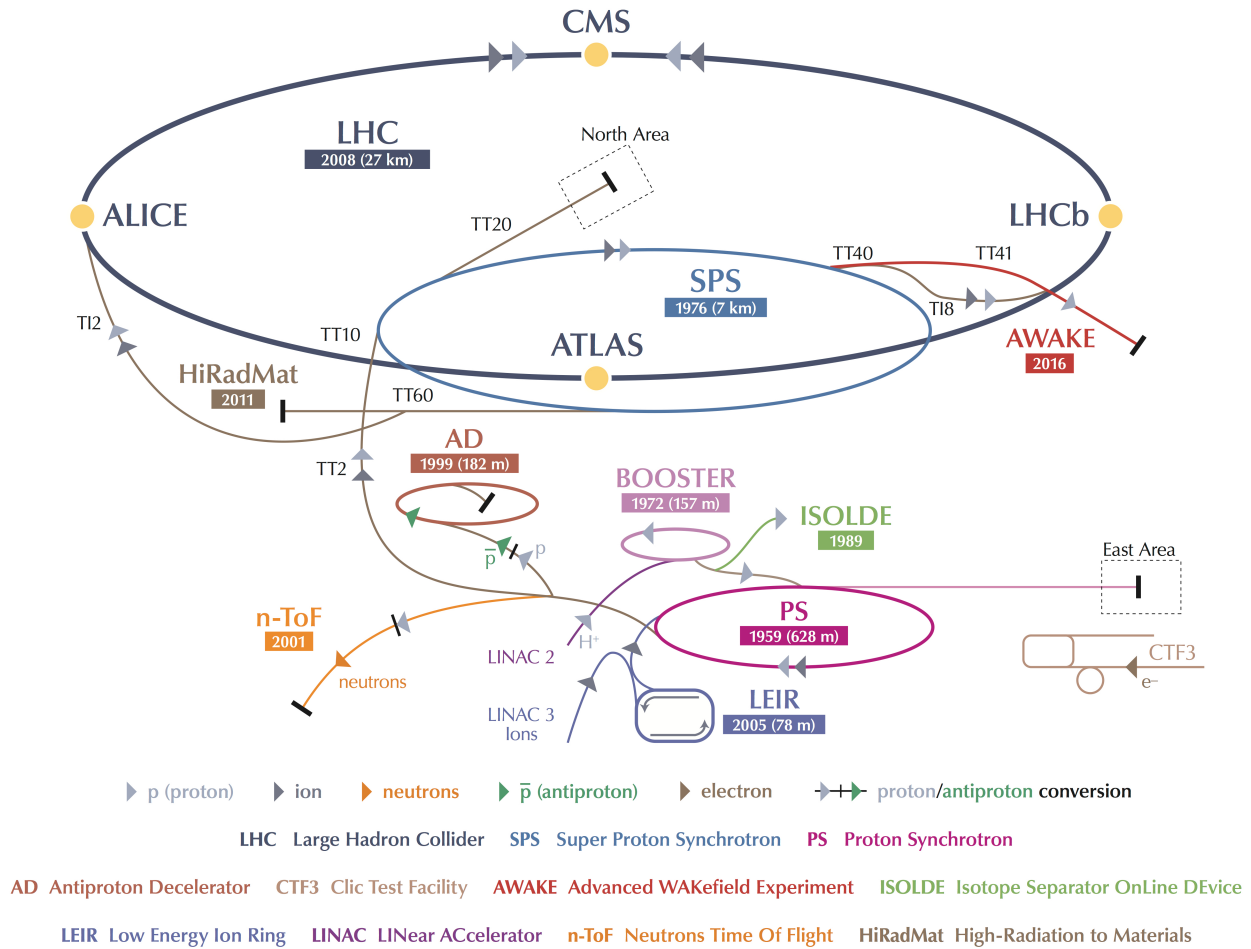
Figure 4.2: The CERN LHC accelerator complex. The LHC is the last ring (dark grey line) in a complex chain of particle accelerators. Protons for pp collisions are accelerated via the following path: LINAC 2 → PS booster → PS → SPS → LHC. Lead ions for $Pb - Pb$ and $Pb - p$ collisions are accelerated via a slightly different path: LINAC 3 → LEIR → PS → SPS → LHC [30].

4.2 The ATLAS Detector
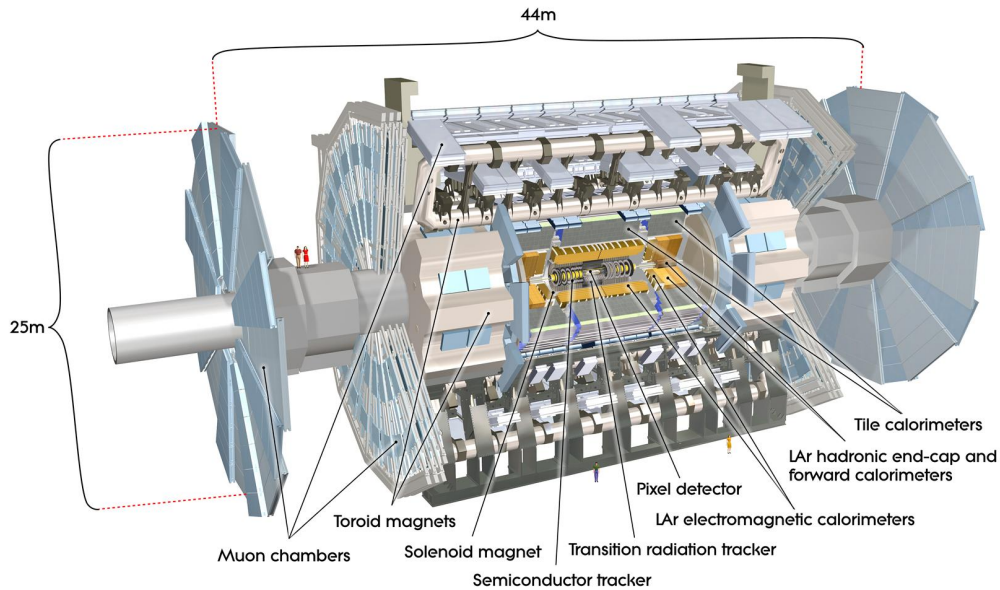
Figure 4.3: Overview of the ATLAS detector.

The ATLAS detector [32, 33] is a general purpose particle detector that sits on the LHC ring in the Point 1 cavern. It is designed to reconstruct and measure the electrons, muons, photons, and hadronic jets that are created from the proton-proton collisions provided by the LHC. The guiding principle behind the optimization of the detector design was to maximize the discovery potential for the Higgs boson and beyond-Standard-Model (BSM) physics. To accomplish this, the detector is comprised of several sub-detector systems which specialize in measuring different particle properties that can be combined at the software level to identify the particle type and reconstruct the particle momentum and energy. The inner detector (ID) gives a fine grained tracking system for charged particles. The calorimeters allow precise measurements of the energy of photons, electrons, and hadronic jets. The muon spectrometer allows precise measurement of the position and momentum of muons. The layout of the detector sub-systems is shown in Figure 4.3.

The following coordinate system is used in all descriptions of the ATLAS detector compo-

nents and in kinematic measurements of physics processes. The z-axis is parallel to the beam line, the x-axis points towards the center of the LHC, and the y-axis points upwards. The spherical coordinates θ and phi are defined in the usual way, with ϕ measuring the azimuthal angle in the x–y plane from the x-axis, and θ measuring the polar angle from the positive z-axis. A commonly used coordinate is the *pseudorapidity*, η, defined as $\eta = -\ln\tan\frac{\theta}{2}$. Distance between objects in η and ϕ is usually defined by $\Delta R = \sqrt{\Delta\eta^2 + \Delta\phi^2}$.

4.2.1 Magnet Systems
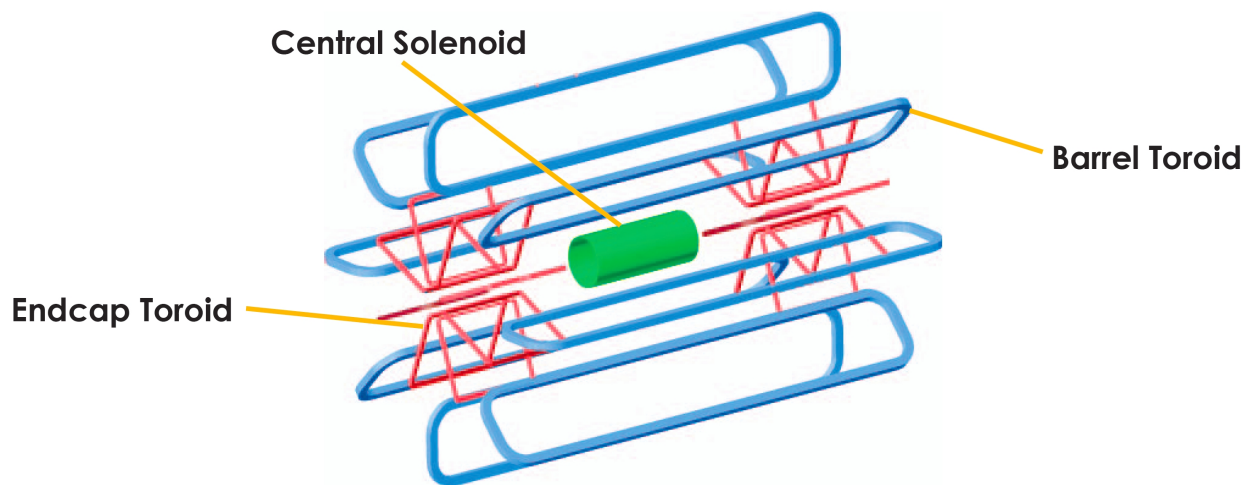
Figure 4.4: The ATLAS magnet system. A central solenoid provides the 2 T magnetic field for the inner detector. A barrel toroid and end-cap toroids provide approximately 0.5 T and 1 T in muon system's barrel and end-cap regions, respectively.

The ATLAS magnet system is an essential component of the detector which provides the magnetic fields necessary to curve the trajectories of charged particles for momentum measurements. Four superconducting magnets (one solenoid and three toroids) are used in different parts of the detector. A central solenoid is aligned along the beam axis and provides 2 T of axial magnetic field for the inner detector. The three toroidal magnets are used by the muon system. A barrel toroid provides approximately 0.5 T in the barrel region and the end-cap toroids provide approximately 1 T in the end-cap regions. The layout of the
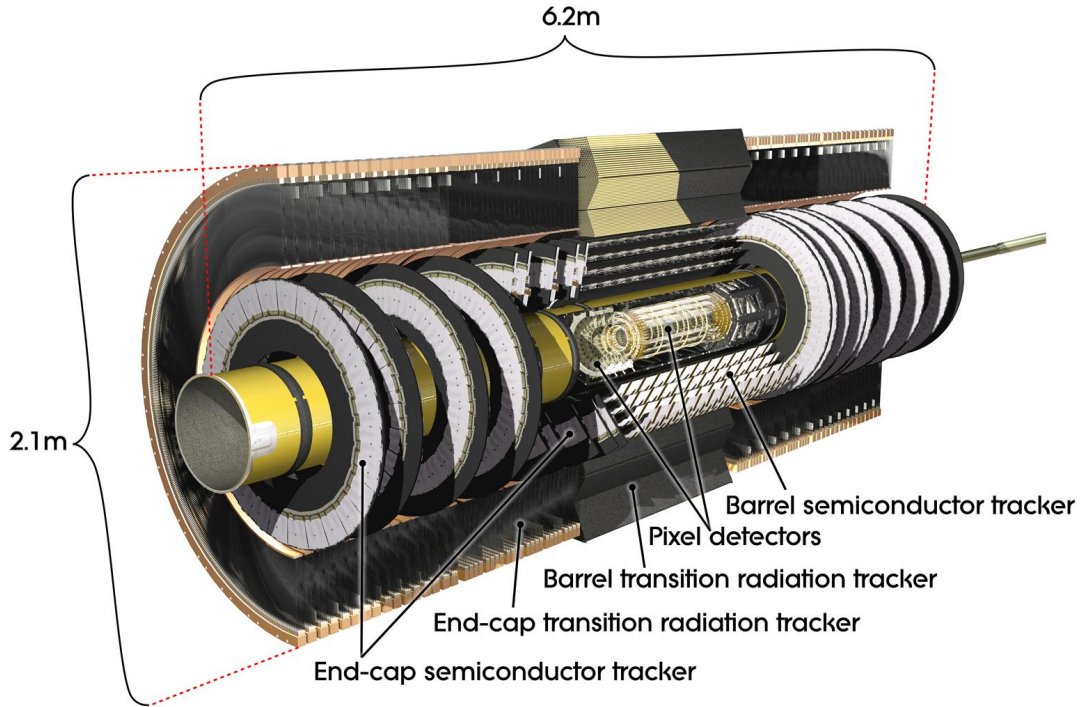
Figure 4.5: Overview of the ATLAS inner detector.

magnets is shown in Figure 4.4.

4.2.2 Inner Detector

The ATLAS inner detector sits closest to the interaction point and is thus the first system encountered by the collision products. It plays a key role in identifying and measuring charged particles. The ID has very high granularity to deal with the high particle multiplicity near the collision. It consists of three detection technologies for finding charged particle tracks: a semiconducting silicon microstrip detector (SCT), a semiconducting pixel detector, and a transition radiation tracker (TRT). The dimensions of the ID are 5.3 m along the beam axis, and 2.5 m diameter. Figure 4.5 shows the layout of the ID. The radial layout of the barrel components can be seen in Figure 4.6.
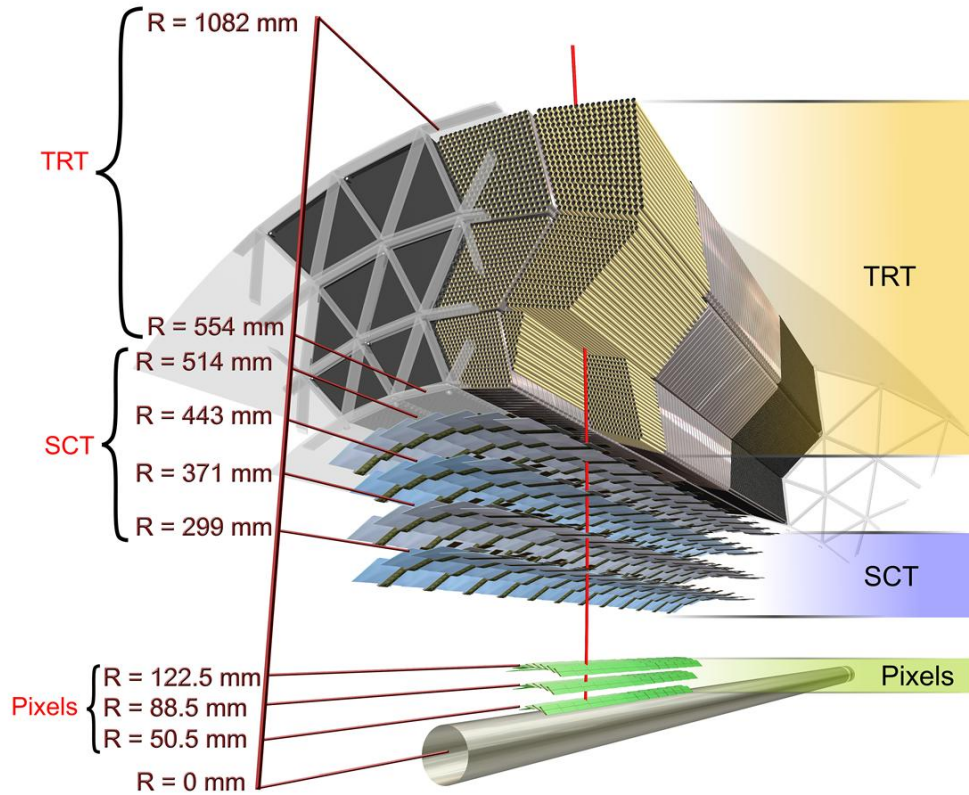
Figure 4.6: Radial layout of the ATLAS inner detector. Charged particles with sufficiently high transverse momentum produce tracks first in the Pixel detector, then the SCT, and finally the TRT.

The pixel detector gives the finest granularity of the ID systems. It sits closest to the interaction point ($\sim$ 5 cm) and gives a powerful measurement of the impact parameters of charged particles. This feature allows for precise reconstruction of vertices, which is important for tagging short-lived particles such as B hadrons and τ leptons. In the barrel, three layers of silicon detectors provide instrinsic accuracy of 10 μm in R–ϕ and 115 μm along z. Two end caps each consist of three disks of silicon detectors providing an instrinsic accuracy of 10 μm in R–ϕ and 115 μm along R. The pixel detector has over 80 million readout channels, which is about 90% of the total readout channels in ATLAS.

The SCT detector is also a precision detector in the intermediate radial range which contributes to the measurements of track momentum, impact parameters, and vertexing. The barrel region has four cylindrical layers (2 measurements each) providing an instrinsic accuracy of 17 μm in R–ϕ and 580 μm along z. The end caps each have nine disks with an instrinsic accuracy of 17 μm in R–ϕ and 580 μm along R.

The TRT is a straw detector system which surrounds the SCT and contributes significantly to the momentum measurement. It also allows for very good track pattern recognition performance. This is due to the high number of measurements made per track (typically 36). Each straw is 4 mm diameter and lies parallel to the beam, so the TRT only provides R–ϕ tracking information. In addition, this system is sensitive to the transition radiation emitted from charged particles passing through varying materials which deposits high-threshold hits in the straws. The amount of radiation differs between electrons and pions, so the TRT is effectively able to discriminate between them. The intrinsic accuracy of the TRT is 130 μm along R–ϕ, extending up to $|\eta| = 2.0$.

4.2.3   Calorimeters

The ATLAS calorimeter system provides the energy measurement for electrons, photons, and jets. It is designed to provide good containment for electromagnetic and hadronic showers, and also to limit punch-through into the muon system. This is accomplished by the use of several subdetectors: an electromagnetic (EM) calorimeter covering pseudorapidity range of $|\eta| < 3.2$, a hadronic barrel calorimeter covering $|\eta| < 1.7$, hadronic end-cap calorimeters covering $1.5 < |\eta| < 3.2$, and forward calorimeters covering $3.1 < |\eta| < 4.9$. The layout is shown in Figure 4.7. The calorimeters work by providing alternating layers of stopping material and active detection components. The charged particles interact with the stopping material and produce particle showers which are detected in the active components.
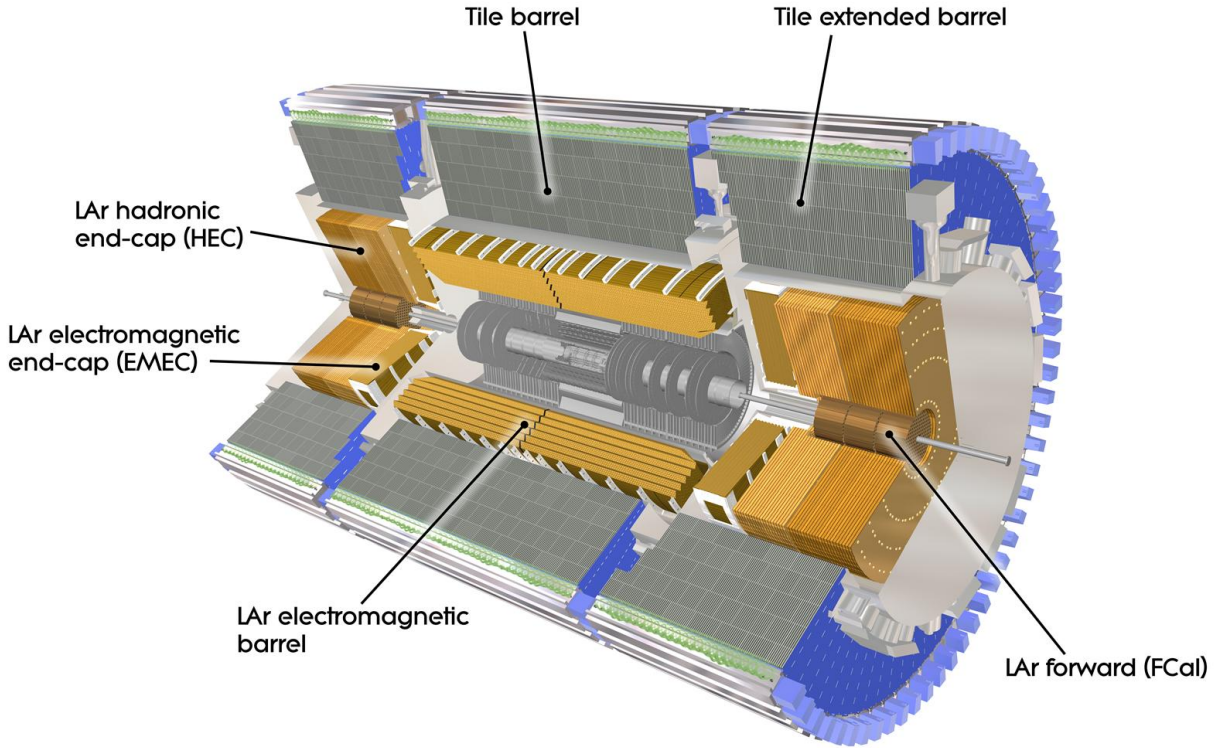
Figure 4.7: Overview of the ATLAS calorimeters.

The EM calorimeter is a liquid Argon (LAr) detector with lead absorber plates. This subdetector is divided into a barrel part covering $|\eta| < 1.475$ and endcaps covering $1.375 < |\eta| < 3.2$. It has an accordion shaped geometry which provides complete azimuthal symmetry and coverage. The thickness of the lead absorber plates varies with η and was optimized for energy resolution. For precise measurements of electrons and photons, the region with $|\eta| < 2.5$ (corresponding to the coverage of the ID) has significantly higher granularity. A presampler detector is used in the region with $|\eta| < 1.8$ to correct for the energy loss of electrons and photons upstream of the calorimeter.

The hadronic calorimeters use both liquid Argon and scintillating tile technologies. The tile calorimeter covers the barrel ($|\eta| < 1.7$) and uses scintillating tiles and iron absorber plates. The LAr calorimeters cover the end-cap and forward region. The large η coverage of the

37
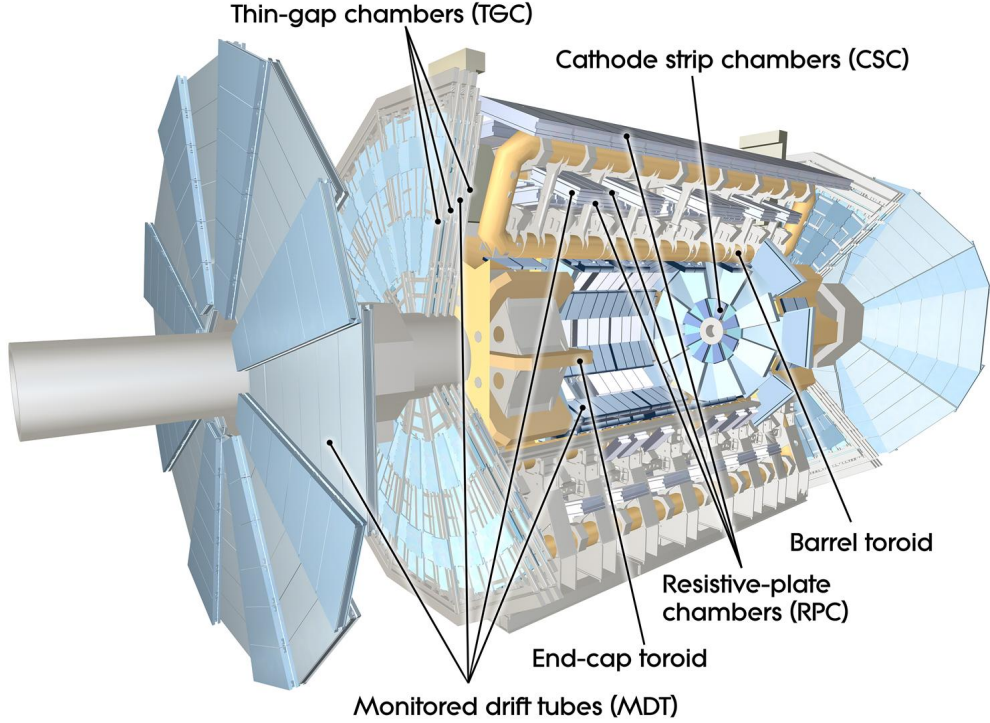
Figure 4.8: Overview of the ATLAS muon spectrometer.

hadronic calorimeters allows for a good measurement of the E_T^{miss}, an important variable for SUSY searches which is described further in Section 4.4.5.

4.2.4 Muon Spectrometer

The ATLAS muon spectrometer consists of four detector technologies for measuring the momentum of muons in the presence of a toroidal magnetic field. It allows identification of muons with transverse momenta above 3 GeV and precise determination of p_T up to about 1 TeV. In the barrel region, tracks are measured in chambers arranged in three cylindrical layers around the beam axis. In the end-caps, the chambers are installed in three-layered planes perpendicular to the beam. The components of the muon system are: resistive plate chambers (RPCs), thin gap chambers (TGCs), cathode strip chambers (CSCs), and monitored drift tube chambers (MDTs). The layout is shown in Figure 4.8.

The MDTs and CSCs are used to precisely measure the muon tracks. The MDTs provide a precision momentum measurement. They cover the pseudorapidity range $|\eta| < 2.7$ in each layer except the innermost end-cap layer where their coverage is limited to $|\eta| < 2.0$. Each chamber consists of three to eight layers of drift tubes, achieving an average resolution of 80 μm per tube, or about 35 μm per chamber. The CSCs are placed at high pseudorapidity $(2.0 < |\eta| < 2.7)$ in the inner-most tracking layer. They have a high rate capability and time resolution. CSCs are multiwire proportional chambers with cathode planes segmented into strips in orthogonal directions, which allows both coordinates to be measured from the induced charge distribution. The resolution of a chamber is 40 mm in the bending plane (η) and about 5 mm in the transverse plane.

The RPCs and TGCs are used to complement the MDTs and CSCs and provide fast measurements for the trigger system. The RPCs are gaseous parallel electrode-plate (i.e. no wire) detectors used in the barrel ($|\eta| < 1.05$). The TGCs are multi-wire proportional chambers used in the end-cap ($1.05 < |\eta| < 2.4$). These trigger chambers provide a complementary measurement of the muon ϕ coordinate. In addition, these systems were designed to deliver tracking information quickly enough that the LHC proton bunch crossing can be precisely identified. Both chambers deliver signals with a spread of 15-25 ns, which is faster than the time between bunches (25–50 ns).

4.2.5   Trigger and Data Acquisition

The ATLAS trigger and data acquisition (TDAQ) systems are designed to select physics events of interest from the very high interaction rate of the LHC and read out the detector information with minimal interruption from hardware and software limitations. To accomplish this, a three-level trigger scheme is used which succesively refines the selection of events to reduce the event rate to a reasonable level. The level 1 trigger is a hardware

based decision based on simple coincidence of high p_T particles. It reduces the interaction rate from $\sim 10^9$ Hz down to ~ 75 kHz by using a subset of the detector information coming from the muon system and the calorimeters. The level 2 and 3 triggers, denoted level 2 and even filter, form the software based high-level trigger. At level 2, regions of interest (ROIs) are determined by considering cones in η and ϕ about the high p_T objects from the level 1 result. Detector systems in these regions are read out in order to fully reconstruct the objects and make a decision to accept or reject the event and bring the event rate down to about $\sim$1 kHz. If the event passes the level 2 trigger, then the entire event is reconstructed and further criteria is applied in the event filter. This final trigger decision must reduce the event rate down to a couple hundred Hz for writing the events to disk.

The data acquisition system which implements the above described trigger scheme and handles the readout of the detector data is shown in Figure 4.9. The very high interaction rate means that event information needs to be preserved while trigger decisions are being made and while new interactions take place. For the level 1 trigger, information from all detector channels is conserved in "pipeline" memories while the hardware processors decide to reject or accept the event. Once an event is accepted at level 1, the detector information is read out into readout drivers (RODs) and temporarily stored in readout buffers (ROBs) for level 2. The level 1 trigger specifies the ROIs to the level 2 algorithms by providing the coordinates (η, ϕ) and p_T of the candidate objects. The level 2 trigger is then able to reconstruct these objects by using the limited detector information in the ROIs (usually only a few percent of the full event data). If the event is then accepted by the level 2 trigger, the event builder (EB) combines the data segmented over many ROBs and stores it in a storage element associated with an event filter (EF) processor. At this point, the full detector for an event resides in one storage element and the event filter is able to make a final decision to reject or accept the event using the full detector data.
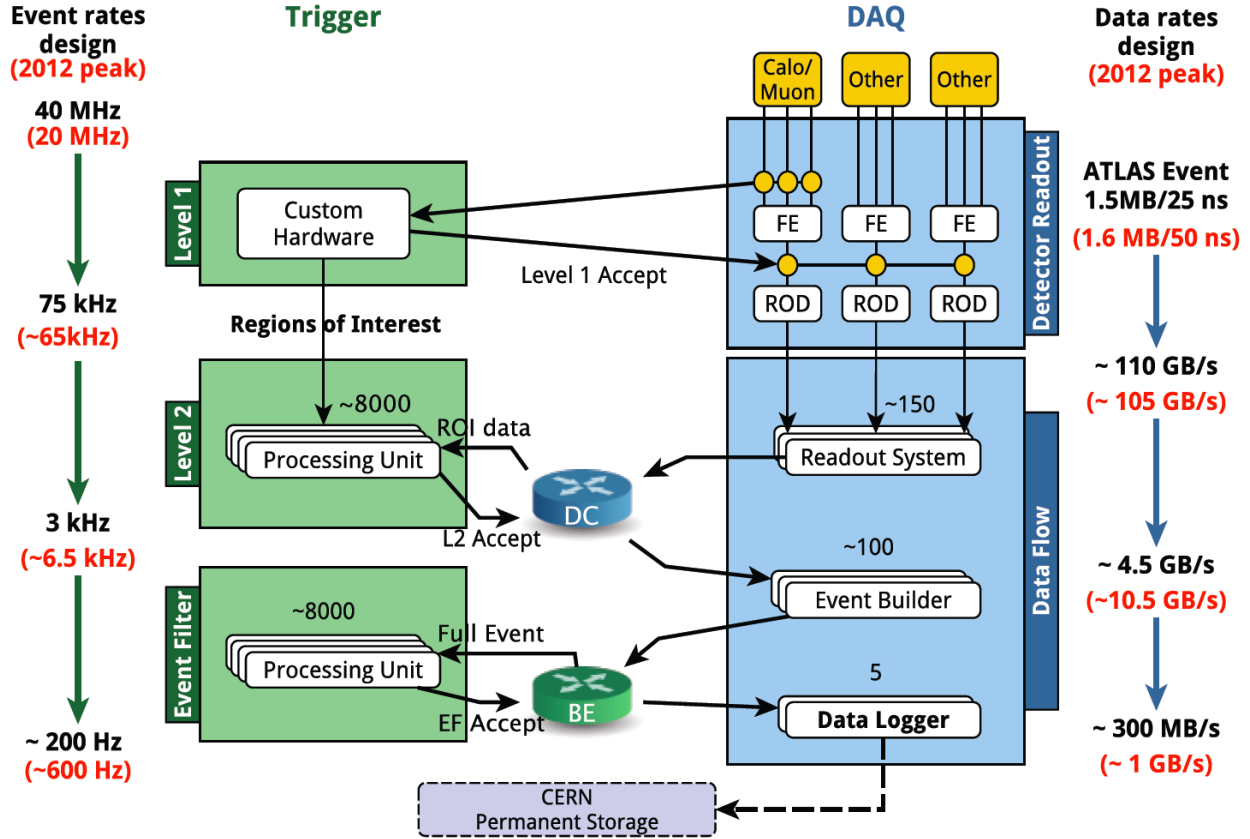
Figure 4.9: The ATLAS trigger and data acquisition system. Event rates for each trigger level are shown on the left, and the corresponding bandwidth used on the right. Numbers in black indicate the design specifications while numbers in red indicate the peak running conditions in 2012.

4.3   Operations and Running Conditions

Operations of the LHC and ATLAS have been, besides one significant set-back in 2008, very successful. The LHC began colliding protons in September 2008 with 450 GeV per beam (LHC injection energy). However, nine days after the first beam circulations, an electrical failure resulted in a magnet quench and an explosive release of liquid helium which damaged 50 superconducting magnets and their mountings. The resulting repairs and recovery took 14 months. Then, in November 2009, the LHC successfully restarted beam circulation again with 450 GeV per beam. During this initial commissioning phase, the beam energies were ramped up first to 1.05 TeV and then finally to 3.5 TeV per beam (center-of-mass energy

$\sqrt{s} = 7$ TeV)[4] for physics collisions near the end of March 2010.

The luminosity delivered to ATLAS is measured with dedicated detectors and algorithms. A subset of the ATLAS sub-detectors (the ID, tile calorimeter, and forward calorimeter) are used for these measurements. The additional detectors include the Minimum Bias Trigger Scintillators (MBTS), the Beam Conditions Monitor (BCM), and the LUCID detector. The primary algorithm consists of counting events which meet a minimal hit criteria. Additional algorithms rely on hit counting and average particle rate counting and provide a cross-check of the measurement. Calibration of the luminosity calculation is done via dedicated beam conditions in *van der Meer* scans, in which the beams are spatially separated, allowing for precise measurements of the beam dimensions. More information on the luminosity measurements and the specialized detectors can be found at [34].

Throughout 2010 the LHC continued to run at $\sqrt{s} = 7$ TeV, delivering a total integrated luminosity of 48.1 pb^{-1} to the ATLAS experiment with a peak instantaneous luminosity of about 2×10^{32} cm^{-2}s^{-1}. In 2011 the LHC continued to run at $\sqrt{s} = 7$ TeV, but with significant improvements to the beam which increased the instantaneous luminosity up to a peak value of 3.5×10^{33} cm^{-2}s^{-1}. Integrated luminosity delivered to ATLAS during 2011 was 5.61 fb^{-1}. Further improvements were made to the LHC beams for collisions in 2012. The energy of the beams was raised to 4 TeV ($\sqrt{s} = 8$ TeV) and the instantaneous luminosity was again increased to a peak value of approximately 7.5×10^{33} cm^{-2}s^{-1}. The total integrated luminosity delivered to ATLAS in 2012 was 23.3 fb^{-1}. The improvements to the instantaneous luminosity from year to year were due to increases in the number of proton bunches, increases in the number of protons per bunch, and improvements in beam focusing. The number of proton bunches in each year of data taking versus time can be seen in Figure 4.10. The peak instantaneous luminosity in each year of data taking versus time can be seen in Figure 4.11.

---

[4]This set the world record for proton beam energy until the LHC broke it again in 2012.
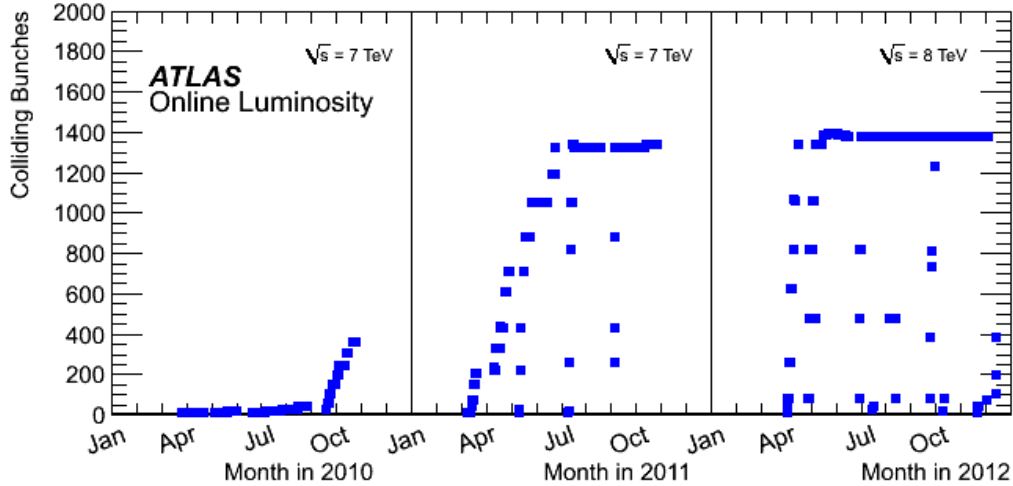
Figure 4.10: The number of colliding bunches in ATLAS versus time during the pp runs of 2010, 2011 and 2012.

The recorded luminosity in ATLAS is always a little less than the LHC delivered luminosity. This is due to inefficiencies of the TDAQ system as well as time spent in "warm-starts", which is when the tracking detectors undergo a ramp of the high-voltage and the pixel system preamplifiers are turned on. The integrated delivered and recorded luminosity in ATLAS versus time in 2010, 2011, and 2012 can be seen in Figure 4.12.

As the instantaneous luminosity of the LHC increases, so do the number of interactions per bunch crossing. This effect is called "pileup" and has significant impact on physics measurements. Pileup interactions are usually softer (less-energetic) than the triggered interactions of interest. However, they still contribute additional vertices and tracks in the inner detector and additional energy deposits in the calorimeters. So, they affect the energy calibration of electrons and jets, the isolation variables used to distinguish real leptons from fake or non-prompt leptons, and they impact the measurement of the missing transverse momentum, $E_{\mathrm{T}}^{\mathrm{miss}}$, defined in the next section. Figure 4.13 shows the average number of interactions per bunch crossing, μ, for data collected in 2011 and 2012. In 2011, an average event of interest would have about 8 additional pileup events. In 2012, this number increased to about 20, with some events having as many as 40 proton-proton interactions.

43
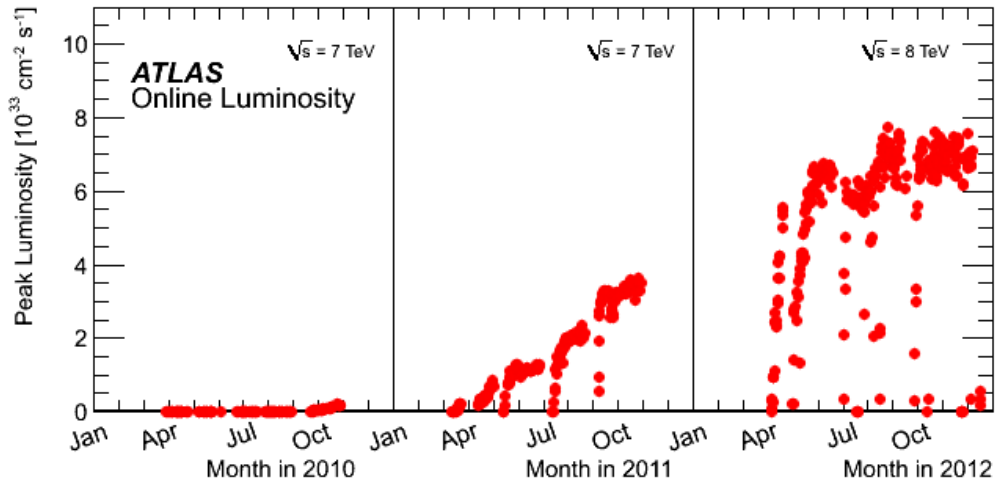
Figure 4.11: The peak instantaneous luminosity delivered to ATLAS per day versus time during the *pp* runs of 2010, 2011 and 2012.

(a) 2010

(b) 2011

(c) 2012
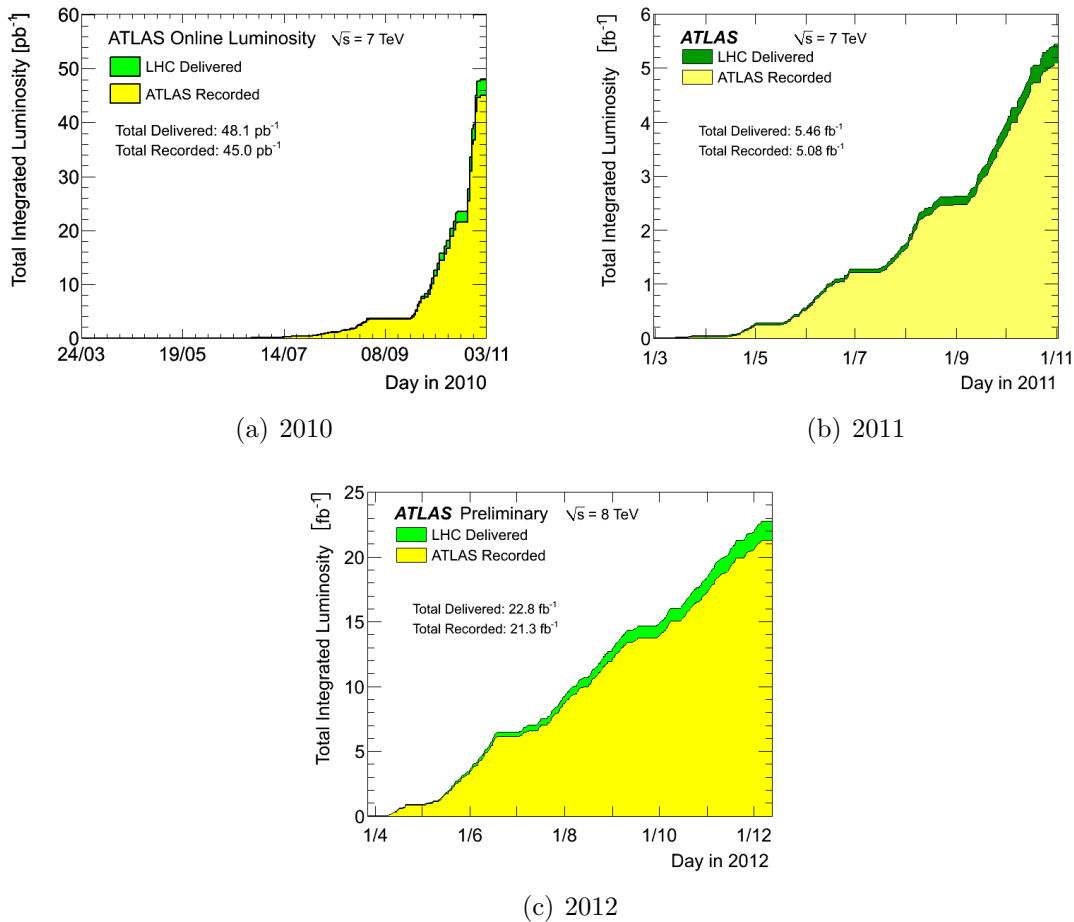
Figure 4.12: Integrated delivered and recorded luminosity in ATLAS versus day in 2010, 2011, and 2012.
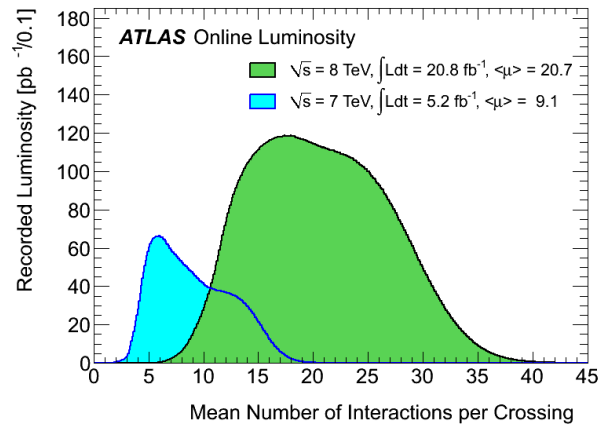
Figure 4.13: Mean number of *pp* interactions per bunch crossing in 2011 and 2012.

4.4 ATLAS Reconstruction

The ATLAS offline reconstruction software processes the raw detector data to reconstruct the high-p_T objects in the events. The building blocks of object reconstruction are tracks in the inner detector and muon spectrometer, and clustered energy deposits in the calorimeters. By constructing these low-level objects and combining them with dedicated algorithms, the offline software reconstructs electrons, muons, photons, jets, b-jets, hadronic tau decays, and missing transverse momentum.

The relevant algorithms for reconstruction of the objects used in the analyses of Chapters 6 and 7 are described in the following sections. Further information about the performance of the reconstruction algorithms can be found in [32].

4.4.1 Electrons

Electrons are reconstructed from a combination of a shower in the EM calorimeter and an inner detector track. The algorithm begins by locating clusters in the EM calorimeter with a sliding window algorithm. Then, inner detector tracks are matched to the clusters within a $\Delta\eta \times \Delta\phi$ window of 0.05×0.10. The energy of the cluster must be consistent with the momentum of the track, such that $E^{clus}/p^{trk} < 10$. Additional information about the shower shape, ID track, and the combined reconstruction is used to form three levels of a cut-based selection criteria [32]:

Loose cuts consist of simple shower-shape cuts and very loose matching requirements between the track and the cluster.

Medium cuts introduce shower-shape requirements on the first layer of the EM calorimeter and tighter track quality cuts.

Tight cuts include tighter criteria on the track matching and $\Delta\eta \times \Delta\phi$. Additional requirements on the track such as a vertexing-layer hit and high threshold TRT hits reject backgrounds from photon conversions and charged hadrons.

The reconstruction and identification efficiencies for electrons can be seen in Figure 4.14. In 2012, the reconstruction efficiency is above 95%. These efficiencies are measured with a tag-and-probe method in $Z \to e^+e^-$ and $J/\psi \to e^+e^-$ events as described in [35].
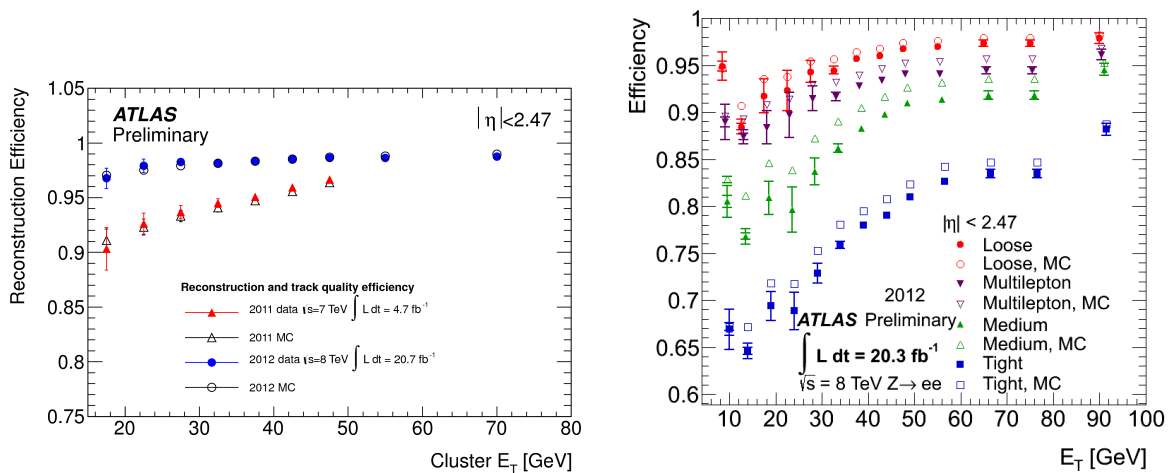
Figure 4.14: Electron reconstruction efficiencies in 2011 and 2012 data and MC measured with respect to electromagnetic clusters (left), and the corresponding identification efficiencies for the loose, medium, and tight criteria (right). Efficiencies are measured with a tag-and-probe method in $Z \to e^+e^-$ and $J/\psi \to e^+e^-$ events [36].

4.4.2   Muons

Muons are reconstructed from combinations of inner detector tracks with muon spectrometer tracks. In fact there are three possibilities [32]:

Stand-alone muons are constructed from muon spectrometer information only. MS track segments are linked in each of the three muon stations to form tracks. The tracks are then extrapolated to the beam line. The η range is limited by the muon spectrometer ($|\eta| < 2.7$).

47

Combined muons are formed by matching stand-alone muons to inner detector tracks. A statistical combination of the two tracks yields the coordinates and momentum of the muon. The η range of combined muons is limited by the inner detector ($|\eta| < 2.5$).

Segment-tagged muons are formed from inner detector tracks and muon spectrometer segments. The ID track is extrapolated to the MS and combined with an MS track segment in an inner muon station. The η range is the same as for combined muons.
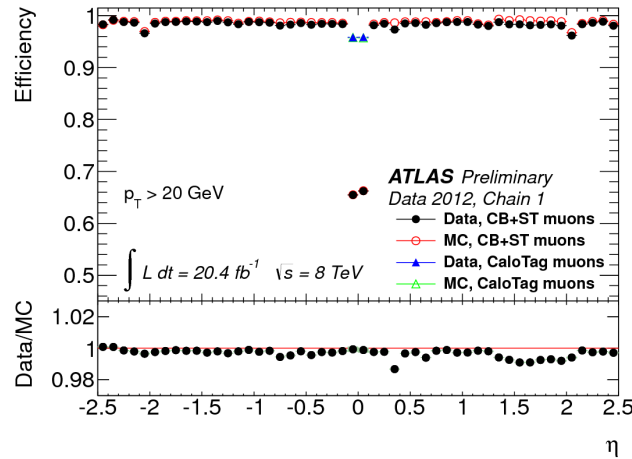
Figure 4.15: Muon reconstruction efficiency as a function of η for 2012 data for combined and segment-tagged muons (CB+ST). Efficiencies are measured with a tag-and-probe method in $Z \rightarrow \mu^+\mu^-$ events. CaloTag muons are not described in this thesis but more information can be found in [37].

The reconstruction efficiency for muons can be seen in Figure 4.15. For $0.1 < |\eta| < 2.5$, the reconstruction efficiency is approximately 98%. In the region $|\eta| < 0.1$, the reconstruction efficiency suffers from poor coverage of the muon chambers due to electronics services for the ID and calorimeters. Efficiencies are measured with a tag-and-probe method in $Z \rightarrow \mu^+\mu^-$ events for muons with $p_{\mathrm{T}} > 20$ GeV. Cross checks are performed with J/ψ and υ events to validate the measurements for muons with 10 GeV$< p_{\mathrm{T}} <$20 GeV [37].

4.4.3 Jets

Hadronic jets are reconstructed from energy clusters in the EM and hadronic calorimeters. Topological (3-dimensional) clusters are first formed by identifying seed cells with significant energy compared to the expected noise ($E_{\text{cell}} > 4\sigma_{\text{cell}}$). Neighboring cells are then added to the cluster. Neighbor cells also above a secondary threshold ($E_{\text{cell}} > 2\sigma_{\text{cell}}$) are treated as secondary seeds and their neighbors are added as well. The process continues until no additional adjacent cells are above the secondary threshold [38]. Clusters are then combined into jets using the anti-k_t algorithm [39] with a distance parameter of $R = 0.4$. A local calibration scheme is used for the cluster energy. The method classifies the energy depositions in each cell as electromagnetic or hadronic, and weighs them appropriately when calculating the energy of the topocluster [32].

After cluster calibration and jet reconstruction, additional corrections are needed to properly calculate the jet energy. The jet energy scale corrections are determined with MC comparing truth jet energy to the reconstructed value. These results are then validated and uncertainties are determined by comparing with in-situ methods such as di-jet and γ-jet p_{T} balancing methods [40].

The presence of pileup events can effect jet reconstruction in multiple ways. The first major effect is that pileup interactions increase the total energy density deposited in the calorimeters, which then affects the energy calibration of the jets. This problem is fixed by subtracting an expected offset pileup contribution parametrized by the number of vertices in the event [41]. The second major effect is that pileup interactions introduce additional jets. Since these jets do not originate from the hard process of interest, it is desirable to suppress them. A useful variable for the suppression of pileup jets is the jet-vertex-fraction (JVF).

The JVF for a jet is defined as

$$\text{JVF} = \sum_{\text{tracks}_{\text{jet}},\text{PV}} p_{\text{T}} \Big/ \sum_{\text{tracks}_{\text{jet}}} p_{\text{T}},$$

where the sums are taken over the tracks matched to the jet and PV denotes the tracks associated to the primary vertex. Jets that have no associated tracks are assigned $\text{JVF} = -1$. The JVF quantifies how much of a jet's energy is associated with the primary vertex of interest in the event. Pileup jets will have a higher fraction of jet energy associated with pileup vertices, so the variable is a good discriminator.

B-hadron jets have a displaced secondary decay vertex due to the long lifetime of the b-quark. Several algorithms are used to "tag" jets as b-jets. The algorithm which is most commonly used with 2012 data is the MV1 algorithm, which is based on a neural network using the output weights of the JetFitter + IP3D, IP3D, and SV1 algorithms as input. The input algorithms are described in [42]. For a b-tagging efficiency of 80%, the algorithm gives rejection factors for c-jets of about 3, for taus of about 5.6, and for light flavor quarks about 27.

4.4.4 Taus

Tau leptons are unstable and can decay to either leptons with a branching ratio of 35% or to hadrons with a branching ratio of 65%. The hadronic decays dominantly include either one or three charged pions or kaons (called "1-prong" and "3-prong" taus, with respective branching ratios of about 50% and 15%) plus additional neutral pions, kaons, and neutrinos.

Taus decaying hadronically have a signature similar to jets. They decay in the beam pipe to charged pions which produce a hadronic shower in the calorimeters. Thus, the reconstruction algorithm is seeded by jets reconstructed via the algorithm described in 4.4.3. Identifica-
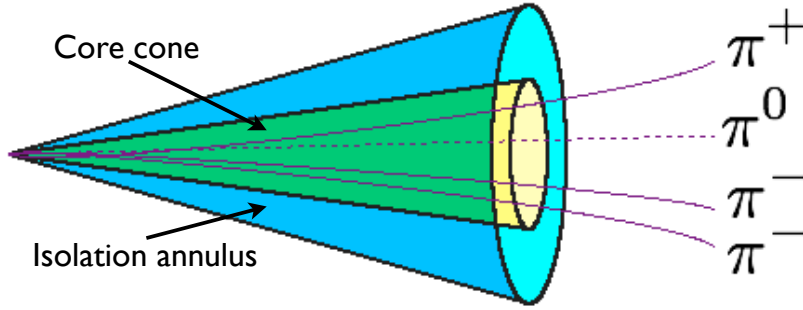
Figure 4.16: Illustration of the reconstruction of a 3-prong tau.

tion of taus is based on a *boosted decision tree* (BDT) which takes many different track and calorimeter related variables as input to discriminate against the hadronic jet background. Tracks passing some quality requirements and falling within the *core cone* defined by $\Delta R = \sqrt{(\Delta\eta)^2 + (\Delta\phi)^2} < 0.2$ about the central axis of the seed jet are associated to the tau. Remaining tracks within the *isolation annulus* of $0.2 < \Delta R < 0.4$ are useful for the discrimination. An illustration of the tau reconstruction cone can be seen in Figure 4.16. Additional quantities used in the BDT include shower shape variables, amount of transition radiation, and coordinates of the tau decay vertex. Two BDT scores are utilized. The first is optimized for discrimination against jets, and the second is optimized for discrimination against electrons. The jet BDT is trained separately for both 1-prong and 3-prong taus. The electron BDT is only applied to 1-prong tau candidates. An additional muon veto is used to reject candidates with hits in the muon spectrometer [43].

The signal and background BDT identification efficiencies for taus is shown in Figure 4.17. The efficiencies are significantly lower than for electrons, muons, and jets, due to the difficulty in distinguishing real taus from the jet background. Signal efficiencies are measured in $Z \to \tau\tau$ and $W \to \tau\nu$ simulated events, while background efficiencies are measured in 2012 collision data with a multi-jet selection.
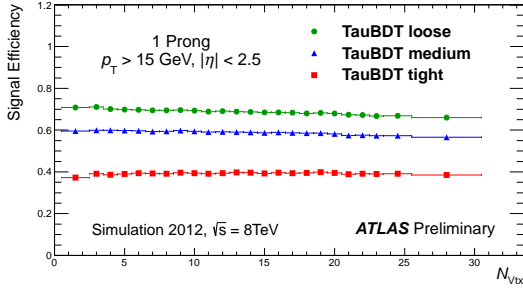
(a) Signal efficiency, 1 prong
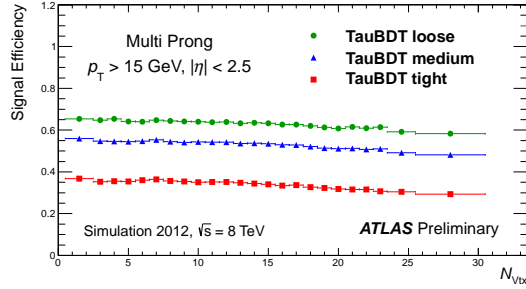
(b) Signal efficiency, multi-prong
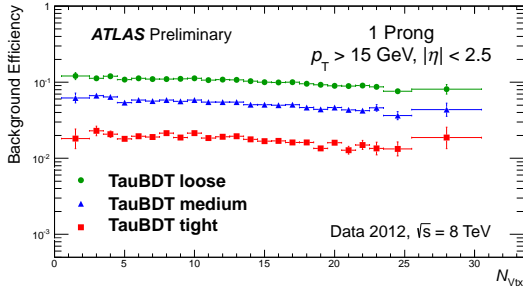
(c) Background efficiency, 1 prong
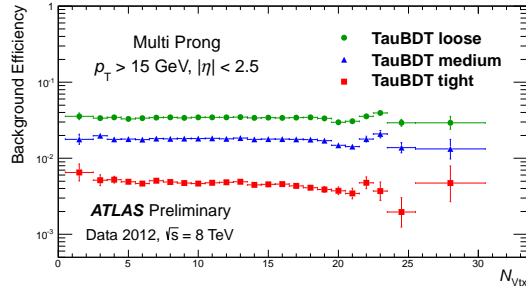
(d) Background efficiency, multi-prong

Figure 4.17: Tau signal and background BDT identification efficiencies as a function of the number of reconstructed vertices for taus with $p_T > 15$ GeV and $|\eta| < 2.5$. Signal efficiencies are measured in $Z \to \tau\tau$ and $W \to \tau\nu$ simulated events. Background efficiencies are measured in 2012 collision data with a multi-jet selection [43].

As with jets in the previous section, additional corrections are needed to properly calculate the visible tau energy[5]. The tau energy scale corrections are derived from simulated $Z \to \tau\tau$ and $W \to \tau\nu$ events by comparing the reconstructed energy to the true visible tau energy. These results are validated and uncertainties are determined by two additional methods: a deconvolution method which propagates single-particle uncertainties to the tau visible energy scale, and an in-situ technique that looks at the reconstructed Z visible mass peak from $Z \to \tau_{\mathrm{had}}\tau_{\mathrm{lep}}$ events [44].

Leptonic decays of taus are indistinguishable from electrons and muons (except for the presence of a small amount of E_T^{miss} due to the neutrinos), so there is no dedicated algorithm for identifying them.

---

[5]The visible energy does not include the momentum carried away by invisible neutrinos

4.4.5 Missing Transverse Momentum

Stable neutral particles produced in ATLAS such as neutrinos or the LSP of supersymmetry will escape detection and lead to an apparent imbalance of momentum. Since the total momentum in the transverse plane is zero before the collision, one can measure the total momentum of all the visible particles to infer the remaining *invisible* momentum.

The ATLAS measurement of missing transverse momentum, $E_{\mathrm{T}}^{\mathrm{miss}}$, can be done in various ways. The approach explained in this section is an object-based $E_{\mathrm{T}}^{\mathrm{miss}}$ as described in [45] and more recently in [46]. Alternative methods are based on inner detector tracks or use calorimeter energy deposits only. Electrons, muons, taus, photons, and jets enter the $E_{\mathrm{T}}^{\mathrm{miss}}$ at their relevant calibrated energies. Remaining energy deposits in the calorimeters are included as topological clusters. The $E_{\mathrm{T}}^{\mathrm{miss}}$ is computed as

$$E_{(\mathrm{x,y})}^{\mathrm{miss}} = -E_{(\mathrm{x,y})}^{e} - E_{(\mathrm{x,y})}^{\gamma} - (E_{(\mathrm{x,y})}^{\tau}) - E_{(\mathrm{x,y})}^{\mathrm{jets}} - E_{(\mathrm{x,y})}^{\mu} - E_{(\mathrm{x,y})}^{soft} \tag{4.1}$$

and $E_{\mathrm{T}}^{\mathrm{miss}} = \sqrt{E_{\mathrm{x}}^{\mathrm{miss}2} + E_{\mathrm{y}}^{\mathrm{miss}2}}$. Each term is calculated as the sum of the corresponding objects projected onto x and y directions. The electron term $E_{(\mathrm{x,y})}^{e}$ is calculated using electrons that pass the medium requirements (Section 4.4.1) with $E_{\mathrm{T}} > 10$ GeV. The photon term $E_{(\mathrm{x,y})}^{\gamma}$ is calculated using photons passing the tight electron selection and with $E_{\mathrm{T}} > 10$ GeV. The tau term $E_{(\mathrm{x,y})}^{\tau}$ is included for some ATLAS analyses, though the analyses described in this thesis do not differentiate between hadronic taus and jets in the $E_{\mathrm{T}}^{\mathrm{miss}}$ calculation. The jet term $E_{(\mathrm{x,y})}^{\mathrm{jets}}$ is calculated using jets reconstructed according to Section 4.4.3 and with $p_{\mathrm{T}} > 20 GeV$. The soft term $E_{(\mathrm{x,y})}^{soft}$ is calculated from topoclusters and tracks not associated to high-p_{T} objects. The topoclusters are calibrated according to the same local calibration scheme used for jets.

Chapter 5

Data Quality in ATLAS

This chapter discusses data quality monitoring and assessment in the ATLAS experiment. The author contributed to various aspects such as the monitoring software framework, the automatic defect calculator, and tools for assessing the impact of detector problems on data-taking efficiency.

5.1 Overview

The ATLAS detector is a very complex piece of machinery with over 100 million readout channels. Since the detector has many different subsystems and technologies, many things can impact the state of the detector in negative ways. For example, a calorimeter module may experience electronics failure or generally be noisy, which can negatively effect the detection capability and energy measurement of charged particles. With so many things that can go wrong, it is necessary to develop a robust system for specifying the state of the detector at any point in time and recording that information in a useful format. This information can then be used to control the quality of the data used for analysis by rejecting data collected

during faulty detector times.

ATLAS has used two different schemes for representing the detector data quality (DQ) during data taking. The original scheme was a "flag" based system used in 2010. In this approach, color codes were used to flag sub-detector status as green (ok), yellow (caution), red (bad), black (disabled), or grey (undecided). The flags from each source were then merged by hand to produce the final detector-wide flags which established the portions of data that were good for analysis. This was problematic because all issues needed to be quickly reduced to a limited and unchanging set of flags, often without sufficient study. Also, tracking detector problems was difficult because the flags did not preserve useful information about which problems were present. The current scheme in ATLAS for representing the data quality is the defect system. It was adopted for the 2011 data taking and was also used in 2012. In this approach, any problem with the detector, such as a non-nominal module voltage, etc., is saved in a database as a defect specifying the period of affected time (the interval of validity, or IOV). The defect system is further described in Section 5.2 [47].

In order to assign flags or defects to intervals of time in collected data, the detector conditions and outputs must be monitored to look for detector problems or general deviations from usual behavior. This is done in multiple ways. Online shifters monitor the detector performance and online-measured distributions while data is being collected. Then, a subset of the data is processed with the full offline reconstruction software so that offline shifters can again check standard distributions for oddities. In addition, detector conditions information is stored in a conditions database, and offline software uses the database to look for detector problems. The results of each of these checks get stored in the defect database for future retrieval. This monitoring scheme is illustrated in Figure 5.1.

The end result of this work is the propagation of the DQ information to the analyzers for physics analysis. This is done via a set of standard XML files called good run lists (GRLs). These files are generated using the defect database and specify the list of luminosity blocks
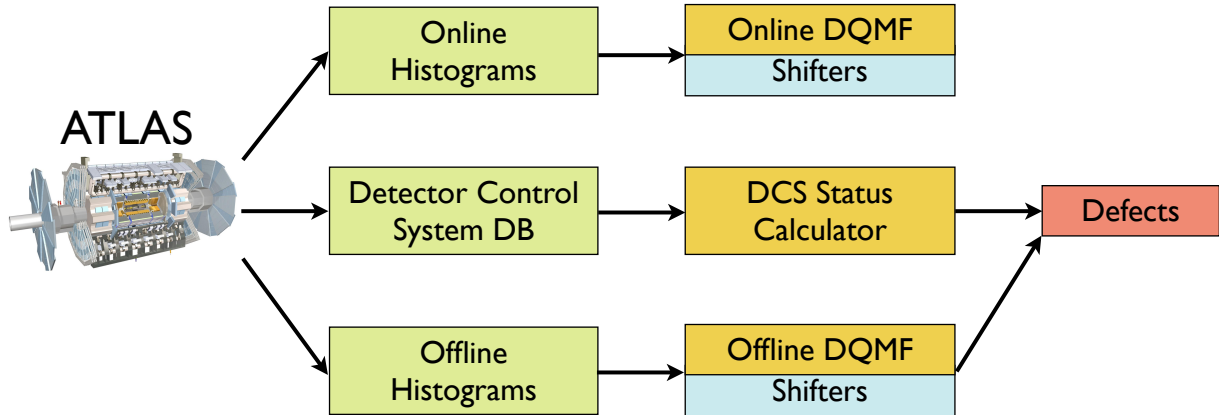
Figure 5.1: The defect system for assessing data quality. Detector data is sent to online and offline histograms for shifter monitoring and manual assignment of defects. Detector control data is sent to the detector control system database for automatic assignment of defects by the DCS calculator.

which are approved for analysis. Several GRLs are generated with varying criteria depending on the needs of the corresponding physics studies.

5.2   Detector Defects

A defect in ATLAS DQ represents a non-ideal state of the detector. It can represent a problem with a single detector module or a combination of modules or detectors. There are two types of defects [47]:

primary defects represent low level detector problems. Things like non-nominal module voltage, noise bursts, and dead modules are examples. Primary defects may be tolerable and have no noticeable effect on physics measurements. These defects are defined once when a new detector problem is discovered, and their definition does not normally change.

virtual defects are logical combinations of primary defects and represent the high level logic of the data quality decisions. For example, a virtual defect might represent a general problem in the LAr EM calorimeter and would be implemented as a logical OR of all intolerable defects in that system. Virtual defect logic can change as studies are done to assess the impacts of primary defects on physics measurements.

The defect system is powerful because of its inherent flexibility. Primary defects can be stored as soon as they are discovered, whereas the virtual defect logic can be updated at any time. In other words, the current approach involves storage of potential *problems* with the detector. In contrast, the old flag-based approach involved storage of DQ *decisions*. Defects are self-documenting and allow for easy tracking of detector issues. Subdetector experts can use this information to make improvements to the detector and its calibration. An example of virtual defect logic is shown for the Electromagnetic Barrel Calorimeter C (EMBC) virtual defect in Figure 5.2. This defect is present whenever there are intolerable problems with the corresponding subdetector such as high voltage trips, noise burts, etc. Some virtual defects are used to improve bookkeeping. For example, UNCHECKED defects (like LAR_UNCHECKED in the figure) are used to signify which portions of data have not been fully reviewed by shifters.

To illustrate the power of the defect approach we consider the case of the high voltage trip in the LAr calorimeter. The voltage, applied to each calorimeter module, determines the response of the detector to the energy deposited by charged particles. Hence, its value impacts the calibration of the particle energy measurement. Occasionally, however, the system fails and the voltage level trips, dropping down well below the nominal value. The system can automatically recover from the situation, but it can take a few minutes for the voltage to ramp back up to the nominal value. In the defect approach, This situation is represented by two primary defects. The first one specifies that a trip has occurred, called HVTRIP. The second one specifies that the voltage is ramping back up, called HVRAMPUP.

Figure 5.3 illustrates this type of event and shows how the two defects are defined. Once these defects are defined, analyzers have the power to assess the impact of these events separately. In this case, the HVTRIP defect is considered intolerable because any energy measurements made in this time window would be untrustworthy. However, during the voltage ramp-up, the energy measurement is still useable as the system is recalibrated as the voltage level changes. Studies were thus able to show that the impact on physics measurements was negligible. Thus, by providing maximal flexibility, the defect system allows for greater optimization of the data-taking efficiency.
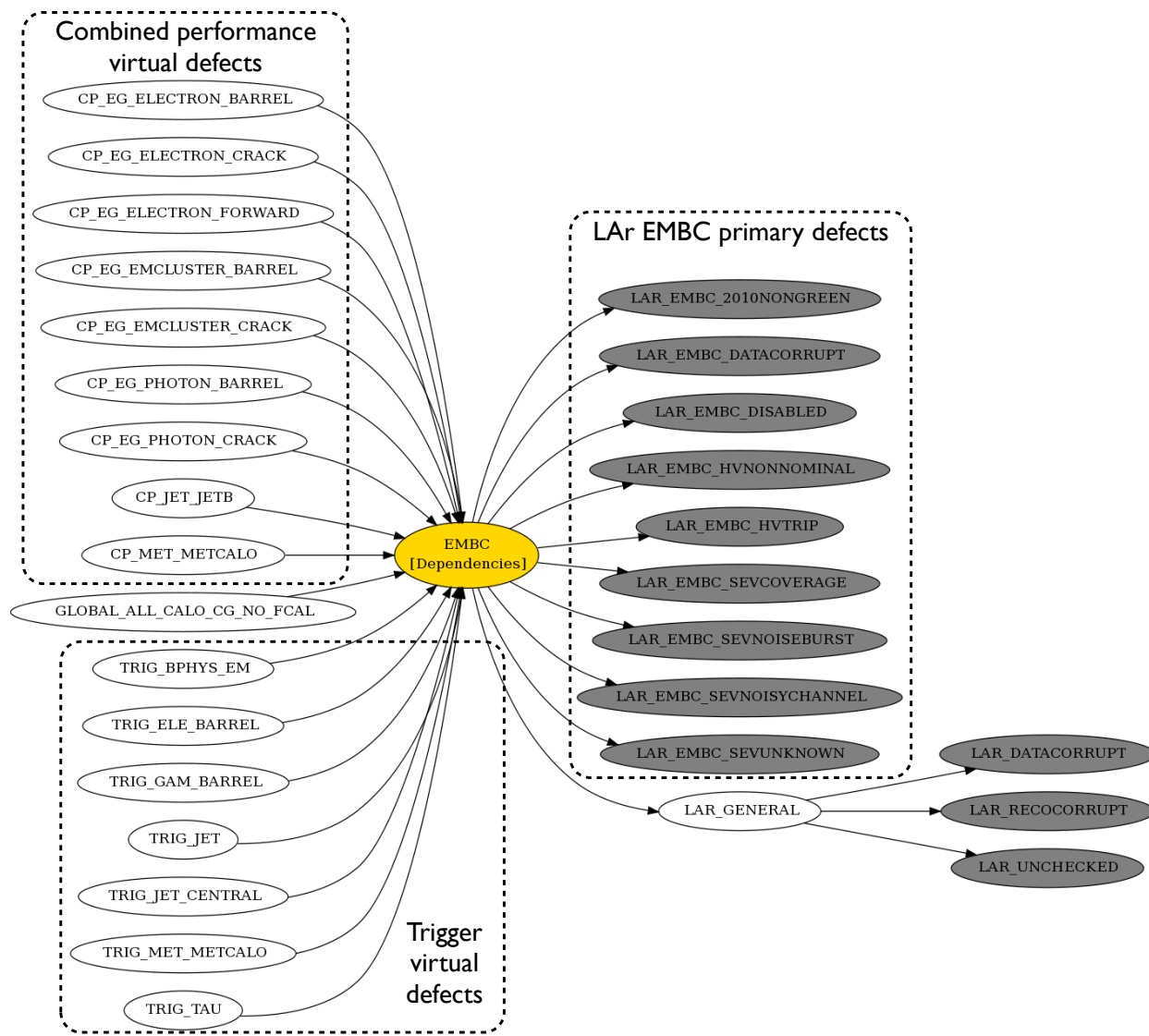
Figure 5.2: Defect relationships for the Electromagnetic Barrel Calorimeter C (EMBC) virtual defect. Dark grey defects are primary, and white defects are virtual. The EMBC defect is a logical OR of all of the defects to the right, which consist of liquid Argon high voltage trips (HVTRIP), noise bursts (SEVNOISEBURST), etc. To the left are virtual defects that depend on EMBC, such as combined performance defects for electrons, photons, jets, the missing transverse momentum measurement (MET), and various trigger-related defects.
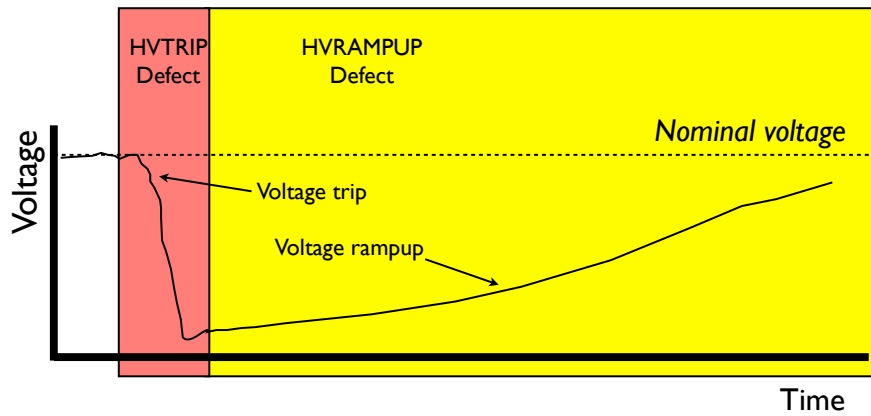
Figure 5.3: The high voltage trip is an example LAr calorimeter problem in which the high voltage is lost. After the trip, the voltage ramps back up to its nominal value. Different defects are used to represent the two stages of this detector issue, the HVTRIP and HVRAMPUP defects. By splitting the event in this way, analyzers are able to study the impacts of these effects separately.

5.3　Data Taking Efficiency

The ATLAS data taking efficiency for pp collisions at $\sqrt{s} = 8$ TeV in 2012 is shown in Figure 5.4. The DAQ system performed very well at over 95% efficiency. The delivered, recorded, and analyzed integrated luminosity as a function of time is shown in Figure 5.5. The recorded luminosity reflects the DAQ inefficiency, as well as the inefficiency of the so-called "warm start": when the stable beam flag is raised, the tracking detectors undergo a ramp of the high-voltage and, for the pixel system, turning on the preamplifiers. The data quality assessment shown corresponds to the All Good efficiency shown in the 2012 DQ table.

ATLAS p-p run: April-December 2012										
Inner Tracker			Calorimeters		Muon Spectrometer				Magnets	
Pixel	SCT	TRT	LAr	Tile	MDT	RPC	CSC	TGC	Solenoid	Toroid
99.9	99.1	99.8	99.1	99.6	99.6	99.8	100.	99.6	99.8	99.5
All good for physics: 95.5%										

Luminosity weighted relative detector uptime and good quality data delivery during 2012 stable beams in pp collisions at √s=8 TeV between April 4th and December 6th (in %) – corresponding to 21.3 fb⁻¹ of recorded data.

Figure 5.4: ATLAS data taking efficiency in 2012 pp collisions during LHC fills with stable beams and after switching the tracking detectors on.
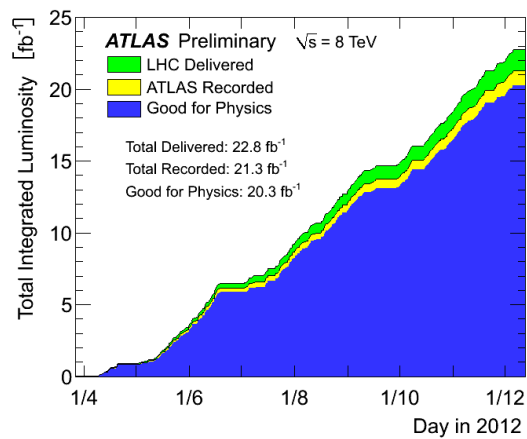
Figure 5.5: Cumulative luminosity versus time delivered by the LHC (green), recorded by ATLAS (yellow), and certified to be good quality data (blue) during stable beams and for *pp* collisions at $\sqrt{s} = 8$ TeV in 2012. The recorded luminosity reflects the DAQ inefficiency, as well as the inefficiency of the so-called "warm start": when the stable beam flag is raised, the tracking detectors undergo a ramp of the high-voltage and, for the pixel system, turning on the preamplifiers. The data quality assessment shown corresponds to the All Good efficiency shown in the 2012 DQ table.

Chapter 6

A Search for Electroweak SUSY in Three-Lepton Final States

6.1 Introduction

This chapter describes a search for electroweak supersymmetry in the three-lepton channel. This work is an update and extension of the work documented in [48]. It uses 20.3 fb^{-1} of 8 TeV ATLAS data collected during 2012. The results are interpreted in terms of generic simplified models as well as the Phenomenological MSSM (pMSSM). Significant improvements have been made to the analysis since the previous result. Previously considered signals with $\tilde{\chi}_1^{\pm}\tilde{\chi}_2^0$ production and decays via sleptons or SM gauge bosons have been reevaluated with a binned signal region to improve sensitivity. The analysis now considers hadronic tau decays, which opens up sensitivity to new scenarios such as $\tilde{\chi}_1^{\pm}\tilde{\chi}_2^0$ production and decays via staus exclusively or via a Higgs boson. The results are currently under ATLAS internal review with a publication expected in the near future.

The author has contributed significantly to this analysis as well as the previous results

presented at [48, 49, 50, 51]. The contributions include development of object and event selection, trigger strategy, fake lepton background estimation, and analysis software.

Electroweak production of SUSY generally refers to pair production of charginos, neutralinos, and sleptons via the supersymmetric electroweak couplings shown in Figure 3.4. While this analysis focuses on the three-lepton channel, other channels are covered by additional analyses described in [52, 53, 54, 55].

While it is important to try and search for supersymmetry in as many manifestations as possible, electroweak production of SUSY particles is particularly well motivated at this point in time. Current LHC limits on the masses of squarks and gluinos are in the TeV range. Figure 6.1 then suggests that production of electroweakinos could be the dominant SUSY production at the LHC. Also, as explained in Section 3.6, naturalness requires fairly light electroweakinos. They are expected to have masses in the hundreds of GeV range, which is accessible at the LHC. Finally, electroweak production can lead to final states with high lepton multiplicity and little to no hadronic activity. At a hadron collider this last feature is particularly attractive because the amount of hadronic activity can then be a strong discriminator between SUSY signal and the SM background.
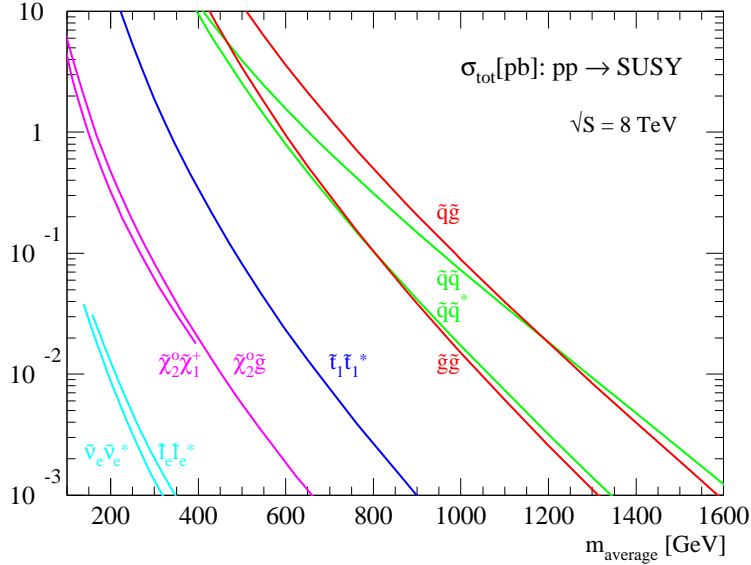
Figure 6.1: SUSY production cross sections in pp collisions at $\sqrt{s} = 8$ TeV calculated with Prospino [56].

6.2 Targeted SUSY Scenarios

This analysis is designed to target SUSY processes containing charginos $(\tilde{\chi}_j^{\pm})$ and neutralinos $(\tilde{\chi}_i^0)$ and discriminate against events from SM processes. The results are interpreted in the context of "simplified models" [57] and the pMSSM. In the case of the pMSSM, the scenario is defined such that direct electroweak production is the dominant source of $\tilde{\chi}_j^{\pm}$s and $\tilde{\chi}_i^0$s.

6.2.1 Simplified Models

With a new physics framework as vast as supersymmetry, it is essential to try and formulate analysis results in a generic way that is flexible for interpretation in many different specific models. This is accomplished via simplified models, which are generic models based around a specific SUSY-like phenomenology. They have the minimal particle content necessary to produce the processes of interest and are parametrized directly in terms of the sparticle masses. In the absence of an observed SUSY signal, limits are then set on the production

cross section times branching ratio as a function of the sparticle masses. This way, a specific SUSY model with the same event topology can be tested by plugging in these values and comparing with the predicted theoretical cross section. The results can also be applied to SUSY-like signatures with similar kinematics [58].

In this analysis, the associated production of the lightest chargino and the second-lightest neutralino are considered. The lightest charginos and the second-lightest neutralinos are assumed to be pure wino-like and the $\tilde{\chi}_1^0$ bino-like. This gives the largest cross-section among the direct electroweakino processes and naturally leads to a multilepton signature. In addition, it is a good approximation in the limit that the $\tilde{\chi}_1^{\pm}$ and $\tilde{\chi}_2^0$ masses are large compared to the Z boson mass. It is also assumed that the $\tilde{\chi}_1^{\pm}$ and $\tilde{\chi}_2^0$ are mass degenerate, $m_{\tilde{\chi}_1^{\pm}} = m_{\tilde{\chi}_2^0}$, which is a common feature of MSSM models [58] and a good approximation as long as the mass difference with the $\tilde{\chi}_1^0$ is large. Four scenarios are considered. In all cases, the squark masses are set as as high as a few hundreds of TeV.

Cross sections are calculated for all of the simplified models for the sake of drawing limit contours. These results are useful as a way to visualize the sensitivity of the analysis, but they should not be interpreted as applicable to all realistic models. The cross sections are calculated with Prospino [56] using the sparticle mass assumptions relevant to each model described below, as well as the assumption that the mass states are pure flavor states.

In the first scenario, referred to as "simplified models with sleptons", the left-handed charged sleptons and sneutrinos are assumed to be light and the right-handed charged sleptons are assumed to be heavy enough that they do not contribute in the decays. In this case the chargino and neutralino will dominantly decay via the left-handed sleptons or sneutrinos as shown in Figure 6.2(a). The process is flavor-democratic, all three lepton flavors are equally present in the final state. The masses of $\tilde{\chi}_1^{\pm}, \tilde{\chi}_2^0, \tilde{l}_L, \tilde{\nu}, \tilde{\chi}_1^0$ are free parameters. The sleptons and sneutrinos are taken to be mass degenerate; the masses are set halfway between the $\tilde{\chi}_1^{\pm}$ and the $\tilde{\chi}_1^0$ masses: $m_{\tilde{l}_L} = \frac{m_{\tilde{\chi}_1^0} + m_{\tilde{\chi}_2^0}}{2}$. This choice is a good approximation to more

realistic models when the mass splitting between the $\tilde{\ell}_L/\tilde{\nu}$ and the $\tilde{\chi}_1^0$ is relatively large. The branching ratios of $\tilde{\chi}_1^\pm$ to $\ell\tilde{\nu}$ and $\tilde{\ell}_L\nu$ are both set to 0.5. The branching ratios of $\tilde{\chi}_2^0$ to $\ell\tilde{\ell}_L$ and $\tilde{\nu}\nu$ are both set to 0.5. The BR to $e/\mu/\tau$ final states are equal, as imposed by the Standard Model.

In the second scenario, referred to as "simplified models with WZ", the sleptons are assumed to be very heavy so as not to contribute to the decays of the $\tilde{\chi}_1^\pm$ and $\tilde{\chi}_2^0$. Then, the $\tilde{\chi}_1^\pm$ and $\tilde{\chi}_2^0$ decay via SM gauge bosons. To ensure a three-lepton signature, only the lepton decays of the bosons are considered. Thus, the chargino decay is $\tilde{\chi}_1^\pm \to W\tilde{\chi}_1^0 \to \ell\nu\tilde{\chi}_1^0$ and the neutralino decay is $\tilde{\chi}_2^0 \to Z\tilde{\chi}_1^0 \to \ell\ell\tilde{\chi}_1^0$. The diagram for this scenario is shown in Figure 6.2(b).

In the third scenario, referred to as "simplified models with staus", the $\tilde{\tau}$ is light while the $\tilde{e}$ and $\tilde{\mu}$ are very heavy. In this case, the charginos and neutralinos decay exclusively via $\tilde{\tau}$ or $\tilde{\nu}_\tau$. The purpose of this signal model is to cover situations in MSSM parameter space in which decays via staus are dominant, which tends to happen for large values of the parameter $\tan\beta$. The diagram for this scenario is shown in Figure 6.2(c). The branching ratios of $\tilde{\chi}_1^\pm$ to $\tau\tilde{\nu}_\tau$ and $\tilde{\tau}\nu_\tau$ are both set to 0.5. The branching ratios of $\tilde{\chi}_2^0$ to $\tau\tilde{\tau}$ and $\tilde{\nu}_\tau\nu_\tau$ are both set to 0.5.

In the fourth scenario, referred to as "simplified models with Higgs", the neutralinos are assumed to be higgsino-like and decay via a Higgs boson only. As with the simplified models with WZ, the sleptons are assumed to be very heavy so that the charginos decay only via a W boson. The mass of the Higgs boson in the models is 125 GeV and decays to $\tau\tau$, WW, or ZZ are considered with SM branching ratios. The considered Feynman diagrams can be seen in Figure 6.2(e) and Figure 6.2(d).

(a) via sleptons

(b) via WZ

(c) via staus

(d) via Higgs with taus

(e) via Higgs with light leptons
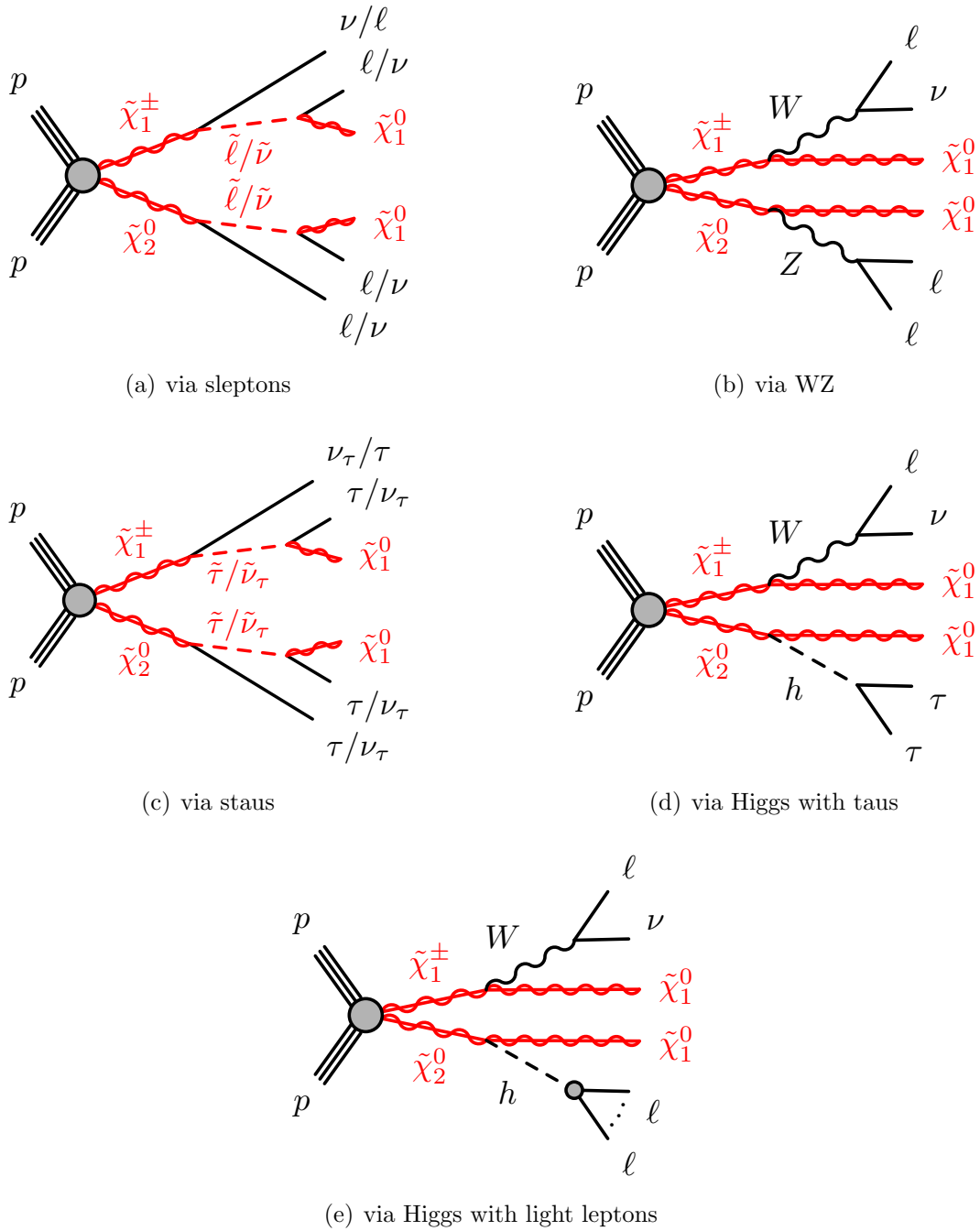
Figure 6.2: The Feynman diagrams for the simplified models.

6.2.2 Phenomenological MSSM

In the phenomenological MSSM (pMSSM), the $\tilde{\chi}_j^\pm \tilde{\chi}_i^0$ cross-sections and the branching ratios are governed by the U(1) gaugino mass M_1, the SU(2) gaugino mass M_2, the higgsino mass $|\mu|$, and the ratio of the vacuum expectation values of the two Higgs fields in the theory $\tan\beta$ [59].

The pMSSM grids were produced by varying the M_1, M_2, and $|\mu|$ parameters. The mass of the CP-odd Higgs (m_A) is set to 500 GeV while the other mass parameters to 2 TeV. The mass of the SM-like Higgs is set to 125 GeV with maximum mixing in the stop sector.

The first grids, called **pMSSM** $\tilde{\ell}_R$, were generated with intermediate mass right handed sleptons ($\tilde{e}_R, \tilde{\mu}_R, \tilde{\tau}_R$), where the masses for the sleptons are degenerate and their value is at midpoint between the $\tilde{\chi}_1^0$ and $\tilde{\chi}_2^0$ masses. The parameter $\tan\beta$ is set to $\tan\beta = 6$.

A second grid, **pMSSM** $\tilde{\tau}_R$, was created with $M_1 = 75$ GeV and $\tan\beta = 50$, where decays via intermediate mass right handed $\tilde{\tau}_R$ dominate. The $\tilde{\tau}_R$ mass is set halfway between the $\tilde{\chi}_1^0$ and $\tilde{\chi}_2^0$ masses.

The final grid, **pMSSM no** $\tilde{\ell}$, was created with $M_1 = 50$ GeV, $\tau\beta = 10$, and all slepton masses set to 3 TeV. This way, only decays via W, Z, and Higgs bosons dominate.

6.3 Data and Monte Carlo Samples

6.3.1 Data Sample

The data sample used in this analysis was collected between April and December of 2012. The data is required to satisfy the criteria in a standard GRL, which requires that the LHC

has declared stable beams, the detector was properly operating, and both the solenoidal and toroidal magnetic fields were at nominal conditions. The total integrated luminosity analyzed was $20.3\,\mathrm{fb}^{-1}$.

6.3.2 Monte Carlo Samples

All MC samples utilised in the analysis are produced using the ATLAS Underlying Event Tune 2B [60] based detector simulation. For the MadGraph [61], Powheg [62] and most ALPGEN [63] samples, PYTHIA [64] is used for the shower. Fragmentation and hadronisation for MC@NLO [65] and some ALPGEN [63] samples are performed with HERWIG [66], using JIMMY [67] for the underlying event.

All MC@NLO and Powheg MC samples are generated using the next-to-leading order PDF set CT10 [68], while the ALPGEN and MADGRAPH samples are generated using the PDF set CTEQ6L1.

Standard Model MC Samples

Monte Carlo samples are used to study and model the Standard Model backgrounds important for the three lepton analysis. Some of them are used directly in the Standard Model background estimate, others are used for auxillary measurements in combination with data, and still others are used for MC systematic uncertainty studies.

Diboson The $ZZ/\gamma^*, WZ/\gamma^*$ and WW diboson processes are generated with the next-to-leading-order (NLO) generator Powheg. Cross sections for normalization are obtained from NLO MCFM. The gluon fusion ZZ process is described using additional samples generated with Jimmy.

$Z/W + \gamma$ processes are generated with the SHERPA generator.

Additional samples are produced at generator-level with aMC@NLO for the evaluation of systematic uncertainties.

Triboson The triboson processes $WWW \rightarrow l\nu l\nu l\nu$, $ZWW \rightarrow lll\nu l\nu$, and $ZZZ \rightarrow llll\nu\nu$ are generated with MadGraph to leading-order in QCD.

Top Top quark pair production processes are generated with Powheg. The Hathor tool is used to compute approximate NNLO cross sections [69]. Single top production is generated with MC@NLO and AcerMC.

$t\bar{t}$+boson The $t\bar{t}+Z(+\text{jets})$ and $t\bar{t}+W(+\text{jets})$ processes are generated using the LO generator Alpgen, while the $t\bar{t}+WW$ and tZ processes are generated using MadGraph. Additional $t\bar{t}+Z(+\text{jets})$ and $t\bar{t}+W(+\text{jets})$ samples are also generated with MadGraph for systematic studies.

Boson+jets The Z/γ^* and W processes produced with associated jets are produced with ALPGEN (+Pythia). Additional Z/γ^* samples with low dilepton invariant mass are also generated using ALPGEN (+Jimmy). The W and Z/γ^* ALPGEN LO cross-sections are scaled to NNLO.

Standard Model Higgs SM Higgs production processes where the Higgs decays to taus or via W or Z bosons to leptons are generated with Pythia. Five production mechanisms are included: gluon fusion (ggF), vector boson fusion (VBF), associated production with a W (WH) or Z boson (ZH), and (for $H \rightarrow WW^*$) associated production with a $t\bar{t}$ pair ($t\bar{t}$H). For the higgs decay to two leptons and two quarks via Z bosons, only assosicated production with a vector boson is considered. All cross-sections are calculated at NNLO QCD + NLO EW precision, except $pp \rightarrow t\bar{t}H$, which is calculated at NLO QCD precision [70].

New Physics MC Samples

The pMSSM and simplified model MC simulated samples were generated using HERWIG++ with the PDF set CTEQ6L1 defined above [71].

6.4 Event Selection

6.4.1 Trigger

This analysis uses a light-lepton-based (e, μ trigger scheme which is chosen to be as inclusive as possible without overwhelming the ATLAS TDAQ system. In order to maximize the selection efficiency of events of interest, events may pass any of the trigger chains listed in Table 6.1. The analysis leptons are required to be within $\Delta R < 0.15$ of the relevant trigger objects. They are also required to be above the offline p_T thresholds shown in Table 6.1. This ensures that the leptons are in the plateau region of the trigger efficiency.

Both single-isolated-lepton and di-lepton triggers are utilized. For the single isolated lepton triggers, only events are considered for which the leading light lepton matches successfully to the trigger element. This is to prevent a bias on the sub-leading lepton fake rates used in the matrix method background estimate described in Section 6.5.3.

Table 6.1: The triggers used to preselect events. The offline thresholds are enforced to ensure that the lepton(s) triggering the event are in the plateau region of the trigger efficiency.

Trigger	Detail	offline threshold [GeV]
Isolated e	EF_el_EF_e24vhi_medium1	25
Isolated μ	EF_mu24i_tight	25
ee	EF_2e12Tvh_loose1	14,14
	EF_e24vh_medium1_e7_medium1	25,10
$\mu\mu$	EF_2mu13	14,14
	EF_mu18_tight_mu8_EFFS	18,10
$e\mu$	EF_e12Tvh_medium1_mu8	14,10
	EF_mu18_tight_e7_medium1	18,10

Events in MC are selected using the trigger simulation. Studies were performed to compare the trigger performance between data and MC. Discrepancies are typically smaller than 2% for the trigger chains mentioned above. A conservative systematic uncertainty of 5% is

applied to the MC sample yields to account for this discrepancy.

6.4.2   Event Quality Cuts

To reject background events or events suffering from reconstruction or other problems, some
quality cuts are applied to the data and MC samples:

- Events with jets potentially originating from instrumental effects are rejected.

- Events with fake $E_{\mathrm{T}}^{\mathrm{miss}}$ due to non operational cells in the tile and the HEC are rejected

- Events with noise bursts and data integrity errors in the LAr calorimeter are removed.

- Events with corrupted Tile event data are removed.

- Events with missing detector information due to the TTC restart procedure are re-
  moved.

- Events with jets pointing to the tile calorimeter hot spot ($-0.2 < \eta < 0.1$ and $2.65 <$
  $\phi < 2.75$) are rejected.

- The leading primary vertex must have five or more tracks.

- Events are discarded if there is a muon surviving overlap removal with a longitudinal
  impact parameter $|z_0| > 1\,\mathrm{mm}$ or a transverse impact parameter $|d_0| > 0.2\,\mathrm{mm}$. This
  selection is designed to suppress potential cosmic background.

- Events containing muons with $\frac{\sigma_{q/p}}{|q/p|} \geq 0.2$ before overlap removal are excluded from the
  analysis selection to veto events with potentially mis-measured muons.

6.4.3   Object Selection

The object selection criteria used in this analysis are optimized for SUSY signal signifi-
cance and include official recommended cleaning cuts from the relevant ATLAS performance

groups. Most objects are defined with two levels of selection criteria: "baseline" object selection and "signal" object selection. Baseline objects include basic reconstruction criteria and overlap removal and are generally used for determining the exclusive channel of the event. Signal objects have tighter selection criteria (e.g. isolation) used to further discriminate against background objects. For the light leptons, the baseline selection is used as a loose criteria for the matrix matrix background estimate (Section 6.5.3).

Electrons

Electrons are reconstructed using the standard algorithm described in Section 4.4.1. Additional criteria including standard identification cuts, kinematic cuts, isolation cuts, and impact parameter cuts, are used to refine the identification.

Baseline electrons are required to pass the following selection cuts:

- The *medium* identification criteria (see Section 4.4.1).

- Transverse energy $E_{\mathrm{T}} > 10\,\mathrm{GeV}$.

- Cluster pseudorapidity $|\eta^{cl}| < 2.47$.

- Electrons must not pass through regions of the electromagnetic calorimeter where the signal cannot be read due to dead optical transmitters or other calorimeter problems.

- Overlap removal scheme explained in Section 6.4.3.

Signal electrons are baseline electrons satisfying:

- The *tight* identification criteria (see Section 4.4.1).

- d_0 significance (unbiased $|d_0/\sigma_{d_0}|$) less than 5

- Unbiased $|z_0 \sin\theta|$ less than $0.4\,\mathrm{mm}$

- An isolation requirement defined as $p_\mathrm{T}\mathrm{cone}30/E_\mathrm{T} < 0.16$ where $p_\mathrm{T}\mathrm{cone}30$ is the the transverse momentum of all other tracks[6] with $p_\mathrm{T} > 1$ GeV within a cone of $\Delta R = \sqrt{(\Delta\eta)^2 + (\Delta\phi)^2} \leq 0.3$ around the electron track and E_T is the electron transverse energy.

- An isolation requirement defined as $E_\mathrm{T}\mathrm{cone}30^{\mathrm{corrected}}/E_\mathrm{T} < 0.18$, where

$$E_\mathrm{T}\mathrm{cone}30^{\mathrm{corrected}} = E_\mathrm{T}\mathrm{cone}30 - C \times N_{\mathrm{vtx}},$$

$C = 20.15$ MeV (17.94 MeV) in data (MC simulation), N_{vtx} is the number of vertices with at least 5 tracks, and $E_\mathrm{T}\mathrm{cone}30$ is a p_T and energy-density corrected isolation as measured in the EM calorimeter. The dependence on the number of vertices is introduced to correct for pileup effects. The dependence of the isolation variable $E_\mathrm{T}\mathrm{cone}30$ on the number of vertices was measured in data and MC and observed to be nearly linear with a slope of C.

Muons

Muons are reconstructed using the algorithm described in Section 4.4.2. This analysis uses combined and segment-tagged muons only. Additional criteria for identification include kinematic cuts, track hit requirements, isolation cuts, and impact parameter cuts.

Baseline muons are required to pass the following selection cuts:

- Transverse momentum $p_\mathrm{T} > 10\,\mathrm{GeV}$.

- Pseudorapidity $|\eta| < 2.5$.

- The track must have at least one b-layer hit (if expected).

- The track must have more than 1 pixel hit and at least 6 SCT hits.

---

[6] $|d_0| < 1$ mm, $|z_0| < 1.0$ mm, nHitBlayer>=1, nHitSilicon$\geq$7

- The track must have less than 3 holes in the pixel and SCT.

- The track must satisfy the following TRT requirements:

  - $(0.1 < |\eta| < 1.9)$: require $n > 5$ and $n_{TRT}^{outliers} < 0.9 \times n$,

  - $(|\eta| < 0.1$ or $|\eta| > 1.9)$: if $n > 5$, require $n_{TRT}^{outliers} < 0.9 \times n$,

  where $n = n_{TRT}^{hits} + n_{TRT}^{outliers}$.

- Overlap removal scheme explained in Section 6.4.3.

Signal muons are baseline muons satistfying:

- d_0 significance (unbiased $|d_0/\sigma(d_0)|$) less than 3.

- Unbiased $|z_0 \sin\theta|$ less than $1\,\mathrm{mm}$.

- An isolation requirement defined as $p_T\mathrm{cone}30^{\mathrm{corrected}}/p_T < 0.12$, where

$$p_T\mathrm{cone}30^{\mathrm{corrected}} = p_T\mathrm{cone}30 - C \times N_{\mathrm{vtx}},$$

and $C = 10.98$ MeV (6.27 MeV) in data (MC simulation).

Jets

Jets are reconstructed using the algorithm described in Section 4.4.3 with local cluster (LC) calibration. Kinematic cuts and a JVF requirement are used to reduce contribution from poorly reconstructed jets and background jets (e.g., from pileup).

Baseline jets are required to pass the following selection cuts:

- Transverse momentum $p_T > 20\,\mathrm{GeV}$

- Pseudorapidity $|\eta| < 4.5$

- Overlap removal scheme explained in Section 6.4.3.

Signal jets are baseline jets satisfying:

- Pseudorapidity $|\eta| < 2.5$

- Jets with $p_T < 50$ GeV, $|\eta| < 2.4$ must also satisfy JVF > 0.5, where JVF is defined in Section 4.4.3.

B-tagged jets are signal jets tagged as b-jet candidates by the MV1 algorithm with MV1 $>$ 0.3511. This operating point corresponds to an average b-tagging efficiency of $\sim$80%, which means approximately 80% of b-jets should be correctly tagged by the algorithm [42].

As mentioned in Section 6.4.2, events with problematic jets are rejected in order to suppress potential sources of instrumental background and background due to cosmic rays.

Taus

Hadronic tau reconstruction uses the algorithm and identification technique described in Section 4.4.4. Kinematic cuts and BDT based identification cuts are used to refine the selection. Taus only have one selection critieria used for both channel determination and optimized background rejection.

Signal taus are required to pass the following selection cuts:

- Transverse momentum $p_T > 20$ GeV

- Pseudorapidity $|\eta| < 2.5$

- Number of tracks associated to the tau is 1 or 3

- Charge must be ± 1

- Medium tau identification consisting of loose electron BDT, medium jet BDT, and a muon veto.

- Overlap removal scheme explained in Section 6.4.3.

Overlap Removal

ATLAS reconstruction does not fully discriminate between objects. For example, electrons are nearly always also reconstructed as jets due to their calorimeter shower. Thus, the analysis selections must take care to remove the ambiguity between overlapping objects. In addition, background processes such as photon radiation with conversion to electrons and leptonic decays of hadrons in jets result in reconstructed objects that are close together in η–ϕ space. These processes are reduced by vetoing the appropriate nearby objects. The following requirements are applied to the objects as defined in the previous sections, and are applied sequentially such that only surviving objects are used in later steps.

1. $\Delta R_{e1,e2} < 0.05$, discard lowest E_{T} electron to remove duplicated electrons with different clusters and shared tracks.

2. $\Delta R_{e,j} < 0.2$, discard jet to remove electrons duplicated in jet container.

3. $\Delta R_{e,\tau} < 0.2$, discard tau to remove electrons duplicated in tau container.

4. $\Delta R_{\mu,\tau} < 0.2$, discard tau to remove muons duplicated in tau container.

5. $\Delta R_{e,j} < 0.4$, discard electron to remove electrons within jets.

6. $\Delta R_{\mu,j} < 0.4$, discard muon to remove muons within jets.

7. $\Delta R_{e,\mu} < 0.01$, discard both electron and muon due to muons undergoing bremsstrahlung.

8. $\Delta R_{\mu,\mu} < 0.05$, discard both muons due to shared tracks.

9. $\Delta m_{\mathrm{SFOS}} < 12\,\mathrm{GeV}$, discard both leptons from low mass decays.

10. $\Delta R_{signal\,\tau,j} < 0.2$, discard jets to remove taus duplicated among the jets.

Missing Transverse Momentum

The missing transverse momentum, E_T^miss, is an important variable for SUSY analysis because it is used to select events with invisible stable particles (like the LSP). The algorithm used in this analysis is desribed in Section 4.4.5 with a few specific settings used in all ATLAS SUSY searches. The muon term ($E_{(\text{x,y})}^\mu$) is calculated using all baseline muons as defined above. Pileup suppression techniques are not used in this analysis. Typical backgrounds in the three-lepton signal regions have real E_T^miss from neutrinos so the pileup suppression is not necessary.

6.4.4   Signal Regions

To maximize sensitivity of the analysis to the SUSY events of interest, various signal regions are defined to target each of the considered signal processes. The signal regions are exclusive in the number of baseline light leptons and the number of taus. For example, the three light lepton signal regions require exactly three baseline light leptons—all three of which must also pass the signal lepton requirements—and exactly zero hadronic taus. This choice allows for a statistical combination of the results with other ATLAS electroweak channels. A common feature of all signal regions is the usage of a b-tagged jet veto, where the b-tagged jet is defined as in Section 6.4.3. This requirement reduces the background contribution from $t\bar{t}$ and $Z + \text{HF}$ but has a small impact on the signal processes. The event selection criteria in the following signal regions is chosen to maximize the approximate signal significance given by Z_N [72]:

$$Z_N = \sqrt{2} \ \text{erf}^{-1}(1 - 2p) \tag{6.1}$$

where p indicates the p-value which is calculated assuming an uncertainty of 30% on the background yields. Thus, the signal regions are optimized for a discovery of supersymmetry. This gives the best chances for seeing a signal if supersymmetry is realized in nature. In particle physics, a discovery usually corresponds to a signal significance of 5 σ.

The signal regions are split by lepton channel to target the different final states of the $\tilde{\chi}_1^\pm \tilde{\chi}_2^0$ decays. For $\tilde{\chi}_1^\pm \tilde{\chi}_2^0$ **with intermediate sleptons and** WZ, light lepton final states offer the best discrimination against the SM background. Thus, the three light lepton channel is used to target this scenario. The simplified models for this scenario are flavor democratic, so when taus are present only the decays to light leptons are selected in this channel. For $\tilde{\chi}_1^\pm \tilde{\chi}_2^0$ **with intermediate staus**, the high tau multiplicity is exploited by using the channel with one light lepton and two hadronic taus. For $\tilde{\chi}_1^\pm \tilde{\chi}_2^0$ **with intermediate** Wh, two channels are used to maximize sensitivity. The three light lepton channel is sensitive to the case when the Higgs decays to light leptons via taus or gauge bosons. In addition, when the Higgs decays to two taus and one of those tau decays leptonically, a same-sign (SS) signature is possible when the W also decays leptonically. Since same-sign signatures are rare in the SM, the channel with two SS light leptons and one tau has good sensitivity. The signal regions for each lepton channel are defined below.

3 Light Leptons

Two signal regions are defined for the three light lepton channel. The first one, **SR0a**, targets the simplified models with sleptons (Figure 6.2(a)) and WZ (Figure 6.2(b)). The second, **SR0b**, targets the simplified models with Wh and light lepton final states (Figure 6.2(e)).

SR0a   Previous results of this analysis used several exclusive signal regions to target different areas of kinematic phase space for the decays with sleptons and with WZ [48].

For this round, a binned signal region is used which utilizes much more phase space via many sub-regions (bins) that are statistically combined to give the strongest sensitivity. These processes usually have at least one same-flavor opposite-sign (SFOS) lepton pair from $\tilde{\chi}_2^0 \to \ell^\pm \tilde{\ell}^\mp \to \ell^\pm \ell^\mp \tilde{\chi}_1^0$ or $\tilde{\chi}_2^0 \to Z^* \tilde{\chi}_1^0 \to \ell^\pm \ell^\mp \tilde{\chi}_1^0$, so a requirement of at least one SFOS pair is imposed on the signal region events.

The optimization of **SR0a** is done by maximizing the sensitivity to the simplified models with sleptons and WZ. The first step in designing this binned signal is to identify the variables used in the binning. All of the SUSY signatures have true $E_{\mathrm{T}}^{\mathrm{miss}}$ from LSPs and neutrinos, though the actual $E_{\mathrm{T}}^{\mathrm{miss}}$ spectrum depends on the sparticle masses and thus varies throughout the grids. So, it is useful to bin in $E_{\mathrm{T}}^{\mathrm{miss}}$ to maximize sensitivity to many areas of phase space. For the signal region to have sensitivity to decays with resonant (on-shell Z) leptons as well as non-resonant (off-shell Z or slepton) leptons, it is important to bin in the invariant mass of the SFOS lepton pair, m_{SFOS}. The final variable is useful for discriminating against the Standard Model WZ production. In the three lepton channel, the Z decays to two leptons while the W decays to a lepton and a neutrino. The transverse mass, m_{T}, formed from the W lepton and the $E_{\mathrm{T}}^{\mathrm{miss}}$, has a kinematic endpoint at the W mass. Processes without $W \to \ell\nu$ or with additional invisible particles can have a longer m_{T} tail, so this variable is a powerful discriminator against the WZ background and is thus used as the third variable in the SR0a binning.

The next step in the optimization of SR0a is to choose the bins. The low-$E_{\mathrm{T}}^{\mathrm{miss}}$ region defined by $E_{\mathrm{T}}^{\mathrm{miss}} < 50$ GeV has negligible sensitivity to the signal models and is thus reserved for background validation (see Section 6.7). Five bins are used for the m_{SFOS}: $[12, 40, 60, 81.2, 101.2, \infty]$. In each mass bin, the $E_{\mathrm{T}}^{\mathrm{miss}}$ and m_{T} are divided into two bins with the edges adjusted for maximal sensitivity. Thus, the total number of bins is 20[7]. An additional requirement is imposed on bins with background contribution from $Z \to \ell\ell\ell$ where

---

[7] The total number of bins was intentionally kept to a low number (10–40) in order to reduce the fluctuations from low statistics in the background model.

one of the ℓ comes from a converted photon from final state radiation[8]. The MC samples are used to determine which bins have a contribution from this process. The optimized bin choices are shown in Table 6.2.

Table 6.2: Summary of the bins in m_{SFOS}, m_{T}, and $E_{\mathrm{T}}^{\mathrm{miss}}$ for SR0a.

m_{SFOS}	m_{T}	$E_{\mathrm{T}}^{\mathrm{miss}}$	$3\ell\ Z$veto	SR bin
$12-40$	$0-80$	$50-90$		1
		$90-\infty$		2
	$80-\infty$	$50-75$		3
		$75-\infty$		4
$40-60$	$0-80$	$50-75$	yes	5
		$75-\infty$		6
	$80-\infty$	$50-135$		7
		$135-\infty$		8
$60-81.2$	$0-80$	$50-75$	yes	9
	$80-\infty$	$50-75$		10
	$0-110$	$75-\infty$		11
	$110-\infty$	$75-\infty$		12
$81.2-101.2$	$0-110$	$50-90$	yes	13
		$90-\infty$		14
	$110-\infty$	$50-135$		15
		$135-\infty$		16
$101.2-\infty$	$0-180$	$50-210$		17
	$180-\infty$	$50-210$		18
	$0-120$	$210-\infty$		19
	$120-\infty$	$210-\infty$		20

SR0b This region targets the decays with Wh, where the Higgs may decay via taus or gauge bosons to light leptons. The branching ratio for this light lepton final state is very low, though the channel benefits from lower SM background than the channels with taus. A veto on events with SFOS light lepton pairs is applied to discriminate against SM processes with SFOS leptons, particularly WZ. Additional cuts are tested to further improve sensitivity:

- The $E_{\mathrm{T}}^{\mathrm{miss}}$ for events with three leptons, SFOS veto, and a b-jet veto is shown in

---

[8]This requirement is imposed because of problems modeling this process with the matrix method described in Section 6.5.3.

Figure 6.3. The best cut value is chosen to be $E_T^{miss} > 50$ GeV.

- The p_T of the third (softest) lepton after the above cuts are applied is shown in Figure 6.4. The largest background here is $t\bar{t}$, where the third lepton comes from the leptonic decay of a b-hadron. It can be seen that a cut of $p_T^\ell > 20$ GeV is optimal and helps reduce the contribution from $t\bar{t}$.

- The $\Delta\phi$ between opposite-sign (OS) leptons is calculated for all leptons pairs after the above cuts are applied. The minimum value calculated, $\min(\Delta\phi(\ell^\pm, \ell^\mp))$, is plotted in Figure 6.5. The signal process is seen to have OS leptons closer together in ϕ than the SM background, which is fairly flat in this variable. A cut value of $\min(\Delta\phi(\ell^\pm, \ell^\mp)) < 1.0$ is thus chosen to remove the small amounts of remaining backgrounds.
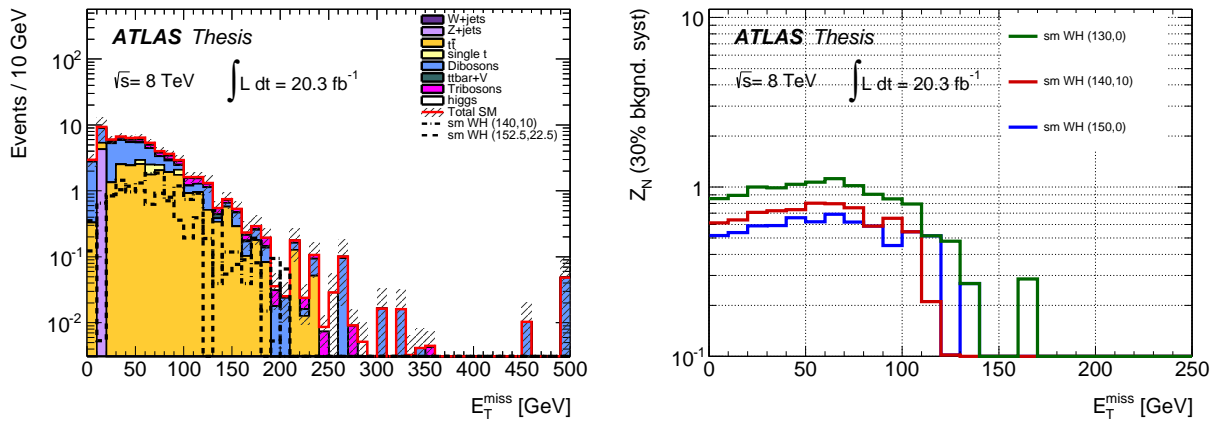
Figure 6.3: The E_T^{miss} distribution in three lepton events where a SFOS veto and a b-jet veto are applied (left), and the signal significance of a E_T^{miss} cut for Wh signal benchmark points (right).

2 Light Leptons + 1 Tau

One signal region is defined for the lepton channel with two light leptons and one tau to target the decays with Wh where the Higgs decays to taus and the W also decays leptonically. This signature can give same-sign (SS) light lepton final states when the $\tilde{\chi}_1^\pm$ decays as $\tilde{\chi}_1^\pm \rightarrow$
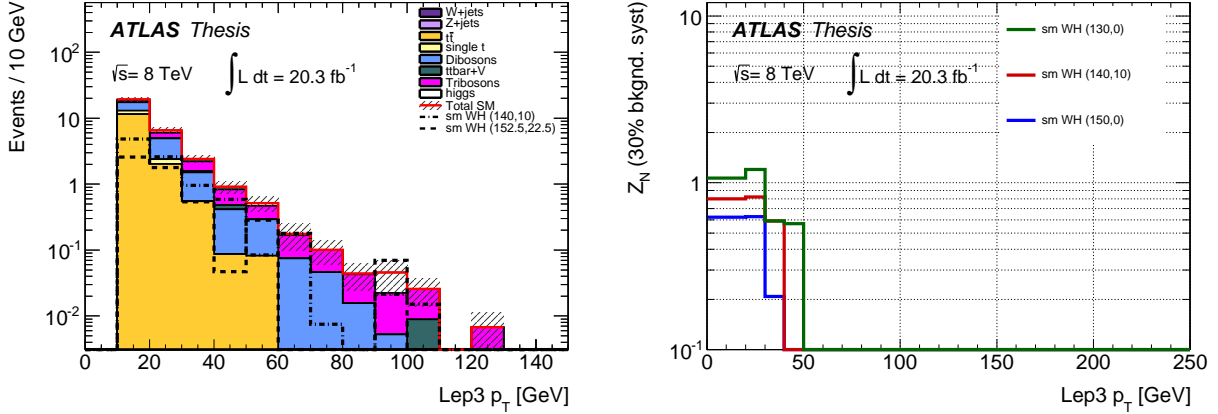
Figure 6.4: The $p_T^{3rd\ell}$ distribution in three lepton events where a SFOS veto, a b-jet veto, and $E_T^{miss} > 50$ GeV cut are applied (left), and the signal significance of a p_T cut for Wh signal benchmark points (right).

$W^{\pm}\tilde{\chi}_1^0 \to \ell^{\pm}\nu\tilde{\chi}_1^0$ and the $\tilde{\chi}_2^0$ decays as $\tilde{\chi}_2^0 \to h\tilde{\chi}_1^0 \to \tau_{lep}^{\mp}\tau_{had}^{\pm}\tilde{\chi}_1^0$. The signal region, **SR1SS**, thus requires SS light leptons, a signature that has very low SM background. Opposite-sign signatures were also considered for the Wh process, but the signal regions had low sensitivity due to large SM background contributions.

SR1SS As explained above, this signal region targets the decays with Wh in a final state with two SS light leptons and one tau. Additional cuts to reduce the background include a E_T^{miss} cut, invariant mass cuts on the leptons and taus, and lepton p_T cuts. Each of the cuts is described below.

- One of the SM background contributions in a SS signature comes from processes where an electron's charge is mis-identified. For example, this can happen in $Z \to ee$ events where one $e^{\pm}$ radiates a hard photon which converts asymmetrically into a hard $e^{\mp}$ and a soft $e^{\pm}$. If the charge identification is performed on the $e^{\mp}$, then the event will look like a SS process. Figure 6.6 shows the invariant mass of the SS lepton pairs in this selection, which peaks at the Z boson mass. To reduce this background, events are rejected that have a SS electron pair with invariant mass consistent with the Z
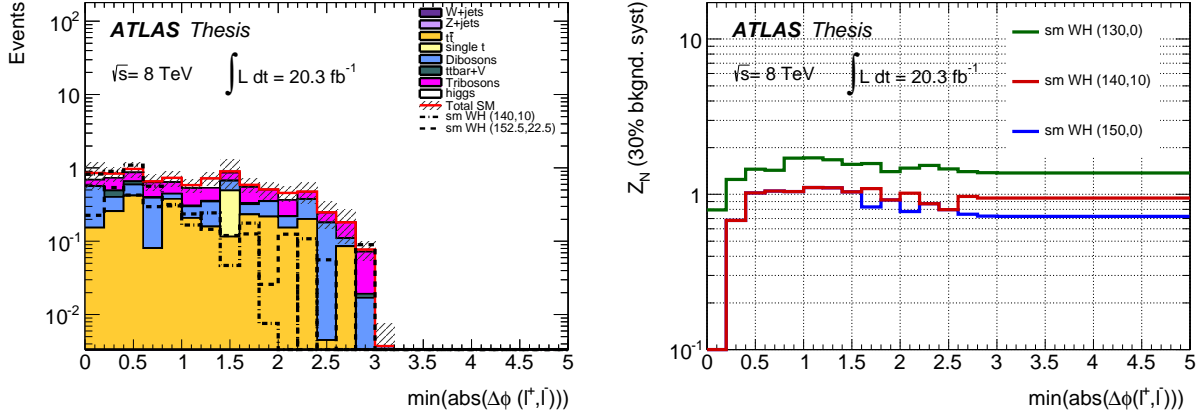
Figure 6.5: The $\min(\Delta\phi(\ell^{\pm}, \ell^{\mp}))$ distribution in three lepton events where a SFOS veto, a b-jet veto, a $E_T^{\text{miss}} > 50$ GeV cut, and a $p_T^\ell > 20$ GeV cut is applied (left) and the signal significance of a corresponding cut for Wh signal benchmark points (right).

boson: 81.2 GeV $< m_{ee} < 101.2$ GeV.

- The E_T^{miss} for events surviving the above cuts is plotted in Figure 6.7. It is seen that a requirement of $E_T^{\text{miss}} > 50$ GeV is optimal to discriminate against SM backgrounds.

- The scalar p_T sum of the two same-sign light leptons for events passing the above cuts is shown in Figure 6.8. The SUSY signal models tend to have larger total energy than the SM events, which results in higher momentum. A moderate requirement on this variable of $\sum p_T^\ell > 70$ GeV seems to discriminate well against the SM backgrounds.

- The Higgs decay products, one hadronic tau and one light lepton from a leptonic tau decay, tend to have a reconstructed invariant mass less than the Higgs mass. From MC studies it is known that the light lepton from the Higgs decay tends to be softer than the lepton from the W decay. So, the invariant mass of the hadronic tau and the second leading light lepton is calculated for events passing the cuts above and plotted in Figure 6.9. A requirement that $m_{\tau\ell}$ is less than 120 GeV is seen to be optimal and removes SM contributions from diboson and triboson production

- The distribution of the p_T of the sub-leading lepton is shown in Figure 6.10. It is seen that the SM backgrounds have softer sub-leading leptons than the SUSY scenarios. A

lepton p_T cut of $p_T^\ell > 30$ GeV is thus applied to further reduce these backgrounds.
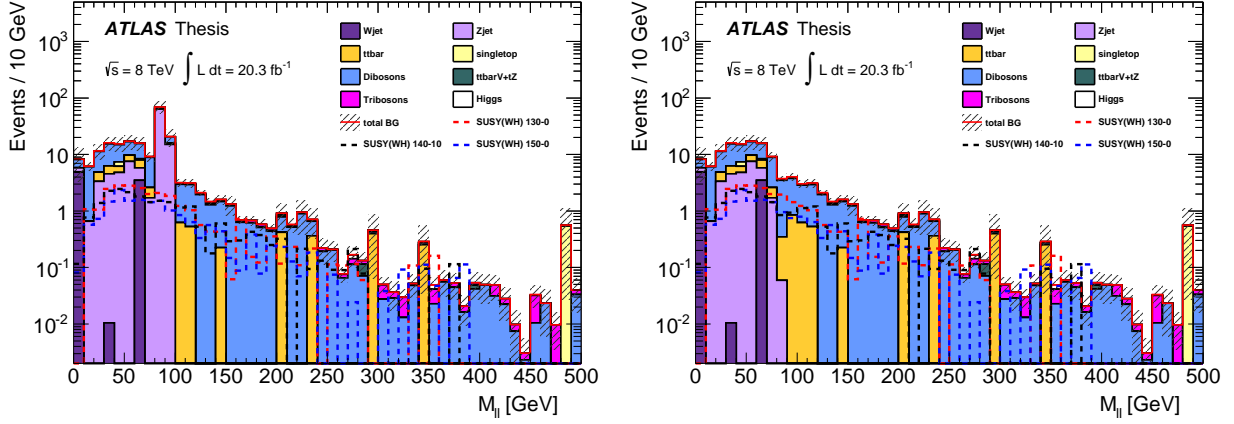
Figure 6.6: The $m_{\ell\ell}$ distribution in $\ell^\pm\ell^\pm\tau^\mp$ events where a b-jet veto is applied (left), and the same distribution after vetoing events with $|m_{ee} - m_Z| < 10$ GeV (right).
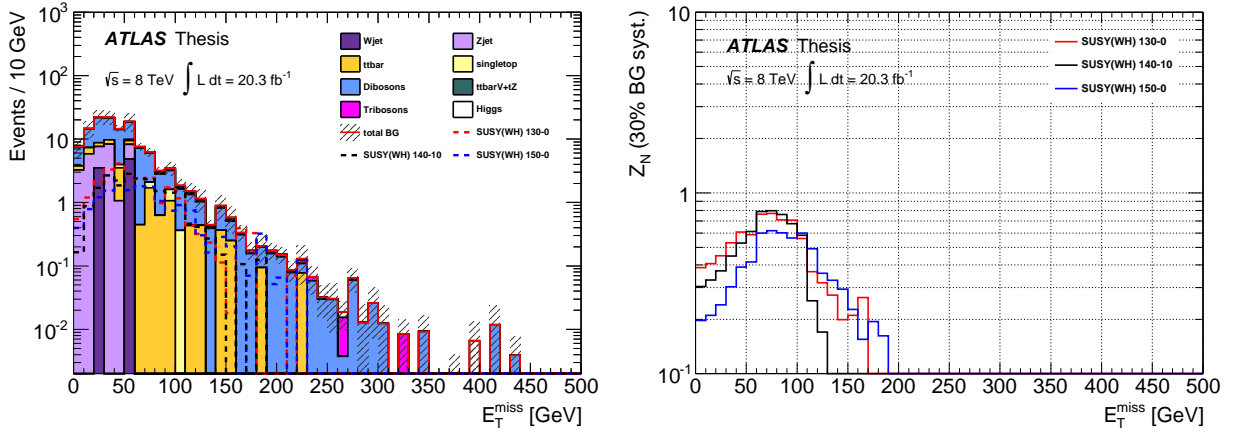
Figure 6.7: The E_T^{miss} distribution in $\ell^\pm\ell^\pm\tau^\mp$ events with a b-jet veto and a $Z(ee)$ veto applied (left), and the signal significance of a E_T^{miss} cut for the Wh benchmark points.
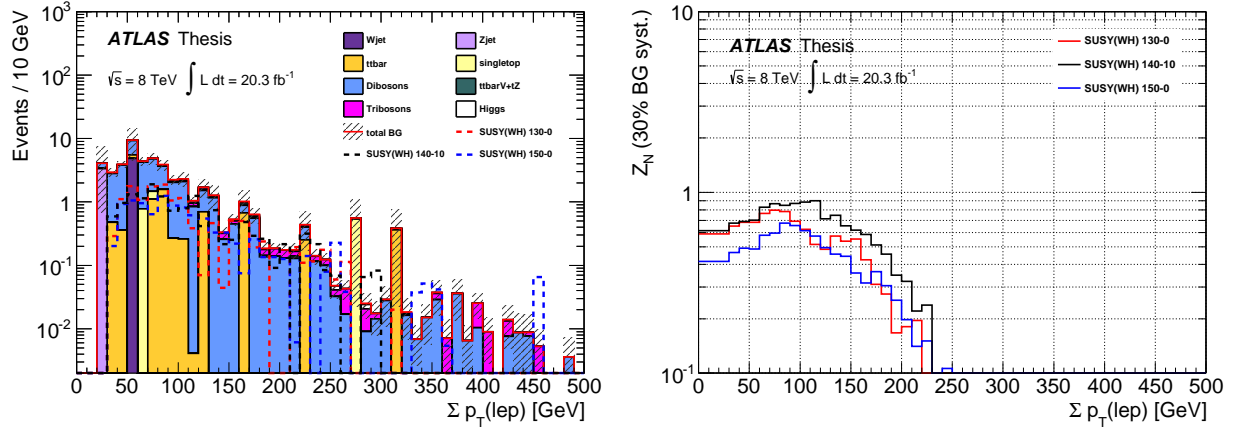
Figure 6.8: The $\sum p_T^\ell$ distribution in $\ell^\pm \ell^\pm \tau^\mp$ events with a b-jet veto, a $Z(ee)$ veto, and $E_T^{\text{miss}} > 50$ GeV cut applied (left), and the signal significance of a $\sum p_T^\ell$ cut for the Wh benchmark points.
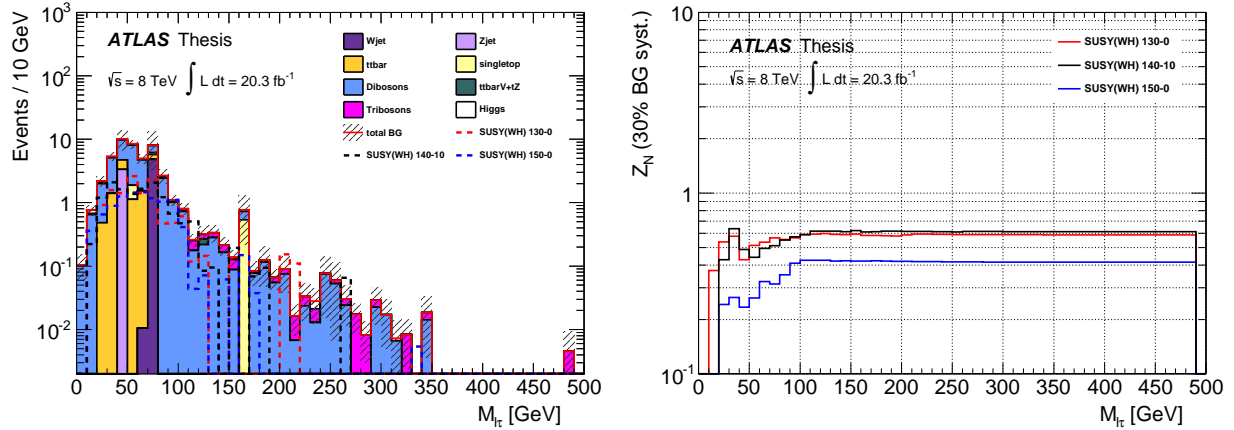
Figure 6.9: The $m_{\ell\tau}$ distribution in $\ell^\pm \ell^\pm \tau^\mp$ events with a b-jet veto, a $Z(ee)$ veto, a $E_T^{\text{miss}} > 50$ GeV cut, and a $\sum p_T^\ell > 70$ GeV cut applied (left), and the signal significance of an $m_{\ell\tau}$ cut for the Wh benchmark points. The sub-leading light lepton is used in the calculation of $m_{\ell\tau}$.
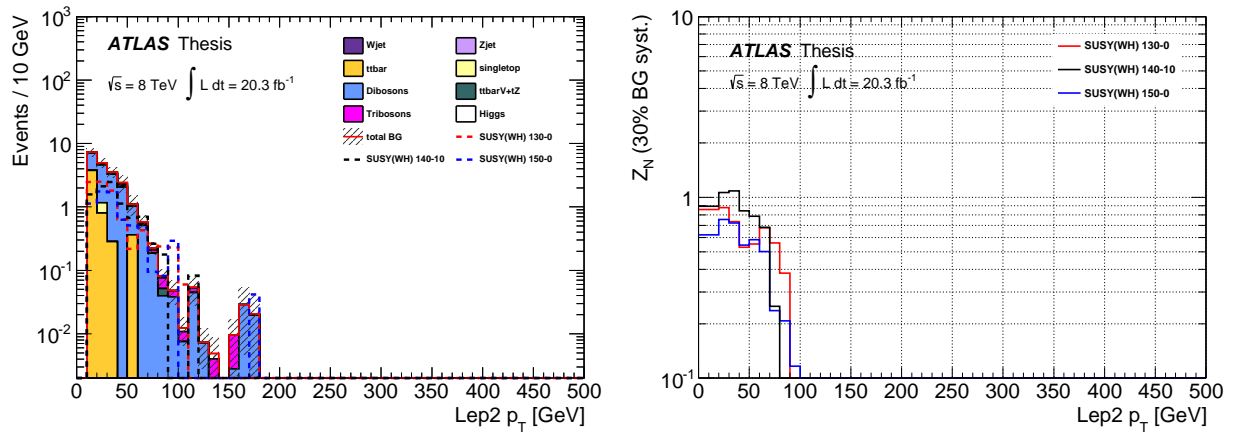
Figure 6.10: The $p_{\mathrm{T}}^{\mathrm{2nd}\ell}$ distribution in $\ell^{\pm}\ell^{\pm}\tau^{\mp}$ events with a b-jet veto, a $Z(ee)$ veto, $E_{\mathrm{T}}^{\mathrm{miss}} > 50$ GeV, $\sum p_{\mathrm{T}}^{\ell} > 70$ GeV, and $m_{\ell\tau} < 120$ GeV cuts applied (left), and the signal significance of a p_{T}^{ℓ} cut for the Wh benchmark points.

1 Light Lepton + 2 Taus

Two signal regions are defined in the channel with one light lepton and two hadronic taus. The first one, **SR2a**, targets the $\tilde{\chi}_1^{\pm}\tilde{\chi}_2^0$ decay via staus (Figure 6.2(c)). The second one, **SR2b**, targets again the decay via Wh with Higgs decaying to hadronic taus (Figure 6.2(d)).

SR2a   In the $\tilde{\chi}_1^{\pm}\tilde{\chi}_2^0$ decay with staus, the final state has three taus. This signal region is thus sensitive to the case when two of those taus decay hadronically and one leptonically. The cuts used to maximize the sensitivity are described below.

- The $E_{\mathrm{T}}^{\mathrm{miss}}$ distribution for $\ell\tau\tau$ events with a b-jet veto is shown in Figure 6.11. A cut of $E_{\mathrm{T}}^{\mathrm{miss}} > 50$ GeV is effective at reducing the W+jets and Z+jets contributions. It appear that cutting much harder on the $E_{\mathrm{T}}^{\mathrm{miss}}$ may be preferable, but it turns out that keeping this cut somewhat loose and instead cutting hard on m_{T2} gives a more optimal signal region.

- The "stransverse mass", m_{T2} [73, 74], is commonly used for discrimination of events with two heavy particles that each decay to one visible particle and one invisible particle. Like the m_{T} variable, the m_{T2} variable has a kinematic endpoint at the mass of the heavy decaying particle. For WW events then it would have a kinematic endpoint at the W boson mass. The variable can be constructed with just two of the $e/\mu/\tau$ and the $E_{\mathrm{T}}^{\mathrm{miss}}$ in the $\ell\tau\tau$ events to provide an effective discriminator between signal and background. The kinematic endpoint of the distribution remains at roughly the decaying particle mass, but is less pronounced since the information from one of the three leptons is not included. The m_{T2} variable is thus calculated for all pairs of leptons $(e/\mu/\tau)$ and the $E_{\mathrm{T}}^{\mathrm{miss}}$, and the maximum value, $\max(m_{\mathrm{T2}})$, is plotted after the above cuts are applied in Figure 6.12. The dominating background, W+jets, is seen to lie at values below ~ 100 GeV. Thus, a cut of $\max(m_{\mathrm{T2}}) > 100$ GeV is applied to

reduce this background.
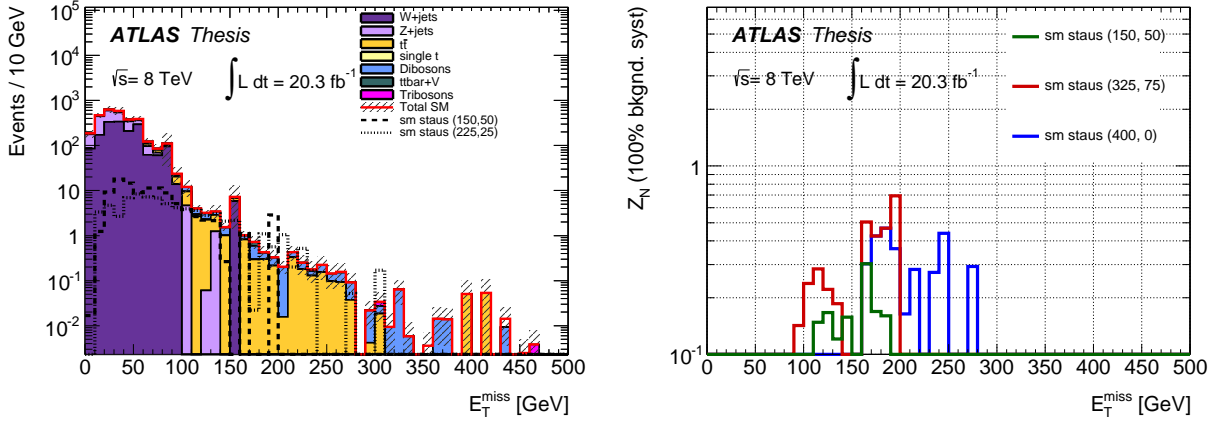
Figure 6.11: The E_T^{miss} distribution in $\ell\tau\tau$ events with a b-jet veto applied (left), and the signal significance of a E_T^{miss} cut for the $\tilde{\tau}$ benchmark points (right).
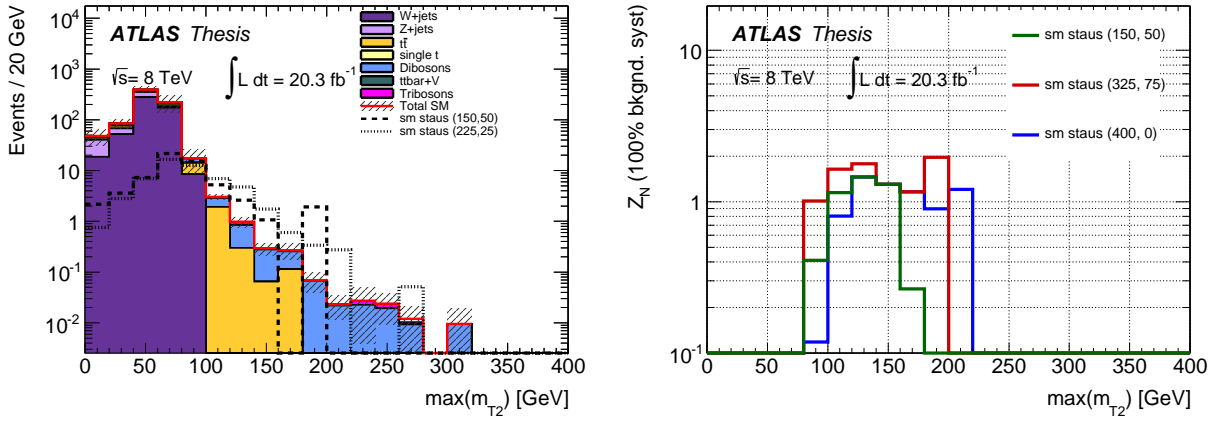
Figure 6.12: The $\max(m_{T2})$ distribution in $\ell\tau\tau$ events with a b-jet veto and $E_T^{miss} > 50$ GeV cut applied (left), and the signal significance of a $\max(m_{T2})$ cut for the $\tilde{\tau}$ benchmark points (right).

SR2b This signal region complements the coverage of $\tilde{\chi}_1^\pm \tilde{\chi}_2^0$ decay via Wh by SR0b and SR1SS by being sensitive to the case where the taus from the Higgs both decay hadronically. Since both taus are assume to come from the Higgs decay, they are required to have opposite charge. Additional cuts are described below.

- The E_T^{miss} distribution for $\ell\tau^\pm\tau^\mp$ events with a b-jet veto applied is shown in Figure 6.11.

A cut of $E_T^{miss} > 60$ GeV is seen to be optimal for discriminating against the W+jets and Z+jets backgrounds.

- Since both taus come from the Higgs decay, the invariant mass distribution $m_{\tau\tau}$ will have a different shape than taus originating from other SM sources. This is despite the fact that the Higgs mass cannot be accurately reconstructed due to the neutrino component of the tau decays as well as the additional $\tilde{\chi}_1^0$s in the event. The $m_{\tau\tau}$ distribution for events passing the above cuts is shown in Figure 6.14. It is seen that a mass window cut of 70 GeV$< m_{\tau\tau} < 120$ GeV is optimal for reducing the SM background contributions.

- The scalar sum of the p_T of the two taus is shown in Figure 6.15 for events passing the above cuts. The SUSY events tend to have a harder spectrum than the SM events. A requirement of $\sum p_T^\tau > 110$ GeV is seen to discriminate well against the background processes.
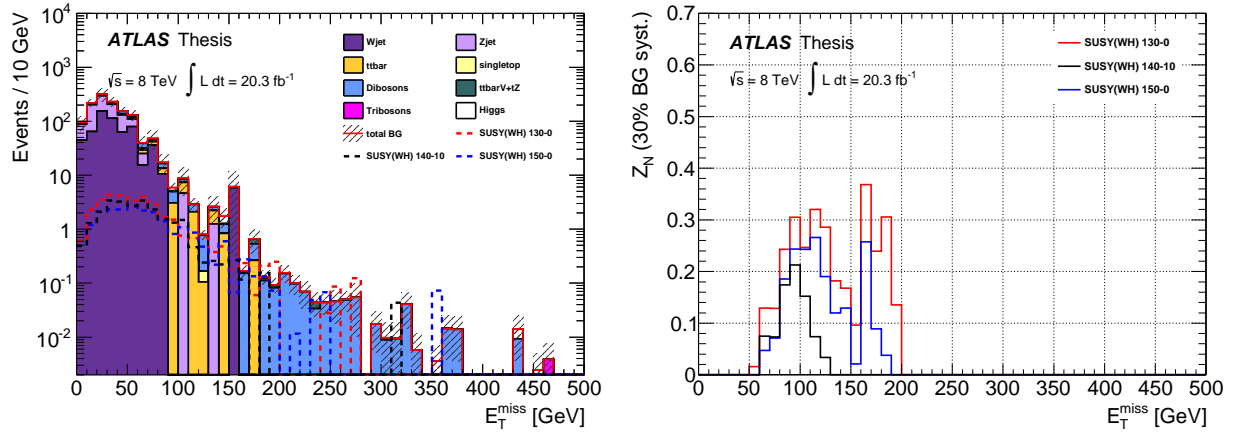

Figure 6.13: The E_T^{miss} distribution in $\ell\tau^\pm\tau^\mp$ events with a b-jet veto applied (left), and the signal significance of a E_T^{miss} cut for the Wh benchmark points (right).
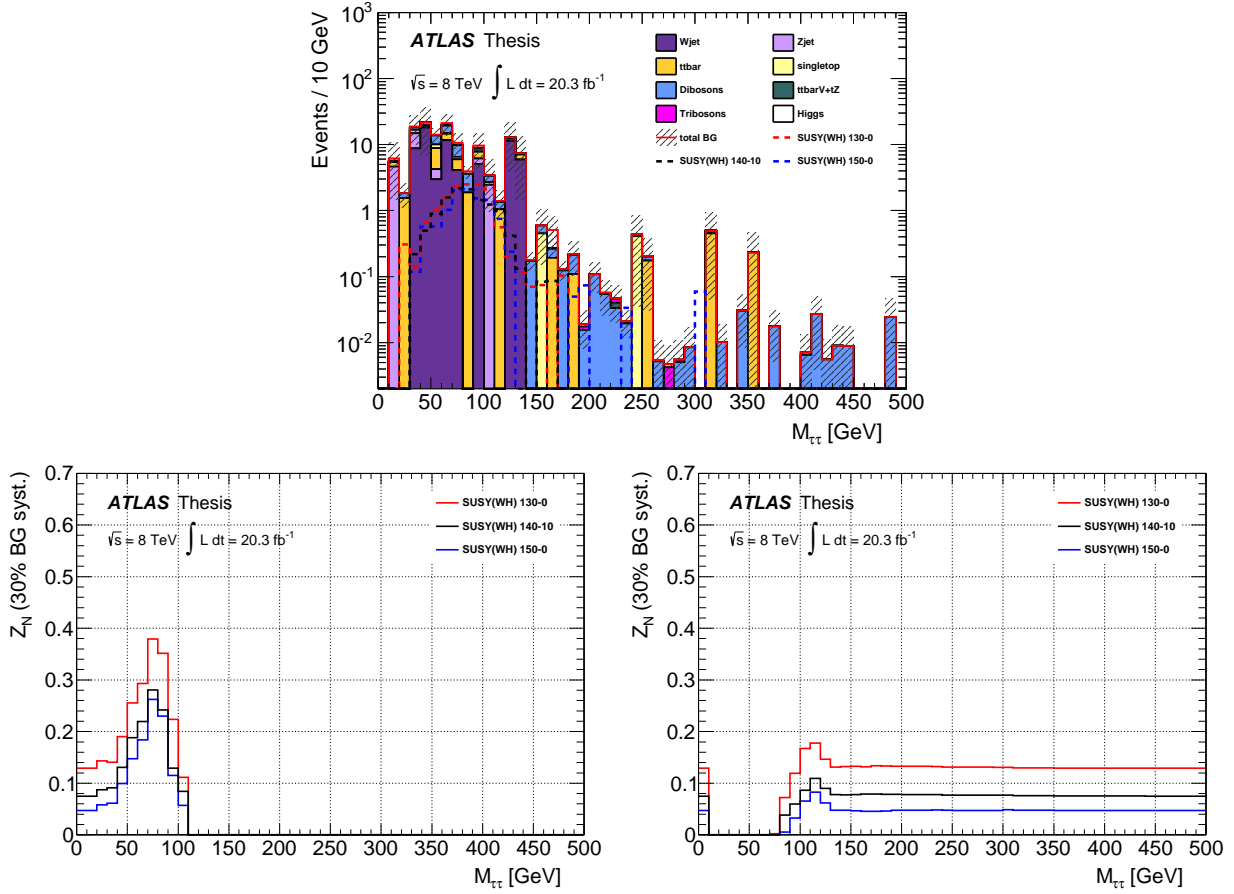
Figure 6.14: The $m_{\tau\tau}$ distribution in $\ell\tau^{\pm}\tau^{\mp}$ events with a b-jet veto and $E_{\mathrm{T}}^{\mathrm{miss}} > 60$ GeV cut applied (top), and the signal significance of a $m_{\tau\tau}$ lower cut (bottom left) and an upper cut (bottom right) for the Wh benchmark points.
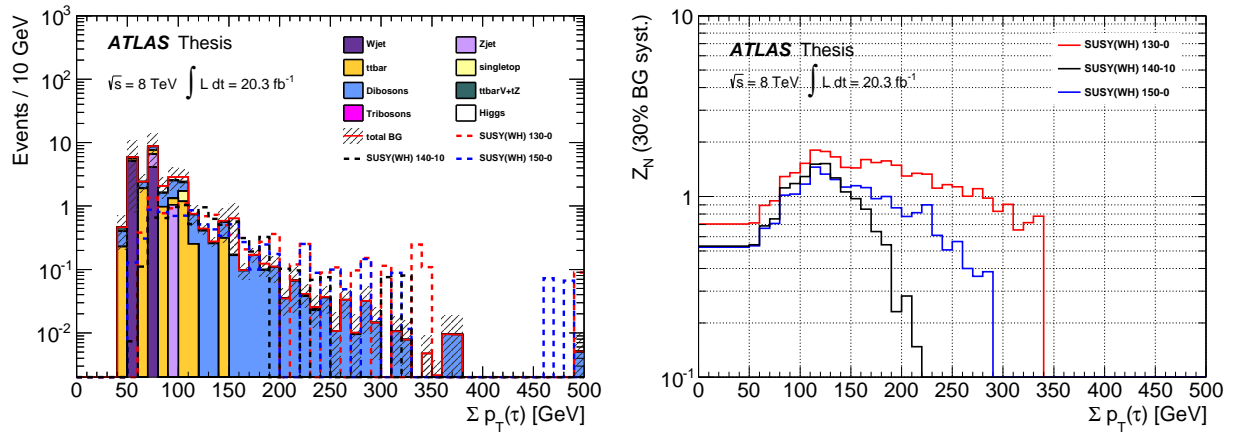
Figure 6.15: The $\sum p_{\mathrm{T}}^{\tau}$ distribution in $\ell\tau^{\pm}\tau^{\mp}$ events with a b-jet veto, $E_{\mathrm{T}}^{\mathrm{miss}} > 60$ GeV cut, and 70 GeV$< m_{\tau\tau} < 120$ GeV cut applied (left), and the signal significance of a $\sum p_{\mathrm{T}}^{\tau}$ cut for the Wh benchmark points (right).

Signal Region Summary

Table 6.3 summarizes the definitions of the signal regions.

Table 6.3: The selection requirements for the signal regions. The notation differentiates between light leptons (ℓ) and hadronic taus (τ). The units are GeV.

SR	SR0a	SR0b	SR1SS	SR2a	SR2b
ℓ flavor/sign	SFOS-ℓ	$\ell^\pm\ell^\pm\ell'^\mp$	$\tau^\pm\ell^\mp\ell^\mp$	$\tau\tau\ell$	$\tau^\pm\tau^\mp\ell$
Z boson	binned	–	veto (ee)	–	–
b-jet	veto	veto	veto	veto	veto
$E_\mathrm{T}^\mathrm{miss}$	binned	> 50	> 50	> 50	> 60
m_T	binned	–	–	–	–
m_T2	–	–	–	> 100	–
p_T^ℓ	–	> 20	> 30	–	–
$\min(\Delta\phi(\ell^\pm, \ell^\mp))$	–	≤ 1.0	–	–	–
$\sum p_\mathrm{T}^\ell$	–	–	> 70	–	–
$\sum p_\mathrm{T}^\tau$	–	–	–	–	> 110
$m_{\ell\tau}$	–	–	< 120	–	–
$m_{\tau\tau}$	–	–	–	–	70–120

6.5 Standard Model Background Estimation

6.5.1 Standard Model Background Model Overview

Standard Model processes can mimic the SUSY signal signature of three leptons and missing transverse momentum in multiple ways. Several processes give final states with high lepton multiplicity and one or more neutrinos. For example, $WZ \to \ell\ell\ell\nu$ gives a signature very similar to the simplified models with intermediate WZ, though the $E_{\mathrm{T}}^{\mathrm{miss}}$ spectrum differs due to the additional $\tilde{\chi}_1^0$s in the SUSY process. Others in this category like $t\bar{t}W \to 3\ell\, 5\nu\, 2b$ have the desired lepton and $E_{\mathrm{T}}^{\mathrm{miss}}$ signature but also have additional hadronic activity. Several processes give final states with fake or non-prompt leptons. These objects, collectively called "fake leptons", come from various sources:

- Hadronic jets mis-reconstructed as leptons

- Real but non-prompt leptons originating from the decays of hadrons within hadronic jets

- Real electrons produced from Bremsstrahlung photon conversions

A few examples of these types of objects are illustrated in Figure 6.16. Hadronic taus are mostly faked by light-flavor jets, though heavy flavor and electron conversions can also both mimic the displaced vertex feature of the tau decay. Besides lepton concerns, some processes can additionally mimic the $E_{\mathrm{T}}^{\mathrm{miss}}$ signature due to detector or reconstruction issues. This feature, referred to as "fake $E_{\mathrm{T}}^{\mathrm{miss}}$", can occur when the momentum of a lepton or jet is mis-measured resulting in a large imbalance of momentum in the calculation described in Section 4.4.

The event selection criteria defined in Section 6.4.4 reduces the contributions from these types of processes substantially, but they cannot be reduced completely. Thus, it is important to

(a) Prompt lepton   (b) Hadron decay in a jet   (c) Conversion lepton
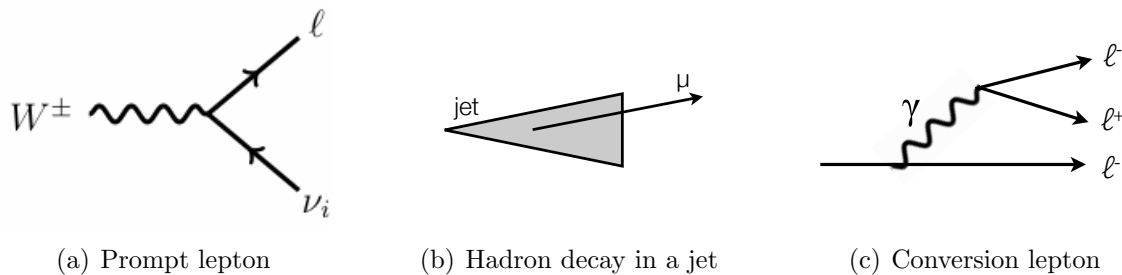
Figure 6.16: Illustrations of prompt and fake lepton types

have powerful methods to estimate their contributions in order to assess the compatibility of the observed data results with the Standard Model.

For a robust background estimate, we divide the background processes into two categories and model them with different methods. The first category includes processes with at least three real, prompt leptons. In this category the dominant ones are WZ/γ^*, ZZ/γ^*, triboson and $t\bar{t} + Z/W/WW$. These processes are modeled with the MC simulation which is generally powerful at modeling prompt leptons and event kinematics. The second category includes processes with at least one fake lepton referred to as "fake lepton backgrounds". The dominant fake-lepton backgrounds are $t\bar{t}$, Wt, Z/γ^*, and WW. These processes are difficult to model with MC simulation. Instead, a data-driven method which extrapolates the background estimate from control regions in the data to the signal regions is employed. The method used is a simplified matrix method and is described in detail in Section 6.5.3. The list below provides an overview of all sources of backgrounds considered in the analysis:

- Backgrounds with 3 real leptons:

  - WZ/γ^*, ZZ/γ^*, $t\bar{t} + Z/W/WW$, tZ where the gauge boson can be off-shell, and Higgs production

- Backgrounds with 2 real leptons and 1 fake lepton:

  - $t\bar{t}$, single top (Wt), WW, Z/γ^*, accompanied by a heavy flavor jet, or a light

flavor jet, or a conversion

- Backgrounds with 1 real lepton and 2 fake leptons:

  - single top (s-channel, t-channel), W accompanied by two fake leptons (from heavy flavor, light flavor, conversion)

The approach described above is used for the primary background model in the analysis. It provides the backgrounds for the signal regions. However, for auxillary studies and measurements it is often useful to use the MC simulation for modeling additional backgrounds. For example, the measurement of the weighted average efficiencies for the matrix method described in Section 6.5.3 uses MC samples to model the fake lepton backgrounds. For these studies and measurements it will be made clear how the SM processes are modeled.

6.5.2 Monte Carlo Background

In this analysis, Monte Carlo simulated samples are used in a few different ways. First, they are primarily used to estimate the backgrounds from processes that give three prompt leptons in the final state. Second, they are used in the matrix method described in the next section to extract efficiencies of real and fake leptons. Finally, they are used in purely MC-based studies of the three lepton background, such as the optimization of the signal regions described in Section 6.4.4. So, it is important to have samples that can describe the ATLAS data as closely as possible.

The ATLAS simulated samples listed in Section 6.3.2 do not describe the ATLAS data perfectly. Some of the discrepancies are due to a lack of knowledge about the exact run conditions of ATLAS when the samples are simulated (such as the amount of pileup). Other discrepancies are expected to require data-driven corrections because of the difficulty in making a perfect ATLAS detector simulation (like reconstruction efficiencies). Corrections

for these effects are derived from data-driven measurements and applied to the MC samples to improve their modeling of the data. A list of the corrections applied to the MC is given below.

- The MC samples simulate pileup by overlaying soft QCD interactions on top of the usual SM events. The distribution in the number of pileup interactions in the MC does not, however, agree with the distribution in data, because the distribution in the MC is usually fixed before all of the data is collected. To correct for this, a reweighting of the MC events is done to make the distributions the same.

- Electron reconstruction and identification scale factors are used to account for differences in the reconstruction and identification efficiencies between MC and data. The scale factors are measured by the ATLAS Egamma performance group in $Z \rightarrow ee$ events with a tag-and-probe method and applied to events with electrons to correct the MC event weight.

- Muon reconstruction scale factors are similarly used to account for differences in the reconstruction efficiency between MC and data. The ATLAS Muon performance group provides the scale factors, which are measured in $Z \rightarrow \mu\mu$ and $J/\psi \rightarrow \mu\mu$ events. The scale factors are then applied to events with muons to correct the MC event weight.

- The muon p_T resolution in the MC does not agree perfectly with the data, so a smearing of the muon p_T in the MC events is done to improve the agreement.

- Tau identification scale factors are measured by the ATLAS Tau performance group for correcting the tau BDT efficiency.

- Scale factors for b-tagging algorithm described in Section 4.4.3 are used to correct for b-tagging efficiency differences between MC and data. These scale factors take into account both the efficiency to tag real b-jets as well as the mis-tag rate for non-b-jets.

6.5.3 The Matrix Method

Description of the Matrix Method

The matrix method is a technique for estimating the fake lepton background that exploits differences in object characteristics between real and fake leptons. By defining two sets of criteria for each lepton, a "loose" and "tight" selection, with different compositions of real and fake leptons, one can write down a set of linear equations which relates the number of loose and tight leptons in the events to the number of real and fake leptons in terms of the probabilities for real and fake leptons to pass the tight selection. For a more thorough and academic description of the matrix method algebra, see Appendix A.

In this analysis, tight leptons are defined as the signal leptons from Section 6.4.3. For the light leptons, the loose selection is the same as the baseline lepton criteria. The differences between loose and tight light leptons are the isolation, impact parameters, and (for the electrons only) the object quality requirements. For the hadronic taus, the BDT and muon veto requirements are removed to define the loose selection. Since these tight criteria are effective at reducing the fake lepton contributions, the loose selection has a much higher concentration of fake leptons than the tight selection. This is equivalent to saying that the probabilities for real and fake leptons to pass the tight criteria are *well separated*. This is an important feature for the stability of the method as described in Appendix A.

From MC studies it is known that for fake lepton background processes in a three lepton selection, the leading (light) lepton in p_{T} will be real the majority of the time ($> 95\%$ of events). This is because light lepton fakes have a generally softer p_{T} spectrum than their real lepton counterparts. For final states with light leptons and taus, the fake lepton background is dominated by processes in which the leading light lepton is real and the taus are faked by hadronic jets. We take this feature into account by ignoring the leading light lepton in

the three-lepton matrix method. This simplifies the method and allows for the usage of single-isolated-lepton triggers with the leading light lepton. Both of these statements will be explained more fully below.

Since only two leptons in the events are used in the method, the method is given by the two-lepton matrix method equation (same as equation A.4):

$$
\begin{pmatrix} N_{TT} \\ N_{TL} \\ N_{LT} \\ N_{LL} \end{pmatrix} = \begin{pmatrix} \epsilon_1\epsilon_2 & \epsilon_1 f_2 & f_1\epsilon_2 & f_1 f_2 \\ \epsilon_1\bar{\epsilon}_2 & \epsilon_1\bar{f}_2 & f_1\bar{\epsilon}_2 & f_1\bar{f}_2 \\ \bar{\epsilon}_1\epsilon_2 & \bar{\epsilon}_1 f_2 & \bar{f}_1\epsilon_2 & \bar{f}_1 f_2 \\ \bar{\epsilon}_1\bar{\epsilon}_2 & \bar{\epsilon}_1\bar{f}_2 & \bar{f}_1\bar{\epsilon}_2 & \bar{f}_1\bar{f}_2 \end{pmatrix} \begin{pmatrix} N_{RR} \\ N_{RF} \\ N_{FR} \\ N_{FF} \end{pmatrix},
\tag{6.2}
$$

On the left hand side of equation 6.2, N_{TT} denotes the number of events with two tight leptons, $N_{TL} + N_{LT}$ denotes the number of events with one tight and one loose lepton (indices are p_T ordered), and N_{LL} denotes the number of events with two loose leptons. Note that since the leading light lepton is ignored, each of these categories has an additional tight light lepton. On the right hand side, N_{RR} denotes the number of events with two real leptons, $N_{RF} + N_{FR}$ denotes the number of events with one real and one fake lepton, and N_{FF} denotes the number of events with two fake leptons. The matrix element factors ϵ and f denote the probabilities of real and fake *loose* leptons to pass the *tight* requirements, respectively. The barred quantities are the corresponding probabilities for the leptons to fail the tight requirements: $\bar{\epsilon}_i = 1 - \epsilon_i$ and $\bar{f}_i = 1 - f_i$. In the following text, ϵ will be referred to as the *real efficiency*, f will be referred to as the *fake rake*, and the two together will be referred to as the matrix method efficiencies.

Inverting equation 6.2 to solve for the right hand side vector gives the real and fake lepton composition of the $N_{TT} + N_{TL} + N_{LT} + N_{LL}$ events at the *loose* selection level. An additional extrapolation step is needed to estimate the real and fake lepton composition at the *tight*

selection level:

$$N_{RR \to TT} = \epsilon_1 \epsilon_2 \times N_{RR}$$

$$N_{RF \to TT} = \epsilon_1 f_2 \times N_{RF}$$

$$N_{FR \to TT} = f_1 \epsilon_2 \times N_{FR}$$

$$N_{FF \to TT} = f_1 f_2 \times N_{FF}$$

$$N_{Fake \to TT} = N_{RF \to TT} + N_{FR \to TT} + N_{FF \to TT}$$

$$= \epsilon_1 f_2 \times N_{RF} + f_1 \epsilon_2 \times N_{FR} + f_1 f_2 \times N_{FF}. \tag{6.3}$$

Note that in the expression for $N_{Fake \to TT}$, the real-real component, N_{RR}, is neglected because it does not contribute to the fake lepton estimate. The explicit full solution is shown in the Appendix in equations A.5–A.9.

To complete the method, the remaining variables of equation 6.2 need to be measured. The measurement and parametrization of the fake rates and real efficiencies is described in the next section. For each signal region, the left hand side of equation 6.2 is obtained by applying all of the signal region cuts except that loose selected leptons are used in place of signal leptons. The leading light lepton is required to be tight since it does not participate in the method. Each event then falls into one of the TT, TL, LT, or LL categories. The matrix equation is used once for every event to get a "fake weight". The sum of the fake weights for each event gives the fake lepton estimate for the corresponding signal region. This method is not only able to provide the normalization of the fake lepton background, but it can also provide the shape in many kinematic distributions (with some caveats to be described later). In addition, it can provide separately the estimate for backgrounds with 1 or 2 fake leptons by using the appropriate components in equation 6.3.

Matrix Method Efficiencies

Measurement of the fake rates and real efficiencies for the matrix method presents several challenges. Different sources of fake leptons will have different fake rates, and the composition of the fake object types will change in each signal region or in kinematic distributions. Even for an individual type of object, the efficiency may depend on the object and event kinematics in a complicated way. For example, the fake rate for muons from heavy flavor jets in a $b\bar{b}$ process will differ from the fake rate for muons from heavy flavor jets in a $t\bar{t}$ process because of the difference in b-quark p_T spectra. Because of these effects, a fake rate or real efficiency measured in a single control region may not be representative of the real and fake objects in the signal regions. The fake rates and real efficiencies for each considered process and object type are shown in Figures 6.17-6.26.

(a) $|\eta| < 1.5$ (b) $|\eta| > 1.5$
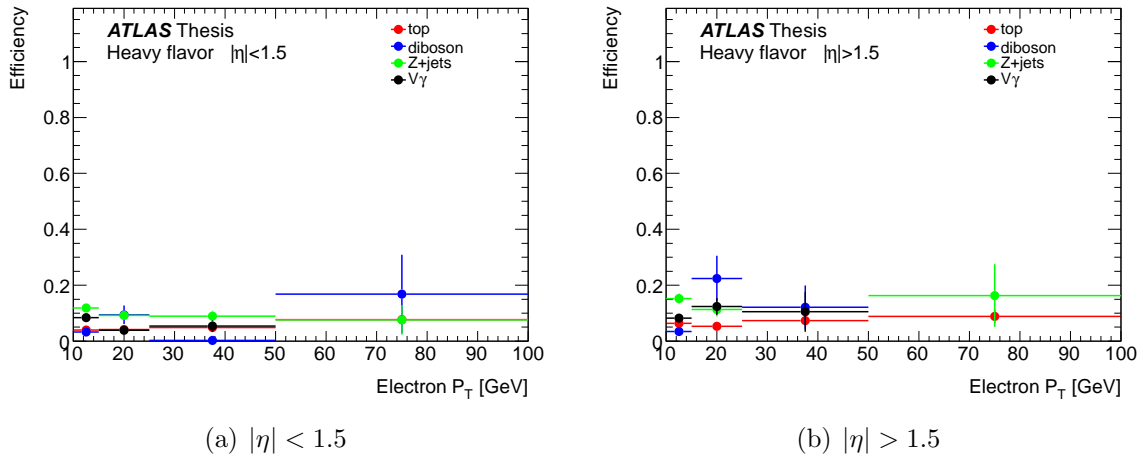
Figure 6.17: Electron heavy flavor fake rates per SM process measured in events with at least three baseline leptons.

The solution adopted in the analysis is to construct weighted average efficiencies for each signal region parametrized in the important object kinematics. Electrons are parametrized in p_T and η, Muons in p_T only, and taus in p_T and prong-ness (1 or 3). The efficiencies for each object type and process are extracted from MC events, corrected for data/MC discrepancies, and then averaged together with the appropriate proportions for each signal region.

(a) $|\eta| < 1.5$ (b) $|\eta| > 1.5$
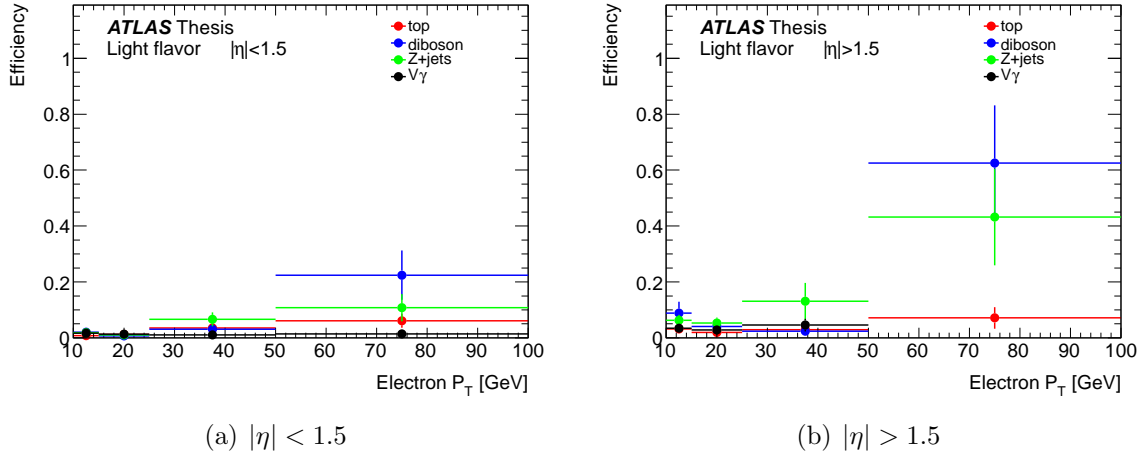
Figure 6.18: Electron light flavor fake rates per SM process measured in events with at least three baseline leptons.

The weighted average fake rate and real efficiency for a specific lepton flavor and event selection region XR are defined as:

$$f_{XR} = \Sigma_{i,j}(f^{ij} \times sf^{i} \times R^{ij}_{XR}) \qquad (6.4)$$

$$\epsilon_{XR} = \Sigma_{j} \ (\epsilon^{j} \times sf^{Real} \times P^{j}_{XR}) \qquad (6.5)$$

In the above equations, i indicates the fake type and j indicates the production process. The fake types considered for electrons are heavy flavor, light flavor, and conversion. The fake types considered for muons are heavy flavor and light flavor. Finally, the fake types considered for taus are heavy flavor, light quark jet, gluon jet, and conversion. The real efficiencies only have one type: real. The remaining factors of equations 6.4-6.5 are described below:

The baseline efficiencies, f^{ij} and ϵ^{j}, are the fake rates and real efficiencies for each object type i and process j. For the light leptons, there is some dependency of the efficiencies on event topology, so they are measured in a region with similar topology as the matrix method control regions. I.e., a three light lepton selection is used where the leading lepton is required to be tight and the sub-leading leptons are used in the
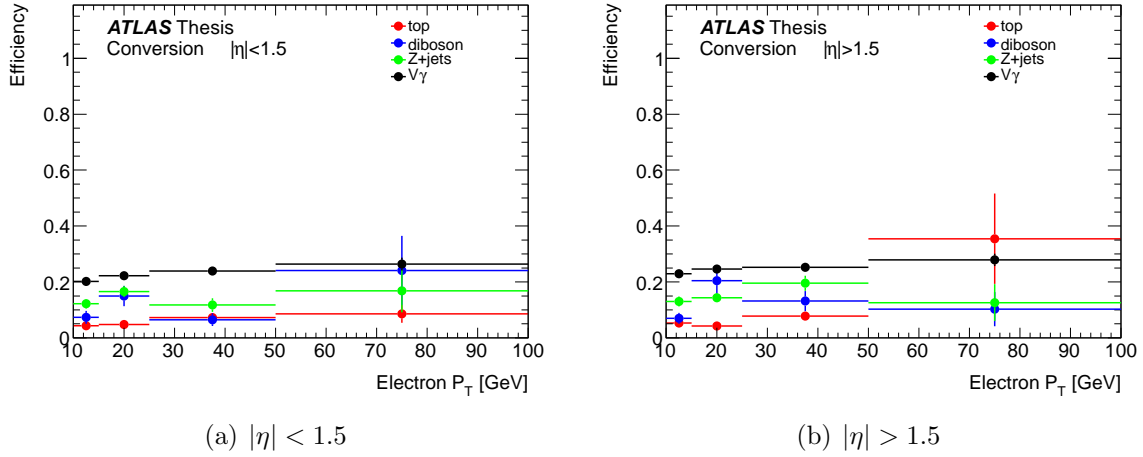
Figure 6.19: Electron conversion fake rates per SM process measured in events with at least three baseline leptons.

calculation. The efficiencies are then defined as the number of leptons passing the tight requirements over the total number of considered leptons at the loose level. For the taus, the dependence on event topology is smaller so all taus from all simulated events are used in the calculation. The baseline efficiencies are parametrized as described above.

The scale factors, sf^i **and** sf^{Real}**,** are correction factors for the baseline efficiencies to account for differences between data and MC for each object type i. They are measured in dedicated control regions which are described in the next section.

The fractions, R_{XR}^{ij} **and** P_{XR}^{j}**,** are the proportionality factors for each object type i and originating process j used to average the fake rates and real efficiencies together. The fractions are measured strictly in MC samples using the matrix method loose lepton control regions for each signal region. They are parametrized in the same variables as the baseline efficiencies.

(a) $|\eta| < 1.5$ (b) $|\eta| > 1.5$
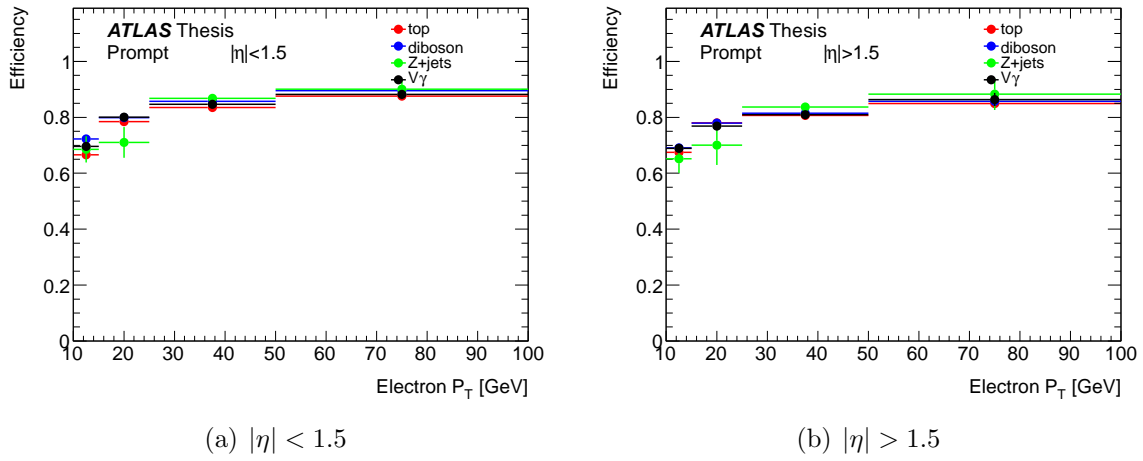
Figure 6.20: Electron real efficiencies per SM process measured in events with at least three baseline leptons.

(a) Muon heavy flavor   (b) Muon light flavor

(c) Muon prompt
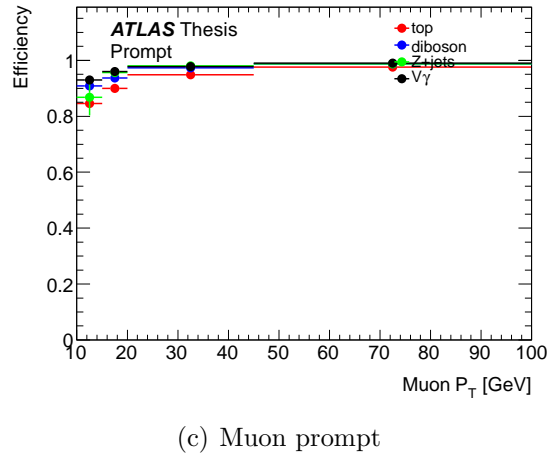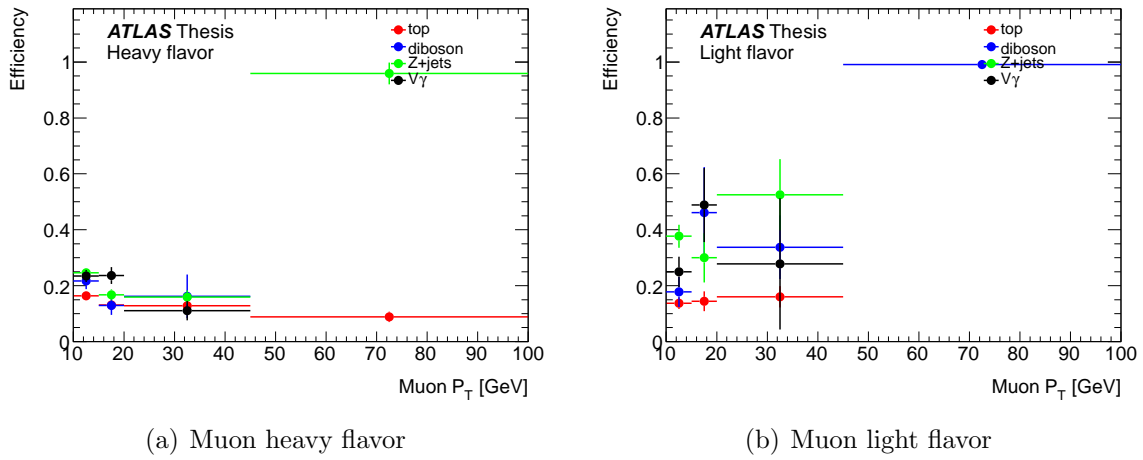
Figure 6.21: Muon heavy flavor fake rates, light flavor fake rates, and real efficiencies per SM process measured in events with at least three baseline leptons.
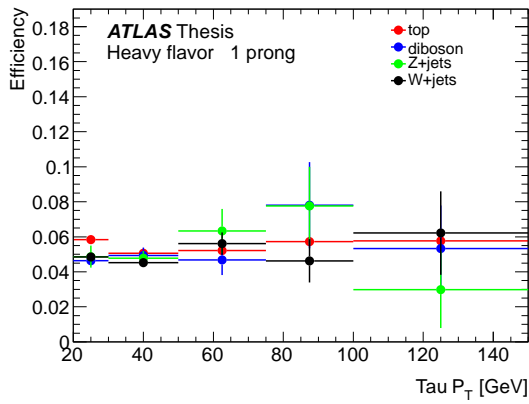
(a) 1 prong
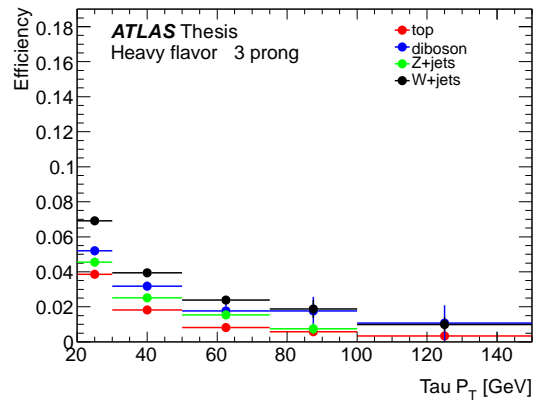
(b) 3 prong

Figure 6.22: Tau heavy flavor fake rates per SM process measured in inclusive MC events.
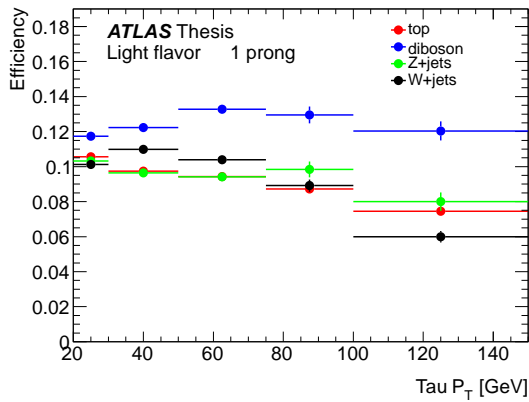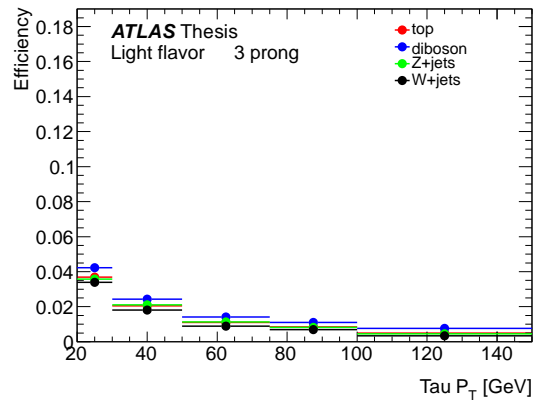
(a) 1 prong

(b) 3 prong

Figure 6.23: Tau quark jet fake rates per SM process measured in inclusive MC events.
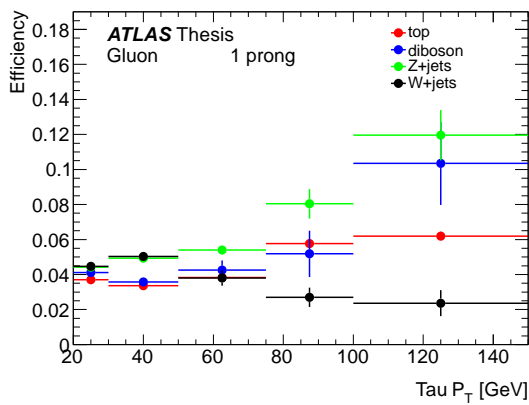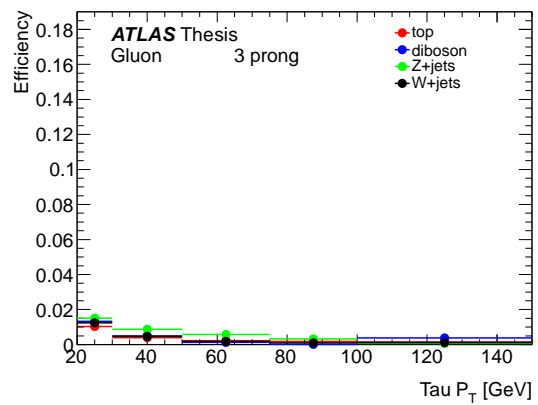
(a) 1 prong

(b) 3 prong

Figure 6.24: Tau gluon jet fake rates per SM process measured in inclusive MC events.
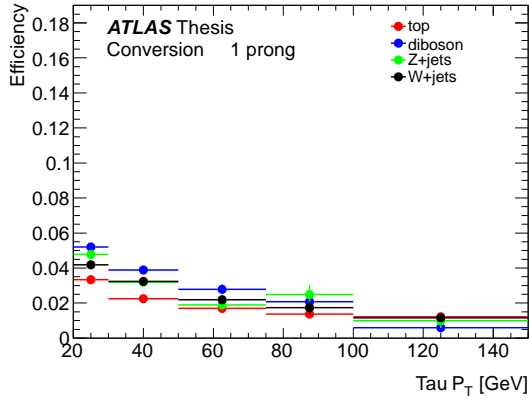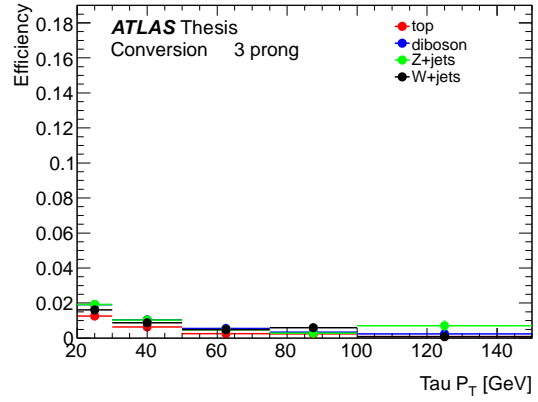
(a) 1 prong   (b) 3 prong

Figure 6.25: Tau conversion fake rates per SM process measured in inclusive MC events.
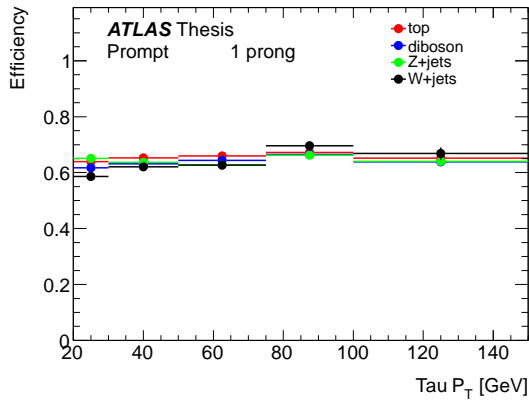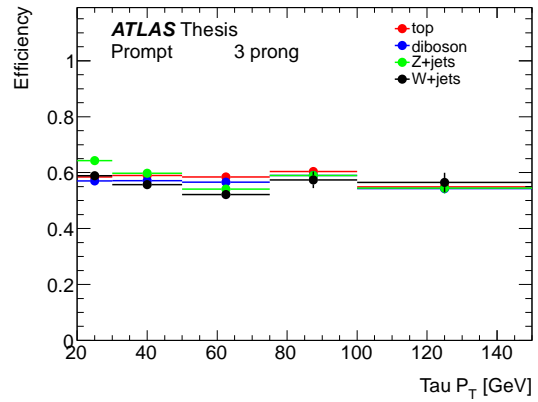
(a) 1 prong   (b) 3 prong

Figure 6.26: Tau real efficiencies per SM process measured in inclusive MC events.

Efficiency Scale Factors

As mentioned above, the efficiency scale factors are intended to correct for differences in the baseline efficiencies between data and MC. They are measured per object type in dedicated control regions and can then be applied to efficiencies from various processes. The scale factors are defined as the ratio of the efficiency measured in data over the efficiency measured in MC with the same selection.

Real lepton scale factors The real lepton efficiency scale factors for light leptons are measured using a tag-and-probe method with the $Z \rightarrow \ell\ell$ process. Events are selected to have two SFOS baseline leptons with an invariant mass consistent with the Z boson ($|M_{ll} - M_Z| < 10$ GeV). The tag lepton is requested to also satisfy the tight requirements and to be matched to the relevant single-lepton trigger chain. The other lepton, the *probe*, is tested for the efficiency calculation. Both leptons can be considered as tags if they pass the tight requirements.

A similar control region using $Z \rightarrow \tau\tau$ events to measure the efficiency of real taus has been also studied. Unfortunately, the contamination from fake taus is very difficult to suppress and a reliable efficiency cannot be found. Therefore, the real tau efficiency scale factor is assumed to be 1.0. This is a reasonable approach since real tau efficiency scale factors (and corresponding uncertainties) from the ATLAS Tau Working Group are already applied. Unlike electrons and muons, which have additional isolation and impact parameter requirements, the tau identification is not changed in this analysis from the basic working point provided by the Tau working group.

The real electron and muon efficiencies parametrized by p_T, η and number of vertices both in MC and data are shown in Figure 6.27 and Figure 6.28 along with the corresponding scale factors. No significant dependence on p_T, η, or number of vertices has been observed for the

real lepton efficiency scale factor. Therefore, the final result is obtained without binning:

$$sf_e^{Real} = 1.00 \pm 0.01 \qquad sf_\mu^{Real} = 1.00 \pm 0.01 \qquad sf_\tau^{Real} = 1.0$$

Errors are statistical.
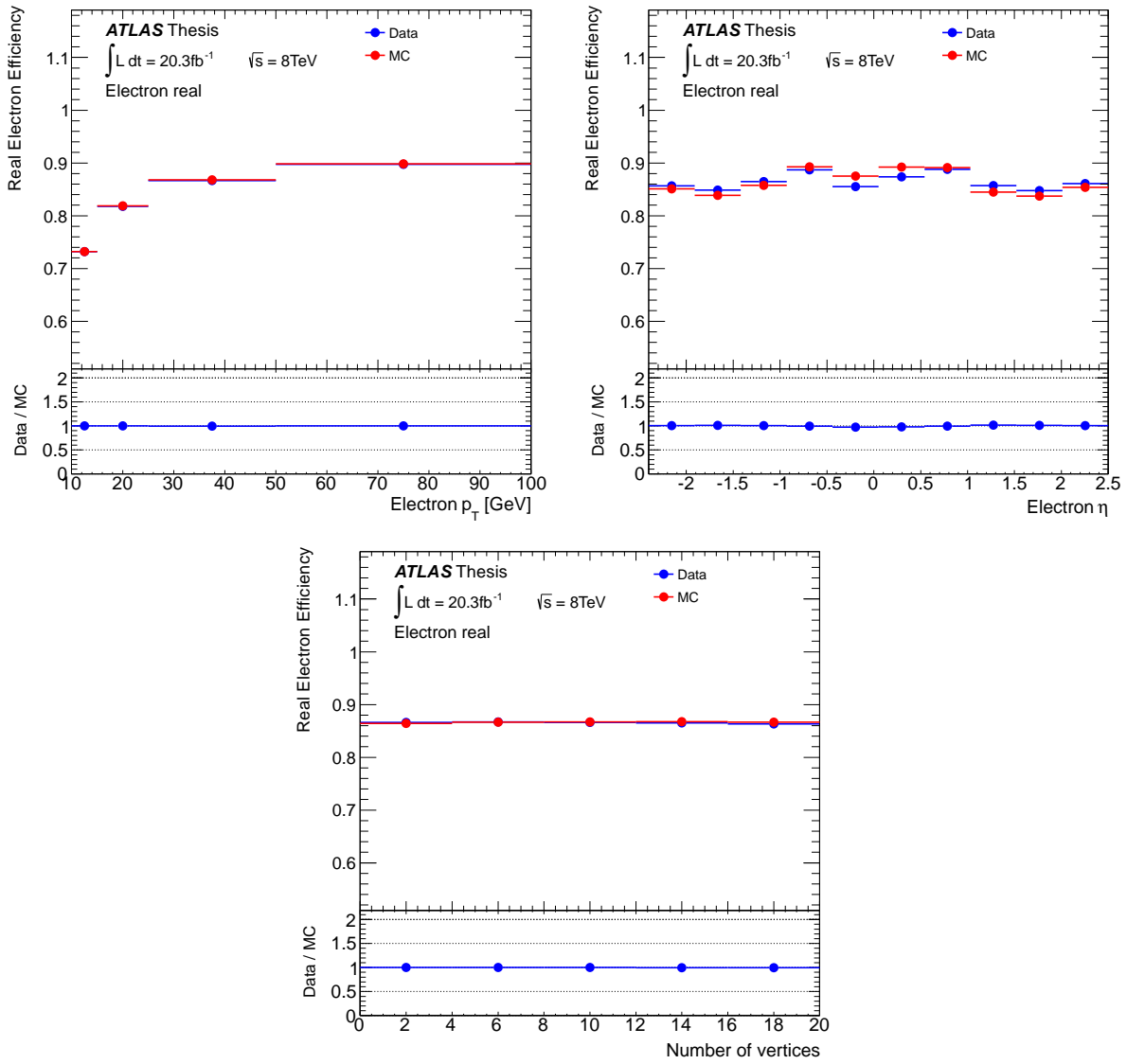
Figure 6.27: Real electron efficiency and scale factor as a function of p_T, η, and number of vertices in the $Z \to \ell\ell$ control region. Uncertainties are statistical.

Heavy flavor scale factors The heavy flavor scale factor sf^{HF} is measured with a tag-and-probe method with a $b\bar{b}$ and $c\bar{c}$ selection. Events are selected that have one tag muon within $\Delta R < 0.4$ of a b-tagged jet which matches to the single muon trigger chain and one additional electron or muon probe which is tested for the fake rate calculation. There is required to be exactly one b-tagged jet. To suppress the background, an event is rejected if the E_T^{miss} is larger than 60 GeV or if the transverse mass of the probe lepton and the E_T^{miss} is larger than 50 GeV. The remaining background in data due to non heavy flavor leptons is subtracted using the predictions of all relevant processes from MC normalized to the luminosity in the data. The scale factor is then the ratio of the fake rate in data to the fake rate in MC.

The fake rates and scale factors for electrons and muons are shown in Figure 6.29 and Figure 6.30. Since the scale factor versus p_T, $|\eta|$, and number of good vertices are flat within the uncertainties, they are fitted to a constant function. The central value of the scale factor is calculated without binning in any variable and the differences with respect to the results of the fit in p_T,$|\eta|$ and number of good vertices are assigned as a systematic uncertainty. The final results are:

$$sf_\mu^{HF} = 0.87 \pm 0.09 \qquad sf_e^{HF} = 0.72 \pm 0.05$$

Light flavor scale factors The light flavor tau scale factor is measured with a W+jets selection. Events are selected that have one muon and one additional container tau. The muon is required to match the single isolated muon trigger with $p_T > 25$ GeV. Significant reduction of the $Z \to \tau\tau$ background is obtained by requiring the transverse mass $m_T(\mu, E_T^{\text{miss}})$ to be greater than 60 GeV and $\sum \cos(\Delta\phi) = \cos(\Delta\phi(E_T^{\text{miss}}, \tau)) + \cos(\Delta\phi(E_T^{\text{miss}}, \mu)) \leq$ -0.15. The $\sum \cos(\Delta\phi)$ is a good discriminator between $Z \to \tau\tau$ and W+jets processes as shown in [75]. In addition, a b-jet veto is applied to separate the light and heavy flavor fake rates.

The remaining background ($<10\%$) is subtracted using a MC based estimate, as with the heavy flavor measurement. Since the $W \rightarrow \tau\nu$+jets contributions which pass our selection criteria are over estimated from simulation, this background is normalized to the data before calculating the fake rate. Careful attention is taken to normalize the $W \rightarrow \tau\nu$+jets contributions regardless whether the probe tau passing or fails the signal requirement to avoid biasing the measurement.

The light tau scale factors are separated into 1 and 3-prong taus due to observed differences in the fake rates and scale factors. The fake rates parametrized by p_T, η and number of vertices both in MC and data are shown in Figure 6.31 and Figure 6.32 alongside their corresponding scale factors.

The LF tau fake rate scale factor for 1 and 3-prong taus show strong dependence on the tau p_T. Therefore, a p_T dependent scale factor is applied to correct the MC based fake rates.

Conversion scale factors The conversion scale factor is only relevant for electrons and is measured with a $Z \rightarrow \mu\mu e$ selection in which the electron comes from converted radiation. Events are selected that have two OS signal muons and one loose electron such that the $\mu\mu e$ invariant mass is consistent with a Z boson ($|M_{\mu\mu e} - M_Z| < 10$ GeV). The remaining contributions from other processes like diboson and $t\bar{t}$ are subtracted from the data using the MC, as done above.

Figure 6.33 shows the fake rates and corresponding scale factors as a function of electron p_T, η, and the number of good vertices. Errors are statistical only.

No significant dependence on p_T, η, or number of vertices is observed. Therefore, the unbinned computed scale factor is:

$$sf_e^{Conv} = 1.14 \pm 0.12$$

Weighted Average Efficiencies

The final weighted average matrix method efficiencies for the signal regions are shown in Figures 6.34–6.38.
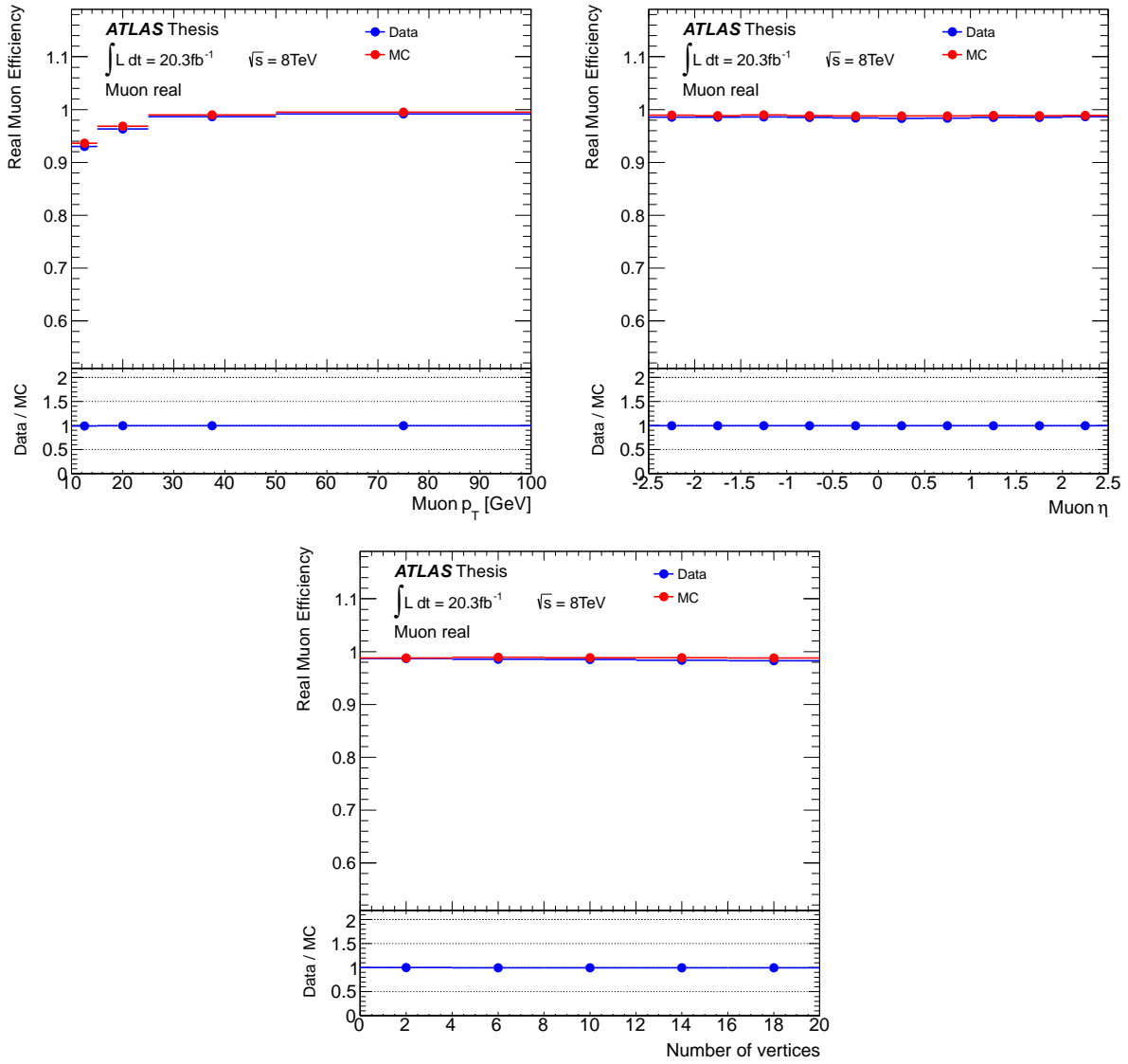
Figure 6.28: Real muon efficiency and scale factor as a function of p_T, η, and number of vertices in the $Z \to \ell\ell$ control region. Uncertainties are statistical.
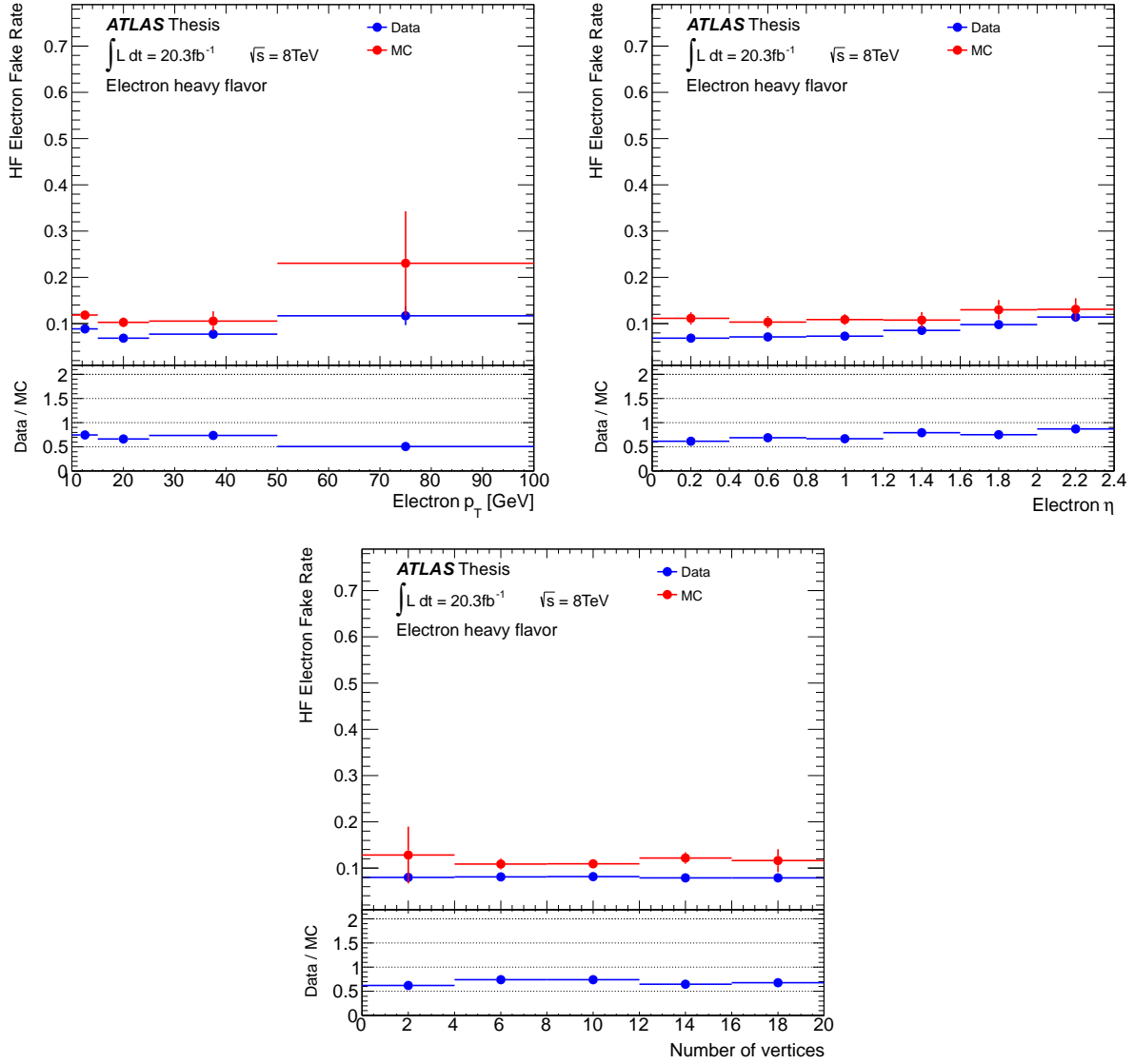
Figure 6.29: Muon heavy flavor fake rate and scale factor as a function of p_T, η, and number of vertices in the $b\bar{b}$ control region. Uncertainties are statistical.
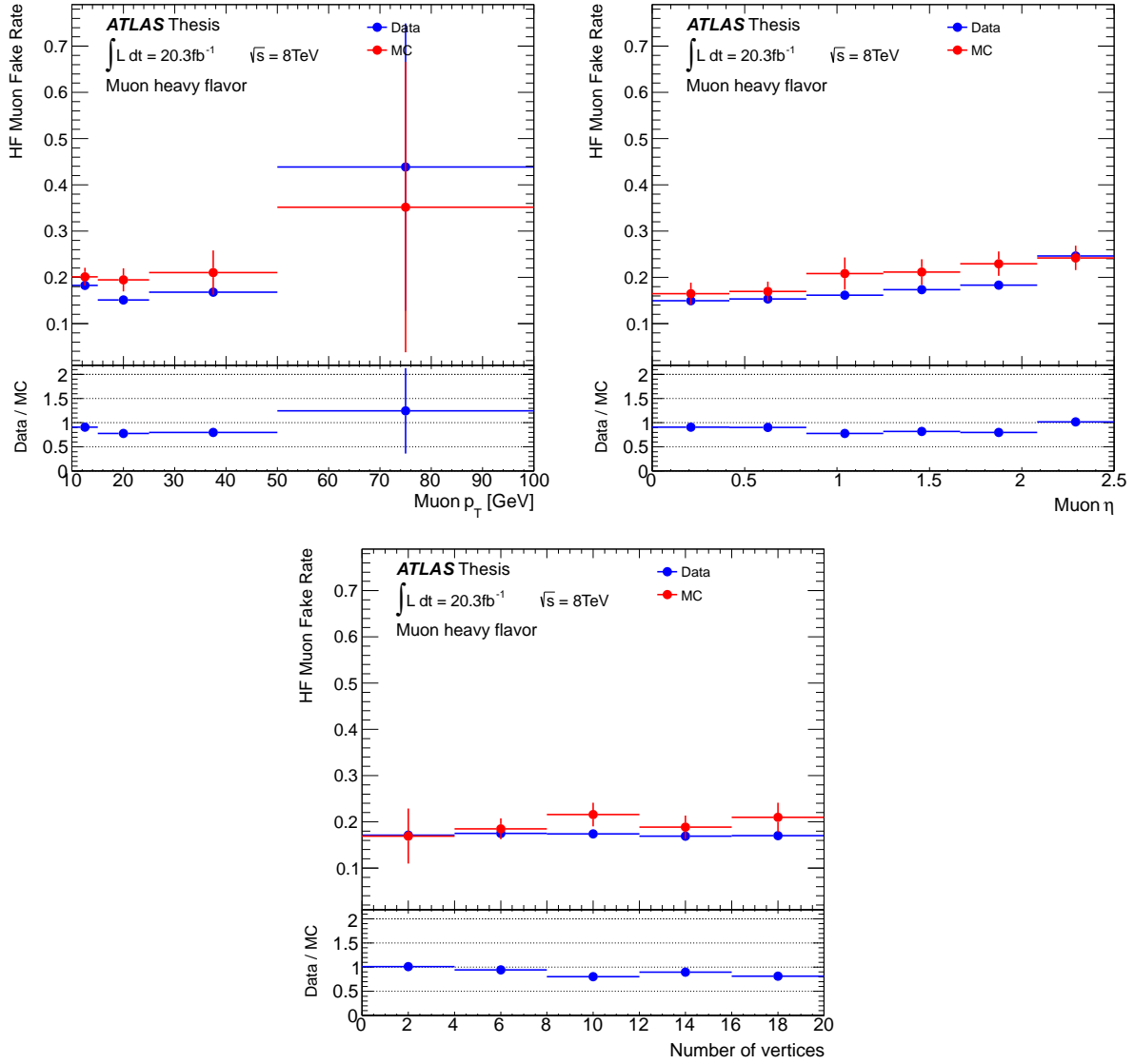
Figure 6.30: Electron heavy flavor fake rate and scale factor as a function of p_T, η, and number of vertices in the $b\bar{b}$ control region. Uncertainties are statistical.
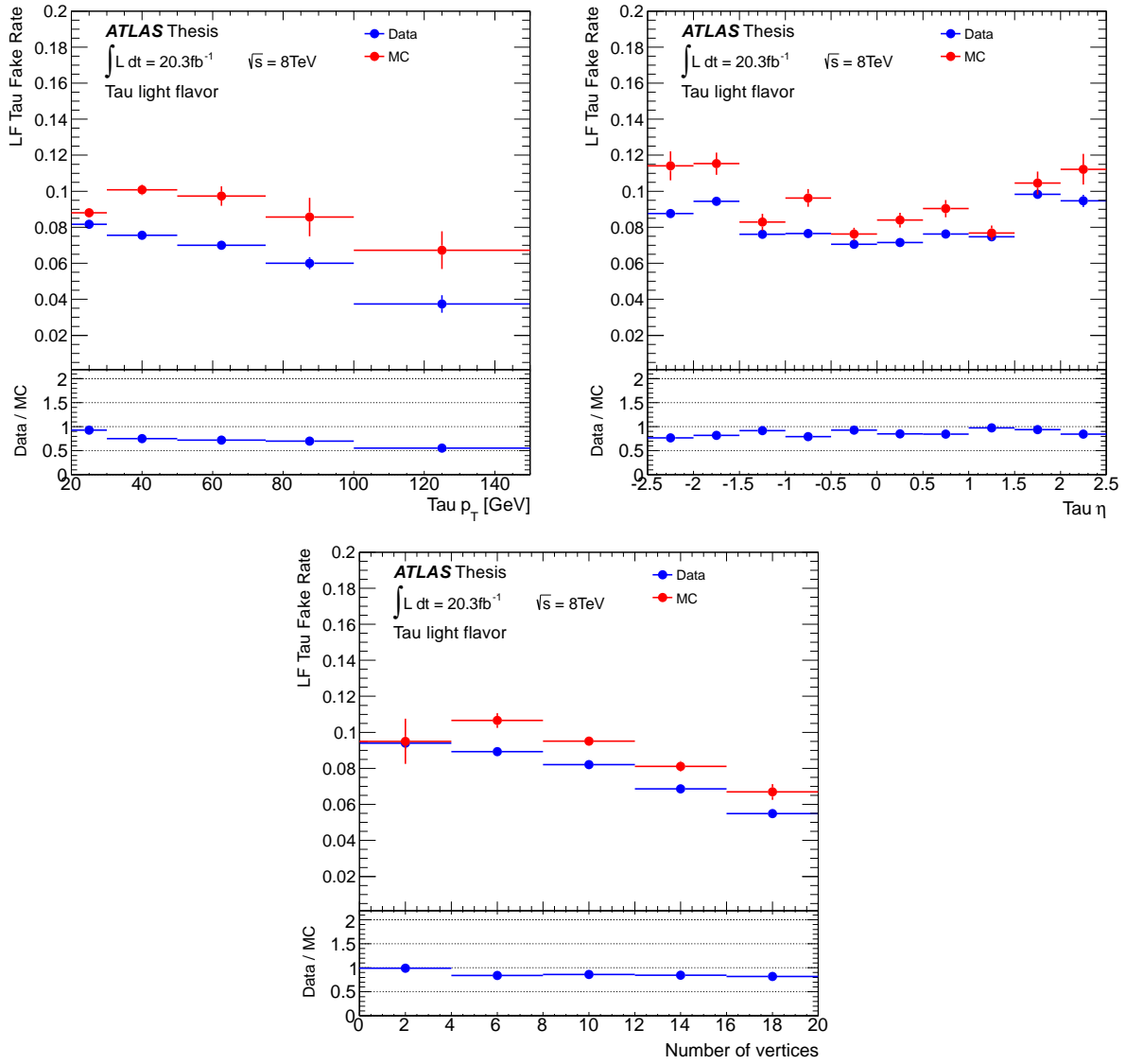
Figure 6.31: 1-prong tau light flavor fake rate and scale factor as a function of p_{T}, η, and number of vertices in the W+jets control region. Uncertainties are statistical.
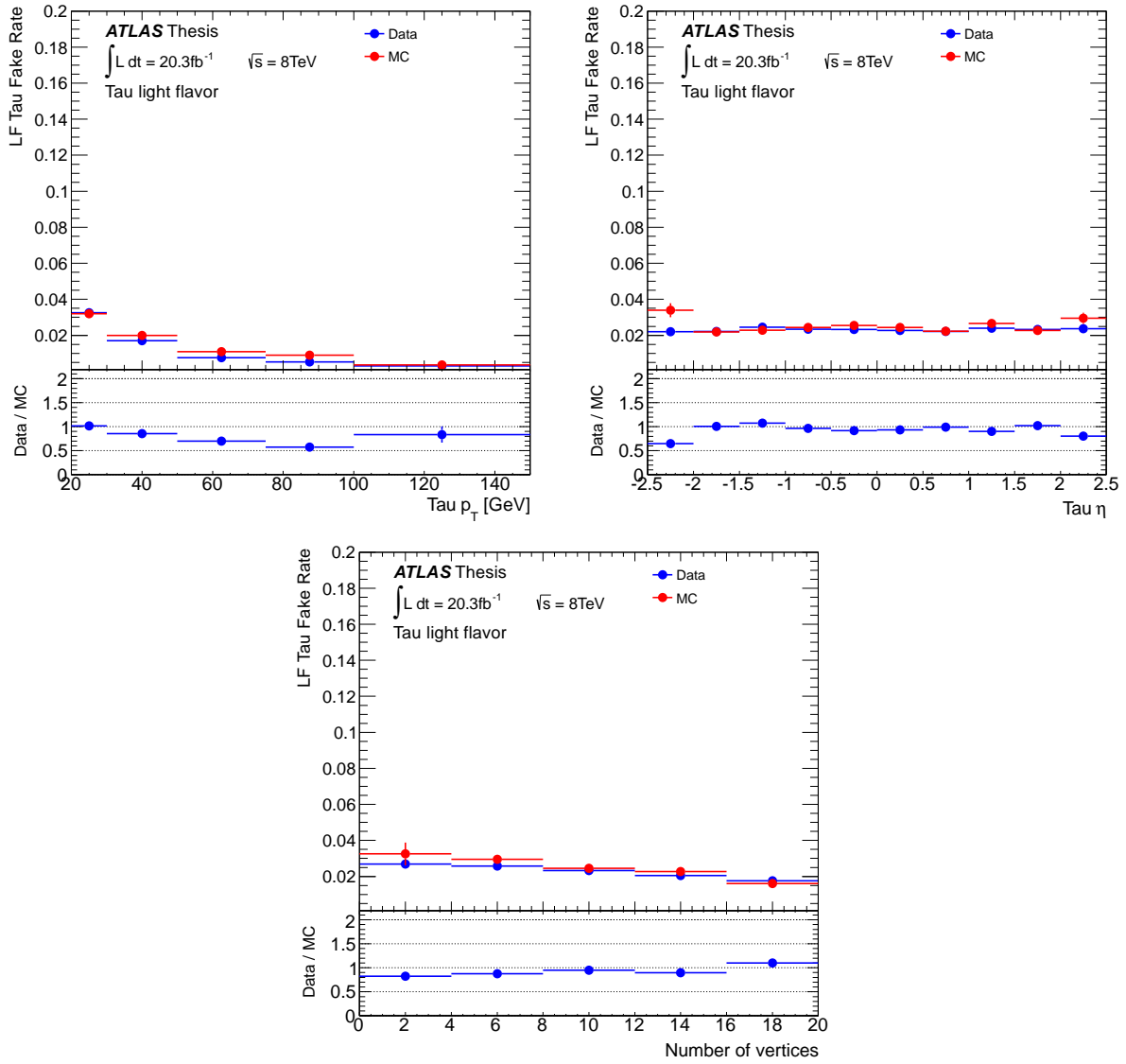
Figure 6.32: 3-prong tau light flavor fake rate and scale factor as a function of p_T, η, and number of vertices in the W+jets control region. Uncertainties are statistical.
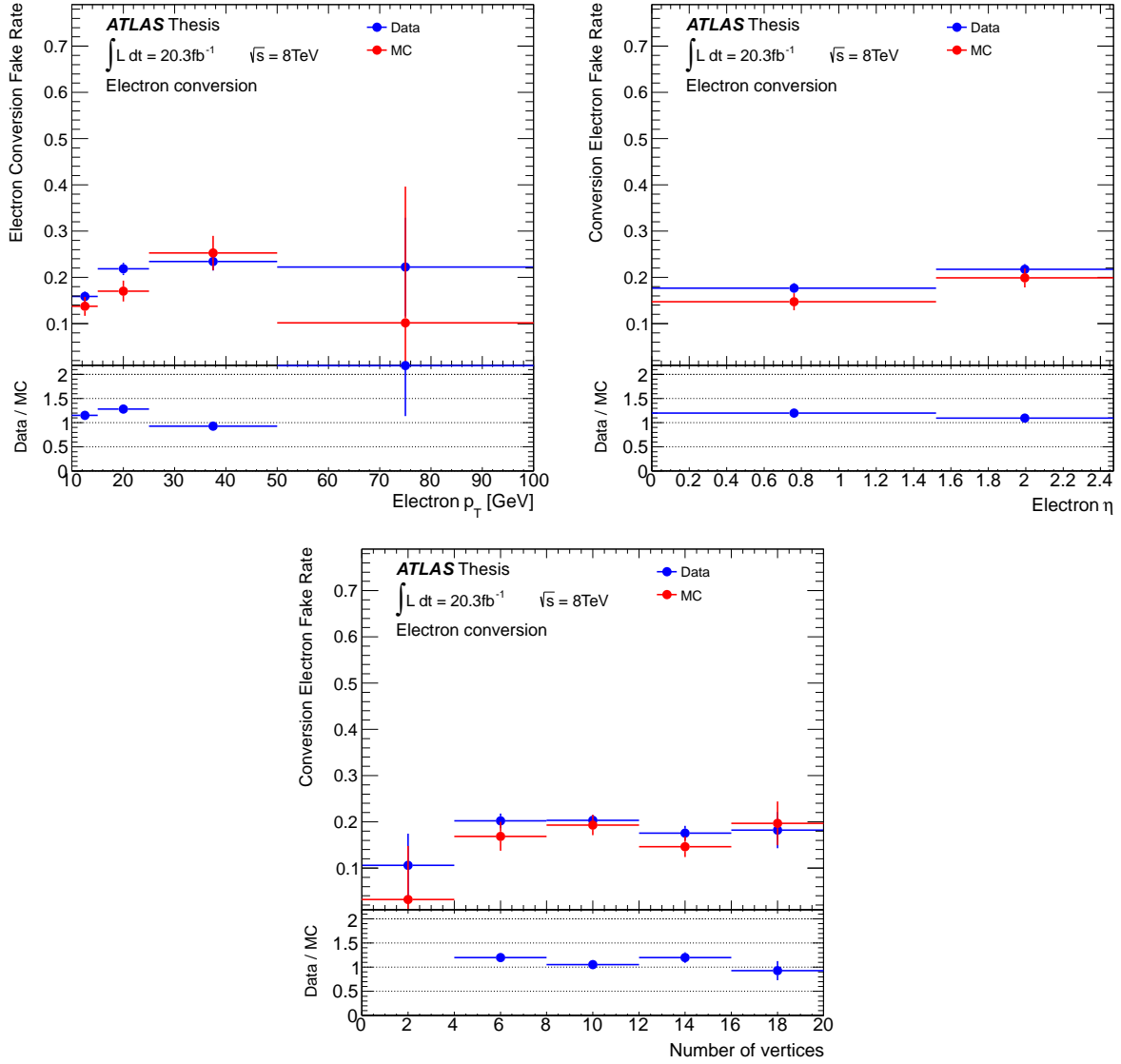
Figure 6.33: Electron conversion fake rate and scale factor as a function of p_{T}, η, and number of vertices in the $Z \to \mu\mu e$ control region. Uncertainties are statistical.
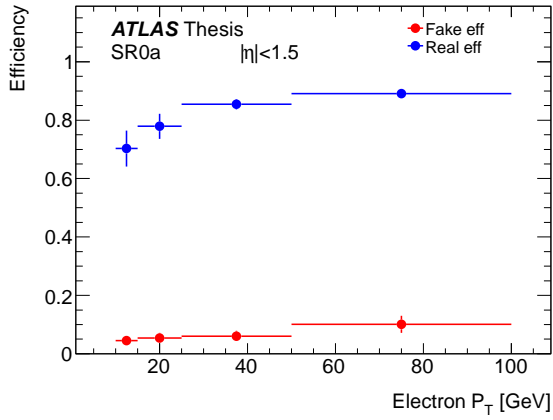
(a) Electron $|\eta| < 1.5$
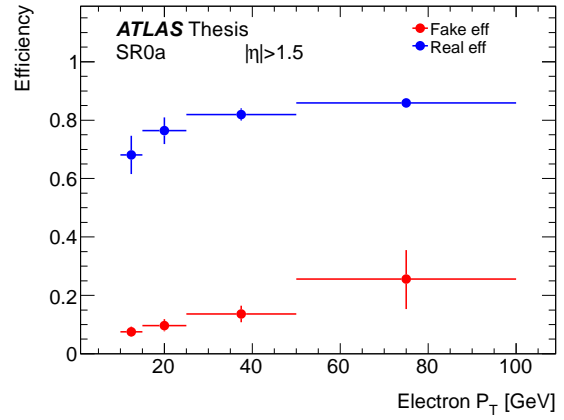
(b) Electron $|\eta| > 1.5$
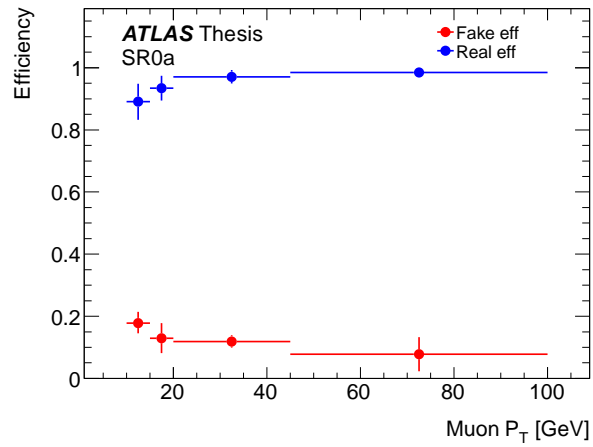
(c) Muon

Figure 6.34: Weighted average efficiencies for SR0a. Only the combined region is shown here, but weighted average efficiencies are derived for each bin.
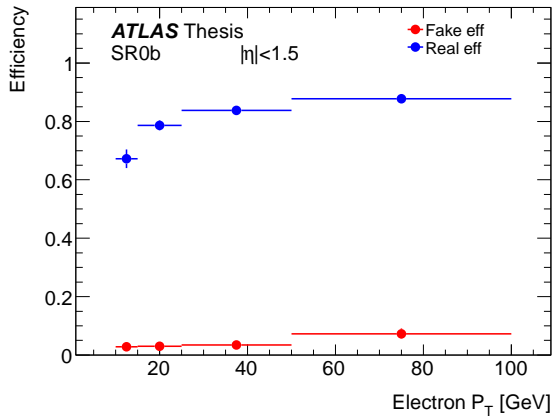
(a) Electron $|\eta| > 1.5$
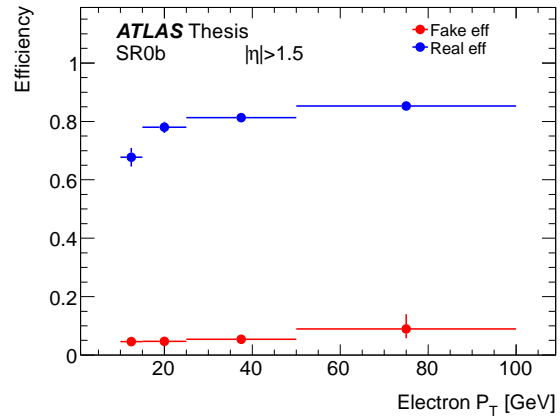
(b) Electron $|\eta| > 1.5$
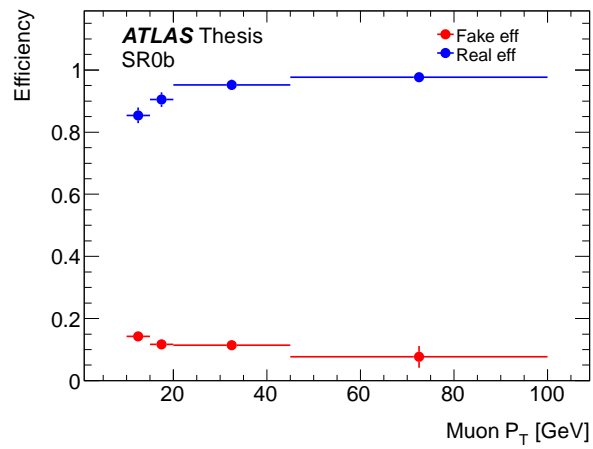
(c) Muon

Figure 6.35: Weighted average efficiencies for SR0b.
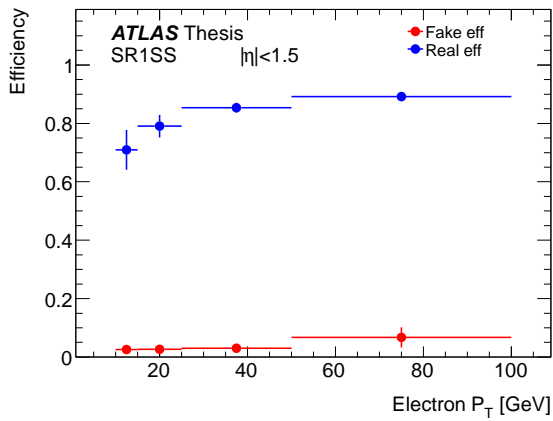
(a) Electron $|\eta| > 1.5$
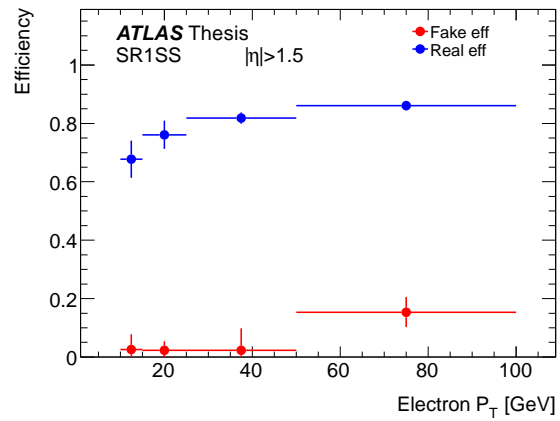
(b) Electron $|\eta| > 1.5$
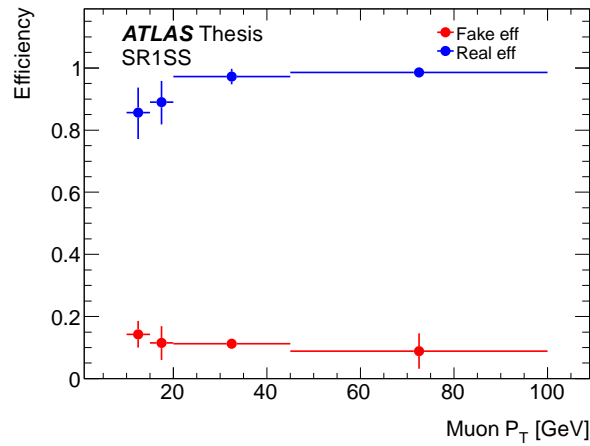
(c) Muon
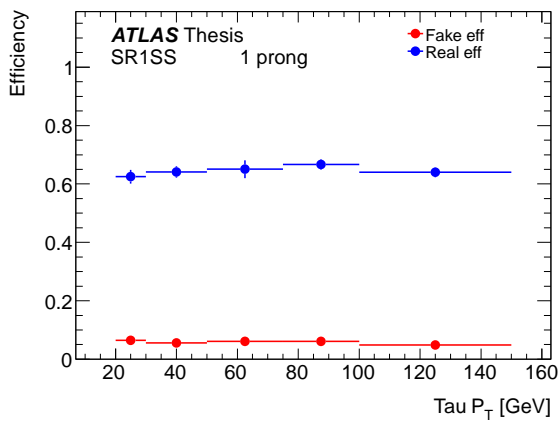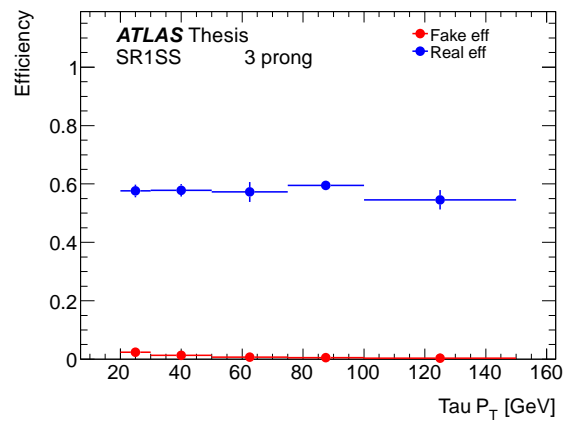
(d) Tau 1 prong

(e) Tau 3 prong

Figure 6.36: Weighted average efficiencies for SR1SS.
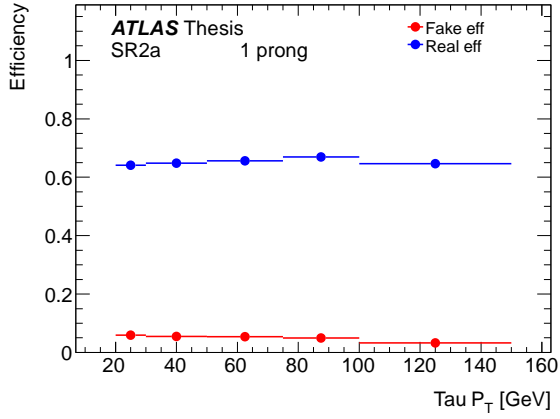
(a) Tau 1 prong
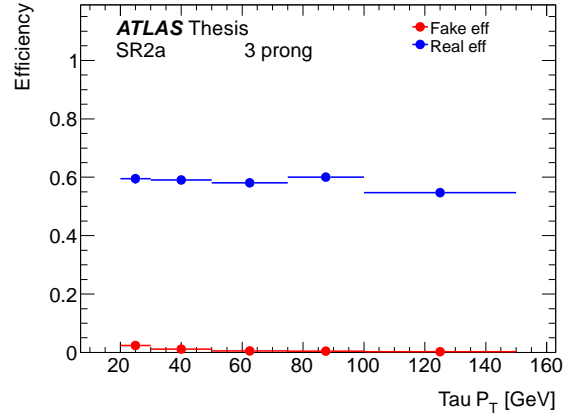
(b) Tau 3 prong

Figure 6.37: Weighted average efficiencies for SR2a.
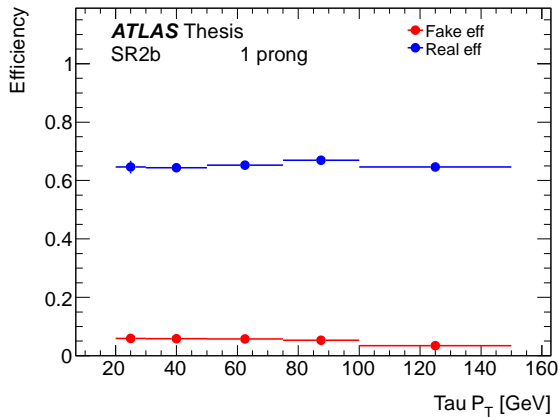
(a) Tau 1 prong
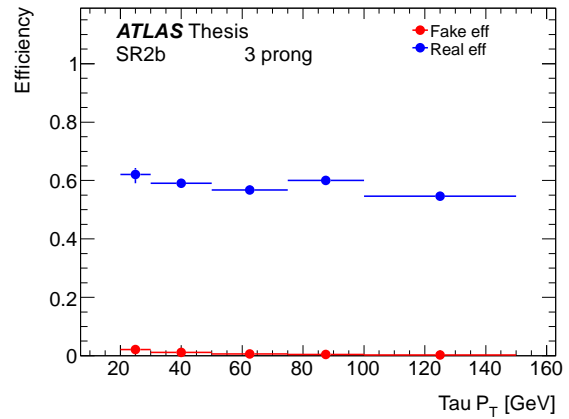
(b) Tau 3 prong

Figure 6.38: Weighted average efficiencies for SR2b.

6.6 Uncertainties

There are several sources of uncertainty in the analysis, from both the MC-modeled background and the matrix method estimate. The impact on the number of expected events is determined by varying a given uncertainty between extremes ($\pm 1\sigma$).

6.6.1 Uncertainties on the Monte Carlo Background

The three-prompt-lepton background is modeled with Monte Carlo simulation, which is subject to various sources of statistical and systematic uncertainty. These include uncertainties on the reconstructed objects' energy measurements, reconstruction and identification efficiencies, and the generation and simulation of the physics processes and detector interaction. A full description of the considered uncertainties is below.

Monte Carlo Statistics The uncertainty due to limited Monte Carlo statistics.

Jets The Jet Energy Scale (JES) uncertainty is estimated by scaling the energy of all jets in each event up and down according to their uncertainties. The changes are also propagated to the $E_{\mathrm{T}}^{\mathrm{miss}}$ calculation. The Jet Energy Resolution (JER) uncertainty is determined by smearing the transverse momentum of each jet.

Electrons The Electron Energy Scale (EES) and Electron Energy Resolution (EER) uncertainties are found using an E_{T}- and η-dependent function selecting Z and W events in data and J/Ψ events for low-p_{T} electrons. The uncertainty is applied to both the relevant objects in the event and to the corresponding components of the $E_{\mathrm{T}}^{\mathrm{miss}}$. The uncertainty in the Electron Scale Factor (ESF), or the electron reconstruction and identification efficiency correction, is η and E_{T} dependent and based on reconstruction and identification efficiency measurements from W and Z events.

Muons The Muon Energy Scale uncertainties of the inner detector track (MID) and the spectrometer track (MMS) are measured in Z, J/ψ, and υ events. The uncertainty is applied to both the muons in the event and to the corresponding components of the $E_{\mathrm{T}}^{\mathrm{miss}}$. The uncertainty in the Muon Scale Factor (MSF), or the muon reconstruction and identification efficiency correction, is measured as a function of the muon momentum in the same way as the ESF.

Taus The Tau Energy Scale uncertainty is determined by varying the tau transverse momenta up and down according to their uncertainties (see Section 4.4.4). The uncertainty in the Tau Identification Scale Factor (TSF) includes uncertainties in the jet-BDT and electron veto-BDT identification.

b-tagging efficiency The uncertainty in the performance of the b-tagging algorithm in MC is taken into account by varying the efficiency scale factor up and down according to its uncertainty.

MET The $E_{\mathrm{T}}^{\mathrm{miss}}$ calculation has its own inherent uncertainty from the soft term (see Section 4.4.5). It is estimated by adjusting the energy scale (5%) and resolution of this term. This source of uncertainty is seen to be negligible for the SM samples studied.

Luminosity The luminosity uncertainty for 2012 data is 2.8% [34].

Trigger The uncertainty due to the trigger efficiency in the simulation is taken to be 5% based on comparisons between data and siulation in Z+jets events.

Pile-up The uncertainty on the modeling of the pile-up is assesed by reweighting the MC events to shift the distribution of the number of pileup interactions up and down.

MC Cross Section The uncertainty in MC cross-sections for the backgrounds used in this analysis is 30% for $t\bar{t}+Z/W/WW$) [76, 77], 5% for ZZ, 7% for WZ, and a conservative 100% for the triboson samples. The WZ and ZZ cross-sections are normalised to the

124

MCFM prediction and the uncertainty taken from MCFM calculations. The ATLAS WZ and ZZ cross-section measurements [78, 79] are seen to be in excellent agreement with the MCFM prediction. For the Higgs samples, a conservative 20% uncertainty is used for VH and VBF production, while a 100% uncertainty is assigned to $t\bar{t}H$ and ggF production, based on studies of the VH production channel in [70].

MC Generator The uncertainty arising from the MC generator used to simulate the diboson backgrounds ZZ/WZ is found by comparing the acceptance of the signal region selections in the Powheg and aMC@NLO samples and includes uncertainties from the scale variation and parton shower. For the $t\bar{t} + Z/W$ background, the Madgraph generator is compared to the Alpgen generator. The statistical uncertainty of the Powheg and Alpgen samples is also included.

PDF Uncertainties on the parton distribution function are taken into account for ZZ and WZ samples. Since the PDF uncertainty is already taken into account in the cross-section uncertainty for the $t\bar{t}W^{(*)}/Z^{(*)}/WW$ samples, no additional uncertainty is applied here.

6.6.2   Uncertainties on the Matrix Method Background

The matrix method fake lepton background estimate has several of its own sources of uncertainty. Based on equations 6.4 and 6.5, the systematic uncertainties on the estimate can be classified into systematics on the baseline efficiencies, on the scale factors, and on the fractions.

The impact of these sources is determined as follows:

Baseline Efficiencies Since the baseline efficiencies are only parametrized in p_T, η, and tau prongs, additional dependencies on event kinematics are taken as systematic un-

certainties. The dependence on these additional variables is determined as follows: In each p_T bin, the variation of the fake rate or real efficiency along the additional variable with respect to the average is applied as an uncertainty. This following variables are tested and applied only in the applicable signal regions where the variable is used in the event selection: E_T^{miss}, m_T, $m_T 2$, m_{SFOS}, SFOS veto, and η. The ranges of uncertainties across p_T bins for each truth category are shown in Tables 6.4-6.6. Some large dependencies are observed for light flavor muons (up to 38% E_T^{miss} dependence, up to 45% m_T dependence, and up to 35% m_{SFOS} dependence), but the overall effects on the final uncertainty is generally smaller because the large errors are in categories or pt bins that do not contribute significantly in the fake-lepton background.

Table 6.4: Absolute systematic uncertainty on the matrix method baseline efficiencies due to the E_T^{miss} dependence. The following notation is used: HF–heavy flavor jet, LF–light flavor jet, CO–converted photon, QJ–quark jet, GJ–gluon jet.

Type	Top category (%)	diboson category (%)	Z+jets category (%)
muon HF	1-2	5-20	3-6
muon LF	3-4	8-38	5-13
muon prompt	0.2-1.4	0-17	5-14
electron HF	0.2-1.2	3-11	5-9
electron LF	0.4-5.8	1-15	5-8
electron CO	1-10	8-13	4-7
electron prompt	1	1-10	3-27
tau HF	0.1	1-6	0.4-2.2
tau QJ	0.1-0.2	0.3-1.0	0.2-1.2
tau GJ	0.1-0.3	0.2-2.9	0.6-1.4
tau CO	0.1	0.3-1.1	0.3-0.5
tau prompt	0.1-0.3	0.3-1.3	0.4-2.9

Fake Rate Scale Factors The uncertainty on the heavy flavor scale factor has been calculated in Section 6.5.3: since both the scale factor versus p_T and the scale factor versus $|\eta|$ are flat within the uncertainties, they are fitted to a constant. The central value of the scale factor is calculated without binning in any variable and the differences with respect to the results of the fit in p_T and in $|\eta|$ are assigned as a systematic uncertainty of the order of 5%.

Table 6.5: Absolute systematic uncertainty on the matrix method baseline efficiencies due to the m_{T} dependence for electrons and muons and the m_{T2} dependence for taus. The following notation is used: HF–heavy flavor jet, LF–light flavor jet, CO–converted photon, QJ–quark jet, GJ–gluon jet.

Type	Top category (%)	diboson category (%)	Z+jets category (%)
muon HF	0-2	5-11	2-6
muon LF	2-3	7-45	4-14
muon prompt	1-2	2-7	2-19
electron HF	0-1	1-4	2-8
electron LF	1-2	1-15	4-6
electron CO	1-4	2-13	2-7
electron prompt	1-2	2-3	4-15
tau HF	0.1	0.4-7.4	1-3
tau QJ	0.1-0.2	0.2-0.9	1
tau GJ	0.1-0.4	0.1-3.1	0.2-1.9
tau CO	0.1	0.3-1.1	0.2-1.0
tau prompt	1-2	1-4	0-2

Table 6.6: Absolute systematic uncertainty on the matrix method baseline efficiencies due to the m_{SFOS} dependence. The following notation is used: HF-heavy flavor jet, LF–light flavor jet, CO–converted photon.

Type	Top category (%)	diboson category (%)	Z+jets category (%)
muon HF	1-6	5-13	3-12
muon LF	2-31	5-18	4-15
muon prompt	0-4	1-18	1-4
electron HF	1-3	1-4	2-8
electron LF	0-7	2-15	3-12
electron CO	1-4	4-14	4-9
electron prompt	1-5	3-14	2-8

Statistical uncertainty from data The matrix method prediction has a statistical uncertainty from the data events used to apply the matrix equation. The size of this uncertainty varies from 7.7% up to 578%.

Statistical uncertainty on the fake rates The baseline fake rates and real efficiencies have inherent statistical uncertainties. Because the control regions in which these efficiencies are measured are fairly loose, the statistical uncertainty is quite small (1%-5%). The contribution of this uncertainty on the final estimate is combined with the statistical uncertainty from data.

Fractions R the uncertainty on the fractions R originates from a potential lack of knowledge of the relative contributions in a given region (for instance of the top production versus the Z/γ^* production). This is uncertainty is covered by varying the yields of the physics processes by the following amounts: top processes by 50%, diboson processes by 50%, and single boson processes by 30%.

Real Efficiencies a source of systematic uncertainty affecting the estimate of the fake-lepton background is due to the η dependence of the muon and tau real lepton efficiencies in the matrix. Variations up to 5% for muons and taus are observed and assigned as systematics.

A summary of the systematic uncertainties affecting the fake-lepton background can be seen in Table 6.7 for the signal regions.

Table 6.7: The effect of the considered systematics on the fake-lepton background in the signal regions. The expected fake-lepton background is listed, followed by the relative statistical and systematic uncertainties in %. To calculate the total uncertainty, each of the uncertainties on the matrix method efficiencies are combined in quadrature. Then, the resulting uncertainty on the efficiencies is propagated to the fake-lepton estimate.

	SR0a	SR0b	SR1SS	SR2a	SR2b
Expected Events	136.5	1.48	4.30	5.06	4.86
Statistics	+4,-4%	+25,-25%	+14,-14%	+13,-13%	+13,-13%
Fractions	+14,-10%	+6,-5%	+8,-8%	+2,-3%	+4,-4%
$E_\mathrm{T}^\mathrm{miss}$ dependence	+7,-7%	+5,-5%	+2,-2%	+1,-1%	+2,-2%
m_{ll} dependence	+18,-17%	—	+8,-8%	—	—
$SFOS$ dependence	—	+5,-5%	—	—	—
m_T dependence	+7,-7%	+5,-5%	+2,-2%	+1,-2%	+2,-2%
η dependence	+5,-4%	+4,-4%	+1,-1%	+1,-1%	+1,-1%
Scale factors	+5,-4%	+4,-4%	+1,-1%	+1,-1%	+1,-1%
Total	+24,-21%	+33,-33%	+19,-19%	+13,-14%	+14,-14%

6.6.3 Uncertainties Summary

A summary of the dominating uncertainties in each signal region can be seen in Table 6.8. In this table, the statistical uncertainty is from both the fake-lepton and MC components. The MM sources are given as electron/muon/tau FR, which includes the uncertainties on the fake rates from the fractions, $E_{\mathrm{T}}^{\mathrm{miss}}/m_{\mathrm{SFOS}}/m_{\mathrm{T}}/\eta$ dependencies and scale factors. In the signal regions with no taus, the leading systematics are the theoretical uncertainties on the cross-sections of the MC backgrounds, the choice of generator for the diboson and $t\bar{t}V$ processes, and the statistical uncertainty on the MC and fake-lepton backgrounds. In the super regions SR0a-Zrequest and SR0a-Zveto (three light leptons, a SFOS pair, a b-veto, $E_{\mathrm{T}}^{\mathrm{miss}} > 50\,\mathrm{GeV}$ and with a Z request or veto), the total uncertainty is 10% and 15% respectively. In SR0b, the statistical uncertainty from the MC and fake-lepton backgrounds pushes the total uncertainty to 33%. In SR1SS, the total uncertainty is $\sim$18%, which is dominated by the statistical uncertainty and theoretical uncertainty on the cross-sections of the MC backgrounds. In the two tau signal regions SR2a and SR2b, the total uncertainty is 12% and 13% respectively, dominated by the statistical and tau fake rate uncertainties on the fake-lepton background.

Table 6.8: Summary of the dominating uncertainties in the three-lepton signal regions. Uncertainty quoted is a % of the total expected background. The statistical uncertainty is from both the fake-lepton and MC components. The MM sources are given as electron/muon/tau FR, which includes the uncertainties on the fake rates from the fractions, the $E_{\mathrm{T}}^{\mathrm{miss}}/m_{\mathrm{SFOS}}/m_{\mathrm{T}}/\eta$ dependencies, and the scale factors.

	SR0a Z request		SR0a Z veto		SR0b	
Leading	Cross-section	6.84%	Generator	11.33%	Cross-section	26.23%
Sub-leading	Generator	6.31%	Cross-section	9.60%	stat	11.31%
	Trigger	4.65%	MM elec FR	4.65%	Generator	8.05%
	Luminosity	2.60%	Trigger	3.96%	Trigger	3.08%
	JER	2.32%	MM muon FR	3.33%	Luminosity	1.72%
	SR1SS		SR2a		SR2b	
Leading	stat	6.86%	stat	9.86%	stat	8.89%
Sub-leading	Cross-section	6.01%	Generator	4.07%	MM tau FR	4.26%
	MM tau FR	5.47%	MM tau FR	3.64%	Tau ID SF	2.38%
	Trigger	2.90%	Cross-section	2.20%	Cross-section	2.13%
	Generator	2.19%	JES	1.96%	Trigger	1.64%

6.7 Background Model Validation

6.7.1 Validation Regions

The interpretation of the analysis results in the signal regions depends on the robustness of the Standard Model background modeling. It is thus essential to demonstrate the validity of the background model prior to unblinding the observed data in the signal regions. To that end, additional event selections, referred to as "validation regions" (VRs), are defined to test the background modeling by targetting the various SM background processes. The matrix method is first validated in a Monte Carlo closure test in the VRs and SRs. Next, the full background method is applied to the validation regions with data, and the agreement with the SM prediction is used to gauge the effectiveness of the modeling.

The validation regions are defined to be relevant for, and yet orthogonal to, the signal regions. The selections are defined for each lepton channel and are split into low-$E_\mathrm{T}^\mathrm{miss}$ ("a") regions and high-$E_\mathrm{T}^\mathrm{miss}$ ("b") regions. The high-$E_\mathrm{T}^\mathrm{miss}$ regions all require one b-jet to ensure orthogonality with the signal regions. To validate the background model in the light lepton signal regions, the light lepton selections are further split into Z enriched and Z depleted regions to target different SM processes. To validate the modeling of the binned SR0a, a corresponding selection (VR0b) is defined with the same binning and a b-jet request.

The definition of the validation regions is shown in Table 6.9.

Table 6.9: The selection requirements for the three-lepton validation regions.

	Channel	Z boson	$E_{\mathrm{T}}^{\mathrm{miss}}$ [GeV]	N(b-jets)	Target process
VR0noZa	$\ell^{\pm}\ell^{\mp}\ell'$	m_{SFOS} & $m_{3\ell}$ veto	35–50	–	WZ^*, Z^*Z^*, Z^*+jets
VR0noZb	$\ell^{\pm}\ell^{\mp}\ell'$	m_{SFOS} & $m_{3\ell}$ veto	> 50	== 1	$t\bar{t}$
VR0Za	$\ell^{\pm}\ell^{\mp}\ell'$	request	35–50	–	WZ, Z+jets
VR0Zb	$\ell^{\pm}\ell^{\mp}\ell'$	request	> 50	== 1	WZ
VR0b	$\ell^{\pm}\ell^{\mp}\ell'$	binned	binned	== 1	WZ, $t\bar{t}$
VR1SSa	$\ell^{\pm}\ell^{\pm}\tau$	–	35–50	–	WZ, Z+jets
VR1SSb	$\ell^{\pm}\ell^{\pm}\tau$	–	> 50	== 1	$t\bar{t}$
VR2a	$\ell\tau\tau$	–	35–50	–	W+jets, Z+jets
VR2b	$\ell\tau^{\pm}\tau^{\mp}$	–	> 50	== 1	$t\bar{t}$

6.7.2 Matrix Method Closure Test

To validate the matrix method algebra and assumptions before applying it to data, a closure test is performed by replacing data with MC and comparing the results of the method to the true fake lepton content in MC. Equation 6.3 shows that the matrix method can also predict the real lepton component of the input sample, $N_{RR \to TT}$, so both the real and fake components are compared to the MC. No scale factors are applied to the matrix method efficiencies, since it is a pure MC comparison. The equations 6.4 and 6.5 then become:

$$f_{XR} = \Sigma_{i,j}(f^{ij} \times R_{XR}^{ij}) \tag{6.6}$$

$$\epsilon_{XR} = \Sigma_j \ (\epsilon^j \ \times P_{XR}^j) \tag{6.7}$$

The results of the closure test can be seen in Table 6.10.

Table 6.10: Matrix method MC closure test in the validation and signal regions. Fake CT is the fake prediction from performing the matrix method on MC. Real CT is the real-lepton component of the matrix method solution. For this comparison, the efficiency scale factors are set to 1. The uncertainty on the matrix method includes systematic uncertainties while the uncertainty on the MC is statistical only.

Sample	fake MC	fake CT	real MC	real CT
VR0noZa	82.49 ± 15.90	78.07 ± 29.37	121.54 ± 2.33	125.96 ± 33.88
VR0noZb	57.21 ± 1.91	57.28 ± 18.68	20.58 ± 0.99	20.51 ± 18.81
VR0Za	183.90 ± 19.56	211.60 ± 61.97	544.63 ± 5.36	516.93 ± 65.48
VR0Zb	20.77 ± 5.01	19.59 ± 5.02	73.20 ± 1.88	74.38 ± 7.37
SR0a	168.77 ± 17.00	146.75 ± 36.37	1163.94 ± 7.93	1185.97 ± 41.27
SR0b	1.85 ± 0.47	1.55 ± 0.39	4.39 ± 0.42	4.68 ± 0.75
VR1SSa	49.84 ± 11.31	68.69 ± 10.96	21.23 ± 1.46	2.35 ± 16.28
VR1SSb	25.60 ± 1.81	23.49 ± 3.51	6.22 ± 0.72	8.66 ± 4.08
VR2a	659.39 ± 95.18	629.69 ± 41.82	19.37 ± 1.42	48.18 ± 111.75
VR2b	167.80 ± 8.52	189.26 ± 11.32	4.55 ± 0.61	-17.04 ± 14.56
SR1SS	1.18 ± 0.52	2.84 ± 1.12	4.59 ± 0.69	2.96 ± 1.44
SR2a	3.98 ± 0.69	5.55 ± 1.22	1.54 ± 0.43	-0.02 ± 1.50
SR2b	2.40 ± 0.58	6.15 ± 1.35	1.23 ± 0.35	-2.50 ± 1.54

6.7.3 Validation with Data

The background expectation and the data in the validation regions is shown in Table 6.11. The agreement indicates that the background is well described by the Monte Carlo and the matrix method.

Kinematic distributions for the validation regions can be seen in Figures 6.39-6.46. Validation regions with three light leptons and no taus generally show good agreement between expected and observed events. The shapes of the kinematic variables m_{SFOS}, $E_{\text{T}}^{\text{miss}}$ and m_{T} used to define the three light lepton signal regions are seen to agree well with data in VR0noZa, VR0Za, VR0noZb and VR0Zb. Validation regions with taus show excellent agreement between expected and observed events. The shapes of the expected $m_{\ell\tau}$, $E_{\text{T}}^{\text{miss}}$, $\sum p_{\text{T}}(e, \mu)$ distributions are seen to agree well with data in VR1SSa and VR1SSb. Meanwhile, the shapes of the expected $m_{\tau\tau}$, $E_{\text{T}}^{\text{miss}}$, m_{T2}, $\sum p_{\text{T}}(\tau)$ distributions are seen to agree

well with data in VR2a and VR2b.

Table 6.11: Data and background yields in the three-lepton validation regions. The VR0b bins are the same as those defined in Table 6.2. All background contributions are normalized to 20.3 fb^{-1}. Uncertainties on the MC and MM components are statistical and systematic.

Sample	WZ	ZZ	Top+V	VVV	Higgs	Fake	Σ SM	Data
VR0b-bin1	$0.66^{+0.34}_{-0.32}$	$0.11^{+0.04}_{-0.04}$	$0.47^{+0.26}_{-0.27}$	$0.019^{+0.022}_{-0.022}$	$0.12^{+0.08}_{-0.08}$	$4.7^{+1.8}_{-1.7}$	$6.1^{+1.9}_{-1.8}$	6
VR0b-bin2	$0.77^{+0.29}_{-0.32}$	$0.012^{+0.010}_{-0.009}$	$0.23^{+0.13}_{-0.13}$	$0.0004^{+0.0009}_{-0.0009}$	$0.09^{+0.06}_{-0.06}$	$2.3^{+1.0}_{-0.9}$	$3.4^{+1.0}_{-1.0}$	2
VR0b-bin3	$0.64^{+0.32}_{-0.34}$	$0.021^{+0.015}_{-0.012}$	$0.39^{+0.25}_{-0.29}$	$0.011^{+0.014}_{-0.015}$	$0.09^{+0.06}_{-0.06}$	$1.1^{+0.5}_{-0.5}$	$2.3^{+0.7}_{-0.7}$	3
VR0b-bin4	$0.28^{+0.17}_{-0.19}$	$0.009^{+0.008}_{-0.008}$	$0.64^{+0.34}_{-0.30}$	$0.026^{+0.030}_{-0.029}$	$0.17^{+0.11}_{-0.11}$	$2.8^{+1.1}_{-1.0}$	$3.9^{+1.2}_{-1.1}$	4
VR0b-bin5	$0.28^{+0.14}_{-0.14}$	$0.09^{+0.04}_{-0.04}$	$0.39^{+0.29}_{-0.29}$	$0.006^{+0.009}_{-0.007}$	$0.07^{+0.05}_{-0.05}$	$4.1^{+1.5}_{-1.4}$	$4.9^{+1.5}_{-1.4}$	5
VR0b-bin6	$0.42^{+0.24}_{-0.26}$	$0.014^{+0.011}_{-0.008}$	$0.40^{+0.19}_{-0.19}$	$0.004^{+0.005}_{-0.005}$	$0.16^{+0.12}_{-0.12}$	$5.4^{+2.0}_{-1.8}$	$6.4^{+2.0}_{-1.9}$	2
VR0b-bin7	$0.38^{+0.17}_{-0.16}$	$0.036^{+0.016}_{-0.018}$	$0.7^{+0.4}_{-0.4}$	$0.024^{+0.027}_{-0.026}$	$0.12^{+0.09}_{-0.09}$	$6.8^{+2.4}_{-2.2}$	$8.1^{+2.4}_{-2.2}$	9
VR0b-bin8	$0.020^{+0.015}_{-0.019}$	$0.001^{+0.001}_{-0.001}$	$0.5^{+0.4}_{-0.4}$	$0.003^{+0.004}_{-0.004}$	$0.06^{+0.05}_{-0.05}$	$0.46^{+0.31}_{-0.29}$	$1.0^{+0.5}_{-0.5}$	2
VR0b-bin9	$1.2^{+0.4}_{-0.4}$	$0.084^{+0.027}_{-0.021}$	$0.31^{+0.23}_{-0.18}$	$0.019^{+0.022}_{-0.022}$	$0.06^{+0.05}_{-0.05}$	$4.9^{+1.6}_{-1.5}$	$6.6^{+1.7}_{-1.6}$	4
VR0b-bin10	$0.56^{+0.25}_{-0.26}$	$0.057^{+0.016}_{-0.022}$	$0.27^{+0.19}_{-0.19}$	$0.014^{+0.019}_{-0.020}$	$0.025^{+0.018}_{-0.020}$	$1.6^{+0.6}_{-0.6}$	$2.5^{+0.7}_{-0.7}$	2
VR0b-bin11	$1.4^{+0.4}_{-0.5}$	$0.06^{+0.08}_{-0.08}$	$1.1^{+0.4}_{-0.4}$	$0.033^{+0.035}_{-0.035}$	$0.17^{+0.12}_{-0.12}$	$6.9^{+2.2}_{-2.1}$	$9.7^{+2.3}_{-2.2}$	12
VR0b-bin12	$0.19^{+0.15}_{-0.26}$	$0.013^{+0.015}_{-0.015}$	$0.35^{+0.21}_{-0.21}$	$0.023^{+0.026}_{-0.021}$	$0.10^{+0.10}_{-0.09}$	$2.1^{+0.8}_{-0.7}$	$2.8^{+0.8}_{-0.8}$	8
VR0b-bin13	34^{+4}_{-4}	$1.80^{+0.30}_{-0.31}$	$8.7^{+2.0}_{-2.0}$	$0.05^{+0.05}_{-0.05}$	$0.33^{+0.13}_{-0.14}$	$14.5^{+3.9}_{-3.5}$	60^{+7}_{-6}	67
VR0b-bin14	$18.4^{+2.9}_{-3.4}$	$0.53^{+0.11}_{-0.11}$	$6.2^{+1.6}_{-1.5}$	$0.07^{+0.07}_{-0.07}$	$0.26^{+0.11}_{-0.11}$	$2.6^{+1.0}_{-1.0}$	28^{+4}_{-4}	30
VR0b-bin15	$4.5^{+1.3}_{-1.1}$	$0.25^{+0.08}_{-0.07}$	$1.8^{+0.7}_{-0.7}$	$0.04^{+0.05}_{-0.04}$	$0.09^{+0.06}_{-0.06}$	$1.0^{+0.7}_{-0.6}$	$7.7^{+1.6}_{-1.5}$	11
VR0b-bin16	$0.32^{+0.66}_{-0.33}$	$0.001^{+0.002}_{-0.002}$	$0.78^{+0.35}_{-0.35}$	$0.024^{+0.025}_{-0.025}$	$0.027^{+0.019}_{-0.019}$	$0.14^{+0.09}_{-0.09}$	$1.3^{+0.8}_{-0.5}$	0
VR0b-bin17	$4.1^{+0.8}_{-0.9}$	$0.19^{+0.06}_{-0.06}$	$3.4^{+1.1}_{-1.1}$	$0.15^{+0.16}_{-0.16}$	$0.44^{+0.31}_{-0.31}$	13^{+4}_{-4}	21^{+4}_{-4}	26
VR0b-bin18	$0.26^{+0.22}_{-0.22}$	$0.011^{+0.009}_{-0.008}$	$0.8^{+0.4}_{-0.4}$	$0.009^{+0.010}_{-0.010}$	$0.020^{+0.023}_{-0.022}$	$0.0^{+0.0}_{-0.0}$	$1.0^{+0.5}_{-0.5}$	2
VR0b-bin19	$0.13^{+0.22}_{-0.10}$	$0.0002^{+0.0004}_{-0.0003}$	$0.12^{+0.11}_{-0.11}$	$0.020^{+0.023}_{-0.023}$	$0.015^{+0.015}_{-0.016}$	$0.0^{+0.0}_{-0.0}$	$0.28^{+0.25}_{-0.15}$	0
VR0b-bin20	$0.0^{+0.0}_{-0.0}$	$0.0^{+0.0}_{-0.0}$	$0.31^{+0.28}_{-0.30}$	$0.006^{+0.007}_{-0.008}$	$0.001^{+0.001}_{-0.001}$	$0.0^{+0.0}_{-0.0}$	$0.31^{+0.28}_{-0.30}$	0
VR0noZa	91^{+12}_{-12}	19^{+4}_{-4}	$3.2^{+1.0}_{-1.0}$	$1.9^{+1.9}_{-1.9}$	$2.7^{+1.3}_{-1.3}$	73^{+20}_{-17}	191^{+24}_{-22}	228
VR0Za	471^{+47}_{-47}	48^{+7}_{-7}	$10.1^{+2.3}_{-2.2}$	$0.7^{+0.7}_{-0.7}$	$2.7^{+1.5}_{-1.5}$	261^{+70}_{-63}	794^{+86}_{-80}	792
VR0noZb	$10.5^{+1.8}_{-2.0}$	$0.62^{+0.12}_{-0.12}$	$9.5^{+3.1}_{-3.1}$	$0.35^{+0.36}_{-0.36}$	$1.5^{+1.0}_{-1.0}$	47^{+15}_{-13}	69^{+15}_{-14}	79
VR0Zb	58^{+7}_{-7}	$2.6^{+0.4}_{-0.4}$	18^{+4}_{-4}	$0.18^{+0.18}_{-0.18}$	$0.71^{+0.29}_{-0.29}$	19^{+5}_{-5}	98^{+10}_{-10}	110
VR1SSa	$14.6^{+1.9}_{-1.9}$	$1.76^{+0.29}_{-0.28}$	$0.9^{+0.9}_{-0.9}$	$0.4^{+0.4}_{-0.4}$	$0.57^{+0.34}_{-0.34}$	71^{+9}_{-9}	89^{+10}_{-9}	82
VR1SSb	$1.99^{+0.35}_{-0.35}$	$0.138^{+0.028}_{-0.028}$	$2.8^{+1.3}_{-1.3}$	$0.08^{+0.08}_{-0.08}$	$0.5^{+0.5}_{-0.5}$	$22.7^{+2.8}_{-2.8}$	$28.2^{+3.2}_{-3.2}$	26
VR2a	$14.3^{+2.4}_{-2.5}$	$1.8^{+0.4}_{-0.4}$	$1.0^{+0.7}_{-0.7}$	$0.12^{+0.12}_{-0.12}$	$0.6^{+0.4}_{-0.4}$	630^{+9}_{-12}	648^{+10}_{-13}	656
VR2b	$1.9^{+0.4}_{-0.4}$	$0.12^{+0.04}_{-0.04}$	$1.7^{+0.7}_{-0.7}$	$0.06^{+0.07}_{-0.07}$	$0.5^{+0.5}_{-0.5}$	162^{+6}_{-8}	166^{+6}_{-8}	158
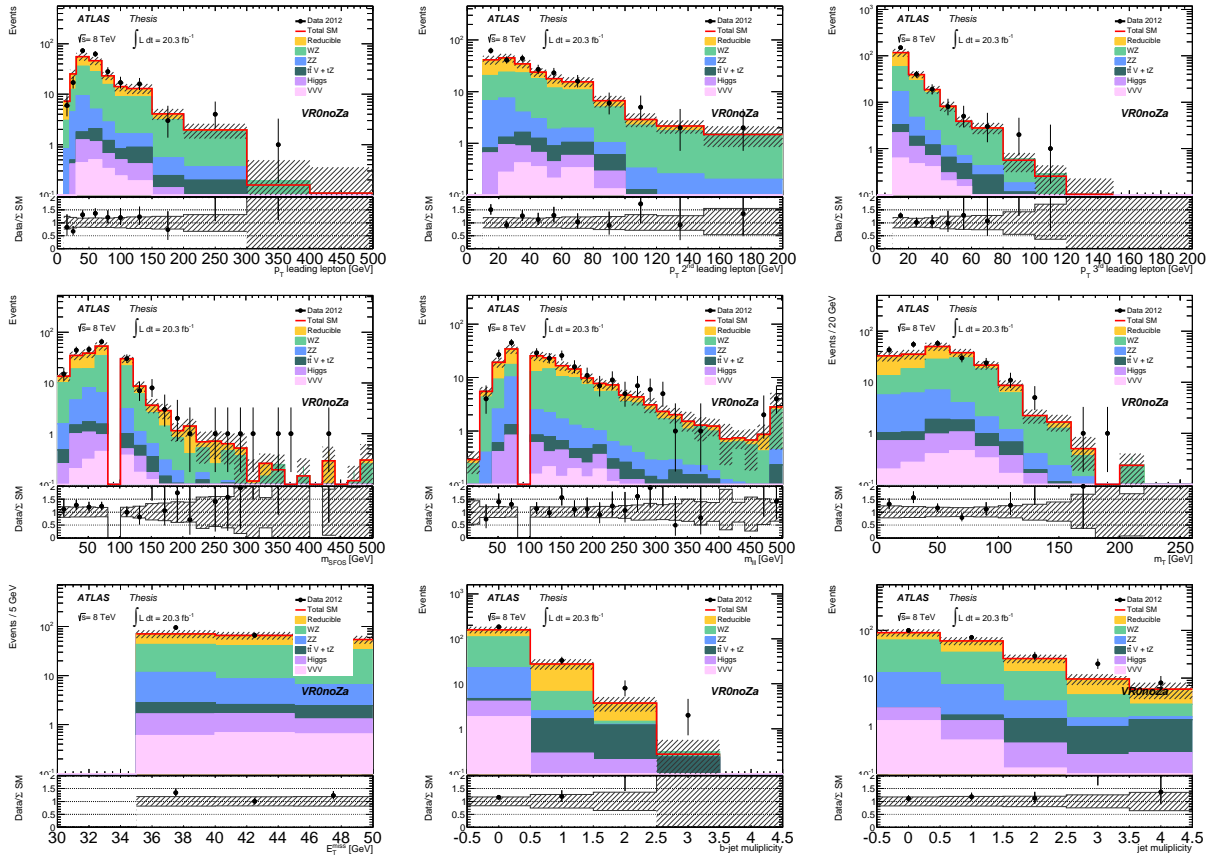
Figure 6.39: Kinematic distributions in VR0noZa. The uncertainties are statistical and systematic.

Figure 6.40: Kinematic distributions in VR0noZb. The uncertainties are statistical and systematic.
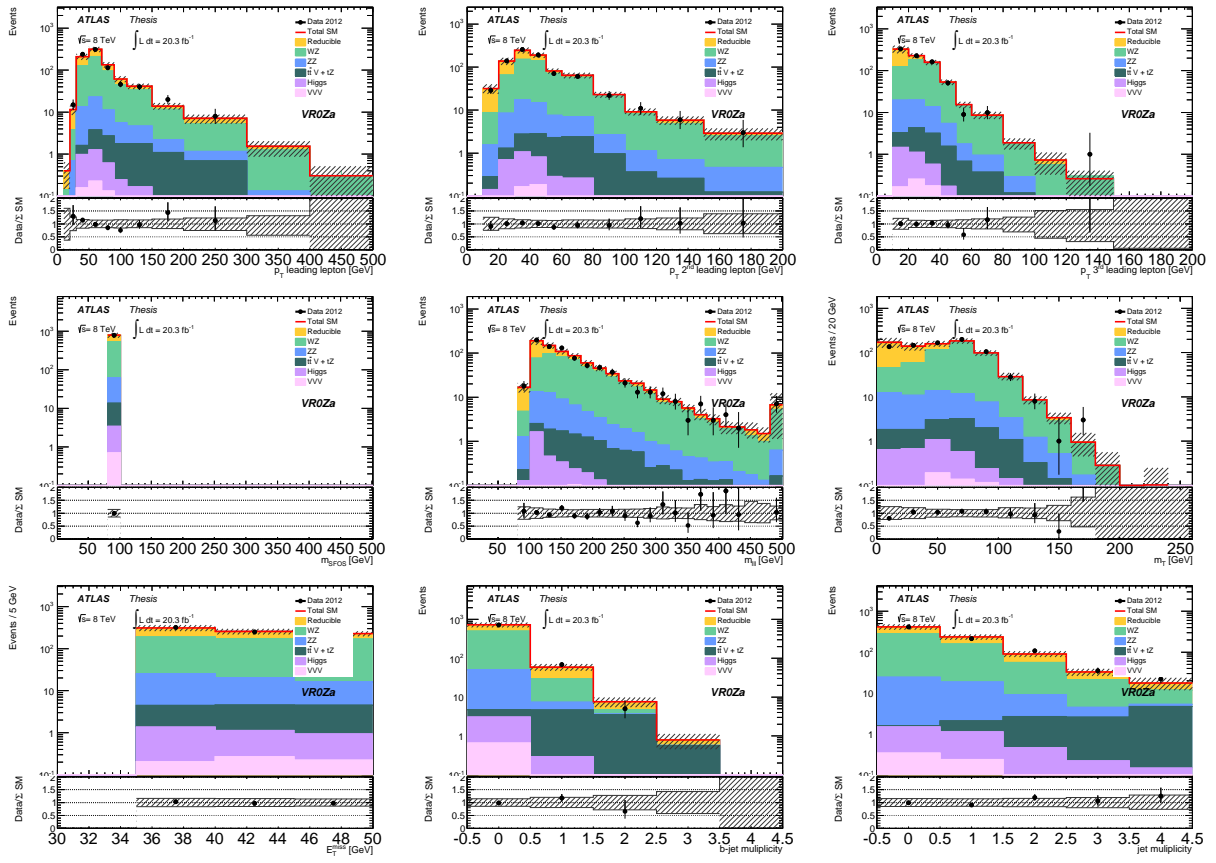
Figure 6.41: Kinematic distributions in VR0Za. The uncertainties are statistical and systematic.
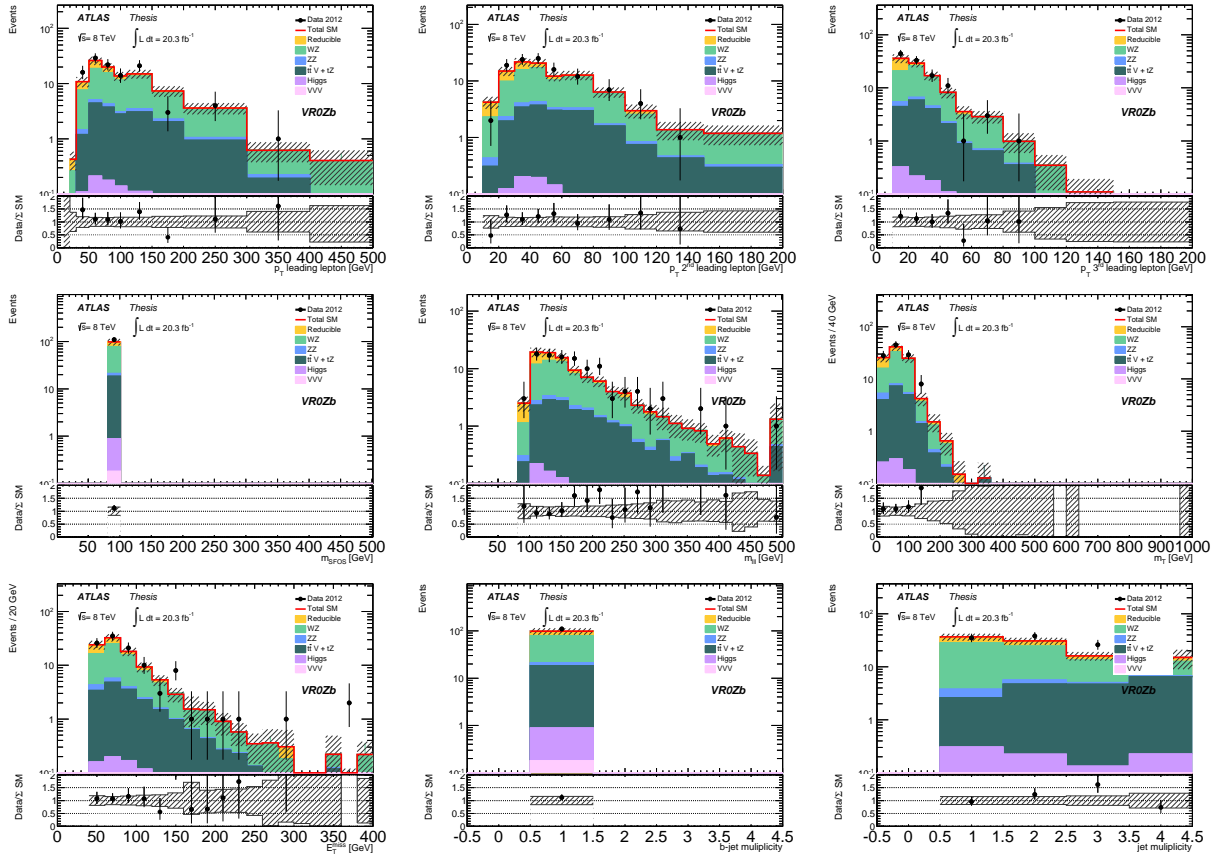
Figure 6.42: Kinematic distributions in VR0Zb. The uncertainties are statistical and systematic.
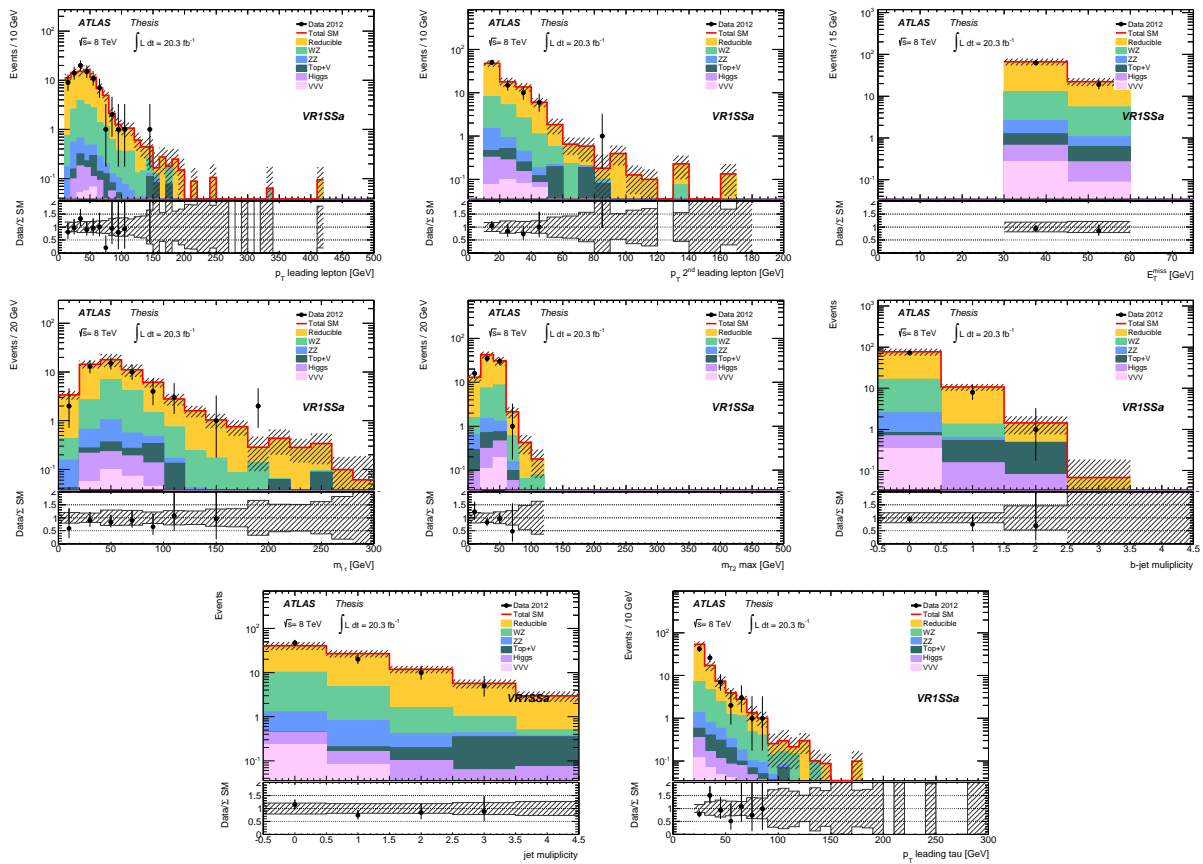
Figure 6.43: Kinematic distributions in VR1SSa. The uncertainties are statistical and systematic.
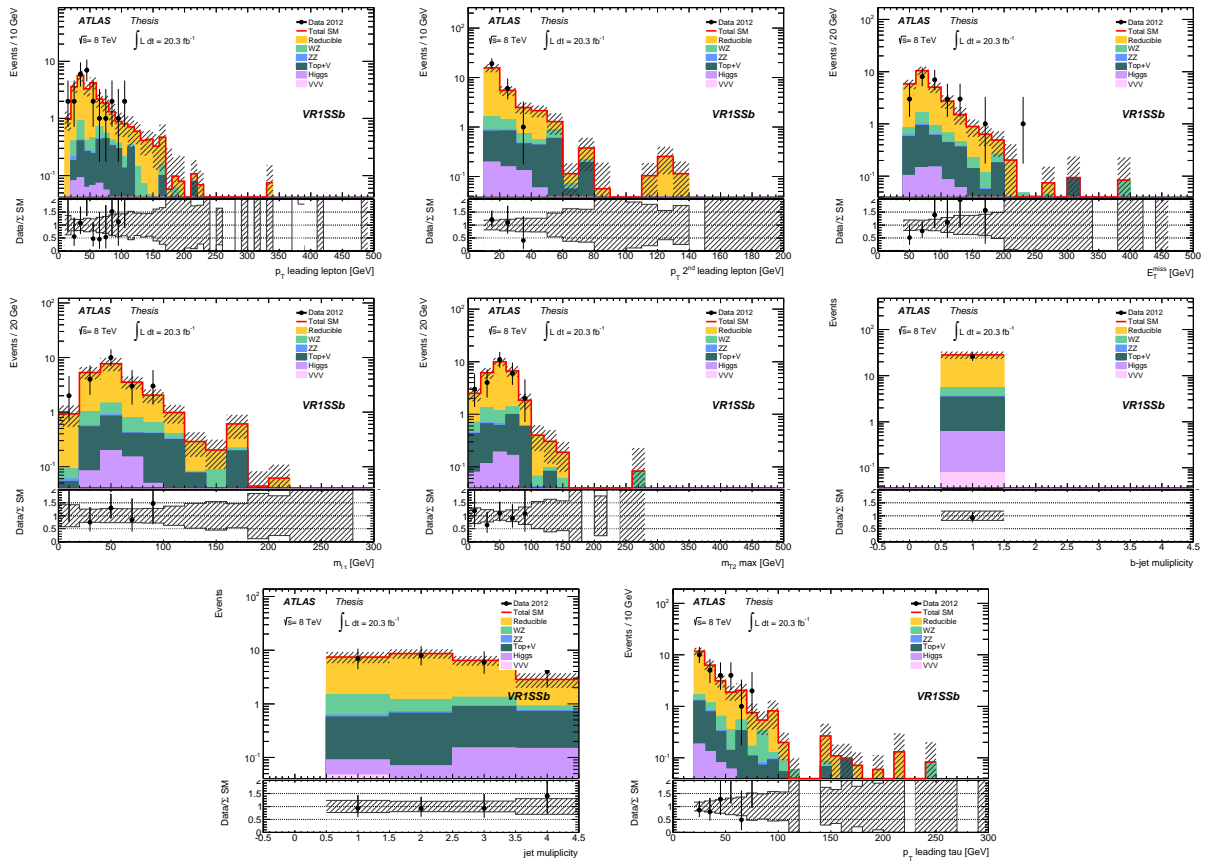
Figure 6.44: Kinematic distributions in VR1SSb. The uncertainties are statistical and systematic.
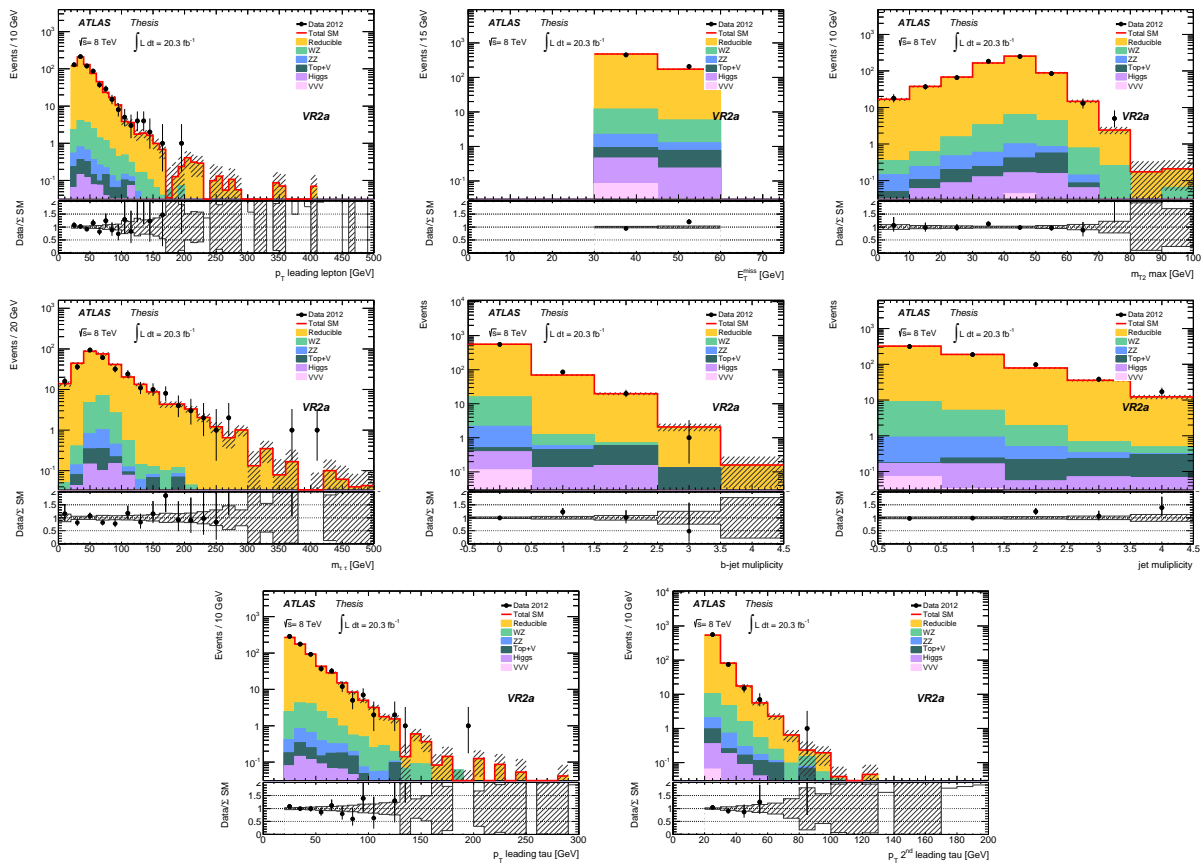
Figure 6.45: Kinematic distributions in VR2a. The uncertainties are statistical and systematic.
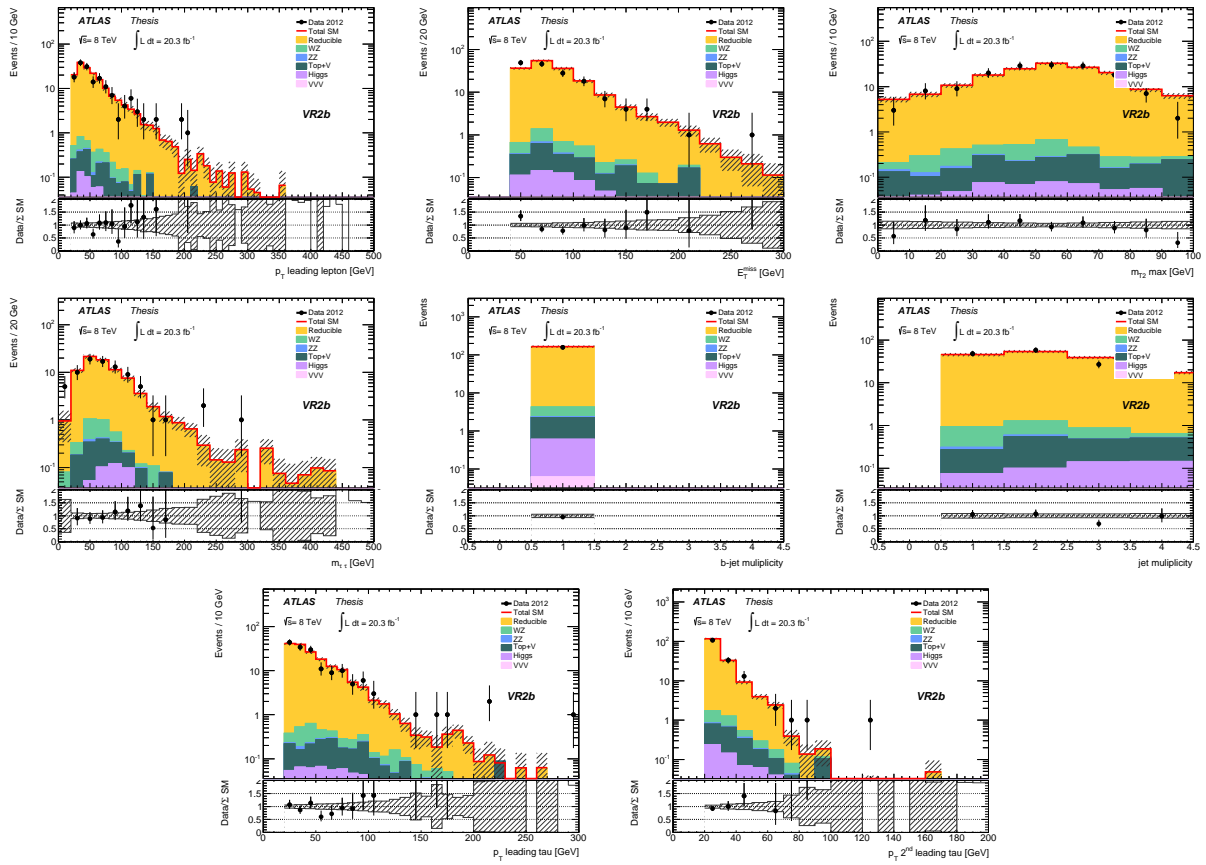
Figure 6.46: Kinematic distributions in VR2b. The uncertainties are statistical and systematic.

6.8 Results

6.8.1 Observations in Data

The successful validation of the background modeling shown in Section 6.7 gives sufficient confidence in the SM background prediction in the signal regions to proceed. The signal regions are thus unblinded and the observed data is shown in Table 6.12. Good agreement is seen with the SM prediction. Kinematic distributions for the signal regions can be seen in Figures 6.47-6.52.

Table 6.12: Expected SM background events and observed number of events in data in the three-lepton signal regions. The 3-prompt-lepton background components are derived purely from MC; fake-lepton components have been computed with the matrix method. All contributions are normalized to $20.3\,\mathrm{fb}^{-1}$. Uncertainties are statistical and systematic. The systematic uncertainties are calculated as described in Section 6.6.

Sample	3-Prompt Leptons	Fake Leptons	Σ SM	Data
SR0a-bin01	$16.4^{+3.0}_{-2.7}$	$6.8^{+2.4}_{-2.4}$	$\mathbf{23^{+4}_{-4}}$	**36**
SR0a-bin02	$3.6^{+1.2}_{-1.2}$	$0.8^{+0.4}_{-0.4}$	$\mathbf{4.4^{+1.3}_{-1.3}}$	**5**
SR0a-bin03	$9.5^{+1.8}_{-1.7}$	$1.6^{+0.7}_{-0.6}$	$\mathbf{11.0^{+1.9}_{-1.9}}$	**9**
SR0a-bin04	$6.3^{+1.5}_{-1.5}$	$2.7^{+1.0}_{-1.0}$	$\mathbf{9.0^{+1.9}_{-1.8}}$	**9**
SR0a-bin05	$9.3^{+2.3}_{-2.3}$	$4.3^{+1.6}_{-1.4}$	$\mathbf{13.5^{+2.8}_{-2.7}}$	**11**
SR0a-bin06	$5.4^{+1.3}_{-1.2}$	$2.0^{+0.8}_{-0.8}$	$\mathbf{7.4^{+1.5}_{-1.4}}$	**13**
SR0a-bin07	$10.3^{+2.2}_{-2.2}$	$4.0^{+1.5}_{-1.4}$	$\mathbf{14.3^{+2.7}_{-2.6}}$	**15**
SR0a-bin08	$0.7^{+0.4}_{-0.4}$	$0.40^{+0.27}_{-0.26}$	$\mathbf{1.1^{+0.5}_{-0.4}}$	**1**
SR0a-bin09	$19.1^{+3.4}_{-3.2}$	$4.1^{+1.3}_{-1.2}$	$\mathbf{23.2^{+3.7}_{-3.4}}$	**28**
SR0a-bin10	$14.3^{+2.6}_{-2.6}$	$2.0^{+0.9}_{-0.8}$	$\mathbf{16.3^{+2.7}_{-2.7}}$	**24**
SR0a-bin11	23^{+5}_{-5}	$5.7^{+2.1}_{-1.9}$	$\mathbf{28^{+5}_{-5}}$	**29**
SR0a-bin12	$4.7^{+1.6}_{-1.6}$	$0.9^{+0.4}_{-0.4}$	$\mathbf{5.6^{+1.6}_{-1.6}}$	**8**
SR0a-bin13	662^{+70}_{-69}	69^{+21}_{-19}	$\mathbf{732^{+73}_{-72}}$	**714**
SR0a-bin14	228^{+27}_{-26}	$2.8^{+1.9}_{-2.0}$	$\mathbf{231^{+27}_{-26}}$	**214**
SR0a-bin15	64^{+10}_{-10}	$1.3^{+0.6}_{-0.6}$	$\mathbf{65^{+10}_{-10}}$	**63**
SR0a-bin16	$4.3^{+1.7}_{-1.4}$	$0.07^{+0.14}_{-0.15}$	$\mathbf{4.4^{+1.7}_{-1.4}}$	**3**
SR0a-bin17	60^{+11}_{-10}	$11.4^{+3.5}_{-3.2}$	$\mathbf{71^{+11}_{-10}}$	**60**
SR0a-bin18	$3.2^{+1.8}_{-1.8}$	$0.27^{+0.19}_{-0.19}$	$\mathbf{3.4^{+1.8}_{-1.8}}$	**1**
SR0a-bin19	$1.2^{+0.5}_{-0.5}$	$0.17^{+0.16}_{-0.15}$	$\mathbf{1.4^{+0.5}_{-0.5}}$	**0**
SR0a-bin20	$0.26^{+0.15}_{-0.15}$	$0.08^{+0.11}_{-0.10}$	$\mathbf{0.34^{+0.19}_{-0.18}}$	**0**
SR0b	$2.8^{+1.3}_{-1.3}$	$1.5^{+0.5}_{-0.5}$	$\mathbf{4.2^{+1.4}_{-1.4}}$	**3**
SR1SS	$5.9^{+1.4}_{-1.4}$	$4.5^{+0.9}_{-0.9}$	$\mathbf{10.4^{+1.7}_{-1.7}}$	**13**
SR2a	$1.5^{+0.5}_{-0.6}$	$5.1^{+0.7}_{-0.7}$	$\mathbf{6.6^{+0.8}_{-0.9}}$	**6**
SR2b	$1.2^{+0.4}_{-0.4}$	$4.9^{+0.7}_{-0.7}$	$\mathbf{6.1^{+0.8}_{-0.8}}$	**5**
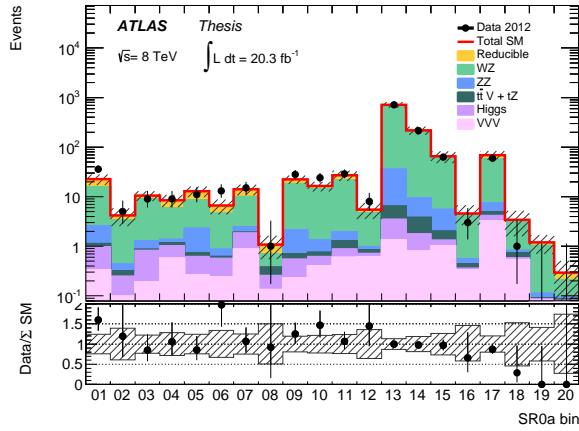
Figure 6.47: Number of expected and observed events in SR0a. The uncertainties are statistical and systematic.
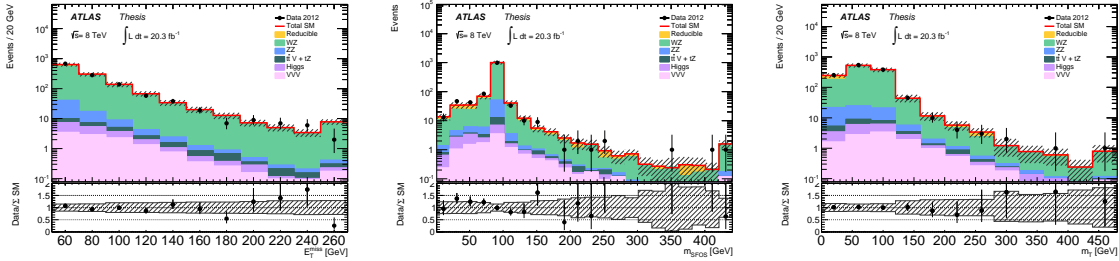
Figure 6.48: Kinematic distributions in the combined SR0a. The uncertainties are statistical and systematic.
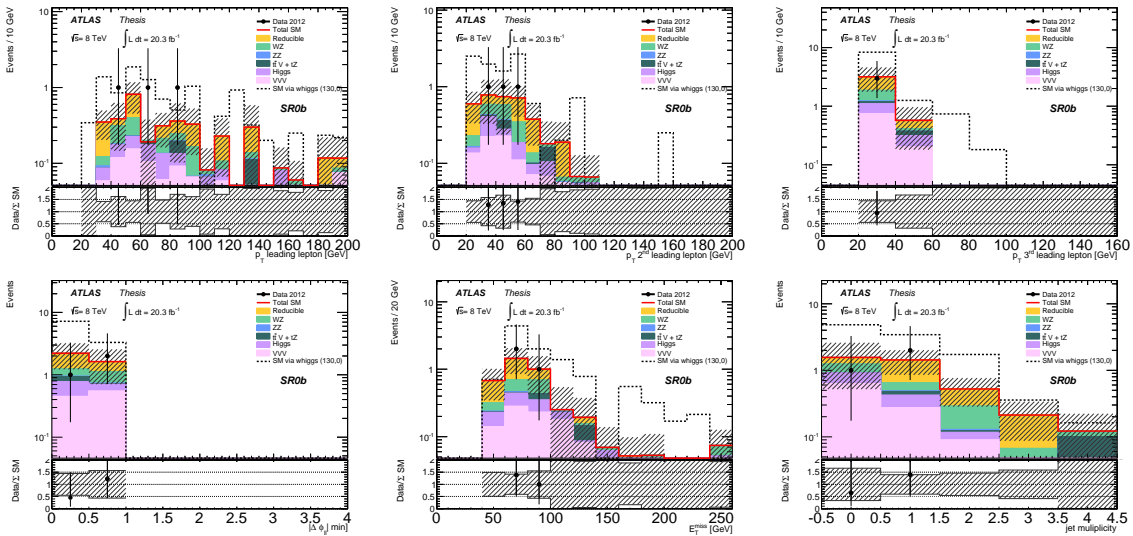
Figure 6.49: Kinematic distributions in SR0b. The uncertainties are statistical and systematic.
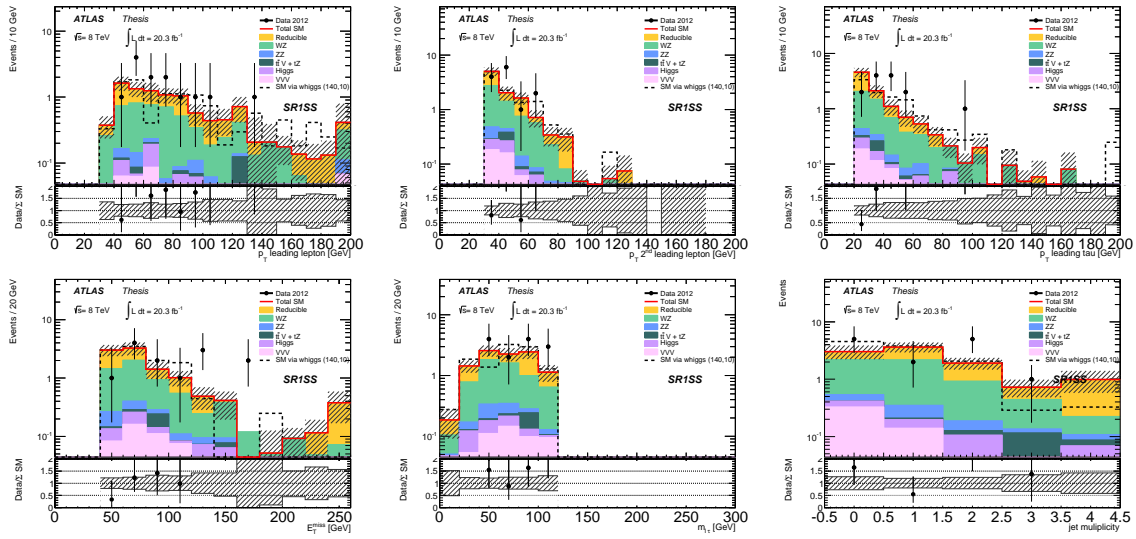
Figure 6.50: Kinematic distributions in SR1SS. The uncertainties are statistical and systematic.
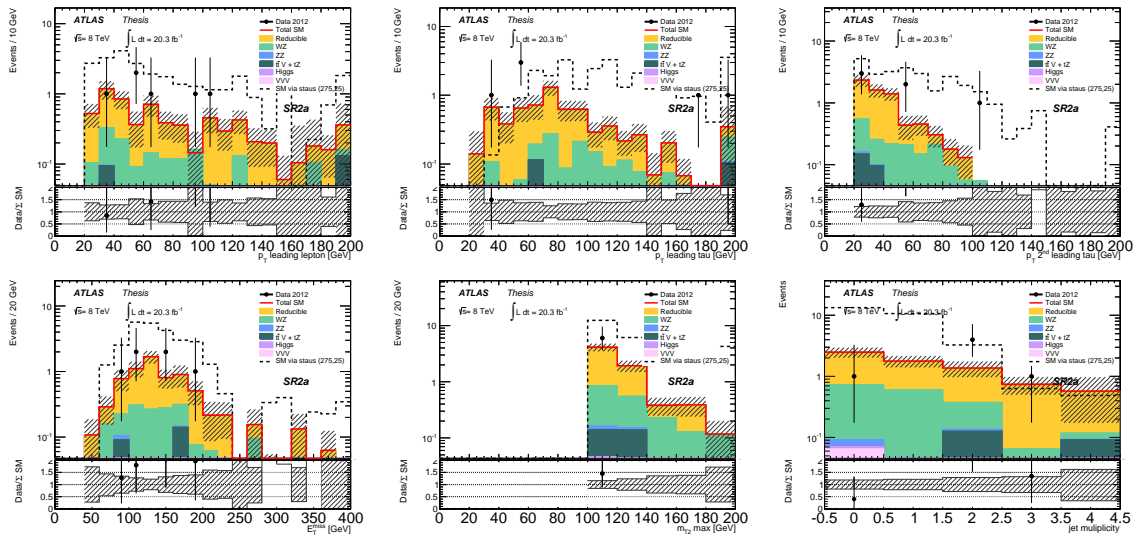

Figure 6.51: Kinematic distributions in SR2a. The uncertainties are statistical and systematic.
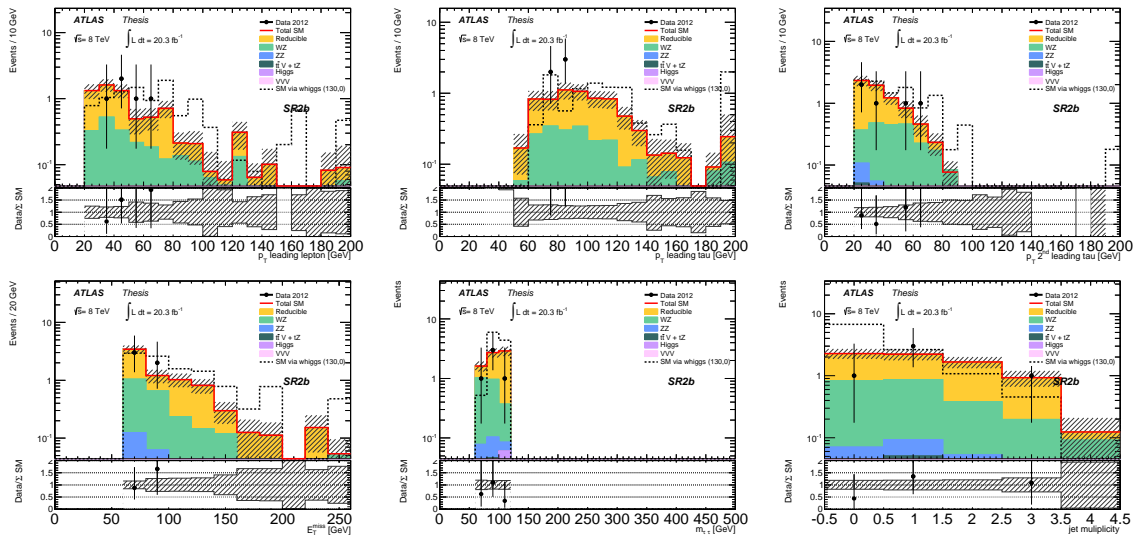
Figure 6.52: Kinematic distributions in SR2b. The uncertainties are statistical and systematic.

6.8.2 Statistical Interpretation

The compatibility of the observed data with the Standard Model, limits on the visible cross sections for new physics, and the exclusions in the considered signal models are assessed with profile log-likelihood ratio tests [80]. The likelihood parametrizes all uncertainties given in Section 6.6 and is defined as

$$L(n_S|\mu, \boldsymbol{b}, \boldsymbol{\theta}) = P(n_S|\lambda_S(\mu, \boldsymbol{b}, \boldsymbol{\theta})) \times P_{\text{syst}}(\boldsymbol{\theta}^0, \boldsymbol{\theta}),$$

where n_S represents the number of observed events in data, and $P(n_S)$ represents a Poisson distribution modeling the expected event count in the signal region as a function of the expectation λ_S. The parameter μ is the SUSY signal strength to be tested, $\boldsymbol{b}$ is the background, and $\boldsymbol{\theta}$ describes the systematic uncertainties as nuisance parameters. P_{syst} represents the constraints on systematic uncertainties and $\boldsymbol{\theta}^0$ are the nominal values around which $\boldsymbol{\theta}$ can be varied when maximizing the likelihood. The constraints used here are that the uncertainties vary according to a Gaussian distribution with $\sigma = 1$. Then P_{syst} is a product of Gaussian distributions, one for each nuisance parameter.

Model Independent Interpretation

The background-only hypothesis is tested by comparing the total SM prediction to the observed data in all the signal regions and computing the discovery p-values. Upper limits at 95% confidence level on the number of signal events and corresponding visible cross section are also computed, where the visible cross section is defined as the cross section times branching ratio times acceptance times efficiency ($\sigma \times \text{BR} \times \text{A} \times \epsilon$) of new physics processes satisfying the signal region requirements. These results are shown in Table 6.13.

147

Model Dependent Interpretation

Since no excess was observed in the data, limits can be set on the signal models described in Section 6.2. Figure 6.53 shows the exclusion contours of the four simplified models, while Figure 6.54 shows the exclusion contours of the six pMSSM models. The simplified models with sleptons have an observed exclusion up to 720 GeV for the $\tilde{\chi}_1^\pm$ and the $\tilde{\chi}_2^0$ masses. The simplified models with WZ see an exclusion up to 350 GeV. In this grid, there are some noticeable differences between expected and observed limits due to the observed fluctuations in particular SR0a bins. For example, bin 16 sees a downward fluctuation which results in a stronger observed limit at high $\tilde{\chi}_1^\pm$ and $\tilde{\chi}_2^0$ mass, while bin 1 sees an upward fluctuation which results in a weaker observed limit near the diagonal. The simplified model via staus scenario shows an observed exclusion of 380 GeV in $\tilde{\chi}_1^\pm$, $\tilde{\chi}_2^0$ masses, which matches the expected limit closely. In the simplified models with Wh, the observed limit extends to ~ 150 GeV, which is complimentary to, but not competitive with, the strong limit of 280 GeV achieved in the recent $1\ell bb$ EWK analysis [52].

Table 6.13: The compatibility of the observed results with the SM for all the signal regions. The expected and observed number of events are shown, along with the 95% CL upper limits on the number of signal events S, the limit on the visible cross-section σ_{vis}, and the CL$_b$ values. Finally the discovery p_0-value of the background only hypothesis (p_0^{bkg}) is shown.

| SR	N_{exp}	N_{obs}	S_{obs}	S_{exp}	$\sigma^{\text{obs}}_{\text{vis}}$[fb]	$\sigma^{\text{exp}}_{\text{vis}}$[fb]	CL$_b$	p_0^{bkg}
SR0a-01	$23.^{+4.}_{-4.}$	36	26.12	$14.14^{+6.08}_{-3.95}$	1.29	$0.70^{+0.30}_{-0.19}$	0.96	0.02
SR0a-02	$4.2^{+1.5}_{-1.5}$	5	6.81	$6.21^{+3.04}_{-1.83}$	0.34	$0.31^{+0.15}_{-0.09}$	0.60	0.38
SR0a-03	$10.6^{+1.8}_{-1.8}$	9	7.26	$8.29^{+3.92}_{-2.37}$	0.36	$0.41^{+0.19}_{-0.12}$	0.35	0.50
SR0a-04	$8.5^{+1.7}_{-1.6}$	9	7.99	$7.71^{+3.68}_{-2.23}$	0.39	$0.38^{+0.18}_{-0.11}$	0.55	0.44
SR0a-05	$12.9^{+2.4}_{-2.3}$	11	7.86	$9.03^{+4.22}_{-2.56}$	0.39	$0.45^{+0.21}_{-0.13}$	0.34	0.50
SR0a-06	$6.6^{+1.9}_{-1.8}$	13	14.09	$8.05^{+3.75}_{-2.29}$	0.69	$0.40^{+0.18}_{-0.11}$	0.93	0.04
SR0a-07	$14.1^{+2.2}_{-2.2}$	15	10.41	$9.52^{+4.44}_{-2.69}$	0.51	$0.47^{+0.22}_{-0.13}$	0.58	0.41
SR0a-08	$1.1^{+0.4}_{-0.4}$	1	3.45	$3.56^{+2.20}_{-1.28}$	0.17	$0.18^{+0.11}_{-0.06}$	0.47	0.50
SR0a-09	$22.4^{+3.6}_{-3.4}$	28	17.46	$12.61^{+5.66}_{-3.49}$	0.86	$0.62^{+0.28}_{-0.17}$	0.80	0.18
SR0a-10	$16.4^{+2.8}_{-2.8}$	24	18.07	$11.20^{+5.07}_{-3.11}$	0.89	$0.55^{+0.25}_{-0.15}$	0.91	0.08
SR0a-11	$27.^{+5.}_{-5.}$	29	15.42	$13.75^{+5.94}_{-3.90}$	0.76	$0.68^{+0.29}_{-0.19}$	0.60	0.39
SR0a-12	$5.5^{+1.5}_{-1.4}$	8	9.11	$6.95^{+3.33}_{-2.03}$	0.45	$0.34^{+0.16}_{-0.10}$	0.77	0.20
SR0a-13	$715.^{+70.}_{-68.}$	714	133.52	$134.26^{+45.91}_{-34.06}$	6.58	$6.61^{+2.26}_{-1.68}$	0.49	0.50
SR0a-14	$219.^{+33.}_{-33.}$	214	64.46	$67.15^{+22.68}_{-17.40}$	3.18	$3.31^{+1.12}_{-0.86}$	0.45	0.50
SR0a-15	$65.^{+13.}_{-13.}$	63	28.05	$29.60^{+10.51}_{-7.28}$	1.38	$1.46^{+0.52}_{-0.36}$	0.45	0.50
SR0a-16	$4.6^{+1.7}_{-1.5}$	3	4.76	$6.02^{+2.95}_{-1.78}$	0.23	$0.30^{+0.15}_{-0.09}$	0.31	0.50
SR0a-17	$69.^{+9.}_{-8.}$	60	17.04	$21.67^{+7.90}_{-6.10}$	0.84	$1.07^{+0.39}_{-0.30}$	0.22	0.50
SR0a-18	$3.4^{+1.4}_{-1.4}$	1	3.58	$5.05^{+2.56}_{-1.53}$	0.18	$0.25^{+0.13}_{-0.08}$	0.22	0.50
SR0a-19	$1.2^{+0.4}_{-0.4}$	0	2.44	$3.56^{+2.19}_{-1.34}$	0.12	$0.18^{+0.11}_{-0.07}$	0.20	0.50
SR0a-20	$0.29^{+0.18}_{-0.17}$	0	2.24	$2.64^{+1.90}_{-0.97}$	0.11	$0.13^{+0.09}_{-0.05}$	0.37	0.50
SR0b	$3.8^{+1.2}_{-1.2}$	3	5.04	$5.68^{+2.78}_{-1.67}$	0.25	$0.28^{+0.14}_{-0.08}$	0.38	0.50
SR1SS	$10.3^{+1.2}_{-1.2}$	13	10.57	$8.17^{+3.86}_{-2.37}$	0.52	$0.40^{+0.19}_{-0.12}$	0.75	0.22
SR2a	$6.9^{+1.2}_{-1.2}$	6	6.00	$6.85^{+3.31}_{-2.04}$	0.30	$0.34^{+0.16}_{-0.10}$	0.39	0.50
SR2b	$7.2^{+0.7}_{-0.8}$	5	5.17	$6.84^{+3.37}_{-2.03}$	0.25	$0.34^{+0.17}_{-0.10}$	0.23	0.50
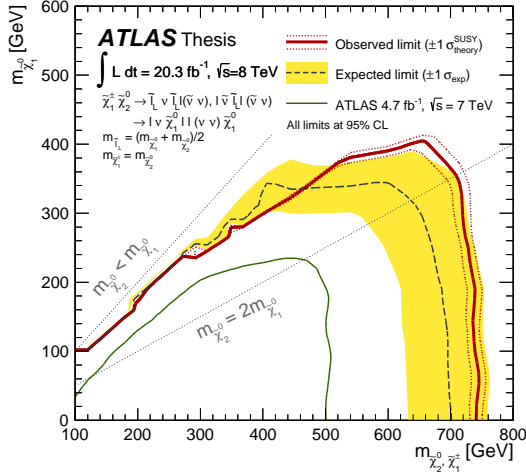
(a) Simplified models with sleptons
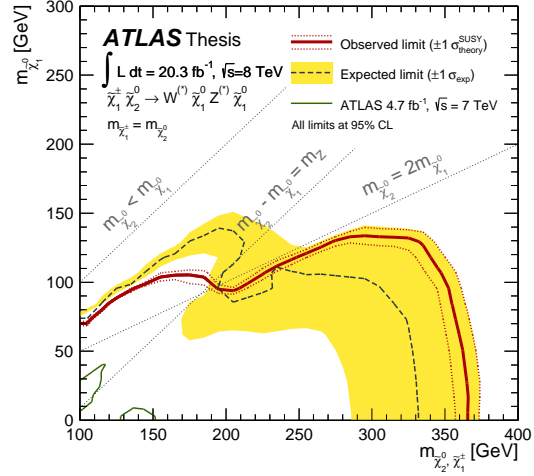
(b) Simplified models with WZ
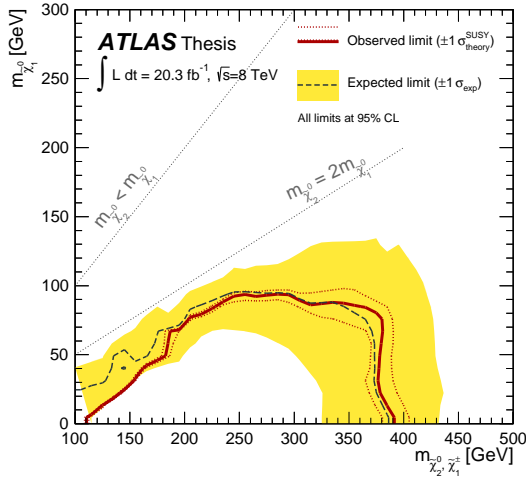
(c) Simplified models with staus
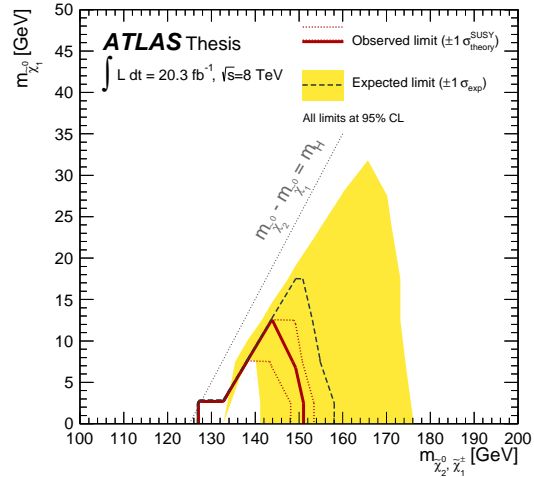
(d) Simplified models with Wh

Figure 6.53: Exclusion limit contours for the simplified models. For the grids with sleptons and WZ, a statistical combination of the binned SR0a, SR0b, SR1SS, and SR2a are used. For the grid with staus, the binned SR0a, SR1SS and SR2a are used. for the grid with Wh, the binned SR0a, SR0b, SR1SS, and SR2b are used.
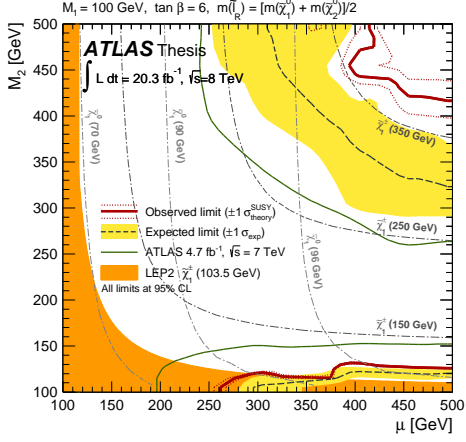
(a) pMSSM $\tilde{\ell}_{\mathrm{R}}$, M_1=100 GeV, $\tan\beta = 6$
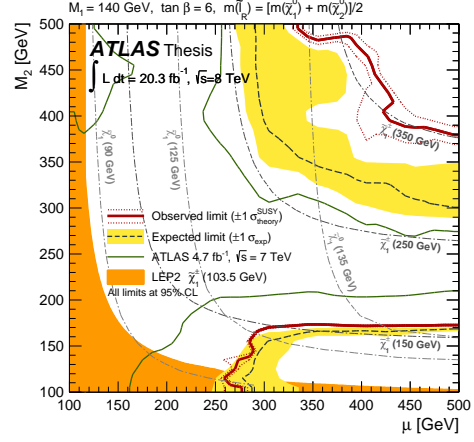
(b) pMSSM $\tilde{\ell}_{\mathrm{R}}$, M_1=140 GeV, $\tan\beta = 6$
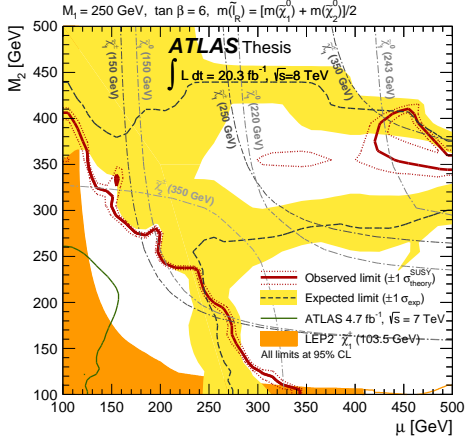
(c) pMSSM $\tilde{\ell}_{\mathrm{R}}$, M_1=250 GeV, $\tan\beta = 6$
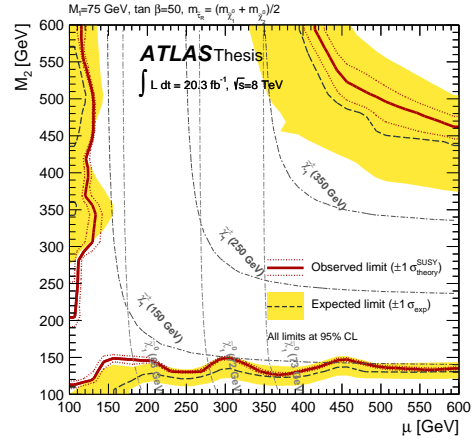
(d) pMSSM $\tilde{\tau}_{\mathrm{R}}$, M_1=75 GeV, $\tan\beta = 50$
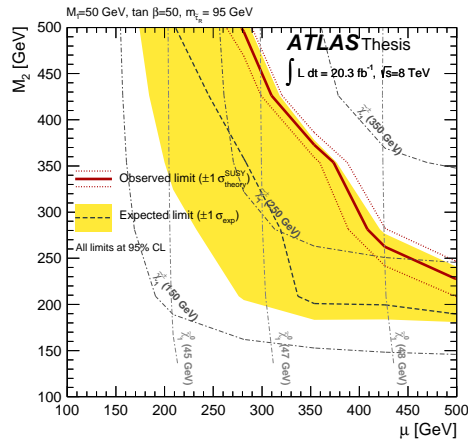
(e) pMSSM no $\tilde{\ell}$, M_1=50 GeV, $\tan\beta = 10$

Figure 6.54: Exclusion limit contours for the pMSSM models with right handed sleptons (a)-(c), with staus (d), and without sleptons (e). The statistical combination of the binned SR0a, SR0b, SR1SS, and SR2a are used in the slepton limit. SR2a is used in the stau limit, and the binned SR0a is used in the no-slepton limit.

Chapter 7

A Search for Electroweak SUSY and RPV SUSY in Four-Lepton Final States

7.1 Introduction

This chapter describes a search for R-parity-violating (RPV) and R-parity-conserving (RPC) supersymmetry in the four-lepton channel. The results, which are detailed here [54], were shown at the CERN seminar on Natural SUSY in 2012 [81]. The analysis uses 20.7 fb^{-1} of 8 TeV ATLAS data collected during 2012. The following details of the analysis are the same as the three-lepton analysis of Chapter 6 and will not be duplicated:

- Data sample, SM MC samples, and general settings for new physics MC samples (Section 6.3).

- Event preselection: trigger (Section 6.4.1) and event quality requirements (Section 6.4.2).

- Object selection details (Section 6.4.3), though a modified isolation prescription is used, to be explained in Section 7.3.1.

- The MC systematics details (Section 6.6.1).

The scope of this chapter will reflect the smaller involvement by the author, whose contributions included object selection, fake ratio measurements, and group software and data format development. An updated result of this analysis is currently under ATLAS internal review, but since the author's efforts were focused on the three-lepton analysis of Chapter 6, the details will not be included here.

The results are interpreted in terms of RPV simplified models and RPC $\tilde{\chi}_2^0 \tilde{\chi}_3^0$ production models.

7.2 Targeted SUSY Scenarios

The analysis presented here is interpreted in terms of both R-parity violating and conserving supersymmetry, while being sensitive to a wide range of other models that predict an excess of events with many leptons in the final state. Twenty simplified RPV SUSY physics models are considered, all of which produce a final state with four charged leptons (e, μ, τ) plus neutrinos via an unstable Bino LSP. Two simplified RPC SUSY models are also considered, which describe $\tilde{\chi}_2^0 \tilde{\chi}_3^0$ production and decay via sleptons.

7.2.1 RPV Simplified Models

In the RPV models considered in this analysis, SUSY production modes occur via the usual RPC couplings such as those described throughout this thesis, while the RPV couplings described in Section 3.5 alow for a prompt decay of the LSP. Figure 3.5 shows the possible

decay modes of the LSP via λ, λ', and λ'' couplings. The λ_{ijk} couplings in particular allow for high multiplicity final states. The indices are generational and determine the flavor of the lepton final states as shown in Table 7.1. The models in this analysis thus explore the λ_{121}, λ_{122}, λ_{133}, and λ_{233} couplings while assuming all others are zero.

Table 7.1: RPV decays of a $\tilde{\chi}_1^0$ LSP via a non-zero λ_{ijk} parameter.

	$ij = 12$	$ij = 13$	$ij = 23$
$k = 1$	$ee\nu/e\mu\nu$	$ee\nu/e\tau\nu$	$e\mu\nu/e\tau\nu$
$k = 2$	$e\mu\nu/\mu\mu\nu$	$e\mu\nu/\mu\tau\nu$	$\mu\mu\nu/\mu\tau\nu$
$k = 3$	$e\tau\nu/\mu\tau\nu$	$e\tau\nu/\tau\tau\nu$	$\mu\tau\nu/\tau\tau\nu$

Since LSPs come in pairs, these decays can give four-lepton signatures without the need for long particle cascades. However, in the absence of Wino/Higgsino mixing, the neutralino pair production cross-section is found to be vanishingly small. Therefore, models are analyzed that include one or more next-to-lightest SUSY particles (NLSPs) in order to obtain a reasonably large cross-section. All sparticles other than the LSP and NLSP(s) are decoupled to high masses (4.5 TeV).

Five NLSP choices are considered in this analysis, each being labeled as follows:

Winos, only $\tilde{\chi}^{\pm}$ is considered.

L-sleptons, consisting of equal-mass $\tilde{e}_{\mathrm{L}}$, $\tilde{\mu}_{\mathrm{L}}$ and $\tilde{\tau}_{\mathrm{L}}$.

R-sleptons, consisting of equal-mass $\tilde{e}_{\mathrm{R}}$, $\tilde{\mu}_{\mathrm{R}}$ and $\tilde{\tau}_{\mathrm{R}}$.

Sneutrinos, consisting of equal-mass $\tilde{\nu}_e$, $\tilde{\nu}_\mu$ and $\tilde{\nu}_\tau$.

Gluino.

Four of the models focus on electroweak sparticle production, as this will lead to the most conservative final limits, while the Gluino model serves as an example of how the experimental reach increases when strong production is introduced.

In each model, the LSP is the same $\tilde{\chi}_1^0$, technically a Bino, although this has a limited effect on its phenomenology as all decay channels and rates are defined by hand. LSP and NLSP widths are fixed to $0.1\,\mathrm{GeV}$ to ensure prompt decays, this corresponds to a lifetime of approximately $6.6 \times 10^{-24}\,\mathrm{s}$. The possible small changes in acceptance of the LSP decay due to changes in the virtual sparticle masses are neglected.

To allow some kinematic phase space for the LSP and NLSP decays, the LSP mass is varied from $10\,\mathrm{GeV}$ to $m_{\mathrm{NLSP}} - 10$ GeV. The NLSP mass range considered varies, depending on current constraints and our expected sensitivity to each model.

While the signature is driven by the LSP, the acceptance is also affected by the NLSP→LSP cascade. These decays are fixed in each model as follows:

Winos: $\tilde{\chi}_1^\pm \to W^\pm\,\tilde{\chi}_1^0$, where the gauge boson may be virtual.

L-sleptons: $\tilde{\ell}_{\mathrm{L}} \to \ell\,\tilde{\chi}_1^0$ and $\tilde{\tau}_{\mathrm{L}} \to \tau\,\tilde{\chi}_1^0$.

R-sleptons: $\tilde{\ell}_{\mathrm{R}} \to \ell\,\tilde{\chi}_1^0$ and $\tilde{\tau}_{\mathrm{R}} \to \tau\,\tilde{\chi}_1^0$.

Sneutrinos: $\tilde{\nu}_\ell \to \nu_\ell\,\tilde{\chi}_1^0$ and $\tilde{\nu}_\tau \to \nu_\tau\,\tilde{\chi}_1^0$.

Gluino: $\tilde{g} \to q\bar{q}'\,\tilde{\chi}_1^0$ $(q, \bar{q}' \in u, d, s, c)$.

7.2.2   RPC Simplified Models

In RPC SUSY models, like those explored in the analysis of Chapter 6, the LSP is stable and so the leptons must originate from the cascade decays of sparticles. Heavy neutralino pair production is a prime candidate for decays via sleptons to four lepton final states, with two leptons from each neutralino decay.

Studies of the pMSSM [59] show the $\tilde{\chi}_2^0\,\tilde{\chi}_3^0$ production cross-section to be significantly larger than the $\tilde{\chi}_2^0\,\tilde{\chi}_2^0$ production cross-section (in regions where four leptons searches are compet-

itive with two/three lepton searches). This is due to the mixing in the gaugino sector. Two simplified models are considered here for $\tilde{\chi}_2^0 \tilde{\chi}_3^0$ production and decay to a four lepton final state via $\tilde{\chi}_{2,3}^0 \to \ell^\pm \tilde{\ell}_R^\mp \to \ell^+ \ell^- \tilde{\chi}_1^0$ with 100% BR. Only the $\tilde{\chi}_1^0$, $\tilde{\chi}_2^0$, $\tilde{\chi}_3^0$ and $\tilde{\ell}_R$ are light, with all other sparticles set to be in the TeV range. The $\tilde{\chi}_1^0$ is bino-like and the $\tilde{\chi}_2^0$ and $\tilde{\chi}_3^0$ are higgsino-like. The diagram for this process is shown in Figure 7.1.
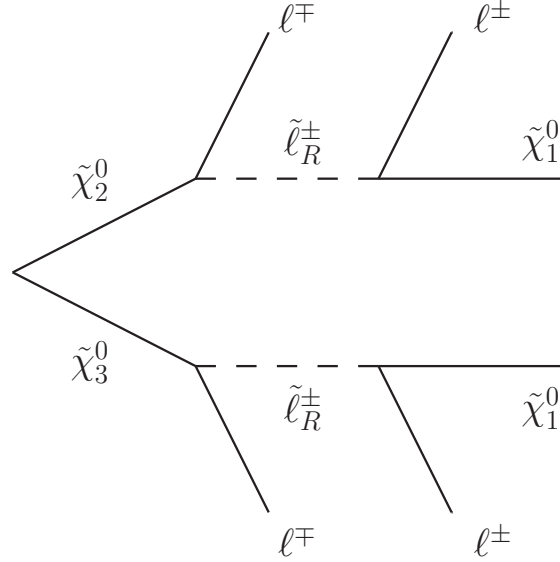
Figure 7.1: Feynman diagram for $\tilde{\chi}_2^0 \tilde{\chi}_3^0$ production and decay via sleptons.

The first $\tilde{\chi}_2^0 \tilde{\chi}_3^0$ simplified model (vA) is pMSSM-like with close to mass degenerate $\tilde{\chi}_2^0$ and $\tilde{\chi}_3^0$, and fixed mass splittings in the neutralino sector: $m(\tilde{\chi}_3^0) - m(\tilde{\chi}_2^0) = 5\,\text{GeV}$, $m(\tilde{\chi}_3^0) - m(\tilde{\chi}_1^0) = 80\,\text{GeV}$. The $\tilde{\chi}_3^0$ mass and the $m(\tilde{\chi}_3^0) - m(\tilde{\ell}_R)$ mass difference are varied in vA.

The second $\tilde{\chi}_2^0 \tilde{\chi}_3^0$ simplified model (vB) is defined with mass degenerate $\tilde{\chi}_2^0$ and $\tilde{\chi}_3^0$, and the sleptons are set midway between the neutralino masses: $m(\tilde{\chi}_3^0) = m(\tilde{\chi}_2^0)$, $m(\tilde{\ell}) = \frac{1}{2}[m(\tilde{\chi}_3^0) + m(\tilde{\chi}_1^0)]$. The $\tilde{\chi}_{2,3}^0$ mass and the $m(\tilde{\chi}_3^0) - m(\tilde{\chi}_1^0)$ mass difference are varied in vB.

7.3 Event Selection

7.3.1 Object Selection

The object selection used in this analysis is nearly the same as the criteria used in the three lepton analysis of Chapter 6. So, most of the details can be found in Section 6.4.3. However, the four lepton analysis uses a modified version of the isolation requirement for electrons and muons which improves signal acceptance for models with boosted $\tilde{\chi}_1^0$.

Electron and Muon Isolation

The isolation criteria used for electrons and muons is the same as the one in Section 6.4.3 except that nearby baseline leptons are subtracted from the $p_\mathrm{T}$cone30 isolation cones.

So, for **signal electrons**, the isolation requirement is given by

- An isolation requirement defined as $(p_\mathrm{T}\mathrm{cone}30 - \sum p_\mathbf{T}^\mathbf{base})/E_\mathrm{T} < 0.16$ where $p_\mathrm{T}\mathrm{cone}30$ is the the transverse momentum of all other tracks [9] with $p_\mathrm{T} > 1$ GeV within a cone of $\Delta R = \sqrt{(\Delta\eta)^2 + (\Delta\phi)^2} \leq 0.3$ around the electron track, $\sum p_\mathbf{T}^\mathbf{base}$ **is the scalar sum of the $p_\mathbf{T}$ of any other baseline electrons and muons in the same cone**, and E_T is the electron transverse energy.

- An isolation requirement defined as $E_\mathrm{T}\mathrm{cone}30^\mathrm{corrected}/E_\mathrm{T} < 0.18$, where

$$E_\mathrm{T}\mathrm{cone}30^\mathrm{corrected} = E_\mathrm{T}\mathrm{cone}30 - C \times N_\mathrm{vtx},$$

$C = 20.15$ MeV (17.94 MeV) in data (MC simulation), N_vtx is the number of vertices with at least 5 tracks, and $E_\mathrm{T}\mathrm{cone}30$ is a p_T and energy-density corrected isolation as

---

[9] $|d_0| < 1$ mm, $|z_0| < 1.0$ mm, nHitBlayer$\geq$1, nHitSilicon$\geq$7

measured in the EM calorimeter[10].

For **signal muons**, the isolation requirement is given by

- An isolation requirement defined as $(p_\mathrm{T}\mathrm{cone}30^{\mathrm{corrected}} - \sum \boldsymbol{p}_\mathrm{T}^{\mathbf{base}})/p_\mathrm{T} < 0.12$, where

$$p_\mathrm{T}\mathrm{cone}30^{\mathrm{corrected}} = p_\mathrm{T}\mathrm{cone}30 - C \times N_{\mathrm{vtx}},$$

$C = 10.98$ MeV (6.27 MeV) in data (MC simulation), and $\sum \boldsymbol{p}_\mathrm{T}^{\mathbf{base}}$ **is the scalar sum of the** $\boldsymbol{p}_\mathrm{T}$ **of any other baseline electrons and muons in the same cone**.

7.3.2   Signal Regions

The signal regions in this analysis depend on the tau multiplicity, similar to the three-lepton analysis treatment. For each channel, the selection is optimized using the RPV signals and MC SM background. The selection for the channel with four light leptons and zero taus is also optimised with the RPC $\tilde{\chi}_2^0 \tilde{\chi}_3^0$ production signals.

4 Light Leptons

After requesting four light leptons, the dominant SM background is rich in Z bosons, particularly ZZ production, which may have up to four prompt leptons in the final state. To suppress these backgrounds, a Z-veto is employed which suppresses not only $Z \to \ell\ell$ but also radiative decays like $Z \to \ell\ell\gamma$ and $Z \to \ell\ell\ell\ell$. This is done by rejecting events with a same-flavor opposite-sign (SFOS) lepton pair, SFOS+ℓ lepton combination, or a SFOS+SFOS lepton combination with an invariant mass within 10 GeV of the Z boson mass.

---

[10]The N_{vtx} term is a pileup correction as described in Section 6.4.3.

The remaining optimal signal region requirements differ between the RPV and the RPC signal models. So, two signal regions are developed. **SR0noZa** is a signal region targetting the RPC $\tilde{\chi}_2^0\tilde{\chi}_3^0$ scenarios while **SR0noZb** is a signal region targetting the RPV models.

SR0noZa   Besides the four lepton requirement and the Z-veto defined above, an additional cut on E_T^{miss} is effective at reducing the background for the RPC signal models. The E_T^{miss} spectrum tends to be relatively soft in these models due to the small mass splitting between the produced $\tilde{\chi}_2^0\tilde{\chi}_3^0$ and the LSP. From the E_T^{miss} distribution in Figure 7.2, it is seen that a cut of $E_T^{\mathrm{miss}} > 50$ GeV has good sensitiviy for the reference points, which are defined as follows:

- **v2A RP1:** $m_{\tilde{\chi}_3^0} = 280\,\mathrm{GeV}$, $m_{\tilde{l}_R} = 245\,\mathrm{GeV}$, $m_{\tilde{\chi}_1^0} = 200\,\mathrm{GeV}$

- **v2A RP2:** $m_{\tilde{\chi}_3^0} = 330\,\mathrm{GeV}$, $m_{\tilde{l}_R} = 285\,\mathrm{GeV}$, $m_{\tilde{\chi}_1^0} = 250\,\mathrm{GeV}$

- **v2B RP1:** $m_{\tilde{\chi}_3^0} = 265\,\mathrm{GeV}$, $m_{\tilde{l}_R} = 232.5\,\mathrm{GeV}$, $m_{\tilde{\chi}_1^0} = 200\,\mathrm{GeV}$

- **v2B RP2:** $m_{\tilde{\chi}_3^0} = 185\,\mathrm{GeV}$, $m_{\tilde{l}_R} = 167.5\,\mathrm{GeV}$, $m_{\tilde{\chi}_1^0} = 150\,\mathrm{GeV}$.
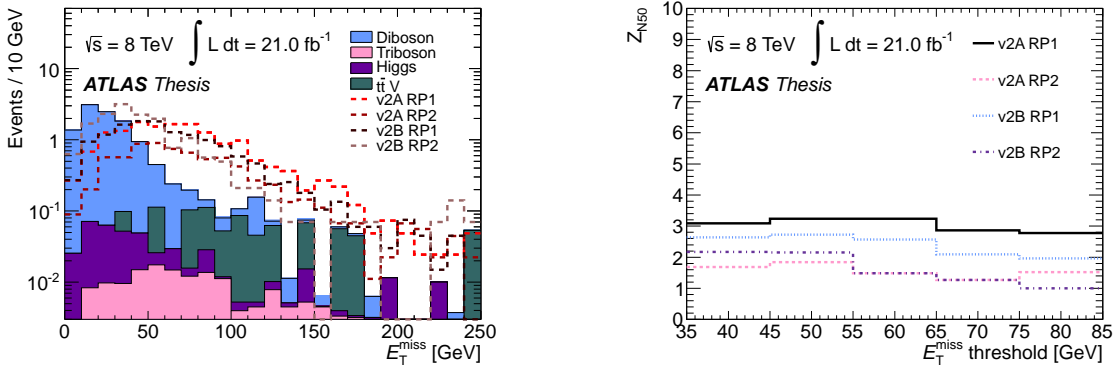
Figure 7.2: The E_T^{miss} distribution in four lepton events with a Z-veto applied (left), and the signal significance of a E_T^{miss} cut for the $\tilde{\chi}_2^0\tilde{\chi}_3^0$ signal reference points (right).

SR0noZb   The RPV signal models do not have a stable LSP like the RPC models, but the E_T^{miss} is still an effective discriminator against the ZZ background because of the neutrinos

present in the SUSY decay. Figure 7.3 shows the $E_{\mathrm{T}}^{\mathrm{miss}}$ distribution for four lepton events after the Z-veto is applied along with some points from the RPV wino grid. It is seen that a cut of $E_{\mathrm{T}}^{\mathrm{miss}} > 75$ GeV significantly suppresses all the SM backgrounds and improves the RPV signal significance.

Further improvements can be made by taking advantage of the large amount of activity in the SUSY decays relative to the SM background in the form of the effective mass variable:

$$m_{\mathrm{eff}} = E_{\mathrm{T}}^{\mathrm{miss}} + \sum_{\mathrm{leptons}} p_{\mathrm{T}}^{\ell} + \sum_{\mathrm{jets\ with\ } p_{\mathrm{T}} > 40\ \mathrm{GeV}} p_{\mathrm{T}}^{\mathrm{jet}}.$$

Figure 7.4 shows the m_{eff} distribution for four-lepton events passing the Z-veto along with some RPV gluino signals. The gluino models were used to optimize this cut because it is more sensitive to a cut on m_{eff}. From the figure it is seen that a cut of 400 GeV suppresses the majority of the background and has a high significance for the signal models.

To maximize sensitivty to both the wino and gluino signal models, events are selected in SR0noZb if they pass either the $E_{\mathrm{T}}^{\mathrm{miss}}$ requirement *or* the m_{eff} requirements.
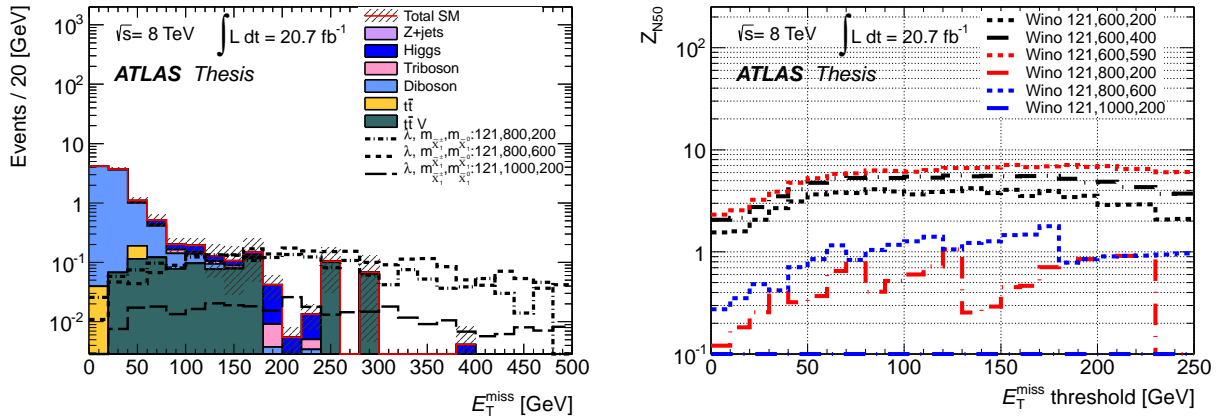
Figure 7.3: The $E_{\mathrm{T}}^{\mathrm{miss}}$ distribution in four-lepton events with a Z-veto applied (left), and the signal significance of a $E_{\mathrm{T}}^{\mathrm{miss}}$ cut for the RPV wino signal models (right).
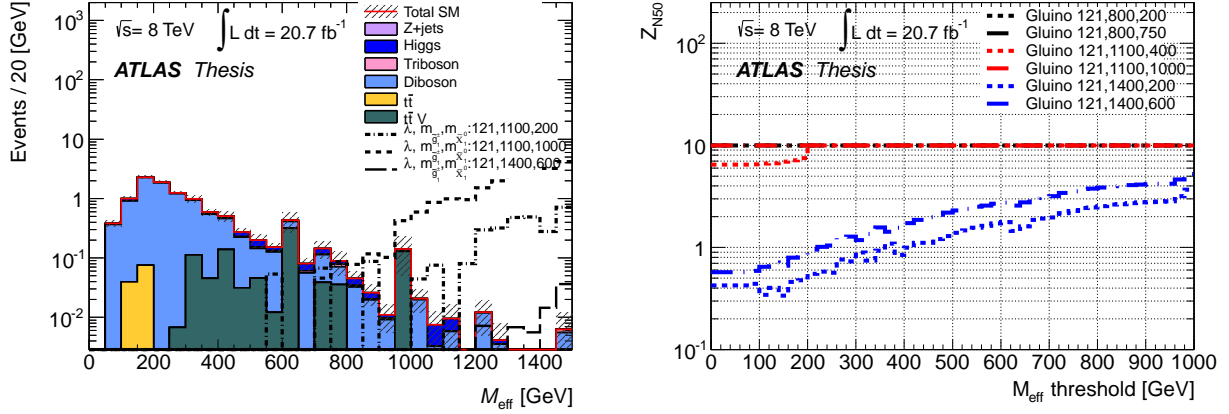
Figure 7.4: The m_{eff} distribution in four-lepton events with a Z-veto applied (left), and the signal significance of a m_{eff} cut for the RPV gluino signal models (right).

3 Light Leptons and 1 Tau

When requesting three light leptons and one tau, the dominant SM background is rich in Z bosons, particularly ZZ and Z+jets production. As for the four light lepton channel, Z-rich SM backgrounds are suppressed by a Z veto. Events are vetoed with a SFOS light lepton pair or a SFOS+ℓ light lepton combination with invariant mass within 10 GeV of the Z-boson mass. The hadronic taus are not considered in the Z-veto as the Z mass resolution is seen to be poor.

One signal region is defined, **SR1noZ**, to target the RPV signal models enhanced in tau production (λ_{133}). The kinematic variables used to optimize the selection are the same as those used to optimize the light lepton signal regions.

SR1noZ Figure 7.5 shows the distribution of E_T^{miss} once three light-leptons and one tau are requested and the Z-veto is applied. A cut of $E_T^{\text{miss}} > 75$ GeV significantly suppresses all the SM backgrounds and improves the significance of the RPV signals.

Figure 7.6 shows the distribution of m_{eff} in the same events considered for the E_T^{miss} cut. As before, the gluino signal models are used to optimize the m_{eff} cut. A cut of $m_{\text{eff}} > 400$ GeV

161

suppresses the majority of the SM backgrounds and has a high significance for the gluino signal models.

As with SR0noZb, to optimize SR1noZ for both wino and gluino signal models, events are selected if they pass either the E_T^{miss} *or* the m_{eff} requirements.
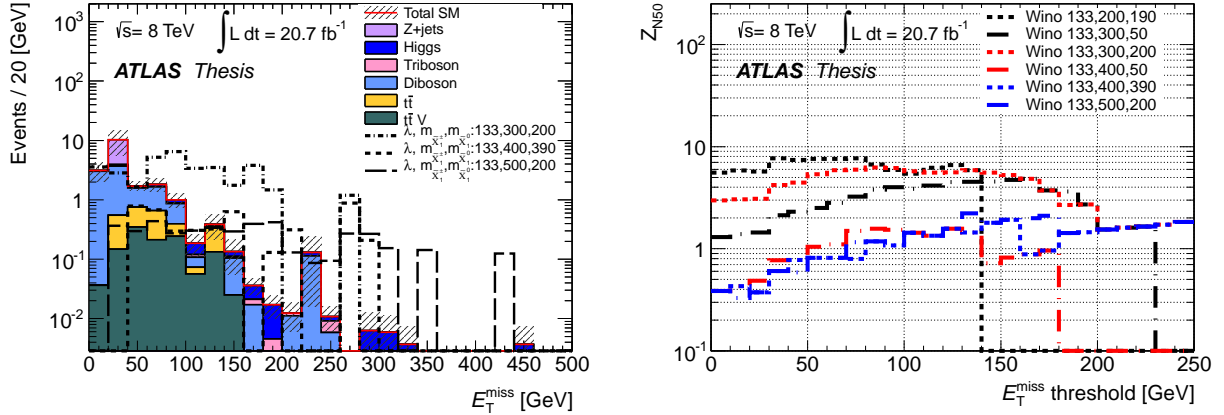

Figure 7.5: The E_T^{miss} distribution in $3\ell1\tau$ events with a Z-veto applied (left), and the signal significance of a E_T^{miss} cut for the RPV wino signal models (right).
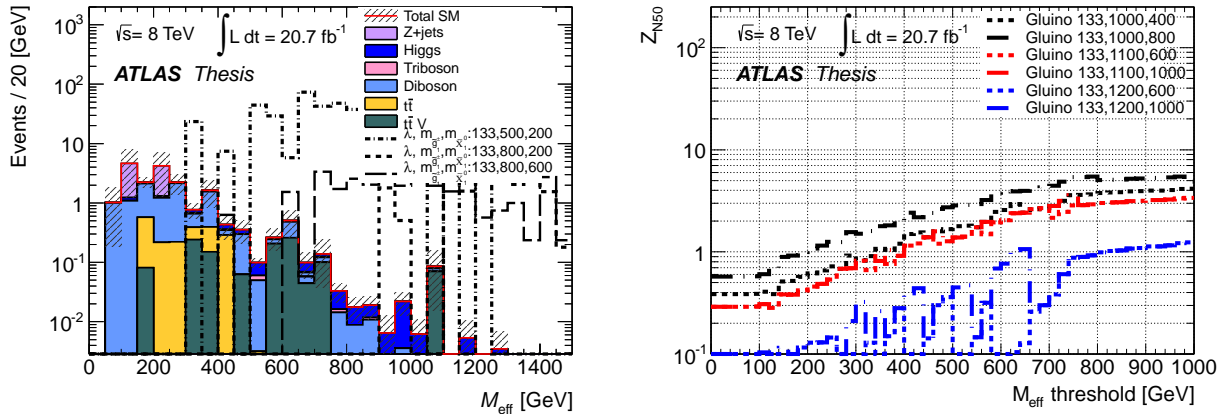

Figure 7.6: The m_{eff} distribution in $3\ell1\tau$ events with a Z-veto applied (left), and the signal significance of a m_{eff} cut for the RPV gluino signal models (right).

Signal Region Summary

Table 7.2: The selection requirements for the four lepton signal regions, where $\ell = e, \mu$.

SR	N(ℓ)	N(τ)	Z veto	$E_\mathrm{T}^\mathrm{miss}$		m_eff
SR0noZa	≥ 4	≥ 0	$(\ell^+\ell^-)$, $(\ell^+\ell^- + \ell)$, $(\ell^+\ell^- + \ell^+\ell^-)$	>50		–
SR0noZb	≥ 4	≥ 0	$(\ell^+\ell^-)$, $(\ell^+\ell^- + \ell)$, $(\ell^+\ell^- + \ell^+\ell^-)$	>75	or	>600
SR1noZ	$=3$	≥ 1	$(\ell^+\ell^-)$, $(\ell^+\ell^- + \ell)$	>100	or	>400

7.4 Standard Model Background Estimation

7.4.1 Standard Model Background Model Overview

The background model used in this analysis is very similar to the one used in the three lepton analysis of Section 6.5. Processes with four prompt leptons are modeled by MC simulation, while processes with one or more fake leptons are modeled with a data-driven method. The MC backgrounds are corrected in the same way as described in Section 6.5.2. The fake lepton backgrounds (processes with one or more fake leptons) are estimated with the weighting method, which is related to, but is a simplified version of, the matrix method.

The SM background processes that enter in the four-lepton selection are listed below, organized by the number of fake leptons:

- SM processes with 4 real leptons:

  - ZZ/γ^*, ZWW, ZZZ, higgs and $t\bar{t} + Z/WW$, where the gauge boson can be off-shell

- SM processes with 3 real leptons and 1 fake lepton:

  - WWW, WZ/γ^*, $t\bar{t} + W$, accompanied by a heavy flavor jet, a light flavor jet, or a conversion

- SM processes with 2 real leptons and 2 fake leptons:

163

- $Z + \gamma^*$, $t\bar{t}$, single top (Wt), WW, accompanied by a heavy flavor jet, or a light flavor jet, or a conversion

- SM processes with 1 real lepton and 3 fake leptons:

  - $W + \gamma^*$, single top (s-channel, t-channel), W accompanied by three fake leptons (from heavy flavor, light flavor, conversion). Backgrounds with three or more fake leptons are found to be negligible for this analysis.

7.4.2   The Weighting Method

Description of the Weighting Method

The weighting method, like the matrix method, is a technique for estimating the fake lepton background by exploiting differences between real and fake leptons. It also utilizes two sets of lepton selections: "loose" and "tight". While the matrix method relies on the probabilities of real and fake leptons to pass the tight selection, ϵ and f, the weighting method relies on a fake ratio $F = f/\bar{f}$, where $\bar{f} = 1 - f$.

The number of events with one or two fake leptons can be determined from the number of events with three tight and one loose lepton ($N(3T + 1L)$) and the number of events with two tight and two loose leptons ($N(2T + 2L)$) as:

$$N_{fake} = [N_{data}(3T + 1L) - N_{MC,4L}(3T + 1L)] \times F$$
$$- [N_{data}(2T + L_1 + L_2) - N_{MC,4L}(2T + L_1 + L_2)] \times F_1 \times F_2, \tag{7.1}$$

where N_{data} is the number of events measured in data and $N_{MC,4L}$ is the MC contribution with four real leptons which needs to be subtracted to estimate only the fake lepton contribution to the $3T + 1L$ selection. The second term in Equation 7.1 removes the double counting of

events with two fake leptons in the first term.

Fake Ratios

The calculation of the fake ratios used in the weighting method is completely analogous to the calculation of the matrix method efficiencies of Section 6.5.3. The fake ratio for each object type and process are extracted from MC events, corrected for data/MC discrepancies via scale factors, and then averaged together with the appropriate proportions for each signal region. Electrons are parametrized in p_T and η, Muons in p_T only, and taus in p_T and prong-ness (1 or 3).

The weighted average fake ratio for a specific lepton flavor and event selection region XR is defined as:

$$F_{XR} = \Sigma_{i,j}(F^{ij} \times sf^i \times R_{XR}^{ij}),$$
(7.2)

where i runs over the fake type: light flavor (LF), heavy flavor (HF), or conversion (CO), and j runs over the process categories: Top (T) or Gauge Boson (V)[11]. Each piece is further described below:

The baseline fake ratios, F^{ij}, are determined from MC for each object type i and process j. They are obtained in a sample of at least three leptons to be as consistent as possible with the weighting method control regions while maintaining sufficient statistics. The ratio is then defined as the number of leptons passing the tight requirements over the number leptons that fail.

The scale factors, sf^i, are correction factors for the baseline fake ratios to account for differences between data and MC for each object type i. They are measured in dedicated

[11]All relevant samples with top quarks are grouped into the Top category, while all single boson and diboson samples are grouped into the Gauge Boson category

control regions which are described in the next section.

The fractions, R_{XR}^{ij}, are the proportionality factors for each object type i and originating

process j used to average the fake ratios together. The fractions are measured strictly

in MC samples by requiring at least two signal leptons (e or μ) and at least one

additional loose e, μ, or τ and applying the same Z-veto, $E_{\mathrm{T}}^{\mathrm{miss}}$, and m_{eff} cuts as the

corresponding signal regions. They are parametrized in the same variables as the fake

ratios.

The average values of the process fractions are shown in Table 7.3.

Table 7.3: The average (unbinned) fake ratio fractions R_{XR}^{ij} of type i originating from process category j in the signal regions.

Type i	from j	SR0noZb	SR0noZa	SR1noZ
e from LF jets	bosons	0.023	0.028	0.051
	top	0.063	0.058	0.070
e from HF jets	bosons	0.010	0.025	0.023
	top	0.811	0.774	0.741
e from conversion	bosons	0.029	0.056	0.045
	top	0.064	0.059	0.070
μ from LF jets	bosons	0.001	0.020	0.000
	top	0.028	0.025	0.025
μ from HF jets	bosons	0.008	0.034	0.026
	top	0.963	0.920	0.949
τ from jets	bosons	0.224	0.538	0.375
	top	0.776	0.462	0.625

Fake Ratio Scale Factors

The fake ratio scale factors sf^i for each fake lepton type i are defined as the ratio of the fake

ratios in data and MC: $sf = F^{\mathrm{data}}/F^{\mathrm{MC}}$. The are measured in the same control regions as

those described in Section 6.5.3. Only the final scale factor results will be shown here.

Heavy flavor scale factors No significant dependence on E_T, p_T, η, or number of vertices is observed, so unbinned scale factors are used. The sf^{HF} for electrons, muons, and taus are

$$sf_e^{\mathrm{HF}} = 0.73 \pm 0.06$$

$$sf_\mu^{\mathrm{HF}} = 0.83 \pm 0.04$$

$$sf_\tau^{\mathrm{HF}} = 1.00 \pm 0.01$$

Light flavor scale factors The light flavor scale factors are measured for fake taus. Considerable dependence on the tau p_T is observed for 1-prong taus, whereas the 3-prong tau scale factor shows no significant dependence on p_T or η. The 1-prong scale factor is thus binned in p_T and is shown in Figure 7.7. The 3-prong scale factor is

$$sf_\tau^{\mathrm{LF}} = 0.95 \pm 0.04.$$
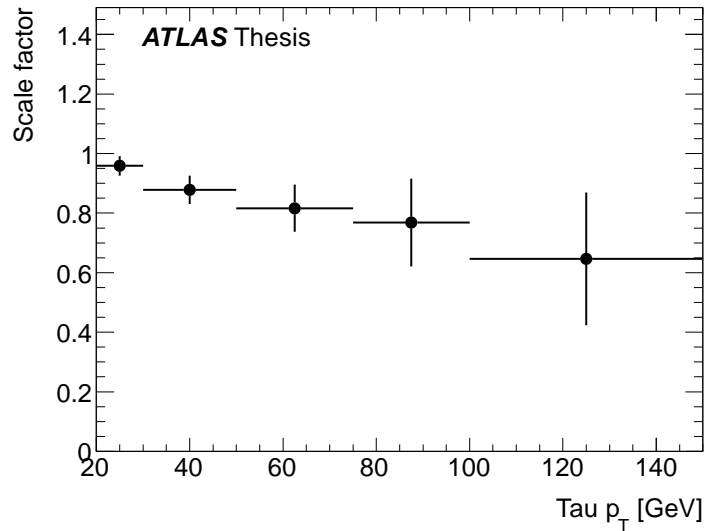
Figure 7.7: Light flavor 1-prong tau fake ratio scale factor as a function of p_T.

Conversion scale factors   No significant dependence on E_T or η is observed for the electron conversion fake ratio scale factor. The unbinned result is

$$sf_e^{\text{CO}} = 1.27 \pm 0.31.$$

Weighted Average Fake Ratios

The weighted average fake ratios for the signal regions are shown in Figures 7.4.2-7.4.2.

(a) Electron $|\eta| < 1.5$
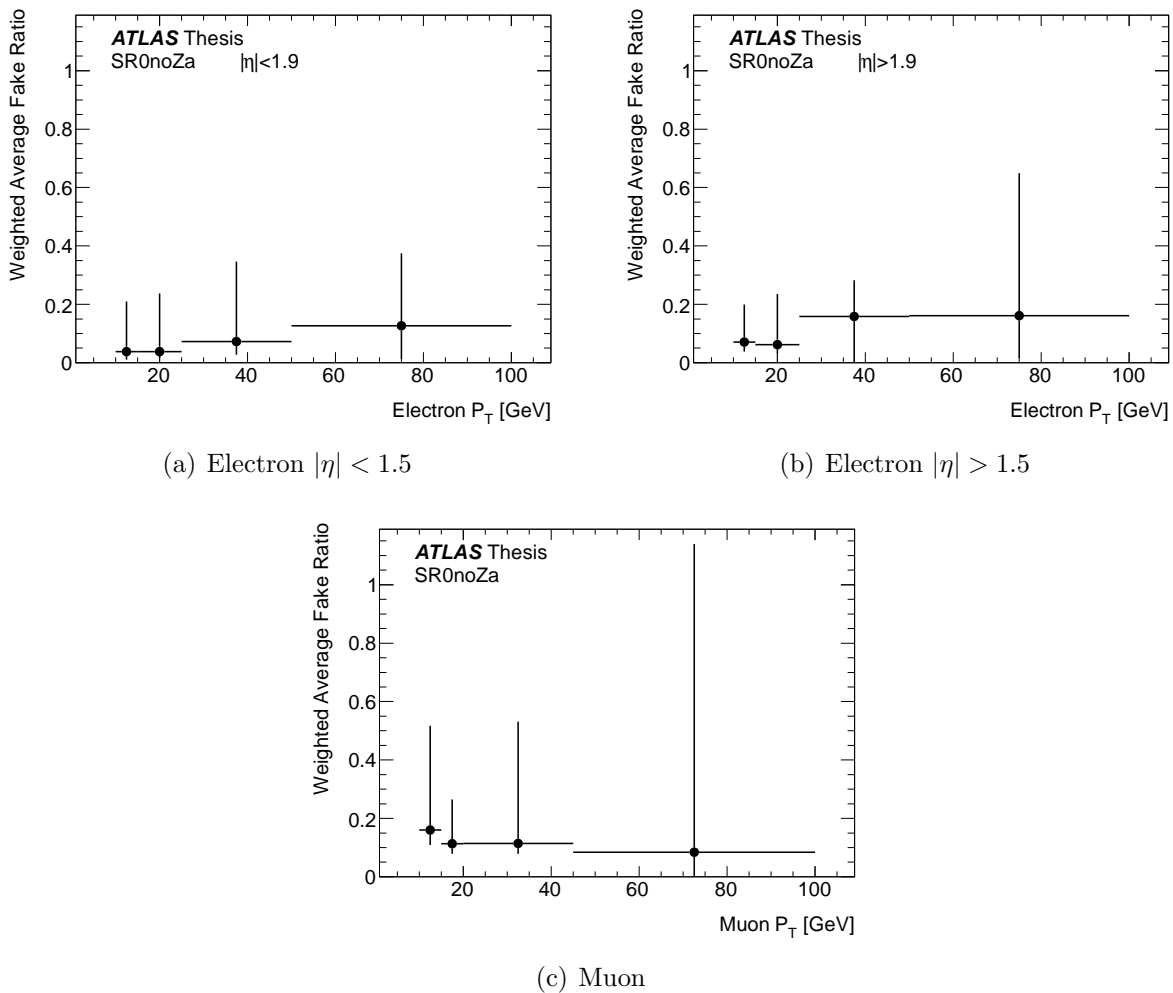
(b) Electron $|\eta| > 1.5$

(c) Muon

Figure 7.8: Weighted average fake ratios for SR0noZa.
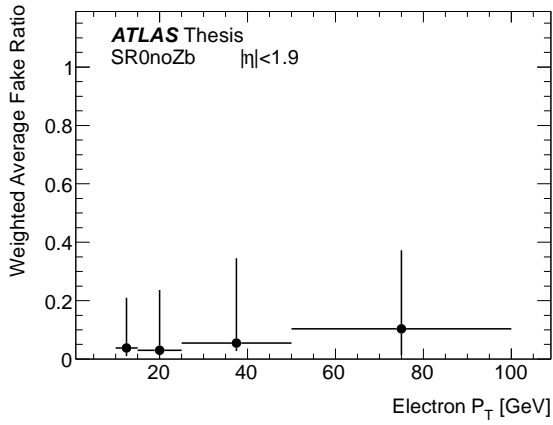
(a) Electron $|\eta| < 1.5$
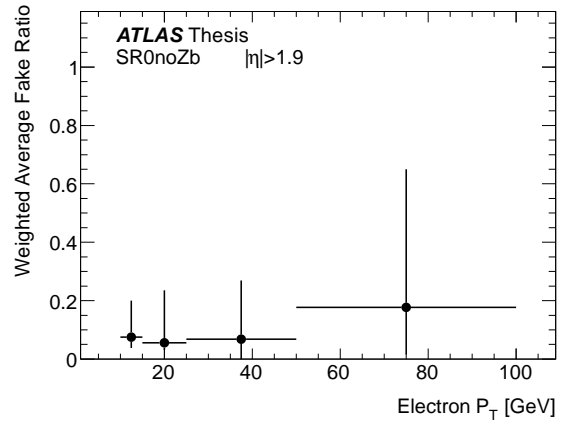
(b) Electron $|\eta| > 1.5$
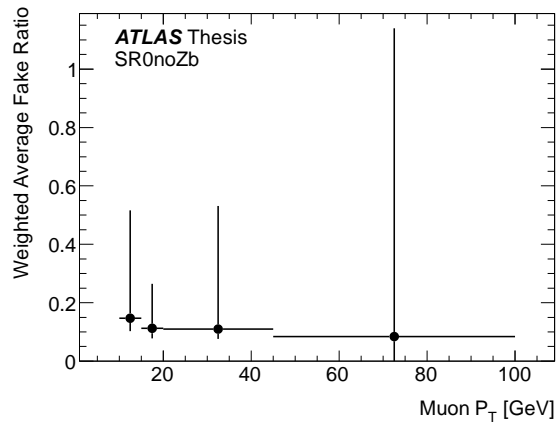
(c) Muon

Figure 7.9: Weighted average fake ratios for SR0noZb.
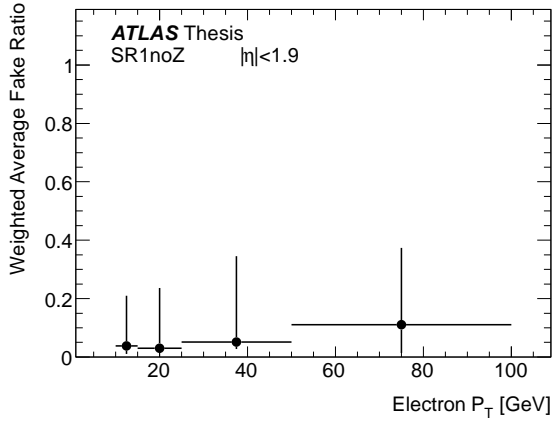
(a) Electron $|\eta| < 1.5$
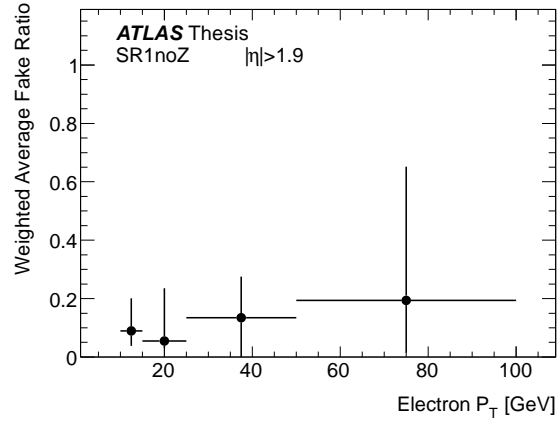
(b) Electron $|\eta| > 1.5$
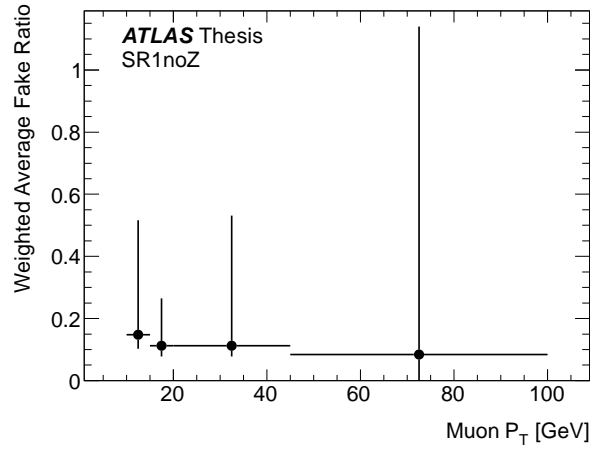
(c) Muon
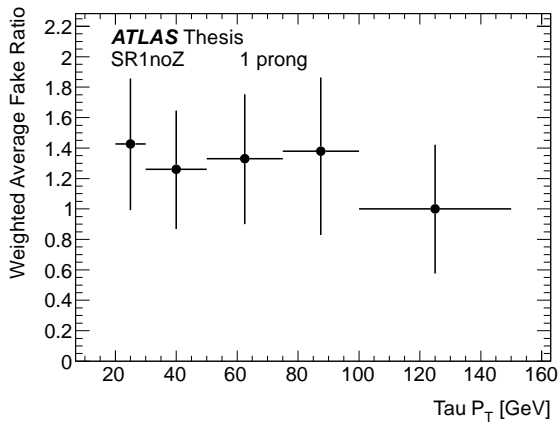
(d) Tau 1-prong
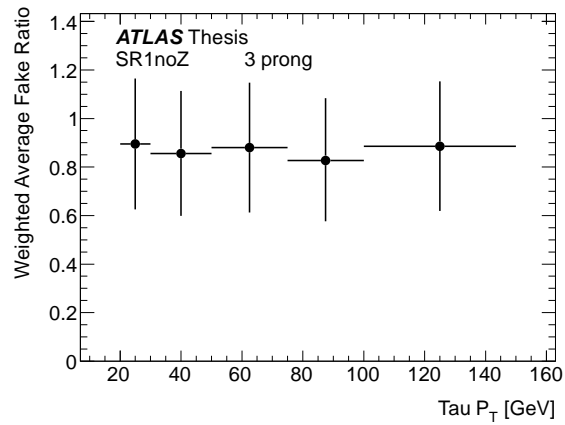
(e) Tau 3-prong

Figure 7.10: Weighted average fake ratios for SR1noZ.

7.5 Uncertainties

7.5.1 Uncertainties on the Monte Carlo Background

The systematics in this analysis are very similar to the ones in the three lepton analysis described in Section 6.6. The uncertainties which differ are listed below.

Luminosity The luminosity uncertainty for 2012 data is 3.6% [34]

MC Generator The uncertainty arising from the MC generator used to simulate the diboson background ZZ is found by comparing the acceptance (with respect to 4ℓ Z-veto events) of the signal region selections in the Sherpa and Powheg samples. For the $t\bar{t}+Z$ background, the Alpgen generator is compared to the Madgraph generator. The statistical uncertainty of the Powheg and Madgraph samples is also included.

7.5.2 Uncertainties on the Weighting Method Background

The systematic uncertainties on the weighting method fake lepton background estimate are classified into uncertainties on the baseline fake ratios, uncertainties on the scale factors, and uncertainties on the process fractions.

Baseline fake ratios A flat systematic relative uncertainty of 30% is applied to the fake ratios for the dependence on the $E_{\mathrm{T}}^{\mathrm{miss}}$.

Scale factors The uncertainties on the scale factors are as reported in Sections 7.4.2.

Process fractions Since the fractions are calculated in a selection with three or more leptons, a very conservative approach is taken to assign the fraction uncertainty. Each contribution is varied from 0–100% of the total.

A summary of the weighting method uncertainties is shown in Table 7.4.

Table 7.4: Summary of the uncertainties on the weighting method fake lepton background. The expected background is listed, followed by the relative statistical and systematic uncertainties in %. The fake-lepton background prediction can be negative due to negative terms in Eq. 7.1. In the limit setting, a negative value is truncated to zero.

	SR0noZa	SR0noZb	SR1noZ
Expected Events	-0.06	0.05	1.4
Statistics	± 231%	± 267%	± 87%
Fake ratios	±5%	±4%	± <0.5%
Fractions	1001% ,-83%	-633% ,46%	1% ,-1%
Scale factors	±11%	±6%	±3%
$E_{\mathrm{T}}^{\mathrm{miss}}$ dependence	46% ,-43%	±27%	±31%
Total Systematics	1003% ,-94%	-635% ,53%	31% ,-31%

7.5.3 Uncertainties Summary

A summary of the dominating systematics in each signal region can be seen in Table 7.5.

Table 7.5: Summary of the dominating uncertainties in the four-lepton signal regions. Uncertainty quoted is a % of the total expected background.

	SR0noZa		SR0noZb		SR1noZ	
Leading	Fake Ratio	38%	Cross Section	23%	MC Statistics	60%
Subleading	Generator	33%	Generator	22%	Fake Ratio	21%
	Cross Section	25%	Fake Ratio	20%	Cross Section	3%
	MC Statistics	16%	MC Statistics	16%	JER	2%

7.6 Background Model Validation

To validate the background model, the total background is estimated in two dedicated validation regions and the obtained results are compared to the observed data. The validation regions are defined in Table 7.6.

Table 7.6: The selection requirements for the four-lepton validation regions.

VR	$N(\ell)$	$N(\tau)$	SFOS pair	Z boson	E_T^{miss}	m_{eff}	dominant bkg.
VR0noZ	≥ 4	≥ 0	–	veto	<50	<400	Z^*Z^*
VR0Z	≥ 4	≥ 0	require	require	<50	-	ZZ
VR1noZ	$==3$	≥ 1	–	veto	<50	<400	Z^*Z^*, WZ, Z+jets
VR1Z	$==3$	≥ 1	require	require	<50	-	ZZ, WZ, Z+jets

The comparison of the expected yields with the observed data can be seen in Table 7.7. Some distributions for the noZ validation regions are shown in Figures 7.11 and 7.12. The background modeling describes the data sufficiently well, with CL_b values ranging from 0.10 to 0.54. The expected and observed distributions also agree sufficiently well.

Table 7.7: Expected and observed events in the validation regions. The systematic uncertainties are calculated as described in Section 7.5. The goodness-of-fit (CL_b) is also given.

| Sample	VR0noZ	VR1noZ	VR0Z	VR1Z
ZZ	7.2 ± 3.6	1.45 ± 0.30	167 ± 38	8.0 ± 1.2
ZWW	0.031 ± 0.031	0.027 ± 0.027	0.35 ± 0.35	0.10 ± 0.10
$t\bar{t}Z$	$0^{+0.05}_{-0}$	$0^{+0.10}_{-0}$	1.5 ± 0.7	0.18 ± 0.14
Higgs	0.17 ± 0.05	0.23 ± 0.05	4.5 ± 0.9	0.64 ± 0.16
MC Bkg.	7.4 ± 3.6	1.70 ± 0.34	173 ± 39	8.9 ± 1.4
Fake Bkg.	$0.3^{+0.7}_{-0.3}$	7.9 ± 3.6	$2.0^{+2.6}_{-2.0}$	28 ± 10
Total Bkg.	7.7 ± 3.4	9.6 ± 3.6	175 ± 37	37 ± 10
Data	3	10	201	31
CL_b	0.10	0.54	0.51	0.30
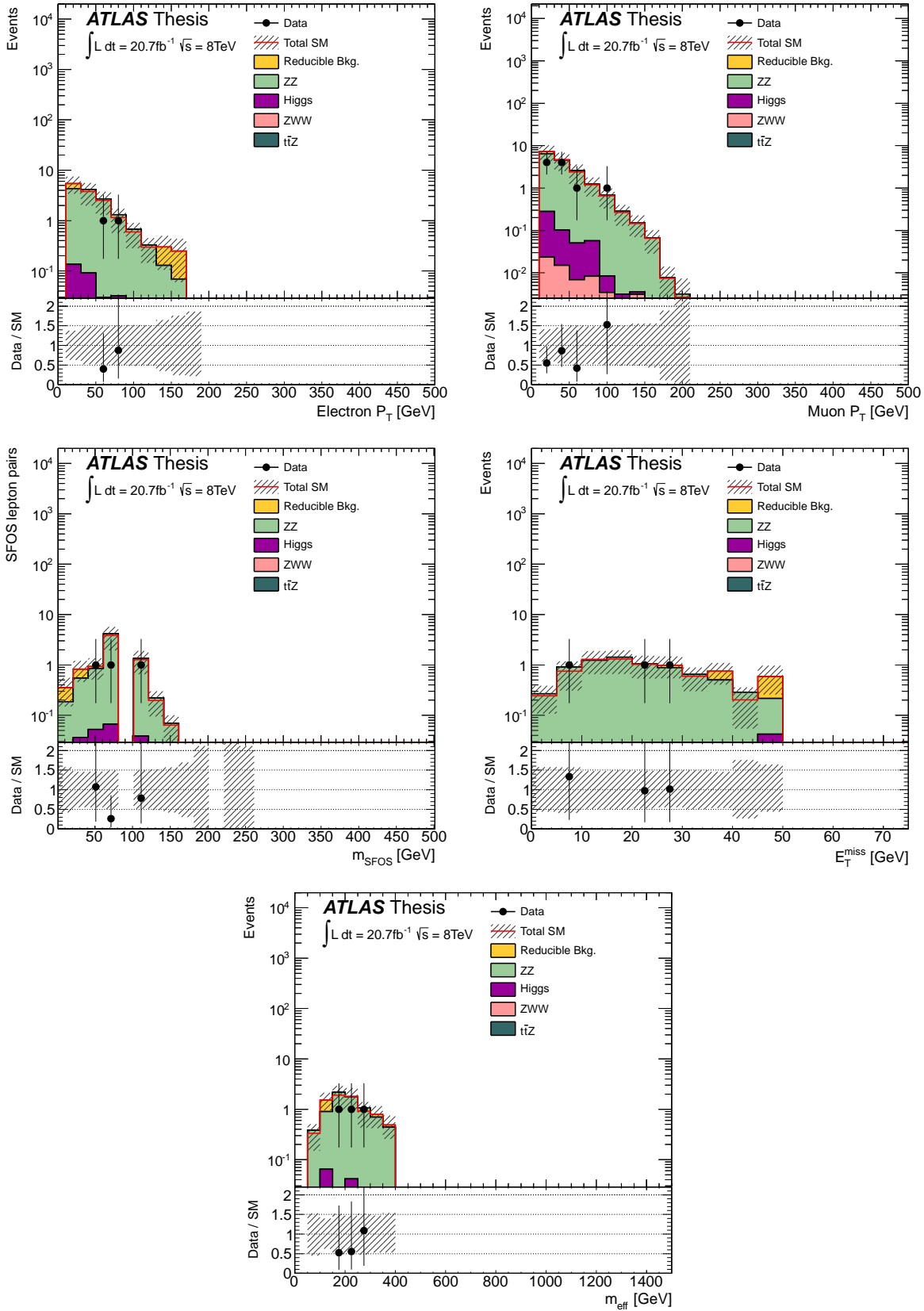
Figure 7.11: Kinematic distributions in VR0noZ. The uncertainties are statistical and systematic.
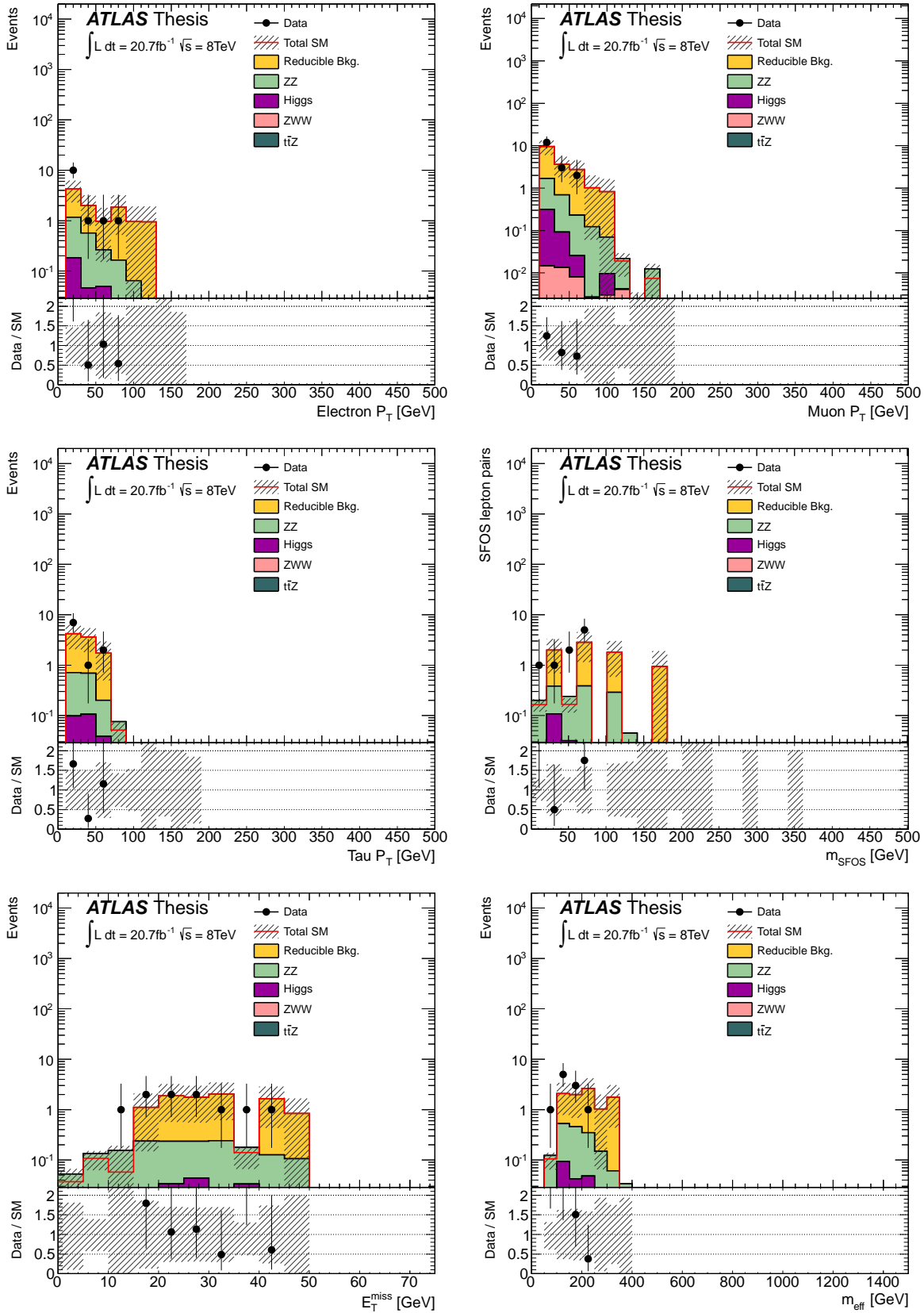
Figure 7.12: Kinematic distributions in VR1noZ. The uncertainties are statistical and systematic.

7.7 Results

7.7.1 Observations in Data

The background validation shown in Section 7.6 is sufficient to allow for unblinding of the signal regions. The observed data is shown in Table 7.8. The observed data agrees well with the expected SM background, so there is no evidence for SUSY. Kinematic distributions for the signal regions can be seen in Figure 7.13.

Table 7.8: Expected SM background events and observed number of events in data in the four-lepton signal regions. 4-prompt-lepton Bkg components are derived purely from MC; fake-lepton components have been computed with the weighting method. All Bkg contributions are normalized to 20.7 fb^{-1}. Uncertainties are statistical and systematic. The systematic uncertainties are calculated as described in Section 7.5.

Sample	SR0noZa	SR0noZb	SR1noZ
ZZ	0.6 ± 0.5	0.50 ± 0.26	0.19 ± 0.05
ZWW	0.12 ± 0.12	0.08 ± 0.08	0.05 ± 0.05
$t\bar{t}Z$	0.73 ± 0.34	0.75 ± 0.35	0.16 ± 0.12
Higgs	0.26 ± 0.07	0.22 ± 0.07	0.23 ± 0.06
MC 4-prompt Bkg.	1.7 ± 0.8	1.6 ± 0.6	0.62 ± 0.21
Fake Lepton Bkg.	$0^{+0.16}_{-0}$	$0.05^{+0.14}_{-0.05}$	1.4 ± 1.3
Total Bkg.	1.7 ± 0.8	1.6 ± 0.6	2.0 ± 1.3
Data	2	1	4
p_0-value	0.29	0.5	0.15

7.7.2 Statistical Interpretation

The compatibility with the Standard Model, limits on the visible cross-sections, and the model-dependent exclusions are assessed with log likelihood ratio tests just like the ones explained in Section 6.8.2.

The compatibility with the Standard Model was calculated in discovery mode and the exclusion contours in the exclusion mode.

Discovery mode: Signal contamination in the control regions is not considered. This leads to higher background estimate in the signal regions and is therefore conservative.

Exclusion mode: In addition to the present uncertainties we introduce a 100% systematic on the fake lepton background to cover for possible signal contamination in the control region.

Model Independent Interpretation

The background-only hypothesis is tested by comparing the total SM prediction to the observed data in all the signal regions and computing the discovery p-values. Upper limits at 95% confidence level on the number of signal events and corresponding visible cross section are also computed, where the visible cross section is defined as the cross section times branching ratio times acceptance times efficiency ($\sigma \times \mathrm{BR} \times \mathrm{A} \times \epsilon$) of new physics processes satisfying the signal region requirements. These results are shown in Table 7.9.

Model Dependent Interpretation

Since no excess was observed in the data, limits can be set on the RPV and RPC signal models from Section 7.2. The results for the RPV grids are shown in Figure 7.14. In the wino simplified models with $\lambda_{121} \neq 0$, chargino masses up to about 750 GeV are excluded. The exclusion weakens in the region where the $m_{\tilde{\chi}_1^0}$ is small. This is because the LSP is highly boosted, so the SFOS-invariant-mass and lepton separation requirements then reduce the selection efficiency for leptons from the LSP decay. The gluino grid has a much stronger exclusion, which is due to much higher cross sections. The limit on the gluino NLSP extends to a maximum of just over 1.4 TeV for the $\lambda_{121} \neq 0$ model. The grids enhanced in tau final

Table 7.9: The compatibility of the observed four-lepton results with the SM for all the signal regions. The expected and observed number of events are shown, along with the 95% CL upper limits on the number of signal events S, the limit on the visible cross-section σ_{vis}, and the CL_b values. Finally the discovery p_0-value of the background only hypothesis (p_0^{bkg}) and its significance in number of standard deviations are shown. Calculations are done with toys.

	SR0noZa	SR0noZb	SR1noZ
Expected Events	1.7 ± 0.8	1.6 ± 0.6	2.0 ± 1.3
Observed Events	2	1	4
p_0-value	0.29	0.5	0.15
N_{signal} excluded (exp)	3.9	3.6	5.3
N_{signal} excluded (obs)	4.7	3.7	7.5
σ_{visible} excluded (exp) [fb]	0.19	0.17	0.26
σ_{visible} excluded (obs) [fb]	0.23	0.18	0.36

states, with $\lambda_{133} \neq 0$, are both weaker. the limit extends up to about 400 GeV in chargino mass in the wino grid, and up to about 1 TeV in gluino mass in the gluino grid. The results for the RPC $\tilde{\chi}_2^0 \tilde{\chi}_3^0$ grids are shown in Figure 7.15. In both grids, the $m_{\tilde{\chi}_1^0}$ limit extends up to about 250 GeV and varies with the mass splittings on the y-axis.
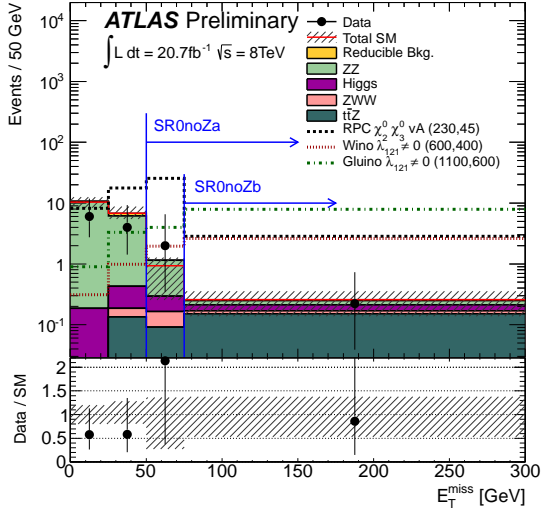
(a) $4\ell0\tau + Z$ veto
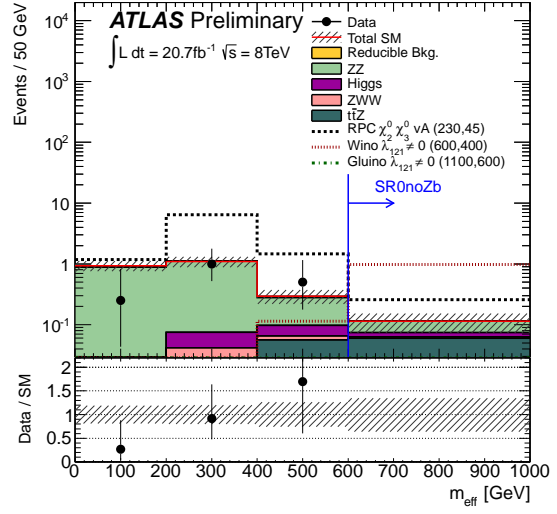
(b) $4\ell0\tau + Z$ veto
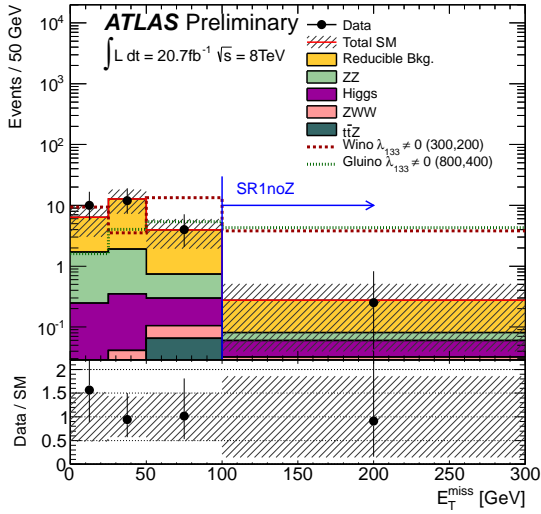
(c) $3\ell1\tau + Z$ veto
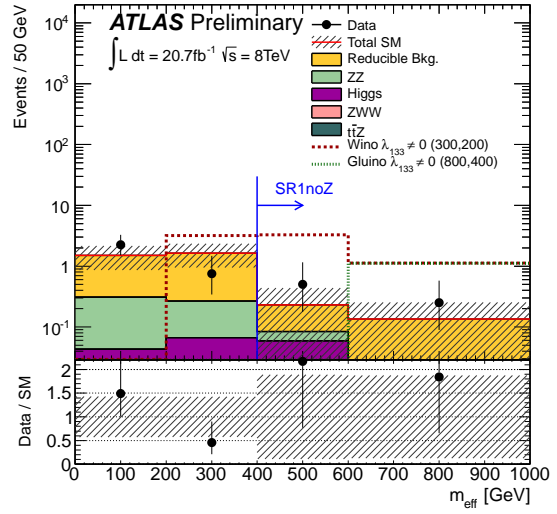
(d) $3\ell1\tau + Z$ veto

Figure 7.13: Distributions of the E_T^{miss} and m_{eff} in the four-lepton signal regions. The signal region cut values are shown on the plots. The uncertainty band includes both statistical and systematic uncertainties.
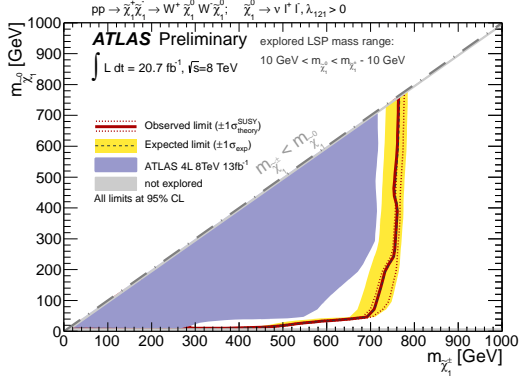
(a) Wino $\lambda_{121} \neq 0$
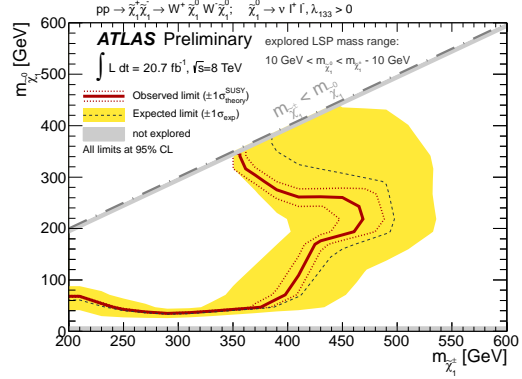
(b) Wino $\lambda_{133} \neq 0$
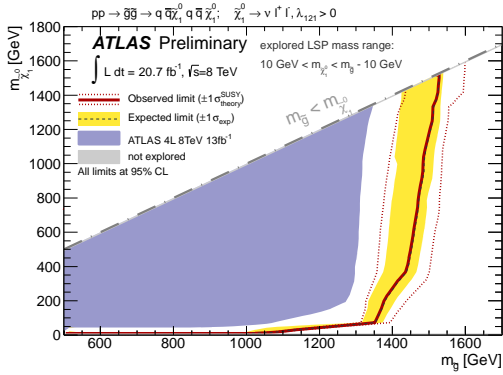
(c) Gluino $\lambda_{121} \neq 0$
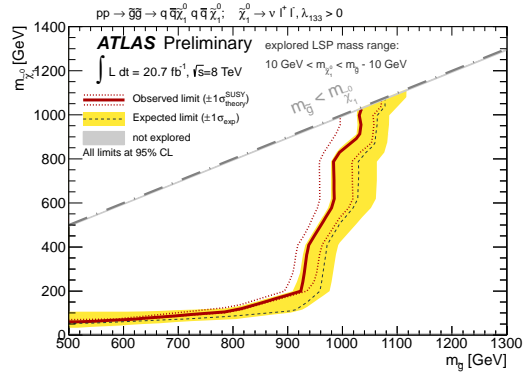
(d) Gluino $\lambda_{133} \neq 0$

Figure 7.14: Observed and expected 95% CL limit contours for the RPV simplified wino and gluino models with $\lambda_{121} \neq 0$ or $\lambda_{133} \neq 0$. The limits are calculated without signal cross-section uncertainty taken into account.

180
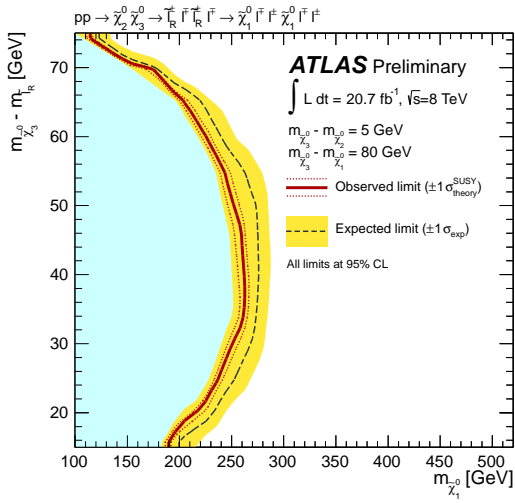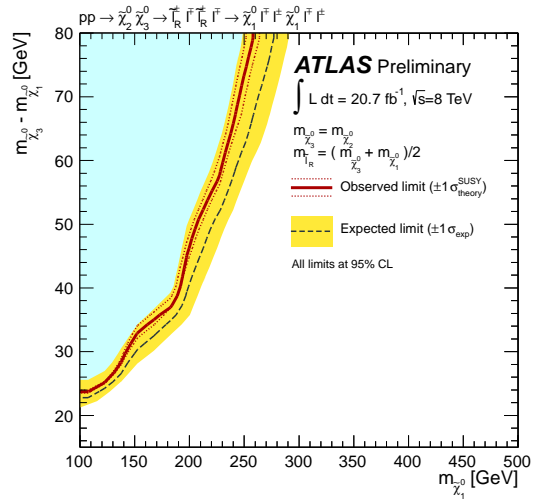
(a) RPC $\tilde{\chi}_2^0 \tilde{\chi}_3^0$ vA
(b) RPC $\tilde{\chi}_2^0 \tilde{\chi}_3^0$ vB

Figure 7.15: Observed and expected 95% CL limit contours for the RPC $\tilde{\chi}_2^0 \tilde{\chi}_3^0$ simplified models. The limits are calculated without signal cross-section uncertainty taken into account.

Chapter 8

Conclusion

Run 1 of data-taking at the LHC has come to an end, and the impacts made on the energy frontier of particle physics have been historic. A Higgs-like boson has been discovered in the ATLAS and CMS experiments [21, 22], possibly filling in the last remaining piece of the Standard Model of particle physics and validating the mechanism of electroweak symmetry breaking which is essential to the consistency of the theory. Many additional measurements have been made which validate the SM parameters and particle content in a whole new energy regime, further solidifying the Standard Model's role as the best description of particle physics at the electroweak scale. Consequently, stringent limits have been placed on beyond-Standard-Model physics models, far surpassing those set by the predecessor experiments at LEP and the Tevatron.

This thesis presented searches for supersymmetry in multilepton final states with the ATLAS detector using 8 TeV data collected in 2012. No evidence for supersymmetry was found and so limits were placed on simplified SUSY models and the pMSSM.

The three lepton analysis uses 20.3 fb^{-1} of data. Limits are placed on simplified models of $\tilde{\chi}_1^{\pm}\tilde{\chi}_2^0$ production and decay via sleptons, SM gauge bosons, and a Higgs boson. Limits

on degenerate $\tilde{\chi}_1^\pm$ and $\tilde{\chi}_2^0$ masses reach up to 720 GeV in the intermediate slepton model, 350 GeV in the intermediate WZ model, 380 GeV in the intermediate stau model, and 148 GeV in the Wh model. Limits are also set in slices of the pmssm parameter space rich in decays via either $\tilde{\ell}_R$, $\tilde{\tau}_R$, or SM bosons.

The four lepton analysis uses 20.7 fb^{-1} of data. Limits are placed on R-parity violating supersymmetry models in which the LSP decays to leptons. In addition, limits are placed on R-parity conserving models of $\tilde{\chi}_2^0 \tilde{\chi}_3^0$ production and decay via intermediate sleptons. In the R-parity violating models, NLSP masses are excluded up to 750 GeV when the NLSP is a $\tilde{\chi}_1^\pm$ and up to 1400 GeV when the NLSP is a $\tilde{g}$.

Bibliography

[1] K. Nakamura and Particle Data Group, "Review of particle physics," *J. Phys. G: Nucl. Part. Phys.* **37** (2010) 075021.

[2] A. H. Peter, "Dark Matter: A Brief Review," arXiv:1201.3942 [astro-ph.CO].

[3] C. Burgess and G. Moore, *The Standard Model, A Primer*. Cambridge University Press, 2007.

[4] F. Englert and R. Brout, "Broken symmetry and the mass of gauge vector mesons," *Phys. Rev. Lett.* **13** (Aug, 1964) 321–323.

[5] P. W. Higgs, "Broken symmetries and the masses of gauge bosons," *Phys. Rev. Lett.* **13** (Oct, 1964) 508–509.

[6] G. S. Guralnik, C. R. Hagen, and T. W. B. Kibble, "Global conservation laws and massless particles," *Phys. Rev. Lett.* **13** (Nov, 1964) 585–587.

[7] **SNO** Collaboration, "Measurement of the Rate of $\nu_e + d \to p + p + e^-$ Interactions Produced by ^8B Solar Neutrinos at the Sudbury Neutrino Observatory," *Phys. Rev. Lett.* **87** (Jul, 2001) 071301.

[8] F. Zwicky, "On the Masses of Nebulae and of Clusters of Nebulae," *Astrophys.J.* **86** (1937) 217–246.

[9] V. Rubin, N. Thonnard, and J. Ford, W.K., "Rotational properties of 21 SC galaxies with a large range of luminosities and radii, from NGC 4605 /R = 4kpc/ to UGC 2885 /R = 122 kpc/," *Astrophys.J.* **238** (1980) 471.

[10] D. Clowe, M. Bradac, A. H. Gonzalez, M. Markevitch, S. W. Randall, *et al.*, "A direct empirical proof of the existence of dark matter," *Astrophys.J.* **648** (2006) L109–L113, arXiv:astro-ph/0608407 [astro-ph].

[11] M. Kamionkowski, "WIMP and axion dark matter," arXiv:hep-ph/9710467 [hep-ph].

[12] P. Peebles and B. Ratra, "The Cosmological constant and dark energy," *Rev.Mod.Phys.* **75** (2003) 559–606, arXiv:astro-ph/0207347 [astro-ph].

[13] S. P. Martin, "A Supersymmetry primer," arXiv:hep-ph/9709356 [hep-ph].

[14] I. J. Aitchison, "Supersymmetry and the MSSM: An Elementary introduction," arXiv:hep-ph/0505105 [hep-ph].

[15] D. Volkov and V. Soroka, "Higgs Effect for Goldstone Particles with Spin 1/2," *JETP Lett.* **18** (1973) 312–314.

[16] D. Volkov and V. Soroka, "Gauge fields for symmetry group with spinor parameters," *Theor.Math.Phys.* **20** (1974) 829.

[17] D. Z. Freedman, P. van Nieuwenhuizen, and S. Ferrara, "Progress Toward a Theory of Supergravity," *Phys.Rev.* **D13** (1976) 3214–3218.

[18] M. Duff, "Erice lectures on 'The Status of local supersymmetry'," arXiv:hep-th/0403160 [hep-th].

[19] P. Fayet, "Supersymmetry and Weak, Electromagnetic and Strong Interactions," *Phys. Lett.* **B 64** (1976) 159.

[20] F. Riva, C. Biggio, and A. Pomarol, "Is the 125 GeV Higgs the superpartner of a neutrino?," *JHEP* **1302** (2013) 081, arXiv:1211.4526 [hep-ph].

[21] **ATLAS** Collaboration, "Observation of a new particle in the search for the Standard Model Higgs boson with the ATLAS detector at the LHC," *Phys.Lett.* **B716** (2012) 1–29, arXiv:1207.7214 [hep-ex].

[22] **CMS** Collaboration, "Observation of a new boson at a mass of 125 GeV with the CMS experiment at the LHC," *Phys.Lett.* **B716** (2012) 30–61, arXiv:1207.7235 [hep-ex].

[23] Y. Shadmi, "Supersymmetry breaking," arXiv:hep-th/0601076 [hep-th].

[24] G. Jungman, M. Kamionkowski, and K. Griest, "Supersymmetric dark matter," *Phys.Rept.* **267** (1996) 195–373, arXiv:hep-ph/9506380 [hep-ph].

[25] R. Barbieri and G. F. Giudice, "Upper bounds on supersymmetric particle masses," *Nucl. Phys. B* **306** no. CERN-TH-4825-87, (Aug, 1987) 63–76. 19 p.

[26] M. Papucci, J. T. Ruderman, and A. Weiler, "Natural SUSY Endures," *JHEP* **1209** (2012) 035, arXiv:1110.6926 [hep-ph].

[27] L. J. Hall, D. Pinner, and J. T. Ruderman, "A Natural SUSY Higgs Near 126 GeV," *JHEP* **1204** (2012) 131, arXiv:1112.2703 [hep-ph].

[28] U. Ellwanger, C. Hugonie, and A. M. Teixeira, "The Next-to-Minimal Supersymmetric Standard Model," *Phys.Rept.* **496** (2010) 1–77, arXiv:0910.1785 [hep-ph].

[29] L. Evans and P. Bryant, "LHC Machine," *JINST* **3** (2008) S08001.

[30] J. Haffner, "The CERN accelerator complex," Oct, 2013. http://cds.cern.ch/record/1621894. General Photo.

[31] M. Benedikt, R. Cappi, M. Chanel, R. Garoby, M. Giovannozzi, S. Hancock, M. Martini, E. Mtral, G. Mtral, K. Schindl, and J. L. Vallet, "Performance of the LHC Pre-Injectors,". https://cds.cern.ch/record/494746.

[32] **ATLAS** Collaboration, "Expected Performance of the ATLAS Experiment - Detector, Trigger and Physics," arXiv:0901.0512 [hep-ex].

[33] **ATLAS** Collaboration, "The atlas experiment at the cern large hadron collider," *JINST* **3** (2008) S08003.

[34] **ATLAS** Collaboration, "Improved luminosity determination in pp collisions at $\sqrt{s} = 7$ TeV using the ATLAS detector at the LHC," *Eur.Phys.J.* **C73** (2013) 2518, arXiv:1302.4393 [hep-ex].

[35] **ATLAS** Collaboration, "Electron performance measurements with the ATLAS detector using the 2010 LHC proton-proton collision data," *Eur. Phys. J.* **C 72** (2012) 1909, arXiv:1110.3174 [hep-ex].

[36] **ATLAS** Collaboration, "Electron efficiency measurements for 2012 and 2011 data." https://atlas.web.cern.ch/Atlas/GROUPS/PHYSICS/EGAMMA/PublicPlots/20130926/ATL-COM-PHYS-2013-1287/index.html.

[37] **ATLAS** Collaboration, "Preliminary results on the muon reconstruction efficiency, momentum resolution, and momentum scale in ATLAS 2012 pp collision data," ATLAS-CONF-2013-088, CERN, Geneva, Aug, 2013. https://cds.cern.ch/record/1580207.

[38] W. Lampl, S. Laplace, D. Lelas, P. Loch, H. Ma, S. Menke, S. Rajagopalan, D. Rousseau, S. Snyder, and G. Unal, "Calorimeter Clustering Algorithms: Description and Performance," ATL-LARG-PUB-2008-002. ATL-COM-LARG-2008-003, CERN, Geneva, Apr, 2008. http://cdsweb.cern.ch/record/1099735.

[39] M. Cacciari, G. P. Salam, and G. Soyez, "The Anti-k(t) jet clustering algorithm," *JHEP* **0804** (2008) 063, arXiv:0802.1189 [hep-ph].

[40] **ATLAS** Collaboration, "Jet energy scale and its systematic uncertainty in proton-proton collisions at sqrt(s)=7 TeV with ATLAS 2011 data," ATLAS-CONF-2013-004, CERN, Geneva, Jan, 2013. https://cds.cern.ch/record/1509552.

[41] **ATLAS** Collaboration, "Pile-up corrections for jets from proton-proton collisions at $\sqrt{s} = 7$ TeV in ATLAS in 2011," ATLAS-CONF-2012-064, CERN, Geneva, Jul, 2012. http://cds.cern.ch/record/1459529.

[42] **ATLAS** Collaboration, "Commissioning of the ATLAS high-performance b-tagging algorithms in the 7 TeV collision data," ATLAS-CONF-2011-102, CERN, Geneva, Jul, 2011. http://cdsweb.cern.ch/record/1369219.

[43] **ATLAS** Collaboration, "Identification of the Hadronic Decays of Tau Leptons in 2012 Data with the ATLAS Detector," ATLAS-CONF-2013-064, CERN, Geneva, Jul, 2013. http://cds.cern.ch/record/1562839.

[44] **ATLAS** Collaboration, "Determination of the tau energy scale and the associated systematic uncertainty in proton-proton collisions at $\sqrt{s} = 8$ TeV with the ATLAS detector at the LHC in 2012," ATLAS-CONF-2013-044, CERN, Geneva, Apr, 2013. http://cds.cern.ch/record/1544036.

[45] **ATLAS** Collaboration, "Performance of Missing Transverse Momentum Reconstruction in Proton-Proton Collisions at 7 TeV with ATLAS," *Eur. Phys. J.* **C 72** (2012) 1844, arXiv:1108.5602 [hep-ex].

[46] **ATLAS** Collaboration, "Performance of Missing Transverse Momentum Reconstruction in ATLAS studied in Proton-Proton Collisions recorded in 2012 at 8 TeV," ATLAS-CONF-2013-082, CERN, Geneva, Aug, 2013. http://cds.cern.ch/record/1570993.

[47] T. Golling, H. S. Hayward, P. U. E. Onyisi, H. J. Stelzer, and P. Waller, "The ATLAS data quality defect database system," *European Physical Journal C* **72** (Apr., 2012) 1960, arXiv:1110.6119 [physics.ins-det].

[48] **ATLAS** Collaboration, "Search for direct production of charginos and neutralinos in events with three leptons and missing transverse momentum in $21\,\mathrm{fb}^{-1}$ of pp collisions at $\sqrt{s} = 8\,\mathrm{TeV}$ with the ATLAS detector," ATLAS-CONF-2013-035, CERN, Geneva, Mar, 2013. http://cdsweb.cern.ch/record/1532426.

[49] **ATLAS** Collaboration, "Search for direct production of charginos and neutralinos in events with three leptons and missing transverse momentum in 13.0 fb-1 of pp collisions at sqrt(s)=8 TeV with the ATLAS detector," ATLAS-CONF-2012-154, CERN, Geneva, Nov, 2012. http://cdsweb.cern.ch/record/1493493.

[50] **ATLAS** Collaboration, "Search for direct production of charginos and neutralinos in events with three leptons and missing transverse momentum in $\sqrt{s} = 7$ TeV pp collisions with the ATLAS detector," *Phys.Lett.* **B718** (2013) 841–859, arXiv:1208.3144 [hep-ex].

[51] **ATLAS** Collaboration, "Search for supersymmetry in events with three leptons and missing transverse momentum in $\sqrt{s} = 7$ TeV pp collisions with the ATLAS detector," *Phys.Rev.Lett.* **108** (2012) 261804, arXiv:1204.5638 [hep-ex].

[52] **ATLAS** Collaboration, "Search for chargino and neutralino production in final states with one lepton, two b-jets consistent with a Higgs boson, and missing transverse momentum with the ATLAS detector in 20.3 fb^{-1} of $\sqrt{s} = 8$ TeV pp collisions," ATLAS-CONF-2013-093, CERN, Geneva, Aug, 2013. http://cdsweb.cern.ch/record/1595756.

187

[53] **ATLAS** Collaboration, "Search for direct-slepton and direct-chargino production in final states with two opposite-sign leptons, missing transverse momentum and no jets in 20/fb of pp collisions at sqrt(s) = 8 TeV with the ATLAS detector," ATLAS-CONF-2013-049, CERN, Geneva, May, 2013. https://cds.cern.ch/record/1547565.

[54] **ATLAS** Collaboration, "Search for supersymmetry in events with four or more leptons in $21\,\mathrm{fb}^{-1}$ of pp collisions at $\sqrt{s} = 8\,\mathrm{TeV}$ with the ATLAS detector," ATLAS-CONF-2013-036, CERN, Geneva, Mar, 2013. https://cds.cern.ch/record/1532429.

[55] **ATLAS** Collaboration, "Search for electroweak production of supersymmetric particles in final states with at least two hadronically decaying taus and missing transverse momentum with the ATLAS detector in proton-proton collisions at $\sqrt{s} = 8$ TeV," ATLAS-CONF-2013-028, CERN, Geneva, Mar, 2013. http://cdsweb.cern.ch/record/1525889.

[56] W. Beenakker, R. Hopker, and M. Spira, "PROSPINO: A Program for the production of supersymmetric particles in next-to-leading order QCD," arXiv:hep-ph/9611232 [hep-ph].

[57] J. Alwall *et al.*, "Simplified Models for a First Characterization of New Physics at the LHC," *Phys. Rev.* **D 79** (2009) 075020, arXiv:0810.3921 [hep-ph].

[58] S. Dube, J. Glatzer, S. Somalwar, A. Sood, and S. Thomas, "Addressing the Multi-Channel Inverse Problem at High Energy Colliders: A Model Independent Approach to the Search for New Physics with Trileptons," *J.Phys.* **G39** (2012) 085004, arXiv:0808.1605 [hep-ph].

[59] A. Djouadi *et al.*, "SuSpect: A Fortran code for the supersymmetric and Higgs particle spectrum in the MSSM," *Comput. Phys. Commun.* **176** (2007) 426–455, arXiv:hep-ph/0211331 [hep-ph].

[60] **ATLAS** Collaboration, "ATLAS tunes of PYTHIA 6 and Pythia 8 for MC11," ATL-PHYS-PUB-2011-009, CERN, Geneva, Jul, 2011. http://cdsweb.cern.ch/record/1363300.

[61] J. Alwall, P. Demin, S. de Visscher, R. Frederix, M. Herquet, *et al.*, "MadGraph/MadEvent v4: The New Web Generation," *JHEP* **0709** (2007) 028, arXiv:0706.2334 [hep-ph].

[62] P. Nason, "A New method for combining NLO QCD with shower Monte Carlo algorithms," *JHEP* **0411** (2004) 040, arXiv:hep-ph/0409146.

[63] M. L. Mangano, M. Moretti, F. Piccinini, R. Pittau, and A. D. Polosa, "ALPGEN, a generator for hard multiparton processes in hadronic collisions," *JHEP* **0307** (2003) 001, arXiv:hep-ph/0206293 [hep-ph].

[64] T. Sjostrand, S. Mrenna, and P. Z. Skands, "PYTHIA 6.4 Physics and Manual," *JHEP* **0605** (2006) 026, `arXiv:hep-ph/0603175 [hep-ph]`.

[65] S. Frixione and B. R. Webber, "The MC@NLO 3.2 event generator," `arXiv:hep-ph/0601192`.

[66] G. Corcella, I. Knowles, G. Marchesini, S. Moretti, K. Odagiri, *et al.*, "HERWIG 6: An Event generator for hadron emission reactions with interfering gluons (including supersymmetric processes)," *JHEP* **0101** (2001) 010, `arXiv:hep-ph/0011363 [hep-ph]`.

[67] J. Butterworth, J. R. Forshaw, and M. Seymour, "Multiparton interactions in photoproduction at HERA," *Z.Phys.* **C72** (1996) 637–646, `arXiv:hep-ph/9601371 [hep-ph]`.

[68] H.-L. Lai *et al.*, "New parton distributions for collider physics," *Phys. Rev.* **D 82** (2010) 074024, `arXiv:1007.2241 [hep-ph]`.

[69] M. Aliev, H. Lacker, U. Langenfeld, S. Moch, P. Uwer, *et al.*, "HATHOR: HAdronic Top and Heavy quarks crOss section calculatoR," *Comput. Phys. Commun.* **182** (2011) 1034–1046, `arXiv:1007.1327 [hep-ph]`.

[70] S. Dittmaier *et al.*, "Handbook of LHC Higgs Cross Sections: 2. Differential Distributions," `arXiv:1201.3084 [hep-ph]`.

[71] M. Bahr, S. Gieseke, M. Gigg, D. Grellscheid, K. Hamilton, *et al.*, "Herwig++ Physics and Manual," *Eur. Phys. J.* **C 58** (2008) 639–707, `arXiv:0803.0883 [hep-ph]`.

[72] "Asymptotic formulae for likelihood-based tests of new physics," *Eur. Phys. J.* **C71** (2011) 1554, `arXiv:1007.1727 [physics.data-an]`.

[73] C. Lester and D. Summers, "Measuring masses of semiinvisibly decaying particles pair produced at hadron colliders," *Phys.Lett.* **B463** (1999) 99–103, `arXiv:hep-ph/9906349 [hep-ph]`.

[74] A. Barr, C. Lester, and P. Stephens, "m(T2): The Truth behind the glamour," *J.Phys.* **G29** (2003) 2343–2363, `arXiv:hep-ph/0304226 [hep-ph]`.

[75] **ATLAS** Collaboration, "Measurement of the Z to tau tau Cross Section with the ATLAS Detector," *Phys.Rev.* **D84** (2011) 112006, `arXiv:1108.2016 [hep-ex]`.

[76] J. M. Campbell and R. K. Ellis, "$t\bar{t}W^{+-}$ production and decay at NLO," *JHEP* **1207** (2012) 052, `arXiv:1204.5678 [hep-ph]`.

[77] A. Kardos, Z. Trocsanyi, and C. Papadopoulos, "Top quark pair production in association with a Z-boson at NLO accuracy," *Phys. Rev.* **D 85** (2012) 054015, `arXiv:1111.0610 [hep-ph]`.

[78] **ATLAS** Collaboration, "A Measurement of WZ Production in Proton-Proton Collisions at sqrt(s)=8TeV with the ATLAS Detector," ATLAS-CONF-2013-021, CERN, Geneva, Mar, 2013. http://cdsweb.cern.ch/record/1525557.

[79] **ATLAS** Collaboration, "Measurement of the total ZZ production cross section in proton-proton collisions at $\sqrt{s} = 8$ TeV in 20 fb^{-1} with the ATLAS detector," ATLAS-CONF-2013-020, CERN, Geneva, Mar, 2013. http://cdsweb.cern.ch/record/1525555.

[80] A. L. Read, "Presentation of search results: The CL(s) technique," *J.Phys.* **G28** (2002) 2693–2704.

[81] I. Vivarelli, "Searches for natural supersymmetry with the atlas detector," Mar, 2013. http://indico.cern.ch/conferenceDisplay.py?confId=240895.

Appendices

A   The Matrix Method Fake Lepton Background Estimate

In this appendix I will work out some of the mathematical details of the matrix method estimate used in Chapter 6. I will start with the simplest case of a one-lepton selection, then show how the method expands to channels with two or three leptons. Much of the discussion is also relevant to the weighting method used in Chapter 7, which is a simplified case of the matrix method.

The purpose of the matrix method is to estimate the contribution (event yield and kinematic shapes) from events with *fake* leptons. Sources of fake leptons include

- misreconstructed jets or photons,

- non-prompt, non-isolated leptons from light flavor quark decays in jets,

- non-prompt, non-isolated leptons from heavy flavor quark decays in jets, and

- non-prompt leptons from radiated photon conversion.

In contrast, *real* leptons come from leptonic decays of $Z/\gamma*$ and W bosons that originate from

the hard process of the particle interaction. They are generally prompt and well-isolated. Thus, properties such as lepton isolation and impact parameters are good discriminators between the two classes of objects. By exploiting the characteristic differences between real and fake leptons one can define a linear system of equations (a matrix equation) which can be solved to yield the desired fake lepton contribution.

It is necessary to first define two selection criteria for the leptons, a *tight* selection (T) and a *loose* selection (L). Different flavors of leptons will generally have different sets of criteria, but it is important that variables used to define the selection be strong discriminators between real and fake objects. In other words, the loose selection should have a much higher purity of fake leptons than the tight selection. A common choice is to use the standard analysis object selection criteria as the tight selection and to loosen variables like isolation and impact parameters for the loose selection.

A.1 The One-Lepton Case

We start with the simplest case: a one-lepton matrix method. We are interested in estimating the number of events with one tight fake lepton, N_T^{fake}. At the loose selection level, the total number of events is given by $N_R + N_F$, where N_R and N_F are the number of events with one real and one fake lepton, respectively. Let ϵ be the probability of a real lepton to pass the tight selection, and f be the probability of a fake lepton to pass the tight selection. Then, the number of events with a tight lepton is given by $N_T = \epsilon N_R + f N_F$. We will also define the corresponding probabilities for these objects to fail the tight selection: $\bar{\epsilon} = 1 - \epsilon$ and $\bar{f} = 1 - f$. Then, the number of events with a loose (not tight) lepton is given by

$N_L = \bar{\epsilon} N_R + \bar{f} N_F$. These two relations define the 2×2 matrix method:

$$\begin{pmatrix} N_T \\ N_L \end{pmatrix} = \begin{pmatrix} \epsilon & f \\ \bar{\epsilon} & \bar{f} \end{pmatrix} \begin{pmatrix} N_R \\ N_F \end{pmatrix}. \tag{A.1}$$

Assuming we can measure the N_T and N_L directly from data, then we can invert the matrix to solve for the RHS:

$$\begin{pmatrix} N_R \\ N_F \end{pmatrix} = \alpha \begin{pmatrix} \bar{f} & -f \\ -\bar{\epsilon} & \epsilon \end{pmatrix} \begin{pmatrix} N_T \\ N_L \end{pmatrix}, \tag{A.2}$$

where the factor $\alpha = (\epsilon - f)^{-1}$ comes from the determinant of the matrix.

There is one more step required to finish the method. The number of events with a fake lepton must be extrapolated to the tight selection:

$$N_T^{fake} = f N_F = \alpha f (\epsilon N_L - \bar{\epsilon} N_T) \tag{A.3}$$

It is important to note now that if $\epsilon = f$, then the determinant of the matrix is zero; i.e., the matrix is singular and the inverse is undefined. Even if $\epsilon \sim f$, the method will be unstable and the estimate somewhat useless due to wild fluctuations. It is thus essential to define the loose and tight criteria to achieve good separation between these quantities.

A.2   The Two-Lepton Case

For a two-lepton selection, the discussion is the same but the size of the matrix grows to 4×4. The matrix equation is

$$
\begin{pmatrix} N_{TT} \\ N_{TL} \\ N_{LT} \\ N_{LL} \end{pmatrix} = \begin{pmatrix} \epsilon_1 \epsilon_2 & \epsilon_1 f_2 & f_1 \epsilon_2 & f_1 f_2 \\ \epsilon_1 \bar{\epsilon}_2 & \epsilon_1 \bar{f}_2 & f_1 \bar{\epsilon}_2 & f_1 \bar{f}_2 \\ \bar{\epsilon}_1 \epsilon_2 & \bar{\epsilon}_1 f_2 & \bar{f}_1 \epsilon_2 & \bar{f}_1 f_2 \\ \bar{\epsilon}_1 \bar{\epsilon}_2 & \bar{\epsilon}_1 \bar{f}_2 & \bar{f}_1 \bar{\epsilon}_2 & \bar{f}_1 \bar{f}_2 \end{pmatrix} \begin{pmatrix} N_{RR} \\ N_{RF} \\ N_{FR} \\ N_{FF} \end{pmatrix}, \tag{A.4}
$$

where the first and second subscripts refer to the leading and sub-leading leptons, respectively, and the indices on ϵ and f follow the same ordering. As before, we invert the matrix to solve the equation for the RHS, and extrapolate the terms to the tight selection to get the full fake estimate:

$$
\begin{aligned}
N_{TT}^{fake} &= \epsilon_1 f_2 N_{RF} + f_1 \epsilon_2 N_{FR} + f_1 f_2 N_{FF} \\
&= \alpha_1 \alpha_2 (C_{TT} N_{TT} + C_{TL} N_{TL} + C_{LT} N_{LT} + C_{LL} N_{LL}),
\end{aligned} \tag{A.5}
$$

where

$$
C_{TT} = f_1 f_2 - \epsilon_1 \bar{\epsilon}_2 f_2 - \epsilon_2 \bar{\epsilon}_1 f_1 - \epsilon_1 \epsilon_2 f_1 f_2 \tag{A.6}
$$

$$
C_{TL} = \epsilon_1 \epsilon_2 \bar{f}_1 f_2 \tag{A.7}
$$

$$
C_{LT} = \epsilon_1 \epsilon_2 f_1 \bar{f}_2 \tag{A.8}
$$

$$
C_{LL} = -\epsilon_1 \epsilon_2 f_1 f_2. \tag{A.9}
$$

In practice, the MM efficiencies ϵ_i and f_i are functions of multiple variables, so the implementation of the method usually involves applying Equation A.5 on per-event basis, such that only one of the terms in the solution is nonzero and the event receives a weight corresponding

to its selection category (TT, TL, etc.). It is thus interesting to look at the behavior of the event weight for each category. In equation A.5, it is clear that TL and LT events always receive a *positive* event weight, while LL events always receive a *negative* event weight. The TT events also always receive a negative weight, which can be shown quite easily:

$$C_{TT} = f_1 f_2 - \epsilon_1 \bar{\epsilon}_2 f_2 - \epsilon_2 \bar{\epsilon}_1 f_1 - \epsilon_1 \epsilon_2 f_1 f_2 \tag{A.10}$$

$$< f_1 f_2 - \epsilon_1 \bar{\epsilon}_2 f_2 \tag{A.11}$$

$$< f_1 f_2 - \epsilon_1 f_2 \tag{A.12}$$

$$< f_1 f_2 - f_1 f_2 \tag{A.13}$$

$$< 0, \tag{A.14}$$

assuming $0 < f_i < \epsilon_i < 1$.

A.3   The Three-Lepton Case

The algebra of the three-lepton case gets considerably messier. Now the matrix is 8×8:

$$\begin{pmatrix} N_{TTT} \\ N_{TTL} \\ \vdots \\ N_{LLL} \end{pmatrix} = \begin{pmatrix} \epsilon_1 \epsilon_2 \epsilon_3 & \epsilon_1 \epsilon_2 f_3 & \cdots & f_1 f_2 f_3 \\ \epsilon_1 \epsilon_2 \bar{\epsilon}_3 & \epsilon_1 \epsilon_2 \bar{f}_3 & \cdots & f_1 f_2 \bar{f}_3 \\ \vdots & \vdots & \ddots & \vdots \\ \bar{\epsilon}_1 \bar{\epsilon}_2 \bar{\epsilon}_3 & \bar{\epsilon}_1 \bar{\epsilon}_2 \bar{f}_3 & \cdots & \bar{f}_1 \bar{f}_2 \bar{f}_3 \end{pmatrix} \begin{pmatrix} N_{RRR} \\ N_{RRF} \\ \vdots \\ N_{FFF} \end{pmatrix}. \tag{A.15}$$

The solution is:

$$N_{TTT}^{fake} = \epsilon_1\epsilon_2 f_3 N_{RRF} + \epsilon_1 f_2 \epsilon_3 N_{RFR} + \epsilon_1 f_2 f_3 N_{RFF} + f_1 \epsilon_2 \epsilon_3 N_{FRR}$$

$$+ f_1 \epsilon_2 f_3 N_{FRF} + f_1 f_2 \epsilon_3 N_{FFR} + f_1 f_2 f_3 N_{FFF}$$

$$= \alpha_1 \alpha_2 \alpha_3 \left(C_{TTT} N_{TTT} + C_{TTL} N_{TTL} + C_{TLT} N_{TLT} + C_{TLL} N_{TLL} \right.$$

$$\left. + C_{LTT} N_{LTT} + C_{LTL} N_{LTL} + C_{LLT} N_{LLT} + C_{LLL} N_{LLL} \right) \tag{A.16}$$

where

$$C_{TTT} = f_1 f_2 f_3 + \frac{1}{\alpha_1} f_2 \epsilon_3 + \frac{1}{\alpha_2} f_3 \epsilon_1 + \frac{1}{\alpha_3} f_1 \epsilon_2 + \epsilon_1 \epsilon_2 \epsilon_3 (1 - \bar{f}_1 \bar{f}_2 \bar{f}_3) \tag{A.17}$$

$$C_{TTL} = -\bar{f}_1 \bar{f}_2 f_3 \epsilon_1 \epsilon_2 \epsilon_3 \tag{A.18}$$

$$C_{TLT} = -\bar{f}_1 f_2 \bar{f}_3 \epsilon_1 \epsilon_2 \epsilon_3 \tag{A.19}$$

$$C_{TLL} = -\bar{f}_1 f_2 f_3 \epsilon_1 \epsilon_2 \epsilon_3 \tag{A.20}$$

$$C_{LTT} = -f_1 \bar{f}_2 \bar{f}_3 \epsilon_1 \epsilon_2 \epsilon_3 \tag{A.21}$$

$$C_{LTL} = -f_1 \bar{f}_2 f_3 \epsilon_1 \epsilon_2 \epsilon_3 \tag{A.22}$$

$$C_{LLT} = -f_1 f_2 \bar{f}_3 \epsilon_1 \epsilon_2 \epsilon_3 \tag{A.23}$$

$$C_{LLL} = f_1 f_2 f_3 \epsilon_1 \epsilon_2 \epsilon_3 \tag{A.24}$$

$$\tag{A.25}$$

A.4   Combinatorics

It is sometimes necessary to acquire the fake lepton estimate for events that are exclusive in the number of tight leptons but allow for additional loose leptons. For example, a one-lepton selection may need, in addition to the fake estimate N_T^{fake}, the estimate for $N_{T,L}^{\text{fake}} + N_{T,LL}^{\text{fake}} + N_{T,LLL}^{\text{fake}} + \ldots$, where I've used commas in the indices to indicate that they are unordered, and it assumed for now that these represent the contributions where the *tight* lepton is fake

and the additional loose leptons can be either real or fake. These problems are solved by a combinatorial loop over loose leptons. I will derive the results for the simple cases.

We first consider the simplest case of a one-tight-lepton selection which allows for additional loose leptons but is blind to the real and fake content of the additional leptons. The estimate for $N_{T,L}^{\text{fake}} = N_{TL}^{\text{fake}} + N_{LT}^{\text{fake}}$ is calculated via the two-lepton matrix equation A.4. After solving for the RHS, we simply need to modify the extrapolation step to get N_{TL}^{fake} and N_{LT}^{fake}:

$$N_{TL}^{\text{fake}} = f_1\bar{\epsilon}_2 N_{FR} + f_1\bar{f}_2 N_{FF} \tag{A.26}$$

$$N_{LT}^{\text{fake}} = \bar{\epsilon}_1 f_2 N_{RF} + \bar{f}_1 f_2 N_{FF}. \tag{A.27}$$

Notice that only the terms are included which contribute a fake lepton in the tight lepton's position. For example, there is no N_{FR} term in the N_{LT}^{fake} relation. After some simplification, the total estimate is

$$\begin{aligned}
N_{TL}^{\text{fake}} &= N_{TL}^{\text{fake}} + N_{LT}^{\text{fake}} \\
&= \alpha_1 f_1(\epsilon_1 N_{LL} - \bar{\epsilon}_1 N_{TL}) + \alpha_2 f_2(\epsilon_2 N_{LL} - \bar{\epsilon}_2 N_{LT}). \tag{A.28}
\end{aligned}$$

The final result has split nicely into two pieces: the N_{TL} piece which only depends on f_1 and ϵ_1, and the N_{LT} piece which only depends on f_2 and ϵ_2. If you compare this result to equation A.3 you see that each piece is the same as the one-lepton matrix method solution. So, the combinatorics work out as a simple sum of one-lepton matrix methods considering each loose lepton independently.

This also works for a two-lepton selection which allows for additional loose leptons. This time we use the three-lepton algebra and try to reduce it down into a sum of two-lepton matrix methods. The fake estimate is $N_{TT,L}^{\text{fake}} = N_{TTL}^{\text{fake}} + N_{TLT}^{\text{fake}} + N_{LTT}^{\text{fake}}$. As before, we only

consider terms contributing fake leptons to the tight lepton positions:

$$N_{TTL}^{\text{fake}} = \epsilon_1 f_2 \bar{\epsilon}_3 N_{RFR} + \epsilon_1 f_2 \bar{f}_3 N_{RFF} + f_1 \epsilon_2 \bar{\epsilon}_3 N_{FRR}$$
$$+ f_1 \epsilon_2 \bar{f}_3 N_{FRF} + f_1 f_2 \bar{\epsilon}_3 N_{FFR} + f_1 f_2 \bar{f}_3 N_{FFF} \tag{A.29}$$

$$N_{TLT}^{\text{fake}} = \epsilon_1 \bar{f}_2 \epsilon_3 N_{RRF} + \epsilon_1 \bar{f}_2 f_3 N_{RFF} + f_1 \bar{\epsilon}_2 \epsilon_3 N_{FRR}$$
$$+ f_1 \bar{\epsilon}_2 f_3 N_{FRF} + f_1 \bar{f}_2 \epsilon_3 N_{FFR} + f_1 \bar{f}_2 f_3 N_{FFF} \tag{A.30}$$

$$N_{LTT}^{\text{fake}} = \bar{\epsilon}_1 f_2 \epsilon_3 N_{RRF} + \bar{\epsilon}_1 f_2 f_3 N_{RFR} + \bar{f}_1 \epsilon_2 \epsilon_3 N_{RFF}$$
$$+ \bar{f}_1 \epsilon_2 f_3 N_{FRF} + \bar{f}_1 f_2 \epsilon_3 N_{FFR} + \bar{f}_1 f_2 f_3 N_{FFF}. \tag{A.31}$$

After some tedious simplification, we have

$$N_{TT,L}^{\text{fake}} = N_{TTL}^{\text{fake}} + N_{TLT}^{\text{fake}} + N_{LTT}^{\text{fake}}$$
$$= \alpha_1 \alpha_2 (f_1 f_2 - f_2 \epsilon_1 \bar{\epsilon}_2 - f_1 \bar{\epsilon}_1 \epsilon_2 - f_1 \epsilon_1 f_2 \epsilon_2) N_{TTL}$$
$$+ \alpha_1 \alpha_3 (f_1 f_3 - f_3 \epsilon_1 \bar{\epsilon}_3 - f_1 \bar{\epsilon}_1 \epsilon_3 - f_1 \epsilon_1 f_3 \epsilon_3) N_{TLT}$$
$$+ \alpha_2 \alpha_3 (f_2 f_3 - f_3 \epsilon_2 \bar{\epsilon}_3 - f_2 \bar{\epsilon}_2 \epsilon_3 - f_2 \epsilon_2 f_3 \epsilon_3) N_{LTT}$$
$$+ (\alpha_1 \alpha_2 \epsilon_1 \epsilon_2 \bar{f}_1 f_2 + \alpha_1 \alpha_3 \epsilon_1 \epsilon_3 \bar{f}_1 f_3) N_{TLL}$$
$$+ (\alpha_1 \alpha_3 \epsilon_1 \epsilon_3 f_1 \bar{f}_3 + \alpha_2 \alpha_3 \epsilon_2 \epsilon_3 f_2 \bar{f}_3) N_{LLT}$$
$$+ (\alpha_1 \alpha_2 \epsilon_1 \epsilon_2 f_1 \bar{f}_2 + \alpha_2 \alpha_3 \epsilon_2 \epsilon_3 \bar{f}_2 f_3) N_{LTL}$$
$$+ (\alpha_1 \alpha_2 \epsilon_1 \epsilon_2 f_1 f_2 + \alpha_1 \alpha_3 \epsilon_1 \epsilon_3 f_1 f_3 + \alpha_2 \alpha_3 \epsilon_2 \epsilon_3 f_2 f_3) N_{LLL}. \tag{A.32}$$

Now we have the desired result. Looking at the N_{TTL}, N_{TLT}, and N_{LTT} terms, and comparing to equation A.6, we see they are the same as the two-lepton $N_T T$ terms where only the tight leptons participate. Next, we compare the N_{TLL} term to equation A.7 and see that it is a sum of two-lepton solutions using the tight and lepton and each of the loose leptons independently. Likewise, the N_{LLT} and N_{LTL} terms also break down into sums of two-lepton solutions pairing the tight lepton with the loose leptons. Finally, the N_{LLL} term breaks down

into a sum over three pieces each taking the same form as the two lepton N_{LL} term. All three pairings of loose leptons contribute in the solution.

To summarize, for one- and two-lepton selections with one additional loose lepton, the matrix method fake estimate can be broken down into a sum over smaller matrix-method solutions such that problem is solved by a simple combinatorial loop. Though it will not be done in this thesis, it is possible to show that the combinatorial loop approach extends to cases of higher numbers of additional loose leptons as well[12]

---

[12]A proof by induction is necessary to show it formally.